



HAL
open science

REDUCTION OF MISMATCH LOSSES IN GRID-CONNECTED PHOTOVOLTAIC SYSTEMS USING ALTERNATIVE TOPOLOGIES

Damien Picault

► **To cite this version:**

Damien Picault. REDUCTION OF MISMATCH LOSSES IN GRID-CONNECTED PHOTOVOLTAIC SYSTEMS USING ALTERNATIVE TOPOLOGIES. Sciences de l'ingénieur [physics]. Institut National Polytechnique de Grenoble - INPG, 2010. Français. NNT: . tel-00545432

HAL Id: tel-00545432

<https://theses.hal.science/tel-00545432>

Submitted on 10 Dec 2010

HAL is a multi-disciplinary open access archive for the deposit and dissemination of scientific research documents, whether they are published or not. The documents may come from teaching and research institutions in France or abroad, or from public or private research centers.

L'archive ouverte pluridisciplinaire **HAL**, est destinée au dépôt et à la diffusion de documents scientifiques de niveau recherche, publiés ou non, émanant des établissements d'enseignement et de recherche français ou étrangers, des laboratoires publics ou privés.

**UNIVERSITE DE GRENOBLE
INSTITUT POLYTECHNIQUE DE GRENOBLE**

N° attribué par la bibliothèque

|_|_|_|_|_|_|_|_|_|_|_|_|_|_|_|

T H È S E

pour obtenir le grade de

**DOCTEUR DE L'Université de Grenoble
délivré par l'Institut polytechnique de Grenoble**

Spécialité : Génie Electrique

préparée au laboratoire Laboratoire de Génie Electrique de Grenoble (G2ELab)

dans le cadre de l'Ecole Doctorale EEATS

« *Électronique, Électrotechnique, Automatique et Traitement du Signal* »

présentée et soutenue publiquement

par

Damien PICAULT

le 1^{er} octobre 2010

**REDUCTION OF MISMATCH LOSSES IN GRID-CONNECTED
PHOTOVOLTAIC SYSTEMS USING ALTERNATIVE TOPOLOGIES**

sous la direction de

***Bertrand RAISON
Seddik BACHA***

JURY

Pr. Daniel ROYE	, Président
Pr. Leopoldo GARCIA-FRANQUELO	, Rapporteur
Pr. Bruno BURGER	, Rapporteur
Pr. Farid MEIBODY-TABAR	, Rapporteur
Pr. Bertrand RAISON	, Directeur de thèse
Pr. Seddik BACHA	, Directeur de thèse
Pr. Gustavo NOFUENTES	, Examineur
Dr. Xavier LEPIVERT	, Examineur

« We are like tenant farmers chopping down the fence around our house for fuel when we should be using Nature's inexhaustible sources of energy—sun, wind and tide... I'd put my money on the sun and solar energy. What a source of power! I hope we don't have to wait until oil and coal run out before we tackle that. »

Thomas A. Edison (1931)

A ma famille...

Acknowledgments

This three year work could not have been possible without the trust and support of those to whom I would like to express my gratitude.

The contributions of the reviewers and jury members have improved this manuscript, for this I thank them.

I am greatly indebted to Pr. Daniel Roye (Grenoble Institute of Technology) for not only accepting to chair the jury, but for introducing me to renewable energies, an interest that I intend to continue to pursue.

I am also grateful to Pr. Bruno Burger (Fraunhofer ISE), Pr. Leopoldo Garcia-Franquelo (University of Sevilla), and Pr. Farid Meibody-Tabar (Lorraine Institute of Technology) for their fruitful comments and for reviewing the manuscript.

A special thanks to Pr. Gustavo Nofuentes (University of Jaén) and Dr. Xavier Le Pivert (CEA-INES National Institute of Solar Energy) for accepting to take part in the jury and for their pertinent remarks during the defense.

I owe a great deal to my directors Pr. Bertrand Raison (Grenoble Institute of Technology) and Pr. Seddik Bacha (University of Grenoble) whose confidence, encouragements, and insights have enabled me to successfully carry out this work.

I want to express my gratitude to Pr. Jorge Aguilera and Pr. Juan de la Casa (University of Jaén) for giving me the opportunity to work in their Solar Energy Laboratory. My *andaluz* experience will remain unforgettable thanks to the scientific expertise and the moments shared with the staff. *Nunca olvidar esa experiencia.*

Many thanks to my colleagues at the G2Elab for whose camaraderie and encouragement helped me persevere through these years successfully. *Une pensée spéciale pour les Moustacos, les anciens et nouveaux de la salle « Sangatte », et ceux qui ont pris le temps de s'arrêter au détour d'un couloir. J'ai énormément apprécié travailler dans cet esprit d'entraide et de convivialité, qui a indéniablement contribué au bon déroulement de ces travaux.*

I would like to deeply thank my friends and family whom countless supported me during these past years.

Ce travail est le fruit de toutes ces rencontres, tant pour leur soutien que pour leur complicité partagée tout au long de mon parcours. Pour cela je les remercie.

Table of contents

SYNTHESE	1
TABLE OF ABBREVIATIONS	23
GENERAL INTRODUCTION	25
CHAPTER I : GRID-CONNECTED PHOTOVOLTAIC SYSTEMS	27
I.1. OVERVIEW OF GRID-CONNECTED PV SYSTEMS	28
I.2. COMPONENTS OF GRID-CONNECTED PV SYSTEMS	29
I.3. PV MODULE TECHNOLOGIES	31
I.3.1. CRYSTALLINE SILICON.....	32
I.3.2. THIN FILM.....	32
I.3.3. NEXT GENERATION SOLAR CELLS.....	32
I.4. POWER CONVERSION UNITS FOR PV SYSTEMS	34
I.4.1. INVERTER	34
I.4.2. DC-DC CONVERTER.....	35
I.5. EVALUATION CRITERIA FOR PV SYSTEM TOPOLOGIES	35
I.5.1. PV SYSTEM PERFORMANCE.....	36
I.5.2. DEGRADED MODE MANAGEMENT.....	36
I.5.3. INVESTMENT COSTS	37
I.5.4. UPGRADEABILITY.....	38
I.6. REVIEW OF GRID-CONNECTED PV SYSTEM TOPOLOGIES	38
I.6.1. CENTRALIZED INVERTER	38
I.6.2. DYNAMIC SWITCHING ARRAY	39
I.6.3. STRING INVERTER	40
I.6.4. MULTI-STRING INVERTER	41
I.6.5. PARALLEL-CONNECTED DC-DC INVERTER.....	42
I.6.6. SERIES CONNECTED DC-DC CONVERTERS	43
I.6.7. MODULE INVERTER.....	44
I.6.8. SINGLE CELL INVERTER.....	45
CHAPTER II : MODELLING PHOTOVOLTAIC ARRAYS	49
II.1. PHOTOVOLTAIC CELL BASICS	50
II.1.1. PHOTOVOLTAIC CELL OPERATION	50
II.1.2. PHOTOVOLTAIC CELL PROTECTION APPARATUS.....	51
II.1.2.1. Overcurrent protection.....	51
II.1.2.2. Backfeed current protection.....	52
II.1.3. PHOTOVOLTAIC CELL MODELLING	52
II.2. PHOTOVOLTAIC MODULE MODELLING	55
II.2.1. ANALYTICAL LAMBERT W-FUNCTION	56
II.2.1.1. Definition	56
II.2.1.2. Infinity asymptote expression.....	57
II.2.2. ANALYTICAL EXPRESSION OF PHOTOVOLTAIC MODULE CURRENT.....	58

II.2.2.1. PV module current expression.....	58
II.2.2.2. Verification of mathematical solution existence.....	59
II.2.2.3. Usage of infinity asymptote expression.....	59
II.2.3. ANALYTICAL EXPRESSION OF PHOTOVOLTAIC MODULE VOLTAGE.....	60
II.2.3.1. PV module voltage expression.....	60
II.2.3.2. Verification of mathematical solution existence.....	61
II.2.3.3. Usage of infinity asymptote.....	61
II.2.4. SIMPLIFIED EXPRESSIONS OF PV MODULE CURRENT AND VOLTAGE.....	62
II.2.5. NUMERICAL CALCULATION OF PV MODULE CHARACTERISTICS.....	63
II.2.5.1. General presentation of Halley's Method.....	63
II.2.5.2. Halley's method applied to the PV module.....	64
II.2.5.3. Comparison between Newton-Raphson and Halley's method applied to photovoltaic modules.....	64
II.3. PV MODULE PARAMETER IDENTIFICATION	66
II.3.1. LEAST SQUARE CURVE FITTING	66
II.3.2. PARAMETER INITIALIZATION USING DATASHEET VALUES	67
II.3.3. PV MODULE PARAMETER EXTRACTION VALIDATION.....	69
II.4. MODULE PARAMETER ENVIRONMENTAL CONDITION TRANSLATION METHOD	70
II.4.1. I-V CURVE TRANSLATION METHOD	71
II.4.2. MODULE PARAMETER TRANSLATION METHOD	72
II.5. PV ARRAY WITH MODIFIABLE INTERCONNECTIONS MODELLING.....	73
II.5.1. TRADITIONAL PHOTOVOLTAIC ARRAY MODEL.....	74
II.5.1.1. Current Laws	75
II.5.1.2. Voltage Laws	75
II.5.1.3. DC-bus voltage law	75
II.5.1.4. Mathematical formulation of PV arrays	75
II.5.2. PHOTOVOLTAIC ARRAYS WITH MODIFIABLE INTERCONNECTIONS.....	76
II.5.2.1. Current law fusion.....	76
II.5.2.2. Voltage law creation	78
II.5.3. CALCULATING PHOTOVOLTAIC ARRAY CHARACTERISTICS	78
II.5.3.1. Interpreting module interconnections: Connection Matrix.....	78
II.5.3.2. Creating the array law matrixes.....	79
II.5.3.3. Solving the PV array equation system	82
CHAPTER III : REDUCING MISMATCH LOSSES WITH ALTERNATIVE ARRAY INTERCONNECTION SCHEMES	87
III.1. MISMATCH LOSSES IN PHOTOVOLTAIC ARRAYS.....	88
III.1.1. INTRINSIC PHOTOVOLTAIC MODULE MISMATCH	88
III.1.1.1 Causes of intrinsic PV module mismatch.....	88
III.1.2. Effect of intrinsic PV module mismatch on array performance.....	89
III.1.2. ENVIRONMENTAL MISMATCH	91
III.1.2.1. Causes of environmental mismatch.....	91
III.1.2.2. Impact of environmental mismatch on array performance	92
III.2. STUDY OF MISMATCH LOSSES IN SERIES-PARALLEL CONNECTED ARRAYS	95
III.2.1. PRELIMINARY VALIDATION OF SIMULATION MODEL USING EXPERIMENTAL RESULTS.....	95
III.2.1.1. Field measurements of 2.2 kW plant at Jaén University campus.....	96
III.2.1.2. Non-shaded Pergola 5 array	97

III.2.1.2. Partially-shaded Pergola 5 array	99
III.2.2. MISMATCH LOSSES IN A 2.2 kW _p BASED ON EXPERIMENTAL DATA	100
III.2.3. MISMATCH LOSSES IN PARTIALLY SHADED SERIES-PARALLEL ARRAYS	102
III.2.3.1. Influence of the number of modules per string	105
III.2.3.2. Influence of the number of strings in an array	105
III.2.3.3. Influence of shade intensity	107
III.2.3.4. Influence of shade intensity with bypass diode-equipped modules	108
III.3. ALTERNATIVE ARRAY INTERCONNECTION SCHEMES	109
III.3.1. EXPERIMENTAL RESULTS OF PERGOLA 5 ARRAY USING ALTERNATIVE INTERCONNECTION SCHEMES	110
III.3.2. PV ARRAY FORECASTING TOOL VALIDATION USING EXPERIMENTAL RESULTS	113
III.3.3. COMPARISON OF ALTERNATIVE TOPOLOGIES	115
CHAPTER IV : MISMATCH LOSS REDUCTION USING ENERGY FLOW CONTROL VIA POWER CONVERTERS	119
IV.1. AVERAGE MODELS OF POWER CONVERTERS	120
IV.1.1. AVERAGED MODELLING OF A SINGLE PHASE GRID-CONNECTED INVERTER	120
IV.1.2. REDUCED AVERAGE MODELLING OF THE DC-DC CONVERTER	122
IV.1.3. POWER CONVERSION LOSSES MODELING	125
IV.1.3.1. Power losses in IGBT switches	126
IV.1.3.2. Power losses in MOSFET switches	128
IV.1.3.3. Power losses in diodes	129
IV.2. CONTROL STRATEGIES FOR PV POWER CONVERTERS	129
IV.2.1. INVERTER CONTROL	130
IV.2.1.1. Current inversion control	130
IV.2.1.2. DC bus voltage control	131
IV.2.2. DC-DC CONVERTER CONTROL	133
IV.2.2.1. Maximum Power Point Tracking implementation	134
IV.2.2.2. Efficiency of MPPT algorithms	135
IV.2.3. SERIES-CONNECTED DC-DC CONVERTER CONTROL STRATEGY	137
IV.2.3.1. Normal Operation Mode	139
IV.2.3.2. Degraded Operation Mode	140
CHAPTER V : ANALYSIS OF PV SYSTEM TOPOLOGIES	143
V.1. POWER PRODUCTION PERFORMANCE	144
V.1.1. RESIDENTIAL PV SYSTEMS	145
V.1.2. COMMERCIAL-SIZED PV SYSTEMS	147
V.2. DEGRADED MODE MANAGEMENT EVALUATION	150
V.3. INVESTMENT COSTS	152
V.4. UPGRADEABILITY	154
V.5. TOPOLOGY GRADING METHOD	156
V.5.1. TOPOLOGY SCORE CALCULATION	157
V.5.2. TOPOLOGY GRADING METHOD	159
GENERAL CONCLUSION	163
BIBLIOGRAPHY	165

PUBLICATIONS..... 173

**ANNEX 1: INFLUENCE OF SINGLE DIODE MODEL PARAMETERS
ON THE I-V CHARACTERISTICS OF PV CELLS..... 177**

ANNEX 2 : PV MODULE MODEL USING LAMBERTW-FUNCTION 181

ANNEX 3 : PARAMETER TRANSLATION RESULTS 183

**ANNEX 4 : APPLYING THE NEWTON-RAPHSON METHOD
FOR PV ARRAY MODEL SOLVING 187**

ANNEX 5 : TOPOSOLVER OVERVIEW..... 191

ANNEX 6 : ISOFOTON I-106 MODULES..... 195

ANNEX 7 : CONNECTION BOX 197

ANNEX 8 : 200 W_P SIMULATION PV MODULE..... 199

ANNEX 9 : PV ARRAY POWER FORECASTING RESULTS..... 201

ANNEX 10 : POWER ELECTRONICS DATASHEET VALUES 211

ANNEX 11 : PI CORRECTOR COEFFICIENT CALCULATIONS..... 213

Synthèse

La demande d'énergie n'a cessé de croître à travers le monde afin de fournir à ses habitants une qualité de vie plus confortable. Récemment, cette demande toujours croissante a suscité l'attention compte tenu de la réduction des ressources fossiles, de l'efficacité énergétique, et du réchauffement climatique, et amène progressivement nos sociétés à rechercher des sources d'énergies alternatives. Les énergies renouvelables ont été mises en avant afin de réduire notre dépendance au pétrole en convertissant l'énergie du soleil, du vent, ou encore de la biomasse en nos vecteurs énergétiques principaux : la chaleur et l'électricité. Dans les années 1950, les recherches ont porté sur les systèmes énergétiques autonomes, visant principalement les applications aérospatiales, et ont mené à la mise au point de la production d'électricité à partir d'énergie solaire par des cellules photovoltaïques (PV). Aujourd'hui, les technologies de cellules PV ont mûri et se sont répandues pour fournir de l'énergie aux systèmes autonomes, mais surtout ceux connectés au réseau électrique.

Au sein des installations PV connectées au réseau, plusieurs champs d'applications se sont développés allant des grandes centrales au plus petites de type résidentiel. Les accords internationaux ainsi que les politiques d'incitation nationales ont stimulé les entreprises et les particuliers pour utiliser l'énergie solaire en vue de produire de l'électricité. Ceci a suscité de l'intérêt dans l'utilisation et l'économie de cette ressource d'énergie intermittente. De plus, l'attractivité des centrales solaires a amené les autorités Françaises, les industriels du domaine, et des laboratoires de recherche à travailler ensemble au sein du projet Solution PV afin de trouver des solutions pour augmenter la production des centrales PV en révisant leur conception. En effet, l'expansion des centrales solaires terrestres a montré que dans la plupart des cas, la puissance produite par les centrales était plus faible que celle attendue, ces pertes par couplage des modules sont le plus communément appelées pertes par mismatch.

L'objectif de ces travaux est d'étudier les pertes par mismatch et de proposer des solutions pour réduire leur impact sur les champs PV. Ce travail est scindé en cinq parties qui présentent successivement la conception actuelle des centrales PV connectées au réseau et les solutions alternatives proposées pour augmenter leur niveau de production. Tout d'abord, un état de l'art de la chaîne de conversion des systèmes solaires sera présenté dans le premier chapitre. Les composants actuels des systèmes connectés au réseau, allant des modules jusqu'au convertisseur de puissance, ainsi que les structures les plus récentes seront exposées. Des éléments pour évaluer et comparer les performances des architectures de centrales PV seront également introduits. Le deuxième chapitre présentera les modèles électriques des cellules et champs solaires afin de prévoir leur production lorsqu'ils sont soumis à des conditions de fonctionnement diverses. Les techniques de modélisation d'éléments PV ainsi qu'une méthode développée au cours de ces travaux pour prévoir la production de centrales seront détaillées. Dans cette thèse, deux solutions pour réduire les pertes par mismatch ont été traitées séparément: l'utilisation de schémas de câblage alternatifs des champs PV et le contrôle des flux d'énergies grâce à de l'électronique de puissance. Le

troisième chapitre montrera l'intérêt d'ajouter des interconnexions au sein du schéma de câblage traditionnel de champs solaires afin de réduire les pertes par mismatch. Cette première solution sera étudiée à travers des résultats de simulation et validée grâce à des relevés expérimentaux menés sur une centrale de type résidentiel. Dans le chapitre IV, les modèles des convertisseurs de puissance ainsi que leur stratégie de contrôle appliquée au domaine PV seront présentés. De plus, la performance des algorithmes MPPT pour les champs solaires sera examinée. Dans le dernier chapitre, la deuxième solution consistant à introduire de l'électronique de puissance à l'intérieur du champ solaire pour réduire les pertes par mismatch sera analysée. En se fondant sur les résultats de simulations des modèles présentés auparavant, l'efficacité des deux solutions dans plusieurs scénarios d'ombrage sera comparée. Enfin, une comparaison globale des solutions proposées sera conduite en intégrant les critères d'évaluation des systèmes photovoltaïques. Dans la conclusion, les éléments clefs de ces travaux seront résumés et les perspectives de travail seront développées.

Chapitre I : Systèmes photovoltaïques connectés au réseau

Cent ans après la découverte de l'effet photovoltaïque par Edouard Becquerel en 1839, la première cellule capable de convertir l'énergie solaire en courant électrique fut mise au point par des chercheurs Américain de Bell Labs. Depuis, les applications PV se sont répandues afin de fournir de l'énergie allant des appareils portables aux centrales de production d'énergie électrique. Récemment, les inquiétudes mondiales sur le changement climatique et la réduction des émissions de carbones ont entraîné une forte croissance des installations photovoltaïques connectées au réseau. A la fin de l'année 2008, les systèmes PV connectés au réseau représentaient 95% des 13,4 GW installés à travers le monde [PVPS'09]. Même si la part des systèmes PV connectés au réseau est prévue de décroître dans le futur, elles représenteront 70% des systèmes PV en 2030 avec une majorité de nouvelles installations en Amérique du Sud et en Asie [SGV'08].

Les centrales solaires connectées au réseau électrique sont composées de plusieurs éléments en vue de garantir un fonctionnement sécurisé : modules PV, convertisseurs de puissance, appareillage de protection électrique, et dispositifs de surveillance. Puisque les modules PV produisent du courant continu, un onduleur est requis pour assurer la connexion au réseau. De plus, un dispositif permettant de suivre le point de puissance maximum du champ PV, mieux connu sous l'appellation Maximum Power Point Tracker (MPPT), est utilisé afin d'extraire le maximum d'énergie de la centrale solaire. Des disjoncteurs sont situés au point de raccordement de la centrale PV afin d'isoler le système lors de défauts sur le réseau ou de réaliser la maintenance de l'installation. La plupart des systèmes contiennent également un disjoncteur pour courant continu installé entre le champ solaire et l'onduleur pour des raisons similaires et pour assurer la protection de l'onduleur contre la foudre. Enfin, des compteurs électriques sont installés au point de raccordement du réseau pour mesurer la production énergétique de la centrale mise sur le réseau et sa

consommation éventuelle. Des schémas de raccordement comportant des systèmes de stockage, le plus souvent des batteries, sont également possibles. Ces installations sont dites sécurisées car elles peuvent fournir à certaines charges du courant lors de pannes du réseau électrique.

Le module PV est composé de plusieurs cellules qui permettent de transformer les photons de la lumière en électrons à travers l'effet photovoltaïque. Plusieurs technologies de cellules coexistent, mais aujourd'hui deux technologies prédominent le marché : le silicium cristallin (90%) et les couches minces (10%). Actuellement, le silicium est très utilisé pour ses propriétés intrinsèques et sa grande disponibilité (c'est le deuxième élément le plus abondant sur Terre). Les technologies au silicium cristallin se distinguent en deux groupes : monocristallin (mono-Si) et polycristallin (poly-Si). Les cellules monocristallines sont constituées d'un seul cristal, ce qui leur confèrent des rendements de conversion supérieurs, alors que les cellules polycristallines sont composées de plusieurs cristaux, ce qui les rend moins chères que les mono-Si. En 2007, les cellules mono-Si et poly-Si représentaient respectivement 43% et 47% du marché PV. La technologie couches minces est la deuxième génération de cellules solaires qui appliquent un semi-conducteur photo-actif sur un substrat à bas coût, ce qui permet de réduire considérablement leur coût de fabrication. Enfin, il existe des technologies de générations futures: organiques, multi-jonction, ou à pigment photosensible. Les rendements et coût des technologies PV sont présentés sur le Tableau 1.

	Part de marché en 2007 [%]	Technologie	Rendement [%]	Coût [€/Wc]
Première Génération	43	Mono-Si	18-25	2,5-3
Silicium Cristallin	47	Poly-Si	12-20	2,5-3
Deuxième Génération		a-Si	6-9	1,5-2
Couches Minces	10	CIGS	9-15	1-1,5
		CdTe	10-16	1-1,5
Troisième Génération	N/A	Organique	4-6	<0,5
		Pigment photosensible	8-11	<0,5
		Multi-jonction	30-40	>3

Tableau 1 : Technologies de cellules photovoltaïques [PWC'09][GRE'09]

L'énergie produite par les modules solaires doit ensuite être transformée, cela se fait grâce aux convertisseurs de puissance : hacheur et onduleur. La conversion de puissance se fait grâce à des interrupteurs de puissance, tel que IGBT et MOSFET, qui peuvent être contrôlés à l'état passant et bloqué. L'onduleur transforme le courant continu en courant alternatif tandis que le hacheur, situé en amont de l'onduleur, tâche d'extraire la puissance maximale du champ solaire. L'onduleur contrôle également la puissance active et réactive fournie au réseau, son taux de distorsion harmonique, ainsi que la détection de fonctionnement en îlotage de la centrale. Dans ce travail, le hacheur élévateur Boost sera utilisé pour extraire l'énergie du champ PV au moyen d'une commande MPPT adaptée. Le rendement des hacheurs dépend fortement de la conception, des composants et du niveau de puissance du système à alimenter et est compris entre 70-95%, tandis que les onduleurs ont des rendements au-delà des 95%.

Les systèmes PV sont conçus pour produire le maximum d'électricité lorsque la ressource solaire est disponible afin de fournir l'énergie au réseau électrique ou à des charges. Dans les deux cas, pendant la phase de conception, les professionnels du secteur doivent choisir une architecture de centrale adaptée à leurs besoins. Plusieurs facteurs comme la ressource solaire, l'environnement proche, la puissance de l'installation, ainsi que les coûts d'investissements doivent être pris en considération. Il existe plusieurs manières d'organiser une centrale solaire allant d'un onduleur unique aux topologies modulaires utilisant un onduleur par module. Afin de comparer la performance de ces architectures, des critères d'évaluation sont nécessaires. Dans cette étude quatre critères sont présentés : performance en conditions normales, gestion des modes de fonctionnement dégradés, coûts d'investissement et évolutivité de l'installation.

Une diversité d'architectures d'installations connectées au réseau a accompagné l'expansion des centrales solaires terrestres, en proposant différents agencements des modules PV avec de l'électronique de puissance pour augmenter l'énergie produite et la fiabilité de l'installation. L'étude bibliographique menée a permis d'identifier six architectures principales qui sont représentées sur la Figure 1.

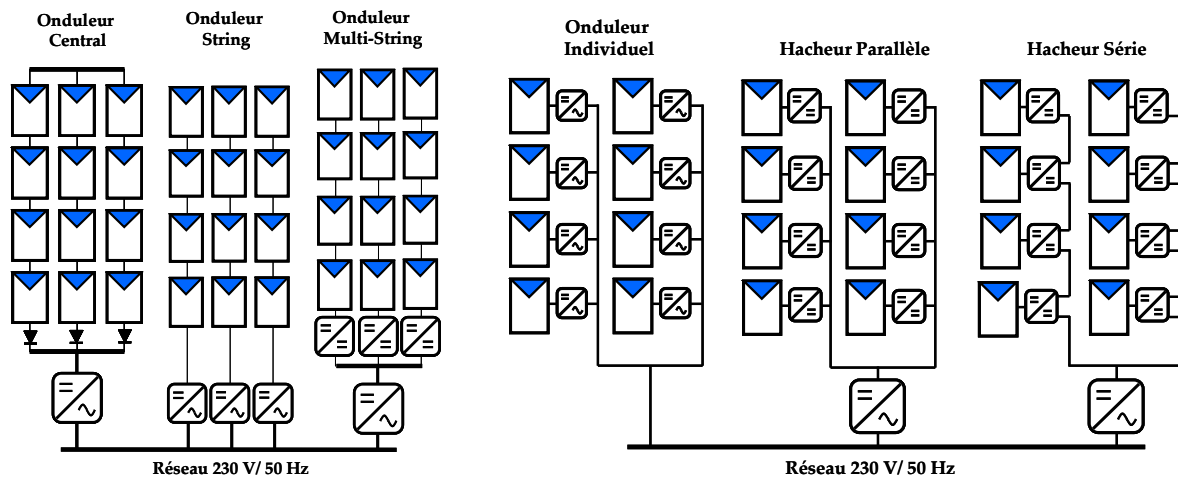


Figure 1 : Schéma des topologies de centrales PV connectées au réseau

L'architecture la plus répandue de nos jours est le montage onduleur central qui consiste à utiliser un seul onduleur interfaçant le champ solaire avec le réseau électrique. Dans cette configuration, le nombre de modules connectés en série est déterminé de telle sorte à correspondre à la plage de tension d'entrée de l'onduleur, puis ensuite plusieurs strings sont connectés en parallèle afin de répondre à la contrainte de puissance de l'installation. L'onduleur central a le plus souvent une plage d'entrée de tension variable, ce qui est possible grâce à la présence d'un hacheur élévateur installé à l'intérieur du dispositif. Cette architecture est très attractive car elle est peu coûteuse, simple à entretenir et à surveiller. Par contre, l'utilisation d'un seul MPPT pour le champ entier ne rend pas optimale l'extraction de puissance du champ ; en particulier lorsque celui-ci est partiellement ombré. Une structure semblable consiste à introduire une matrice de connexion, à laquelle chaque module du champ est connecté, et qui permet une optimisation des connexions entre modules grâce à une mesure individuelle de leur ensoleillement.

L'onduleur string consiste à utiliser un onduleur par chaîne, aussi appelée string, de modules. Ceci a pour effet d'augmenter le nombre de MPPT dans le champ et permet une meilleure continuité de service par rapport au montage centralisé, lors d'une défaillance de l'onduleur par exemple. Cependant, le coût global de l'installation augmente et les rendements des onduleurs string sont faibles lorsque la ressource solaire est diffuse. Afin d'augmenter le rendement des onduleurs lors d'ensoleillements faibles, une amélioration appelée team concept a été mis au point. Le team concept consiste à réduire le nombre d'onduleurs qui transforment la puissance de la centrale en implantant des interrupteurs DC commandés entre les strings, au niveau de l'onduleur. De manière analogue, l'onduleur multi-string permet d'utiliser un seul onduleur, tout en conservant la possibilité d'utiliser un MPPT par string en utilisant un hacheur par string. L'intérêt principal est de réduire le coût d'investissement par rapport à l'utilisation d'onduleurs string en regroupant l'inversion du courant en un seul élément. Par contre, la continuité de service et l'évolutivité de ce montage sont réduites compte tenu du nœud de puissance créé par cet onduleur unique.

Des systèmes plus modulaires ont également vu le jour pour se rapprocher au plus de la source d'énergie tels que les montages onduleur individuel (ou module AC), hacheur parallèle, et hacheur série. L'avantage de ces architectures est de réduire l'impact d'un module sur le fonctionnement global du champ, ce qui permet toujours d'extraire le maximum d'énergie du champ PV. En contrepartie, l'introduction d'électronique de puissance complexifie considérablement l'installation et la maintenance du système. L'onduleur individuel permet directement au module de fournir de l'énergie au réseau. Quant à la topologie hacheur parallèle, elle utilise un hacheur par module connecté à un bus continu de tension plus élevée (400 V), auquel est relié un onduleur. Enfin, le montage hacheur série utilise lui aussi un hacheur par module, mais ceux-ci sont connectés en série afin d'augmenter le rendement de conversion du hacheur. Les montages utilisant un hacheur par modules sont aussi appelées modules DC.

Pour conclure, les architectures centralisées ont l'avantage d'être simples et peu onéreux alors que les structures modulaires offrent parfois une meilleure évolutivité, continuité de service, et monitoring mais sont plus coûteuses comme le montre le Tableau 2.

	Simplicité	Évolutivité	Coûts d'investissement	Continuité de service
Onduleur Central	✓✓	✗	€	✗✗
Onduleur String	✓	✓	€€	✓
Onduleur Multi-string	✓	✗	€€	✗
Modules AC	✗	✓✓	€€€€	✓✓
Modules DC	✗	✓	€€€€	✗

Tableau 2 : Tableau comparatif des topologies d'installations PV suivant les critères d'évaluation

Chapitre II : Modélisation des champs photovoltaïques

Le développement des centrales PV a exigé des techniques de modélisation fiables pour prévoir la production énergétique du champ solaire. L'objectif de ce chapitre est de décrire la modélisation des systèmes solaires, allant de la cellule PV jusqu'au champ solaire en utilisant de nouveaux modèles développés. Par ailleurs, une méthode pour extraire les paramètres des modules PV à partir de relevés expérimentaux sera traitée. Les conditions météorologiques ayant un impact considérable sur le fonctionnement des modules PV, l'influence de l'ensoleillement et la température du module sur sa production électrique sera également menée. Enfin, les équations électriques permettant de décrire le fonctionnement de champ solaires seront présentées afin de construire un outil de prévision précis pour la production d'énergie.

La cellule PV est l'élément de base permettant la conversion des photons issus de la lumière en électron. Sa caractéristique courant-tension ressemble à celle d'une diode Shockley et peut fonctionner dans trois quadrants: source de puissance (zone I), charge de surintensité (zone II), et charge à contre-courant (zone IV) comme le montre la Figure 2.

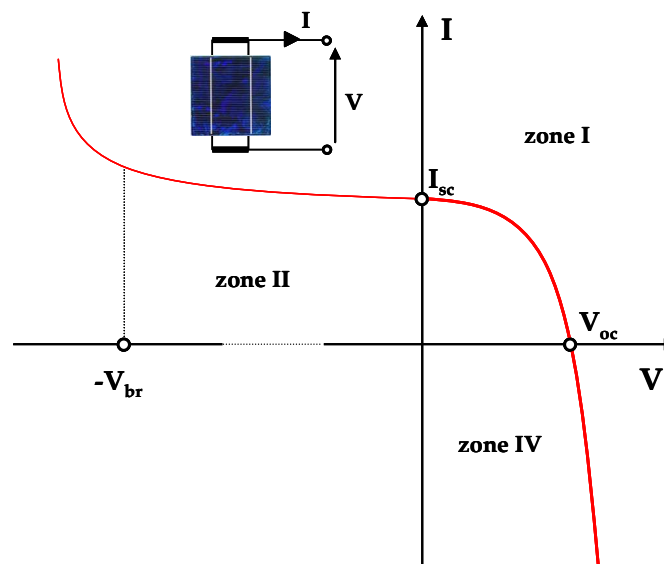


Figure 2: Caractéristique courant-tension d'une cellule photovoltaïque

En fonctionnement nominal, les cellules PV sont utilisées pour produire de l'énergie avec une tension de circuit ouvert (V_{oc}) d'environ 0.6 V pour les technologies cristallines et des courants de court-circuit (I_{sc}) de plusieurs ampères suivant la surface de la cellule et de sa technologie. La cellule PV peut aussi fonctionner en charge de surintensité ou à contre-courant ce qui peut la détruire irrémédiablement. Afin d'éviter ces modes de fonctionnement des appareillages de protection sont utilisés: diodes bypass et protection contre-courant. Les diodes bypass permettent d'éviter qu'un courant de surintensité circule à travers les cellules en lui proposant un chemin alternatif. Pour éviter le fonctionnement de la cellule en contre-courant, des fusibles ou diode sont implantées en entrée d'un string de cellules.

Plusieurs modèles de cellules PV existent et varient en complexité et en précision. Celui qui sera retenu dans ces travaux concerne le modèle à une diode qui contient cinq paramètres présentés sur la Figure 3.

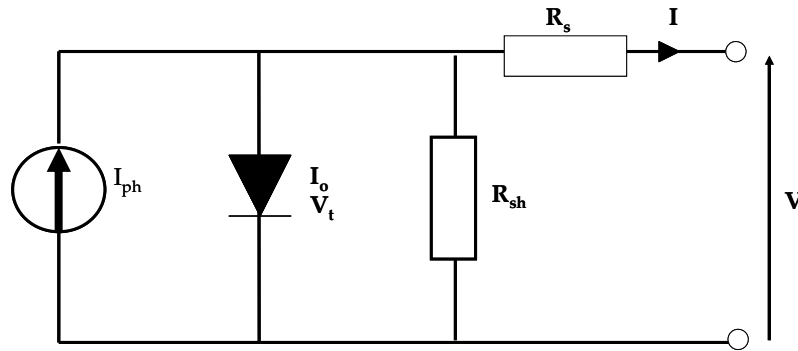


Figure 3 : Schéma électrique du modèle à une diode avec les paramètres I_{ph} , I_o , V_t , R_s , et R_{sh}

Le modèle à une diode est associé à l'équation transcendante reliant le courant du module et sa tension présentée ci-dessous.

$$I = I_{ph} - I_o \cdot \left(e^{\frac{V + R_s \cdot I}{V_t}} - 1 \right) - \frac{V + R_s \cdot I}{R_{sh}} \quad 1$$

La résolution de cette expression se fait en utilisant des méthodes numériques, telle que Newton-Raphson, qui peuvent être longues à converger. C'est pour cela que la recherche d'une solution analytique pouvant exprimer directement le courant en fonction de la tension du module, ou inversement, s'est avéré intéressante pour prévoir la production des modules en un temps limité.

A l'aide de la fonction Lambert W, introduit par J.H. Lambert en 1758 puis mis au point par E.M. Wright en 1959, l'expression analytique du courant en fonction de la tension, et son inverse, ont pu être explicités. Pour réduire la complexité de la formule, des approximations ont été faites et ont abouti aux équations 2 et 3.

$$I = \frac{V_t}{R_s} \cdot \left[\frac{R_s \cdot (I_{ph} + I_o)}{V_t} - W \left(\frac{I_o}{V_t} \cdot R_s \cdot e^{\frac{V}{V_t}} \cdot e^{\frac{R_s \cdot (I_{ph} + I_o)}{V_t}} \right) \right] - \frac{V}{R_{sh}} \quad 2$$

$$V = V_t \cdot \left[\frac{R_{sh}}{V_t} \cdot (I_{ph} + I_o - I) - W \left(\frac{R_{sh} \cdot I_o}{V_t} \cdot e^{\frac{R_{sh} \cdot (I_{ph} + I_o - I)}{V_t}} \right) \right] - R_s \cdot I \quad 3$$

Afin d'évaluer l'intérêt d'utiliser l'expression analytique (Lambert W) par rapport à la méthode de résolution numérique (Newton-Raphson), les deux méthodes ont été utilisées pour calculer les courants correspondant à un vecteur de tensions ayant un nombre de valeurs variables : 100, 500, 1000, 1500 et 2000 points. Les temps de calcul pour chaque méthode sont présentés sur la Figure 4. Ces résultats montrent que la méthode analytique est approximativement 1000 fois plus rapide que la méthode numérique. Pour cette raison la méthode analytique sera utilisée pour les calculs lourds, comme pour celui de la prévision de production d'un champ solaire.

Des travaux de recherche récents portant sur la conception de modules PV ont montrés l'intérêt de modifier le câblage des cellules afin de réduire les pertes par mismatch. Des schémas alternatifs de câblage ont été proposés et simulés grâce à des algorithmes spécifiques pour chaque topologie. Un aspect de ces travaux est de proposer un modèle global qui permet de simuler tout type de topologies grâce à un unique algorithme.

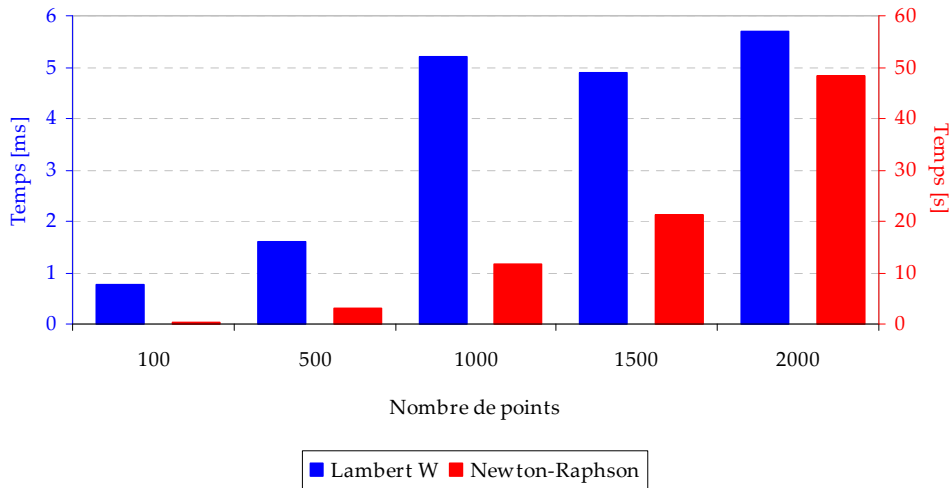


Figure 4 : Temps de simulation des méthodes analytiques (Lambert W) et numérique (Newton-Raphson) pour un nombre de points variables

En considérant qu'un champ solaire est composé de N strings contenant M modules par string, nous pouvons déterminer $(M-1) \cdot N$ nœuds et $(M-1) \cdot (N-1)$ connexions possibles, respectivement illustrés par les nœuds $N_{i,j}$ et les carrés verts $ConMat_{i,j}$ sur la Figure 5. Trois types d'équations permettent de décrire le comportement de chaque module dans le champ : lois de courants, lois de tension, et loi de tension du bus continu. Le programme informatique élaboré repose sur la résolution d'équations matricielles et permet de déterminer la caractéristique d'un champ solaire et du point de fonctionnement de chacun de ses modules sous diverses conditions d'ensoleillement et de température, qu'elles soient homogènes ou hétérogènes sur le champ PV. Grâce à des règles simples de fusion ou de création d'équations suivant la position de l'interconnexion $ConMat_{i,j}$ établie, la caractéristique I-V du champ peut être tracée.

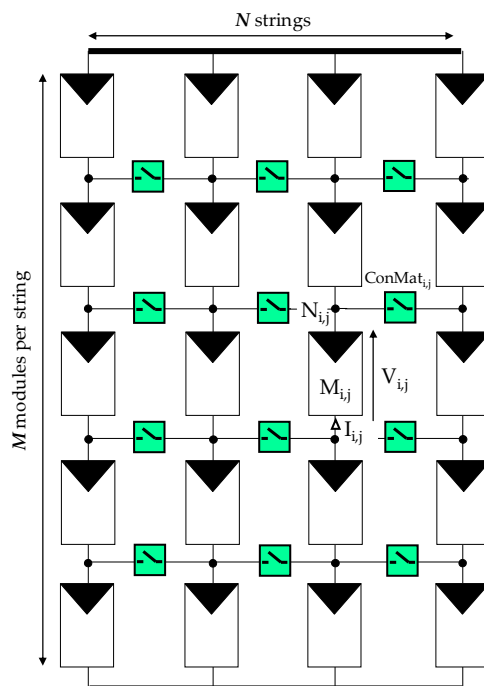


Figure 5 : Schéma d'un champ solaire avec des interconnexions modifiables

Un exemple d'application utilisant un schéma d'interconnexion et un scénario d'ombrage personnalisé est présenté sur la Figure 6.

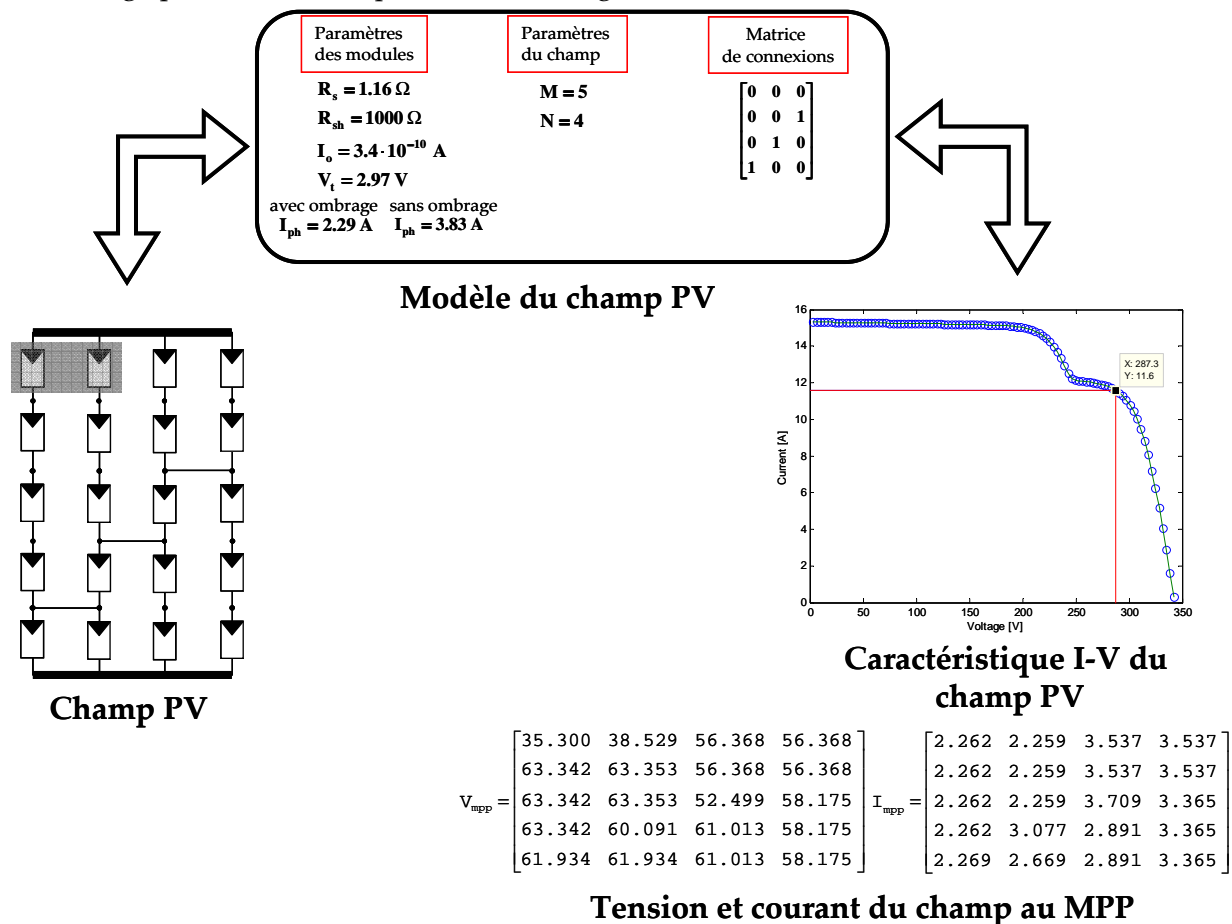


Figure 6 : Exemple de la caractéristique d'un champ solaire utilisant la méthode proposée

Enfin, le programme développé au cours de ces travaux, baptisé *Toposolver*, prend également en compte la translation de caractéristiques I-V de modules pour déterminer leur production dans divers conditions d'ensoleillement et de température. Ce logiciel permet donc de prévoir la production d'un champ réel, en utilisant des relevés expérimentaux, configurés sous différents schémas d'interconnexions et de conditions météorologiques.

Chapitre III : Réduction des pertes par mismatch en modifiant les interconnexions du champ photovoltaïque

Le retour d'expérience de l'exploitation de centrales solaires terrestres a révélé l'incapacité des champs à extraire la totalité de la puissance disponible par les cellules solaires. Ces pertes, mieux connues sous le nom de pertes par mismatch, sont dues à l'hétérogénéité électrique des cellules au sein du champ. Dans ce chapitre, les différentes causes du mismatch seront examinées. Grâce au logiciel de simulation développé, les résultats de simulations tâcheront de mettre en évidence comment évoluent ces pertes dans un champ connecté en série-parallel. L'influence des interconnexions au sein du champ PV sur les pertes mismatch sera également traitée. Des résultats expérimentaux seront confrontés aux simulations afin de valider le modèle informatique décrit dans le chapitre

précédent. Enfin, les performances des schémas de connexion alternatifs seront comparées au schéma traditionnel.

Le retour d'expérience de centrales solaires réelles a pu mettre en évidence que celles-ci produisent généralement moins que leur puissance nominale. La différence entre la puissance maximale du champ PV et la somme des puissances maximales de chaque module est appelée perte par mismatch. Les pertes par mismatch sont essentiellement provoquées par la dispersion des caractéristiques électriques des modules du champ PV. En effet, le plus souvent, les modules composant un champ n'ont pas exactement le même comportement électrique à cause de leur propriété intrinsèques ou bien de leur environnement de fonctionnement. Ceci provoque des pertes par couplage. Les propriétés intrinsèques des modules peuvent être différentes pour plusieurs raisons : tolérances des fabricants de modules PV, dégradation lumineuses ou physiques des cellules au cours de leur vie et détérioration de la cellule lors de son fonctionnement (effet hot spot). L'autre cause principale de mismatch est celle causée par l'environnement du champ et plus particulièrement la distribution de l'ensoleillement et de la température. La caractéristique courant-tension des modules PV varie avec l'ensoleillement et la température comme le montre la Figure 7. Si les modules du champ PV reçoivent un ensoleillement identique et fonctionnent à la même température, alors le mismatch environnemental n'aura pas lieu. En pratique, des ombres sont souvent projetées sur le champ à un moment de la journée, que ce soit dû à des nuages, des arbres, bâtiments ou autres objets aux alentours. Les causes du mismatch peuvent donc être classifiées en deux catégories : celles causées par la dispersion des propriétés électrique intrinsèques et celles causées par l'environnement de fonctionnement des modules.

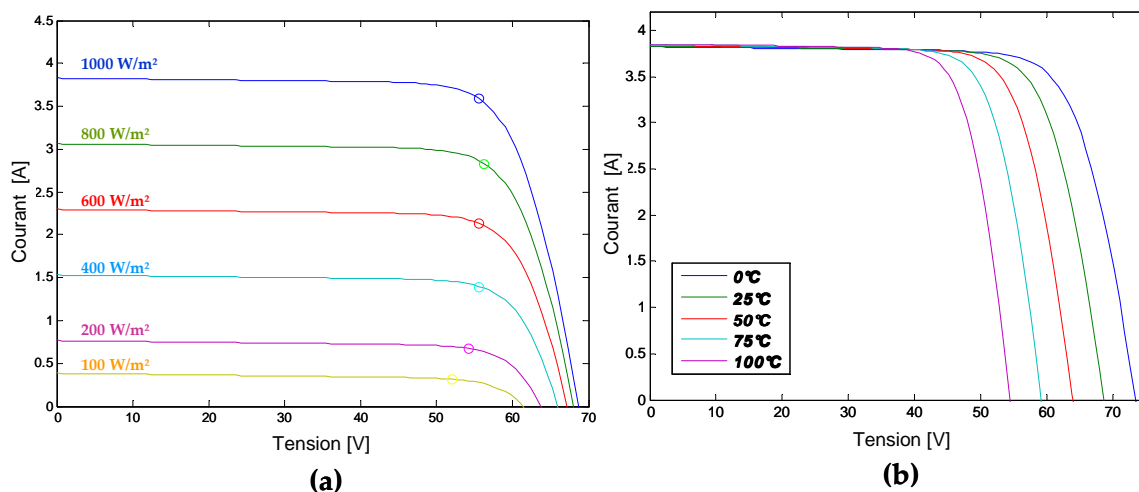


Figure 7 : Influence de (a) l'ensoleillement @25°C et de (b) la température @1000 W/m² sur la caractéristique I-V d'un module en silicium cristallin

Des exemples simulés ont pu mettre en évidence la prédominance des pertes par mismatch causées par l'environnement sur celui des propriétés intrinsèques des modules, particulièrement lorsque ceux-ci sont connectés en série. Pour cette raison, la suite de l'étude se concentrera sur l'influence de l'ombrage partiel d'un champ sur sa production.

Afin de valider l'outil de prévision de production de centrales solaires, une campagne de mesure a été menée sur une centrale 2.2 kW_c à l'Université de Jaén en Espagne. Cette centrale, visible en rouge sur la Figure 8(a), a été reconfigurée à l'aide d'un boîtier de connexion pour réaliser différents schémas d'interconnexion du champ.

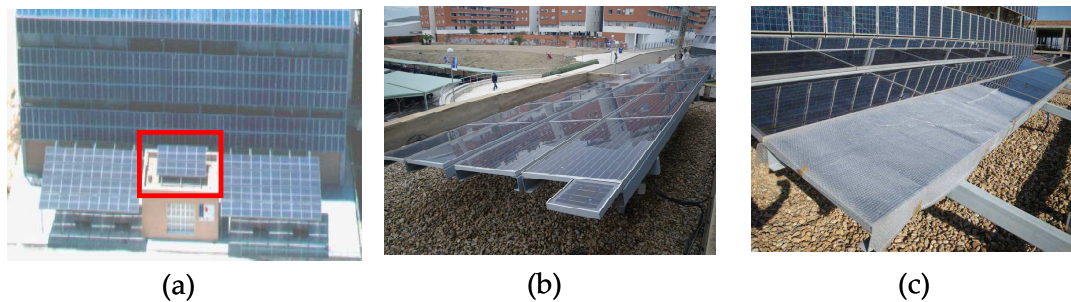


Figure 8 : Photographies (a) du champ PV Pergola 5 de 2,2 kW_c (b) sans ombre, et (c) partiellement ombré

Plusieurs mesures ont été effectuées avec ou sans ombrage sur la centrale comme il peut être vu sur les Figure 8(b) et (c). Les relevés expérimentaux ont alors été confrontés aux résultats de simulations. Les résultats sont présentés sur la Figure 9. Ces résultats montrent une bonne correspondance du modèle développé avec les données expérimentales, surtout dans le cas sans ombrage. Dans le cas où la centrale est partiellement ombrée, la forme de la courbe reste similaire mais l'on peut constater un écart dû principalement à la modélisation de la diode bypass, des équations de translations, et de l'extraction de paramètres. Cependant, la puissance crête de la centrale est correctement estimée et présente seulement une erreur de 2.2% par rapport à la mesure réelle.

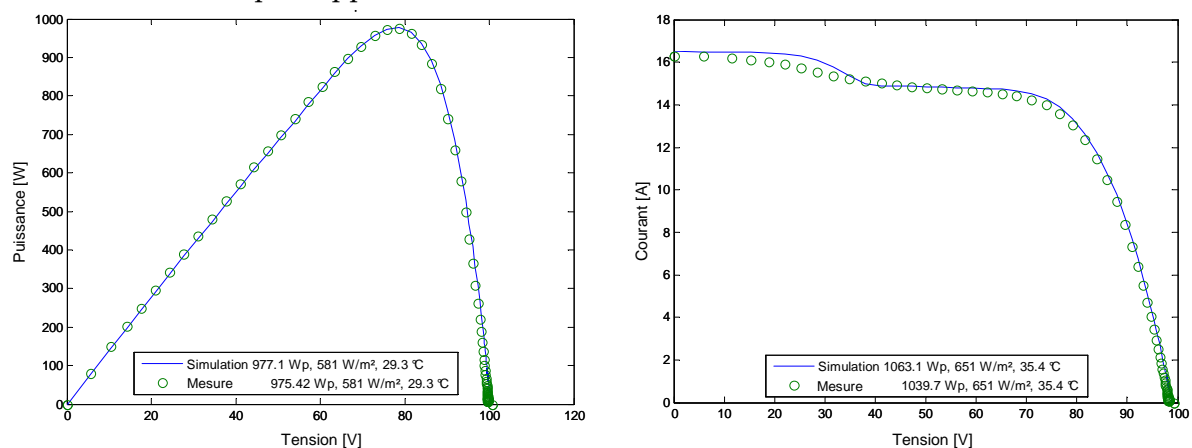


Figure 9 : Courbes expérimentale et simulée du P-V du champ PV (gauche) sans ombrage et (droite) partiellement ombré

L'outil de simulation a ensuite été utilisé pour étudier l'évolution des pertes par mismatch dues à l'ombrage suivant la position de l'ombre. La corrélation linéaire entre le nombre de modules ombrés dans un champ et la quantité de pertes par mismatch a pu être établie. La présence de droites de mismatch, décrit par des traits sur la Figure 10, ainsi que leur évolution avec le nombre de modules par string, le nombre de strings, l'intensité de l'ombre et la présence de diode bypass est détaillée dans le manuscrit. Les résultats ci-dessous montrent que les diodes bypass permettent de réduire considérablement les pertes par mismatch en écartant les points de fonctionnement des droites de mismatch, présenté sur la Figure 10(b), en provoquant un fonctionnement non linéaire au champ PV.

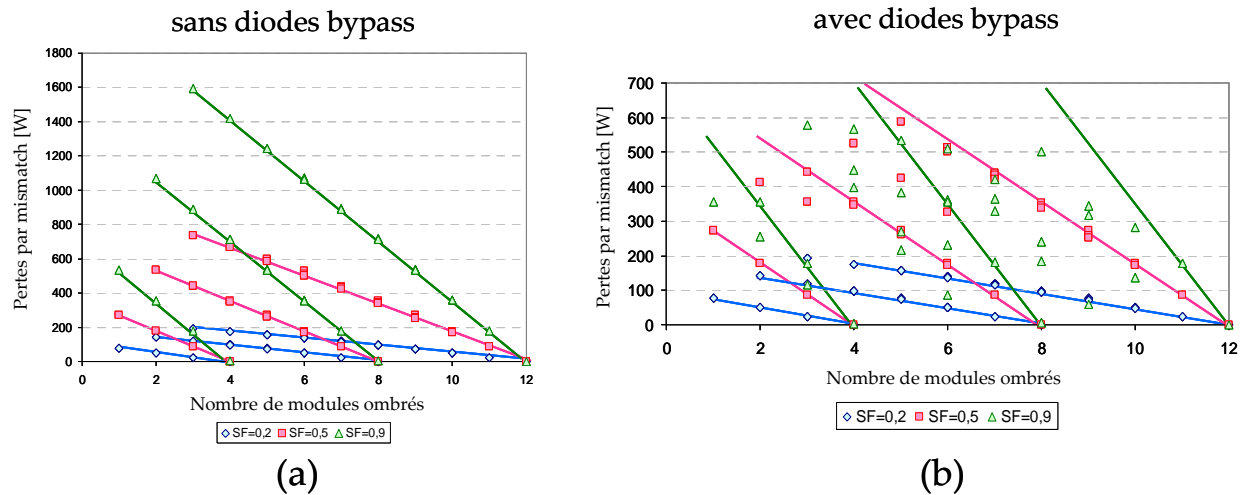


Figure 10 : Évolution des pertes par mismatch dans un champ PV de 12 modules avec différents taux d'ombrage (a) sans diode bypass et (b) avec diode bypass

Des recherches portant sur l'influence de l'ombrage sur la production de champs solaires ont suscité l'intérêt de reconfigurer le câblage des cellules solaires en vue de réduire les pertes par mismatch au sein d'un module. L'application de cette solution au champ PV, en considérant des modules et non plus des cellules, a mené à la première solution consistant à ajouter des connexions supplémentaires entre les modules de strings adjacents. Trois schémas de connexions alternatifs (BL, TCT, et HC présentés sur la Figure 11) ont été retenues pour être comparé au câblage traditionnel en série-parallèle (SP).

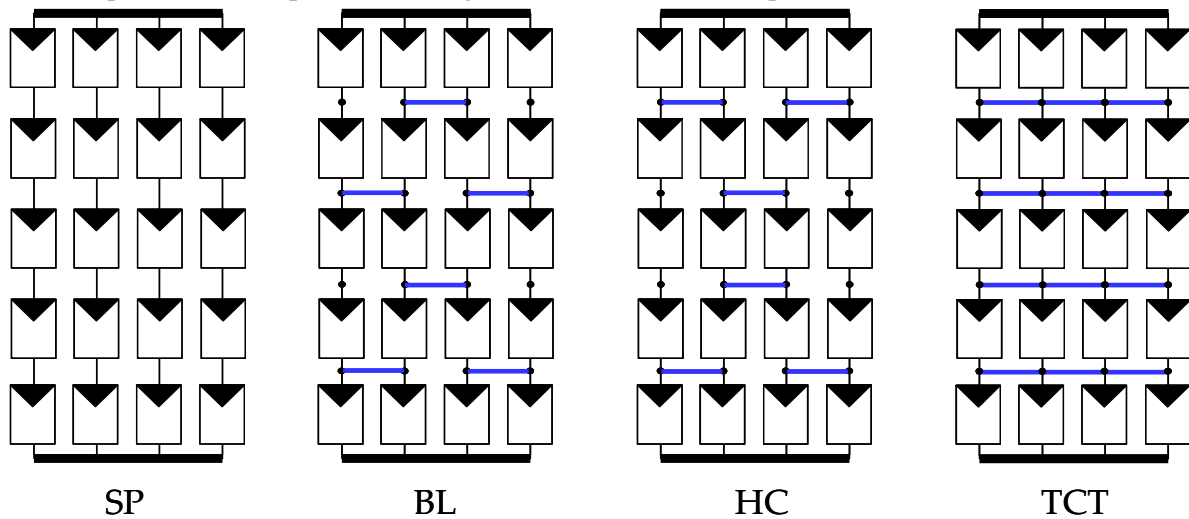


Figure 11 : Schéma de câblage des champs en série-parallèle (SP), en pont (BL), en cuillère à mile (HC), et totalement interconnecté (TCT)

Afin de vérifier expérimentalement les résultats de simulations trouvés dans la littérature, des essais sur champs réels ont été menés sur la centrale Pergola 5 pour comparer la production de la centrale dans différents scénarios d'ombrage pour les trois configurations : SP, BL, et TCT. Les résultats expérimentaux, présentés sur la Figure 12, montrent que les schémas de câblage alternatifs ont des pertes par mismatch plus faibles que la structure SP traditionnelle.

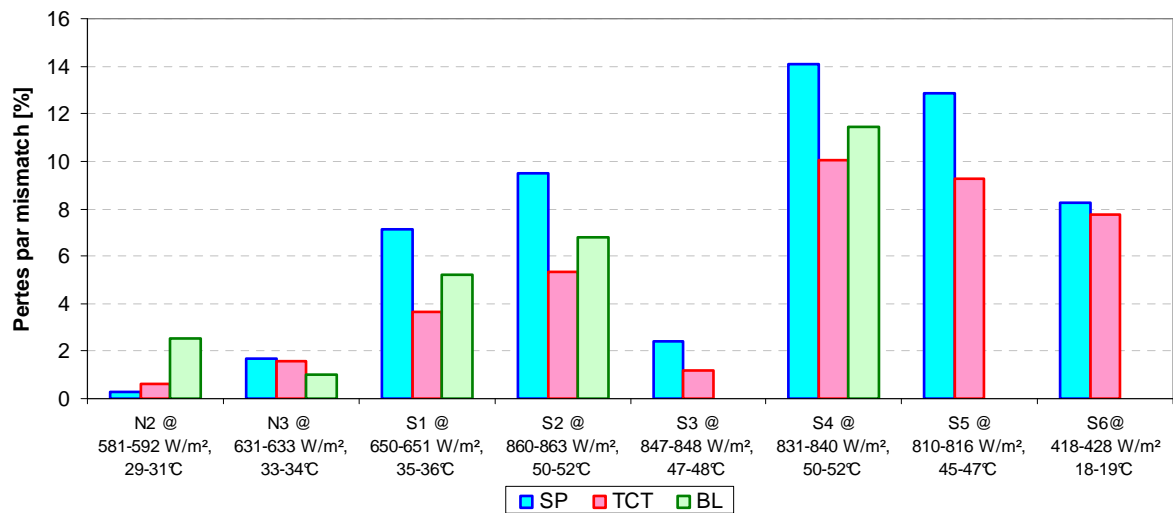


Figure 12 : Pertes par mismatch de la centrale Pergola 5 en utilisant différents schémas de câblage SP, TCT et BL. Dans les scénarios N2 et N3 sont le champ n'est pas ombré, tandis que les scénarios S1 à S6 utilisent une ombre partielle sur le champ PV.

L'addition de redondance dans les circuits électriques dus aux interconnexions supplémentaires entre modules permet d'augmenter la puissance crête de l'installation lors d'ombrage partiel. Les résultats expérimentaux montrent que ces topologies alternatives peuvent augmenter la production de 5% par rapport à celles utilisant le schéma de câblage traditionnel en diminuant les pertes par mismatch. Dans les cas d'ombrage sévères, les résultats sont variables compte tenu de l'action des diodes bypass. Par ailleurs, l'outil de prédiction de la production PV a pu être validé expérimentalement en prévoyant correctement la puissance crête de l'installation dans dix neuf cas sur vingt avec une marge d'erreur inférieure à 5%. Enfin, les résultats de simulations montrent que les pertes par mismatch d'une centrale réelle peuvent atteindre 24% dans le pire scénario d'ombrage.

En conclusion, la modification du schéma de câblage d'un champ PV permet de réduire les pertes par mismatch ce qui augmente la puissance fournie au réseau. Le prochain chapitre présente une autre manière de réduire ces pertes en introduisant des convertisseurs de puissance au sein du champ solaire.

Chapitre IV : Réduction des pertes par mismatch via l'implantation de convertisseurs de puissance

Les convertisseurs de puissance ont l'avantage d'ajouter un degré de liberté dans la gestion des flux de puissance, mais génèrent en contrepartie des pertes supplémentaires. Ce chapitre a pour but de présenter les modèles électriques des convertisseurs utilisés dans les systèmes PV. En vue de réduire le temps de calcul sans pour autant diminuer la précision, des modèles moyens des convertisseurs seront utilisés. Certains modèles moyens sont réduits en utilisant la séparation de modes. Les modèles moyens et moyens réduits des convertisseurs seront présentés ainsi que le calcul de leur pertes associés. Par ailleurs, les convertisseurs PV requièrent des stratégies de commandes spécifiques compte tenu de la forme de la caractéristique courant-tension du champ PV. Les commandes MPPT et de l'onduleur monophasé seront également présentés dans ce chapitre. Enfin, la commande

spécifique de l'architecture hacheur série sera présentée séparément.

Les convertisseurs de puissance sont le plus souvent décrits par un modèle exact qui prend en compte le comportement des interrupteurs de puissance. La modélisation moyenne de composants de puissance consiste à limiter l'étude à la composante fondamentale des interrupteurs. Cela a pour avantage de réduire le temps de simulation tout en conservant la précision et simplifie la conception de la commande des convertisseurs. Le modèle moyen réduit consiste à réduire d'avantage le modèle moyen en considérant les dynamiques des variables rapides comme instantanés.

Les systèmes PV peuvent être connectés au réseau en monophasé ou triphasé suivant la puissance de l'installation et les règles de raccordement. Généralement, les générateurs considèrent le réseau comme une source idéale de tension alternative (AC) avec une impédance associée, dans notre cas une inductance et résistance série présentées sur la Figure 13(2).

Les convertisseurs DC-DC utilisés dans cette étude sont des hacheurs élévateurs Boost, présenté sur la Figure 13(1). Le montage Boost utilise un interrupteur, une diode et une inductance pour élever la tension d'entrée du convertisseur, dans notre cas celle du champ PV, à une tension suffisante pour réaliser l'interfaçage avec le réseau.

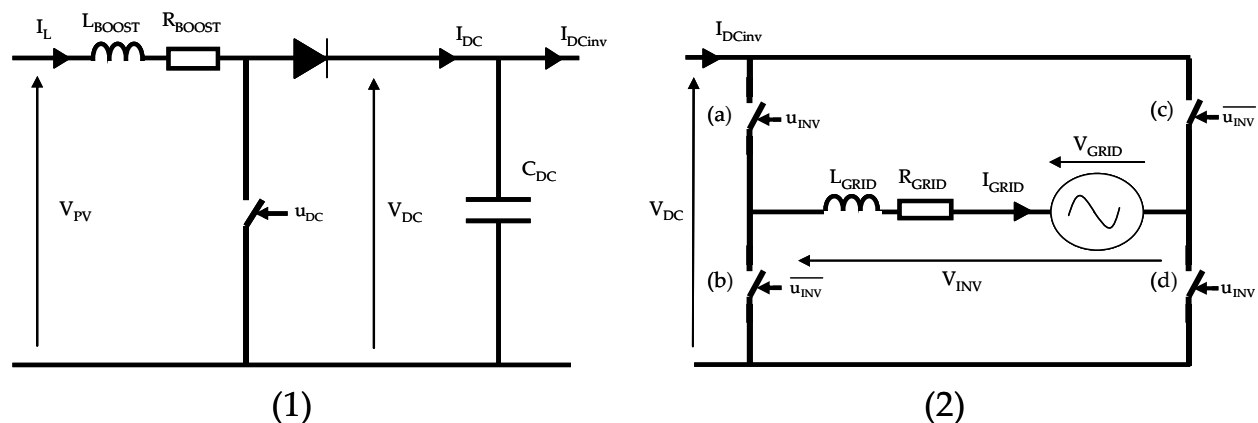


Figure 13 : Schéma électrique du (1) hacheur élévateur Boost et (2) d'un onduleur monophasé connecté au réseau

Le hacheur Boost ayant un rendement acceptable pour un ratio d'élévation de tension inférieure à quatre, des montages Double Boost seront utilisés pour les montages hacheur parallèle et onduleur individuel afin d'élever la tension du module (40 V) à celui du bus continu (400 V). Le Double Boost utilise successivement deux étages de convertisseurs Boost avec un bus continu (DC) intermédiaire et permet donc de réaliser une élévation de tension d'un ratio de 10.

La modélisation des pertes dans les interrupteurs et diodes des convertisseurs de puissances se sont appuyées sur des données de fabricants et des formules dédiées aux convertisseurs. Les composants utilisés ont été dimensionnés pour deux installations, l'une de 3 kW_c et l'autre de 30 kW_c.

La chaîne de conversion PV transforme la puissance DC issue du champ solaire en puissance AC pour d'alimenter le réseau électrique en respectant les contraintes de

raccordements : niveaux de tension, fréquence, et taux de distorsion harmoniques. La première phase de conversion utilise un hacheur élévateur afin d'extraire le maximum de puissance du champ solaire grâce à un algorithme MPPT. La puissance DC est ensuite transformée en puissance AC grâce à l'onduleur qui aura pour fonctions de maintenir la tension du bus DC dans une plage de fonctionnement admissible et d'onduler le courant. Un schéma synoptique de la chaîne de conversion est présenté sur la Figure 14.

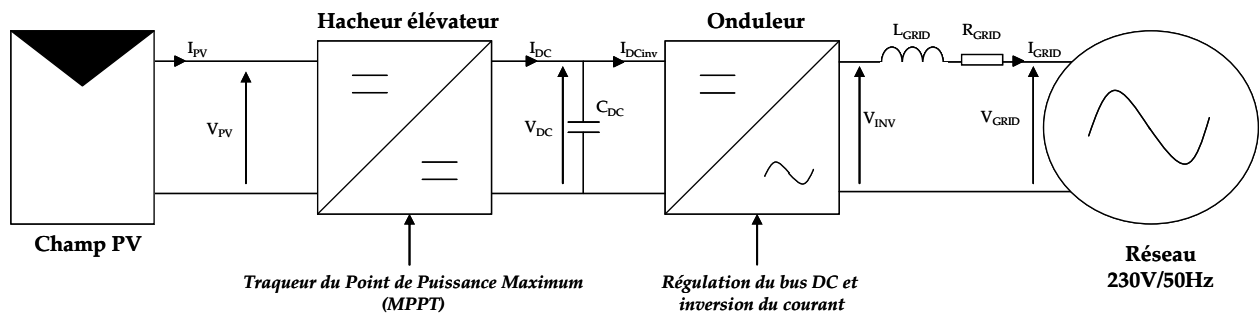


Figure 14 : Schéma d'une centrale PV avec la stratégie de commande des convertisseurs

La stratégie de commande de la conversion PV connecté au réseau est donc composé de trois fonctionnalités : l'inversion du courant, la régulation du bus continu, et du MPPT. Ces fonctionnalités sont implantées dans la commande des convertisseurs via des correcteurs proportionnel-intégrale adaptés. Les modèles des convertisseurs avec leurs stratégies de commande ont été implémentés dans le logiciel MATLAB/Simulink afin de simuler leur comportement. Les résultats de simulations, présentés sur la Figure 15, montrent l'évolution des grandeurs physiques V_{PV} , V_{DC} , et I_{GRID} qui suivent leur grandeurs de commandes respectivement V_{PVref} , V_{DCref} , et $I_{GRIDref}$ afin d'injecter le maximum de puissance disponible sur le réseau.

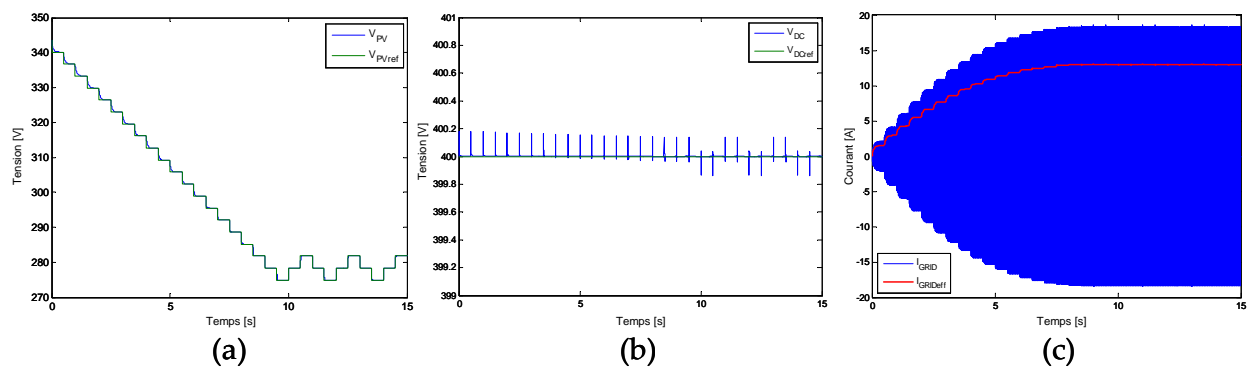


Figure 15 : Résultats de simulations montrant l'évolution (a) la tension du champ PV , (b) la tension du bus continu, et (c) le courant injectée sur le réseau

Le rendement d'un algorithme MPPT peut être définie comme le ratio de la puissance maximale disponible du champ PV et celle extraite par le MPPT. Une étude succincte permet de montrer l'importance de la précision de l'algorithme MPPT et des inconvénients liées aux techniques conventionnelles du Perturb & Observe (P&O), plus particulièrement dans le cas de champs soumis à l'ombrage partiel. La méthode P&O est itérative et évolue en calculant la dérivée de la puissance par rapport à la tension du champ PV. La valeur d'échelon de tension peut donc avoir un impact significatif sur l'efficacité de l'algorithme. Des essais sur

trois champs PV ont été réalisées en utilisant trois échelons différents et proportionnels à la tension de circuit ouvert (V_{oc}) du champ PV : $0.01 \cdot V_{oc}$, $0.05 \cdot V_{oc}$ et $0.1 \cdot V_{oc}$. Ces algorithmes ont ensuite été appliqués à un champ PV de 3 kW_c avec et sans ombrage. Dans le cas d'une centrale sans ombrage les résultats montrent que les trois MPPT convergent de manière similaire au point de puissance maximale. Par contre lors d'ombrage sur le champ PV, le comportement est parfois différent. Dans le cas d'un faible ombrage, les MPPT avec le plus faible pas obtiennent les meilleurs résultats obtenant un rendement de 99.8% tandis que celui ayant un pas de tension de $0.1 \cdot V_{oc}$ extrait seulement 95% de la puissance disponible. Le pas n'étant pas suffisamment petit, l'algorithme oscille autour du point de puissance maximum, comme le montre la Figure 16(a).

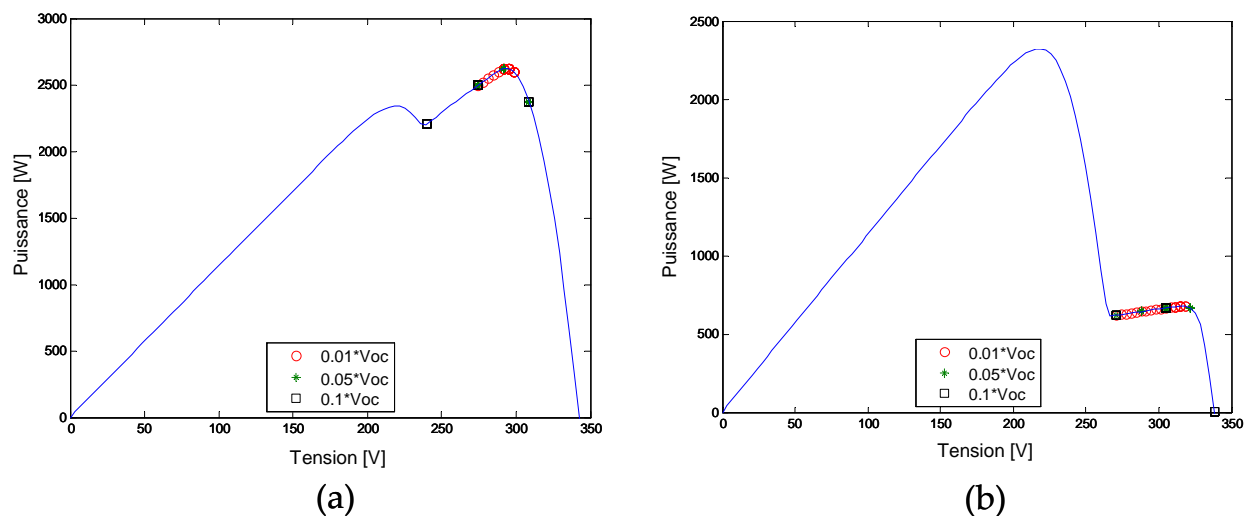


Figure 16 : Evolution de l'algorithme MPPT P&O sur la caractéristique P-V des champs solaires (a) et (b) partiellement ombrés

Dans le cas d'un ombrage sévère, la multiplication des pics de puissance est telle qu'aucun des MPPT n'atteint le maximum global, comme le montre la Figure 16(b). En conséquence, seulement 29% de la puissance du champ PV est extraite. La plupart des systèmes actuels sont équipés avec des MPPT de type P&O, ce qui les rend très sensibles à l'ombrage partiel.

Les stratégies de commande décrites dans ce chapitre seront appliquées à la plupart des architectures de centrales PV présentés dans le chapitre I. Cependant, la structure hacheur série doit être traité séparément compte tenu de son mode de fonctionnement. Le hacheur série est composé de plusieurs hacheurs Boost connectés en série à un bus continu. En régime permanent, le string de hacheurs doit voir un courant unique circuler à travers la sortie des hacheurs tout en maintenant une tension suffisante sur le bus continu quelque soit l'ensoleillement des modules comme le montre la Figure 17. Afin de remplir ces conditions, deux modes de fonctionnement peuvent être distingué: MPPT et régulation du bus DC.

En fonctionnement nominal, lorsque les modules sont suffisamment ensoleillés, la puissance fournie par les modules est telle que la contrainte en courant et tension du bus DC peuvent être satisfait en même temps. Dans ce cas, les hacheurs fonctionnent en mode MPPT, c'est-à-dire que chaque hacheur extrait le maximum de puissance du module auquel il est associé. La tension du bus DC est ensuite régulée par l'onduleur comme décrit

précédemment. Dans le cas d'un ensoleillement insuffisant, les hacheurs pourront fonctionner en mode dégradé qui consiste à limiter la tension de sortie des hacheurs afin de maintenir la tension de consigne du bus continu. L'avantage de cette commande est qu'elle permet un fonctionnement ininterrompu du montage hacheur série quelques soit l'ensoleillement du champ, sauf cas extrêmes. Par contre, lors du fonctionnement en mode dégradé, la gestion de l'énergie n'est pas optimale car les modules les plus puissants se retrouvent les premiers à être limités et donc ne fournissent pas la totalité de leur puissance au réseau.

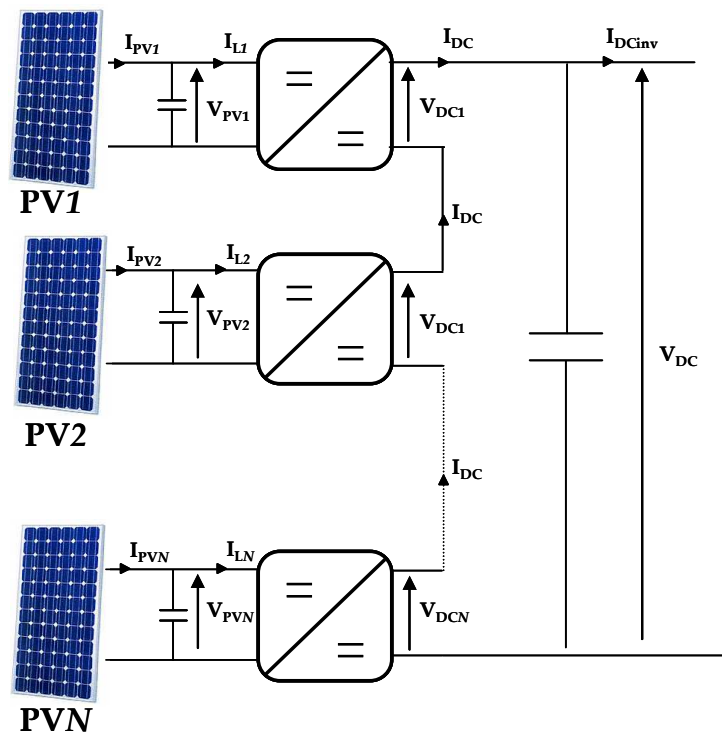


Figure 17 : Schéma d'un string du montage hacheur série

Dans le dernier chapitre, les modèles et stratégies de commandes exposés dans ce chapitre seront appliqués à des installations PV de taille résidentiel et commercial afin d'évaluer leur performances pour réduire les pertes par mismatch.

Chapitre V : Analyse des topologies de systèmes photovoltaïques

Au cours de la conception de centrales photovoltaïques connectées au réseau plusieurs facteurs doivent être pris en compte pour déterminer l'architecture la mieux adaptée comme la puissance et le coût d'investissement par exemple. Selon l'environnement proche de l'installation PV, la production électrique prévue peut être plus faible lorsque le champ est ombré de manière périodique. Dans ce chapitre, les performances des architectures alternatives de centrales PV seront étudiées et comparées. Indépendamment de la puissance produite, les concepteurs de centrales peuvent prendre en compte le coût d'investissement, la performance du système en mode dégradé et leur évolutivité afin d'optimiser l'installation. Un outil destiné à l'évaluation des installations PV considère ces aspects en attribuant une note aux topologies les plus adaptées aux besoins des concepteurs.

Enfin, cette méthode d'évaluation des architectures sera appliquée à une centrale de type résidentiel et commercial à titre d'exemple.

Les modèles des convertisseurs et leurs commandes associées ont été implémentés dans l'environnement Simulink afin de comparer la production des six architectures de systèmes étudiées. Pour évaluer l'intérêt de modifier les interconnexions de champ PV, les configurations SP et TCT ont également été simulés. La production de centrales de type résidentielle (3 kW_c) et commercial (30 kW_c) sont évalués dans six scénarios d'ombrage présentés sur la Figure 18. Ces scénarios ont été conçus afin de représenter, pour des taux d'ombrage faible et fort, des cas fréquents ainsi que le pire scénario d'ombrage.

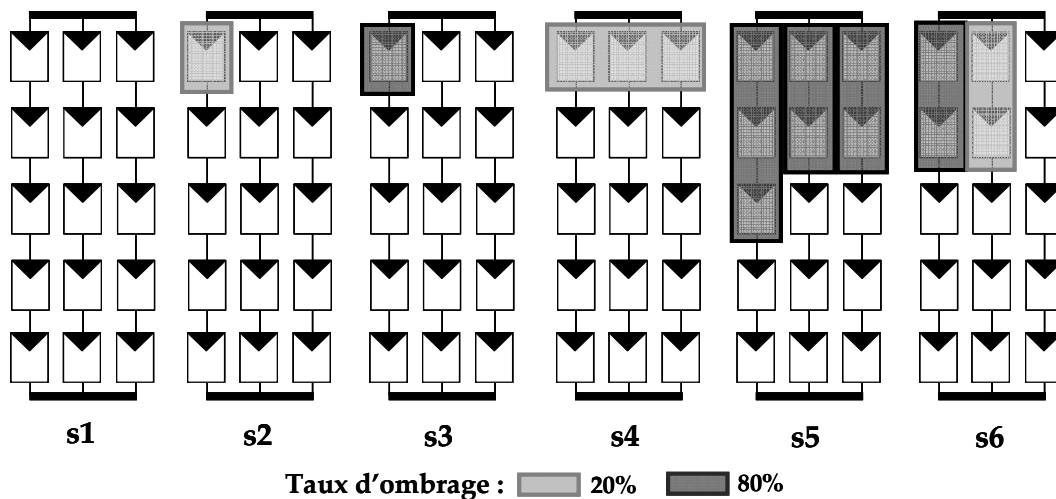


Figure 18 : Schéma des scénarios d'ombrage utilisées pour la comparaison de production

Dans cette synthèse, seuls les résultats d'une installation résidentielle seront présentés car celles-ci représentent la majorité des installations PV en France. D'après les résultats de simulations, présentés sur la Figure 19, plusieurs observations peuvent être constatés.

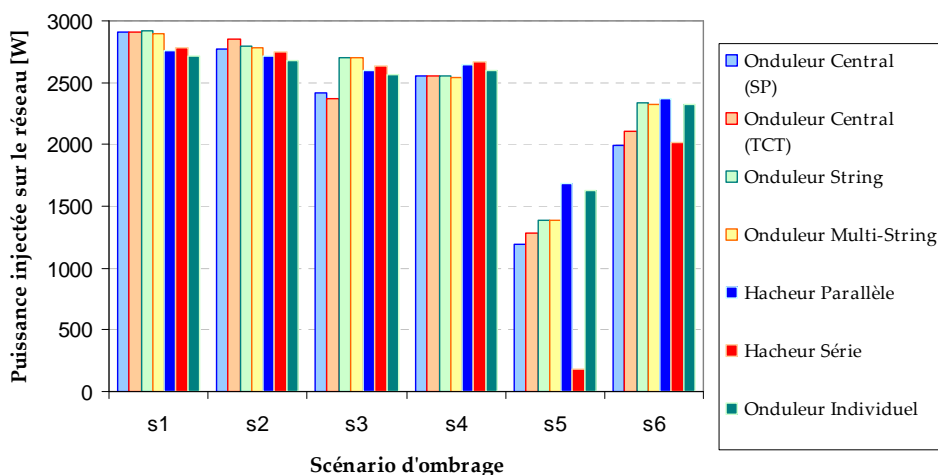


Figure 19 : Puissance injectée sur le réseau des différents architectures d'installations PV dans plusieurs scénarios d'ombrage

Tout d'abord, en conditions de fonctionnement normal l'onduleur central, string, et multi-string obtiennent les meilleurs résultats. Cela s'explique par leur haut rendement de conversion comparés au systèmes plus modulaires: onduleur individuel, hacheurs parallèle

et série. L'écart de production a tendance à décroître lorsque l'ombrage sur la centrale augmente en taille et en intensité jusqu'à dépasser les niveaux de production des structures centralisés, comme le montre le scénario s4. En effet, les rendements plus faibles des structures modulaires sont compensés par leur capacité à dissocier l'influence d'un module sur le fonctionnement du champ, pour cette raison leurs performances sont d'autant meilleures que l'ombrage est important. En ce qui concerne l'architecture hacheur série, sa production est souvent plus grande que celles des autres structures modulaires lorsque l'ombrage reste faible. Par contre, son efficacité est fortement perturbée lors d'ombrage sévère compte tenu de la stratégie de commande implémentée qui n'est pas optimisée.

Par ailleurs, les architectures étudiées se distinguent également par leur capacité de gérer les modes de fonctionnements dégradés: pannes ou maintenance par exemple. Pour cela un indicateur qui évalue la dépendance de chaque module aux convertisseurs de puissance a été mis en place.

Les coûts liés à l'investissement d'une installation PV: coût des modules, coût des convertisseurs, et coûts supplémentaires ont également été pris en compte. Ce calcul s'est basé sur des données récentes et disponibles sur le marché ainsi que des hypothèses sur les coûts auxiliaires d'une installation PV.

Enfin, une analyse sur l'évolutivité des architectures est menée. Celle-ci s'appuie sur une étude au cas par cas de la capacité de la topologie à accepter de nouveaux modules. Une échelle de notation a été mise au point pour déterminer si les architectures sont capables d'évoluer: sans modifications, avec éventuellement des modifications, ou requièrent des modifications inévitablement. Plus de détails sur ces notations sont présentées dans le dernier chapitre du manuscrit.

Une méthode d'évaluation des architectures se basant sur les quatre critères d'évaluation décrits précédemment (production électrique, fonctionnement en mode dégradé, coût d'investissement, et évolutivité) a été développée. Cette méthode a pour but d'évaluer la structure la plus adaptée aux exigences des concepteurs de centrales d'après les quatre critères d'évaluation. L'étude s'appuie sur deux exemples: une exigence équilibrée et l'autre de rentabilité. Dans le scénario *Équilibré*, le concepteur désire avoir une installation qui répond de manière équilibrée aux quatre critères. Par contre dans le scénario *Rentabilité*, le concepteur privilégie le faible coût d'investissement par rapport aux autres critères en utilisant des pondérations présentées sur le Tableau 3.

	Production électrique	Fonctionnement en mode dégradé	Coût d'investissement	Évolutivité
Scénario Équilibré	0,25	0,25	0,25	0,25
Scénario Rentabilité	0,1	0,05	0,8	0,05

Tableau 3 : Poids attribués aux critères d'évaluation dans les deux scénarios

La méthode d'évaluation des architectures permet de prendre en compte les spécificités de chaque topologie et attribue une note comprise entre 0 et 1. Les centrales considérées sont de type résidentiel (3 kW_c) et commercial (30 kW_c) qui sont toutes les deux

ombrés partiellement pendant 20% de leur période de production. Les résultats de l'évaluation dans les deux scénarios sont présentés ci-dessous.

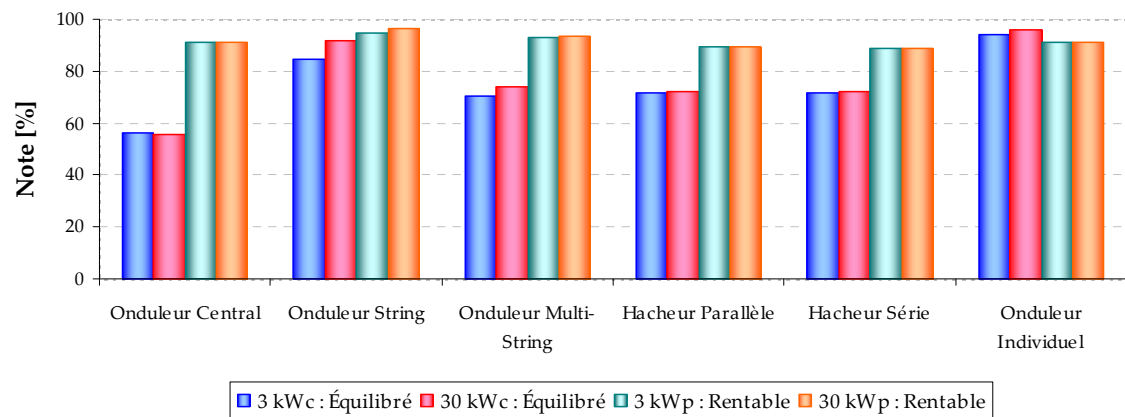


Figure 20 : Résultats de l'évaluation des architectures

D'après les résultats, l'architecture répondant le plus aux attentes d'un scénario équilibré serait l'onduleur individuel. En effet, malgré sa production plus faible et son coût d'investissement plus élevé que les structures classiques, ses performances en termes de continuité de service et d'évolutivité l'amènent en première position quelque soit la puissance de l'installation. En termes de rentabilité, l'onduleur string est le meilleur compromis entre coût et production pour des installations résidentielles peu ombrées, suivi de près par l'onduleur multi-string et l'onduleur central.

D'autres critères d'évaluation peuvent être implémentés afin d'améliorer la méthode : complexité d'installation, capacité à surveiller (monitoring), efficacité énergétique, ou encore analyse du cycle de vie. De plus, les résultats montrent qu'il n'y a pas d'architecture la plus performante, mais que la solution la plus adaptée dépend des critères choisis et de leur importance pour l'utilisateur.

Conclusion

Le développement des applications photovoltaïques terrestres au début du 21^e siècle a abouti au déploiement exponentiel des installations PV connectées au réseau. Au cours de l'expansion de cette ressource d'énergie prometteuse, le retour d'expérience a révélé la présence de pertes par mismatch dans les champs solaires. L'objectif de ces travaux a été de recenser, étudier, et d'évaluer des solutions pour réduire ces pertes dans les systèmes connectés au réseau.

Dans le premier chapitre, une présentation et classification des éléments principaux composant un système PV connecté au réseau ont été exposés. Le chapitre d'introduction s'appuie sur des recherches bibliographiques portant sur huit topologies de systèmes PV où elles ont été présentées et comparées. Le deuxième chapitre traite de la modélisation des champs solaires. Une méthode novatrice de prévoir la production des champs PV en prenant en compte l'ombrage et les schémas de câblage dans diverses conditions de fonctionnement a été présentée. Cette méthode a mené à la mise au point d'un outil de prévision de production de centrales PV qui a été validé expérimentalement sur un champ solaire de 2.2 kW_c. Le

troisième chapitre présente les causes et conséquences des pertes par mismatch sur la production des champs solaire. Une première solution pour les réduire propose de modifier le schéma de câblage des modules. L'étude a montrée que les pertes par mismatch deviennent importantes lors d'ombrage sévère et peut réduire la production électrique du champ de 30% dans les pire cas. Par contre, le mismatch due à l'hétérogénéité des modules reste faible (< 2%). Même si la modification des interconnexions au sein du champ permet de réduire les pertes par mismatch, cette solution ne permet pas de les éliminer totalement.

La deuxième solution consiste à introduire de l'électronique de puissance au sein du champ PV. Les modèles moyens et les stratégies de commandes des convertisseurs de puissance ont été présentés dans le chapitre IV et appliqués dans le dernier chapitre. Cette solution permet d'extraire plus de puissance des modules que la précédente. Cependant, le gain d'énergie solaire est compensé par un rendement de conversion global plus faible pour les architectures modulaires, alors que les architectures centralisées ont des rendements plus élevées mais restent plus sensible à l'ombrage. Afin de comparer les performances de chaque topologie, une méthode d'évaluation a été développé et appliqué à des installations de type résidentiel et commercial. Les résultats de l'étude montrent que l'architecture la plus performante dépend de la puissance de l'installation et des besoins du concepteur de centrales PV en terme de production électrique, continuité de service, coûts d'investissement, et d'évolutivité de l'installation. Les exigences de rentabilité auraient recours aux systèmes centralisés alors que des besoins plus équilibrés auraient intérêt à choisir des systèmes modulaires.

Ce travail a permis de présenter les solutions actuelles pour réduire les pertes par mismatch dans les systèmes PV. La présence de ces pertes est étroitement liée à l'interdépendance des modules au sein du champ. Des solutions futures devraient limiter cette dépendance à travers la gestion des flux de puissance des modules tout en limitant les pertes dans l'appareillage électronique. L'architecture hacheur série semble être un premier pas dans cette approche. Poursuivre le développement de cette solution serait bénéfique en optimisant la stratégie de control et les pertes liées à la conversion. D'autres perspectives pour ce travail consisterait à poursuivre : la compréhension du phénomène de mismatch et de l'évolution des lignes de mismatch lorsque les diodes bypass sont actives, le développement de l'outil de prédiction de production PV en introduisant des modèles avec un comportement de cellules PV en inverse et améliorer la méthode d'évaluation des architectures en ajoutant des critères d'évaluation, tels que le monitoring et l'analyse du cycle de vie.

L'électricité d'origine solaire offre une forte potentialité pour satisfaire nos besoins en énergie avec une ressource à priori inépuisable, dans des quantités colossales et accessible à tous. Les principaux défis pour atteindre un équilibre énergétique durable résident dans l'augmentation de son accessibilité et l'amélioration de son rendement global. Par ailleurs, son empreinte écologique devra être minimisée tout en continuant les efforts de maîtrise des énergies consommées. Ces travaux ont été motivé par ces sujets et espèrent avoir contribué à leur progression.

Table of abbreviations

α	short-circuit current correction factor for temperature
α_{DC}	duty cycle of Boost converter
β	open-circuit voltage correction factor for temperature
β_{INV}	inverter duty cycle
δ	open-circuit voltage correction factor for irradiance
BIPV	building integrated photovoltaic
BL	bridge-link array configuration
C_{DC}	direct current bus capacitor
C_{PV}	Boost converter input capacitor
ConMat	connection matrix
e	Euler's number ($\approx 2,718$)
G_i	solar irradiance at environmental condition i
GCC	generation control circuit
HC	honey-comb array configuration
I_{DCinv}	inverter input current
$I_{i,j}$	current of module $M_{i,j}$
I_{GRID}	grid-fed current
I_L	Boost converter input current
I_{mpp}	maximum power point current
I_o	reverse saturation current of the p-n junction
I_{ph}	light-induced current
I_{sc}	short-circuit current
IGBT	insulated gate bipolar transistor
k_b	Boltzmann constant ($=1.381e-23 \text{ J}\cdot\text{K}^{-1}$)
L_{BOOST}	Boost converter inductance
L_{GRID}	utility-grid inductance
log	natural logarithm function
M	number of modules per string in a PV array
$M_{i,j}$	module located on line i of row j of an array
MOSFET	metal oxide semiconductor field effect transistor
MPP	maximum power point
MPPT	maximum power point tracking
n	diode ideality factor
N	number of strings in a PV array
$N_{i,j}$	node of the array located above module $M_{i,j}$
N_s	number of series-connected PV cells
P_{max}	maximum power
P&O	perturb and observe
PI	proportional-integral
PLL	phase-locked loop
PV	photovoltaic
q	fundamental electric charge ($=1.6e-19 \text{ C}$)
R_{BOOST}	Boost converter resistance
R_{GRID}	utility-grid resistance

R_s	series resistance
R_{sh}	shunt resistance
RMS	root mean square
SF	shade factor
SP	series-parallel array configuration
STC	standard test conditions (1000 W/m ² , 25°C, AM=1.5)
T	module temperature
T_i	module temperature at environmental condition i
TCT	total-cross tied array configuration
TS	topology score
u_{INV}	inverter switch commutation function
V_{DC}	direct current bus voltage
V_{GRID}	utility-grid voltage (=230 V _{RMS})
$V_{i,j}$	voltage of module $M_{i,j}$
V_{mpp}	maximum power point voltage
V_{oc}	open-circuit voltage
V_{PV}	voltage of the photovoltaic element (module, string, or array)
V_t	thermal voltage
W	Lambert W-function
WCS	worst case scenario

General Introduction

The energy demands have continuously increased throughout the world to provide a growing number of inhabitants with more comfortable lifestyles. Recently, energy needs have raised concern regarding fossil fuel depletion, energy efficiency and global warming issues, thus leading our societies to search for alternative energy sources. Renewable energy sources have been put forward to reduce our dependency on fossil fuels by converting the energy from the sun, wind, and biomass into our principal energy vectors: thermal and electric energy. In the 1950's, research on autonomous energy systems, mainly targeting space applications, led to the development of solutions that generate electric power from solar energy by the means of photovoltaic cells. Today, photovoltaic cell technologies have matured and are widely used to provide energy supply in remote, but mostly grid-connected systems.

Among grid-connected photovoltaic installations, several applications have thrived ranging from large utility-sized arrays to smaller residential ones. International agreements and national incentive policies have encouraged companies and homeowners to employ solar power to produce electricity, thus leading to an interest in the forecast and economics of this intermittent power source. This interest in photovoltaic plants has resulted in the collaboration of French public authorities, industrial partners and research laboratories to develop the Solution PV project. This project aims to maximize the power production of photovoltaic installations by reworking their design. The expansion of terrestrial applications has revealed that in most cases the forecasted electric power production is lower than expected, these power losses include mismatch losses.

The purpose of this thesis is to study mismatch losses and develop solutions to reduce their impact on photovoltaic arrays. This work has been divided into five parts which cover the existent design of grid-connected photovoltaic systems and the alternative solutions proposed to raise power production levels. To begin, an overview of the grid-connected solar conversion chain will be presented in Chapter I. The present-day components of grid-connected systems, from solar modules to power conversion units, as well as newer state-of-the-art systems will be exposed. In addition, elements for evaluating and comparing the performances of PV systems will be introduced. Chapter II discusses the electrical models of photovoltaic cells and arrays to predict their behavior when they are exposed to diverse operating conditions. These modelling techniques for photovoltaic elements and the methods are elaborated upon in this work to predict the power production of arrays. In this study, two solutions have been developed separately to reduce mismatch losses in solar arrays by using alternative array interconnection schemes and energy flow control with power electronic devices. Chapter III will demonstrate the interest in adding connections to the traditional array layout to reduce mismatch losses in solar arrays. This first solution will be studied through simulation results and validated using experimental work carried out on a residential-sized installation. In Chapter IV, the simulation models of

power conversion devices and their associated control strategies applied to the photovoltaic domain will be presented. Additionally, performance issues for maximum power point tracking algorithms that are applied to photovoltaic plants will be discussed. In the final chapter, the second solution which introduces power conversion units within the array to reduce mismatch losses will be studied. Through simulation results based on the previously presented models, the effectiveness of both solutions in several shade scenarios will be compared. Furthermore, a global comparison of the proposed solutions will be carried out by integrating evaluation criteria for photovoltaic systems. In the conclusion, the key elements exposed in this work will be summarized and outlooks for future work will be developed.

Chapter I

Grid-connected photovoltaic systems

Introduction

One hundred years after Edouard Becquerel had discovered the photovoltaic effect in 1839, the first solar cell able to convert solar energy into electric current was developed by American researchers from Bell Labs. Since then, photovoltaic applications have flourished throughout the world going from energy supply for portable devices to utility-sized power plants. Recently, global concern for climate change and carbon dioxide emissions reduction have led to a considerable increase in the number of grid-connected photovoltaic power plant installations. The first part of this chapter will present an overview of grid-connected PV systems and present a classification. The second section will detail the different components used in grid-connected systems. Finally, a review of PV system architectures will be exposed and they will be compared.

I.1. Overview of grid-connected PV systems

Originally photovoltaic systems were destined to autonomous energy supply such as space and off-grid applications. Due to global concerns on environment issues, the 21st century has seen a significant growth of grid-connected installations. At the end of 2008, grid-connected systems accounted for 95% of the 13.4 GW cumulated installed PV power throughout the globe [PVPS'09], as can be seen on Figure I.1. Although growth rates of grid-connected systems are expected decrease in the near future, grid-connected systems are foreseen to represent 70% of PV systems by 2030 with a major share of new installations in South America and Asia [SGV'08].

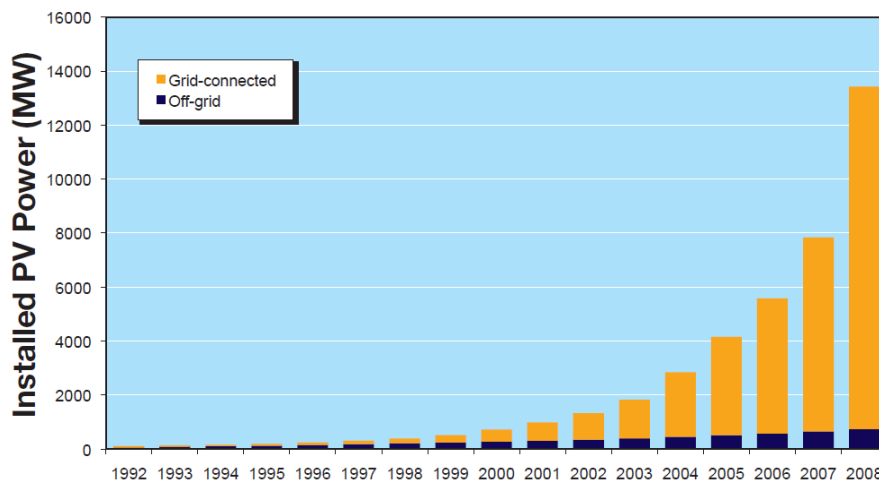


Figure I.1 : Evolution of global cumulated installed PV power between 1992-2008 [PVPS'09]

Among the grid-tied systems, two main types can be distinguished: ground-mounted and building integrated (BIPV) installations. In ground-mounted PV systems, modules are attached onto fixed tilt-angle structures or solar tracking devices which track the sun in order to increase energy generation. These installations are mostly implanted on large open fields used for utility-sized applications ranging from multi-kW to multi-MW plants. Smaller residential ground-mounted systems can also be found but are less common. Building integrated systems are consisted of solar generators integrated into the structures of residential houses, commercial buildings, or other structures (such as shaded parking lots). Other building PV plants can be simply mounted onto the building structures, this is the case of most building applications. In this section both applications will be referred to as BIPV. BIPV systems generally have fixed tilt angles which makes power production more sensitive to the close environment of the building. Indeed, whereas ground-mounted installations are designed to be installed in open areas, BIPV systems must operate in environments containing irremovable surrounding obstacles. Consequently, power generation may not always be optimal due to lower availability of the solar resource. Furthermore, grid-connected system power ratings depend on the application: residential, commercial, and utility-sized as can be seen on Figure I.2.

The rapid development of grid-connected systems has attracted public authorities, industrial partners and research laboratories into developing new solutions aimed at

maximizing grid-tied PV system performance. The *Solution PV* project, initiated in September 2007, has brought together nine leading French industries and research institutes working in the photovoltaic field to work towards this goal. The purpose of *Solution PV* is to design and optimize architectures of the energy conversion chain, monitoring, and control strategies from the PV module to the utility-grid in order to increase reliability of installations by 90% and their productivity by 5%. The project outcomes will be presented throughout this work.

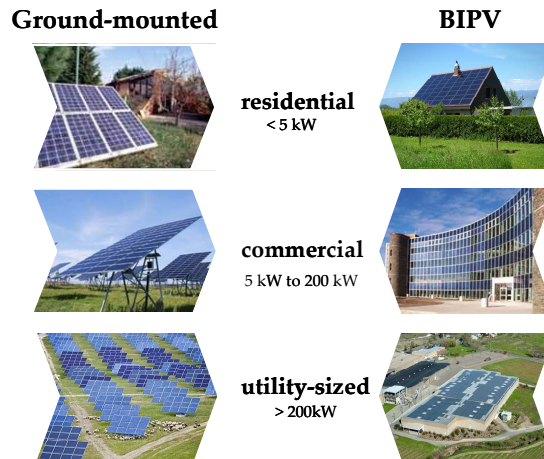


Figure I.2 : Classification of grid-connected PV systems

After having seen how grid-connected systems may differ both in size and in construction type, the next section will present the components of PV installations.

I.2. Components of grid-connected PV systems

Photovoltaic plants connected to the utility grid contain several elements in order to ensure secure power generation: PV modules, power converters, electric protection apparatus and monitoring devices. Since the PV modules produce direct current, an inverter is necessary to interface with the alternative voltage utility grid. Aside from alternating current, maximum power point tracking (MPPT) algorithms are embedded in the inverter control circuit to extract the most power from the array during the day. The MPPT algorithms control the array operation point by sequentially comparing its output power. Several types of algorithms exist including the incremental conductance method, extreme seeking control, but the most common remains the perturb and observe method. The perturb and observe (P&O) method, also known as the hill climbing technique, shifts the reference value according to the variation in power output of the array [FEM'05]. In normal operation, the hill climbing technique is efficient since the power-voltage curves contain a single power peak. However in degraded operation modes, P&O techniques be locked onto local power peaks that are not global maxima which leads to less extracted power.

Furthermore, circuit breakers are installed in the PV system between the inverter and utility-grid in order to isolate the PV system from the grid in case of grid-faults or maintenance must be carried out on the system. Most systems also include direct current circuit breakers in between the PV array and the inverter for the same reasons. This includes a ground fault protection system to be installed on the DC side in order to prevent lightning-

induced faults which can severely deteriorate the inverter. Moreover, meters are implanted at the grid supply terminals in order to count the grid-fed and consumed energy as can be seen on Figure I.3 [EDF'03][CEC'01].

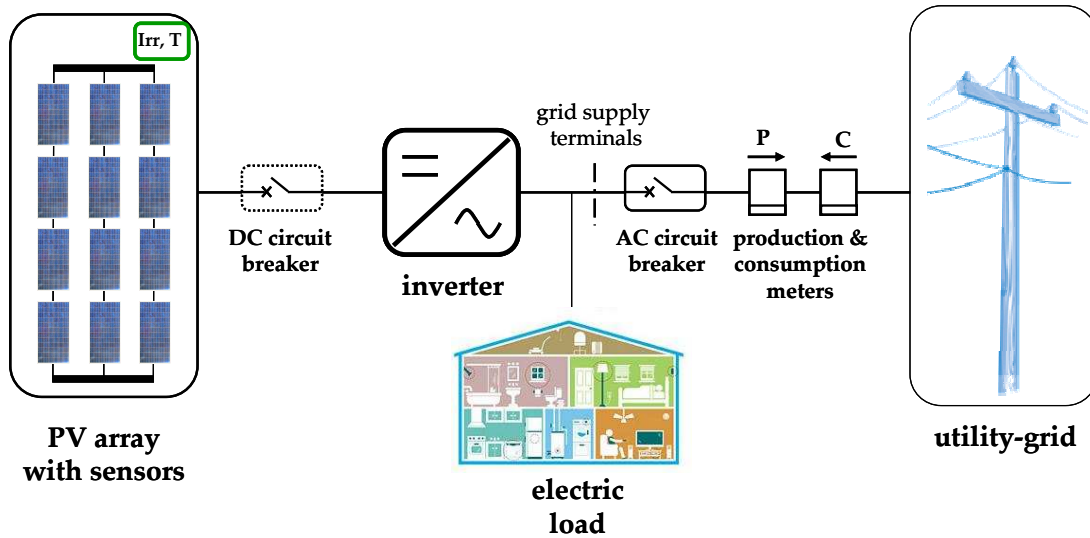
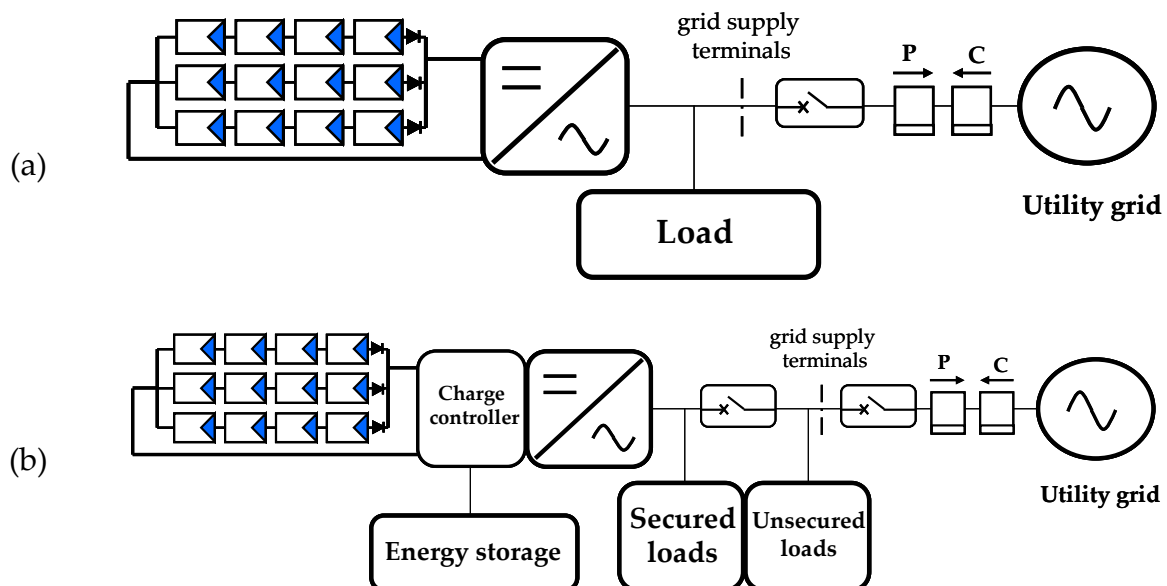


Figure I.3 : Grid-connected PV system diagram

In the above diagram, the grid connection strategy consists in exclusively feeding the grid with exceeding solar power production. Yet, other possible installation designs may entirely feed the solar generated power to the grid by using distinct circuits for the solar array and the electric load, in such cases only a production meter is required at the grid supply terminals. Furthermore, in order to ensure power supply during grid faults an energy storage system can be inserted before grid supply terminals either on the DC bus or after the inverter. The electrical schemes of these installations are presented on Figure I.4

In these partially autonomous systems, specific loads have a secured power supply provided by beforehand charging, using the PV array or the network grid, of the energy storage. However, the design of energy storage equipped grid-interactive installations must not permit the energy storage system feed the grid during discharge [ADE'06].



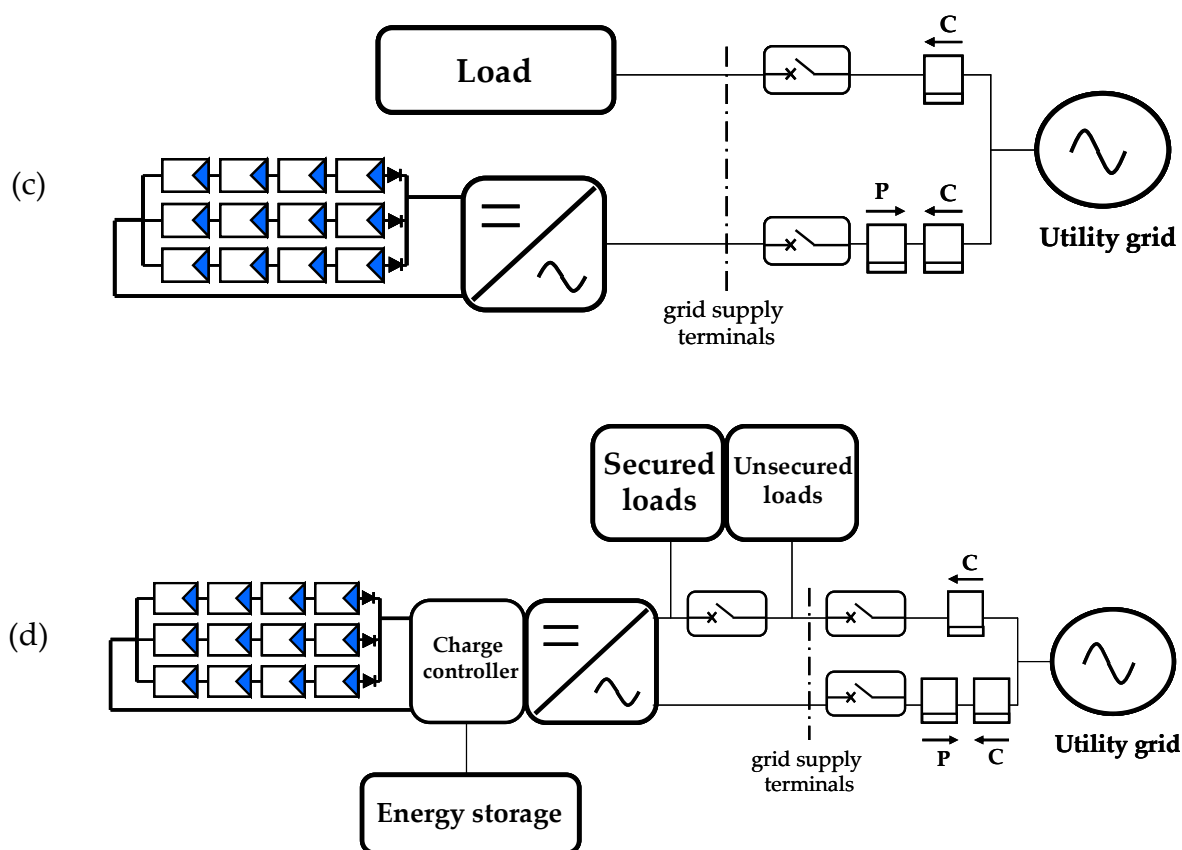


Figure I.4: Electrical schemes of (a) grid-interactive, (b) secure grid-interactive (c) total grid-feeding, and (d) secure total grid-feeding PV systems [EDF'03]

Next, the main components of PV systems will be further described beginning with an overview of photovoltaic modules.

I.3. PV module technologies

Photovoltaic modules are composed of multiple solar cells which convert sunlight into electrons through the photovoltaic effect. In the case of silicon technologies, the solar conversion is carried out with a semi-conductor P-N junction in which (1) solar photons absorbed break electron bonds, (2) the released electrons drift to the N-type region and the holes migrate towards the P-type region, (3) the diffusion of charge carriers to the electrical contacts causes a voltage to appear at the solar cell's terminals as shown on Figure I.5.

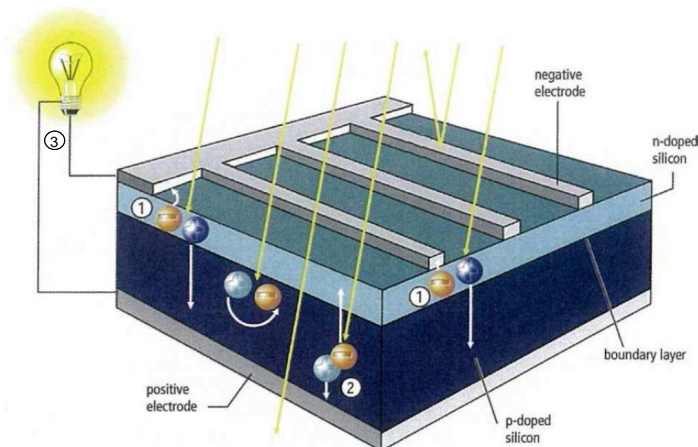


Figure I.5 : Photovoltaic effect diagram in crystalline silicon solar cells [PIPS'08]

Several photovoltaic module technologies coexist, yet currently only two technologies dominate the market: crystalline silicon (90%) and thin film (10%).

I.3.1. Crystalline Silicon

Silicon is frequently used in the photovoltaic industry for its intrinsic semiconductor properties and large availability (silicon is the second most abundant element on earth). Crystalline silicon technologies can be of two types: monocrystalline (mono-Si) and polycrystalline (poly-Si). The principal difference lies in the crystallization process of silicon wafers. In mono-Si solar cells, a single silicon crystal is used, whereas the poly-Si is composed of several smaller crystals. Once the desired purity level is obtained, the silicon is formed into blocks that are sawed into wafers that are 150 to 300 μm thick. The sawing process creates a large amount of waste, since the saw blade has approximately the same size as the thickness of the wafer. At the end of the sawing process the sawdust is collected and melted for reuse. The raw wafers are then P-doped with boron to create the positive junction, cleaned and later N-doped by phosphorous diffusion to create the N-type region. Finally, an anti-reflective coating is applied to the wafers, to increase photonic efficiency, and current collector lines are printed onto the solar cell.

Monocrystalline cells have higher conversion efficiencies than poly-Si cells and are more expensive. In 2007, mono-Si and poly-Si accounted for 43% and 47% of the PV market respectively [PWC'09].

I.3.2. Thin Film

Thin film technologies are the direct competitor of crystalline silicon in the PV market today. This second generation of solar cells applies photoactive semiconductors onto a low-cost substrate, mainly glass, which offers considerable savings in the manufacturing process. The semiconductor materials essentially used include amorphous silicon (a-Si), copper indium gallium selenide (CIGS) and cadmium telluride (CdTe). Thin film solar cells have the advantage of using less semiconductor material (1-6 μm) and energy during the manufacturing process. Consequently, the cost per kW_p is very competitive. Furthermore, the manufacturing process offers a wide variety of module shapes and sizes since the semiconductor is simply deposited onto the substrate. At present the most common design remains rectangular for practical purposes.

However, thin film solar cells efficiencies are 5-10% lower than those of crystalline technologies. All in all, the thin film industry is expected to continue to grow and attain a 25% share of the market by 2013 [EPI'09].

I.3.3. Next generation solar cells

Next generation solar cell technologies have been developed throughout the years with aims to attain efficient production processes, lower specific material consumption, and lower costs. Organic solar cells are built from thin films of organic semiconductors, approximately 100 nm, that offer high light absorbing capacity. A major advantage of

organic solar cells is the low-cost of the manufacturing process, using low energy-consuming printing techniques, and the compatibility with flexible substrates. Still, conversion efficiencies of organic and plastic solar cells remain under 5% which is the principal drawback explaining its absence on the market.

Another promising technology is multi-junction solar cells. They consist in using multiple layers of thin films in order to absorb more of the solar spectrum during the conversion process. The main interest in multi-junction cells is the over 40% conversion efficiencies that have been obtained. However, the materials use a more complex fabrication process using gallium arsenide (GaAs), indium, and phosphore which considerably elevate the solar cell cost.

A synoptic chart showing the evolution of several solar cell technology efficiencies is presented on Figure I.6.

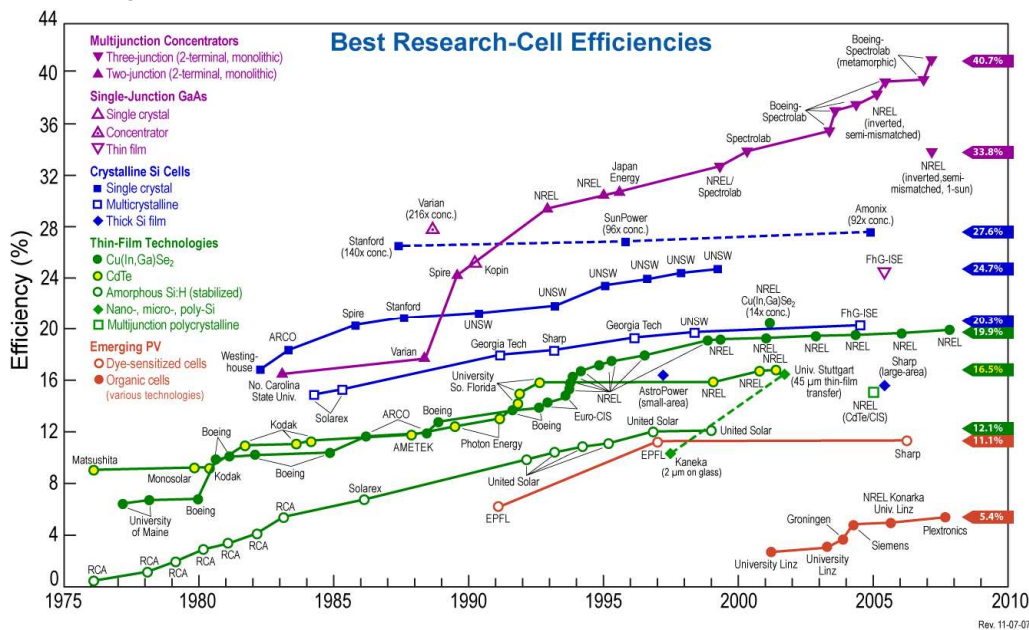


Figure I.6 : Evolution of solar cell technology efficiencies from 1975-2010 [EER'10]

Lastly, dye-sensitized solar cells (DSSC) are third generation solar cells which obtain conversion efficiencies reaching up to 11%. DSSC technology uses photosensitive dye placed on a titanium oxide (TiO₂) coated substrate. The photons captured by the dye excite electrons which are later transported toward the back contact electrode through a redox reaction. As in organic solar cells, this solar technology remains low-cost and easier to manufacture than crystalline solar cells.

	Market Share in 2007 [%]	PV Technology	Efficiency [%]	Cost [€/Wp]
First Generation	43	Mono-Si	18-25	2,5-3
	47	Poly-Si	12-20	2,5-3
Second Generation	10	a-Si	6-9	1,5-2
		CIGS	9-15	1-1,5
		CdTe	10-16	1-1,5
Third Generation	N/A	Organic	4-6	<0,5
		Dye sensitized	8-11	<0,5
		Multi-junction	30-40	>3

Figure I.7 : Solar cell technologies [PWC'09][GRE'09]

In conclusion, crystalline silicon and thin film technologies are the main actors in the current PV market. Next generation technologies are under development to offer lower costs by reducing the solar cell fabrication processes. Figure I.7 presents a comparative overview of the technologies commercially available and under development.

Afterwards, the energy produced by the solar modules must be conditioned, by the means of power electronic devices, to feed the utility-grid.

I.4. Power conversion units for PV systems

I.4.1. Inverter

The DC power produced by the PV generator must be converted into AC power for grid connection. The inverter performs the conversion by the means of electrical switching devices. They are used to control the output waveform both in amplitude and frequency in order to fit grid requirements. Self-commutated inverters use switching technologies, such as IGBT and MOSFET that can be controlled in both on and off states. Therefore, total control of active and reactive power flow as well as current harmonic distortion limitation can be achieved by applying adequate control strategies. Furthermore, the inverter reacts to grid-faults and uses islanding detection to recognize proper grid operation. The response to grid faults is currently less important than for traditional power sources, for example participation in ancillary services is not systematically required. In this case, the inverter disconnects itself from the grid during grid faults. In countries where grid codes require fault ride through, the inverter must follow a voltage dip profile by producing reactive power and fit to requirements set by the grid operator.

Inverter control schemes are implemented using pulse-width modulation (PWM) techniques which compares a reference sine wave to a higher frequency triangular signal. The result generates a pulse of constant amplitude with variable duty-cycles. Maximum power point tracking algorithms can also be implanted directly in the inversion level for high voltage arrays, but in low voltage arrays commercial inverters contain two stages: a DC-DC elevation stage which realizes maximum power extraction and an inversion stage to interface with the utility-grid as shown on Figure I.8.

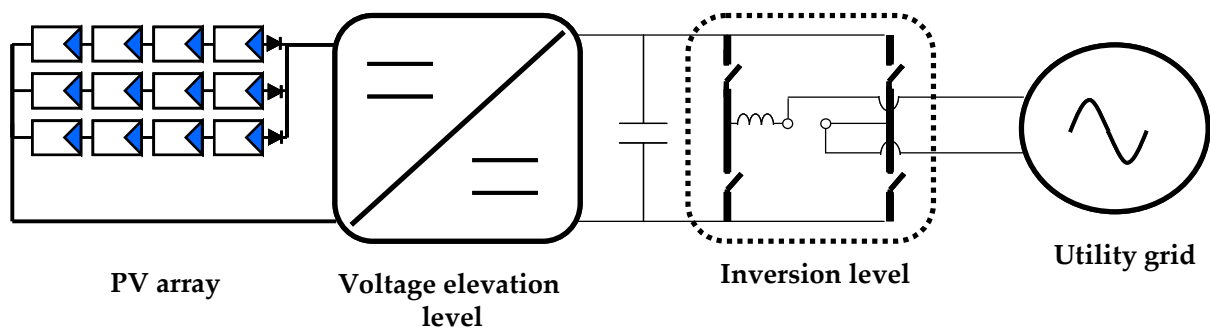


Figure I.8 : Electrical diagram of a commercial single-phase grid-connected inverter with voltage elevation and inversion levels

Since the 1980's when inverters were heavy, unreliable and had efficiencies in the 85-90% range, much progress has been made. Innovations have been brought by increasing

reliability (mean time to failure from 5 to 10 years) and efficiency (>95%), including PV monitoring systems, implementing per string MPPT algorithms, and designing inverters with larger power ratings. The efficiencies of transformless inverters have reached 98% in commercial products and 99% in research [BUR'09]. Current PV inverter costs are in the 1.50-2 \$/kW_p range for residential applications (<5 kW) and 0.40-0.80 \$/kW_p for larger installations (>70kW). The three main goals for the PV inverter industry are to lower prices, increase reliability, and increase conversion efficiency [NREL'06].

I.4.2. DC-DC converter

The control of power extraction at the solar generator level is achieved by a DC-DC converter. The two main types of DC-DC converters used to fulfill this function are: Boost and Buck-Boost converters. They are presented on Figure I.9. The Boost converter is a step-up voltage converter whereas the Buck-Boost converter can either elevate or decrease the input voltage depending on the value of the duty cycle. The basic operation principle consists in accumulating energy into an inductor when the electrical switch is closed and releasing it when the electrical switch is opened. In the case of the Boost converter, the energy release leads to a voltage elevation at the converter output. In the case of the Buck-Boost converter, the output voltage is greater than the input voltage for duty cycles greater than 50% (ie. $\alpha > 0.5$) and lower than the input voltage for the remaining values.

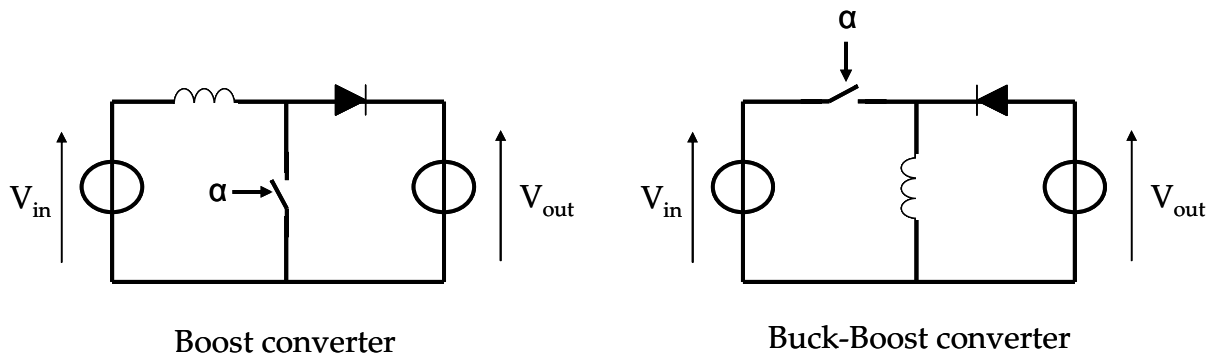


Figure I.9 : Electrical scheme of Boost and Buck-Boost converters

The design, components, and power rating of such DC-DC converters have a considerable impact on the efficiency of the system. Boost converters are generally more efficient than the Buck-Boost converters and have efficiencies greater than 95% for PV applications.

After having presented the elements that make up a grid-connected PV system, it is important to address the aspects used to compare PV system topologies.

I.5. Evaluation criteria for PV system topologies

PV systems are designed to produce a maximum amount of electricity when the solar resource is available either to feed the grid or for direct consumption. In both cases, during the design of a PV installation, professionals need to choose how the plant should be arranged in order to select the best topology for the aimed application. During the design

process, common factors such as the solar resource availability, surrounding environment, power production needs, and investment costs must be taken into account. As will be seen in section I.6., there exists several manners of designing a PV installation going from a centralized plant topology, using a PV array connected to a single inverter, to modular topologies, which use per module power conversion units per module. Evaluation criteria for determining which PV system layout is the best suited for an application can prove to be useful in the system design process. Our topology comparison criteria contain four elements to consider: PV system performance, degraded mode management, investment costs, and upgradeability.

I.5.1. PV system performance

The main requirement for a PV system is to obtain the best performance results during the solar energy conversion process. The evaluation of an installation performance must take into account the entire power conversion chain from module to grid. In other words, efficiencies of the PV modules and power converters during normal operating conditions must be quantified in order to rule on the most adapted plant topology. However, during an installation's lifetime, degradation of the solar resource may occur due to meteorological (soiling, icing, snow, hail or passing clouds), natural (fallen leaves, bird droppings, dust, etc...), human (deterioration during installation process, vandalism) or environmental (nearby buildings, chimneys, TV antennas, trees, etc...) causes. Some of these causes may be unexpected and temporary, while others can be predicted and affect the plant periodically or permanently. All in all, they can considerably degrade the solar conversion process by inducing power losses. Hence, the performance of the system in these conditions must also be taken into account in order to anticipate the efficiency of the topology in the operation modes that apply.

I.5.2. Degraded mode management

The evaluation of degraded mode management consists in determining how the topologies perform in case of faulty operation of the power electronics equipment. Indeed, electrical systems can operate in three distinct operation modes: correct operation, safe improper operation and dangerous improper operation. In the case of a PV system, the correct operation mode has been taken into account in the previous paragraph when studying the system that functions properly. However, field experience has shown that PV systems can reach between 20 and 41 failures per hundred systems with a 5% per year decrease of the failure rate as shown on Figure I.10. The least reliable component was the inverter accounting for 66% of the reported failures [PVPS'02].

A reliability evaluation of the topology can use indicators such as Mean operating Time Between Failure (MTBF), Mean Time To Failure (MTTF), or Mean Up Time (MUT). In order to take into account the necessary time to repair a faulty inverter the Mean Time To Repair (MTTR) or Mean Down Time (MDT) may also be considered [MEG'04]. The capacity of a topology to rapidly detect the type of failure and its location, thanks to its associated

monitoring system, is advantageous and should be considered while conducting a comparison of plant topologies.

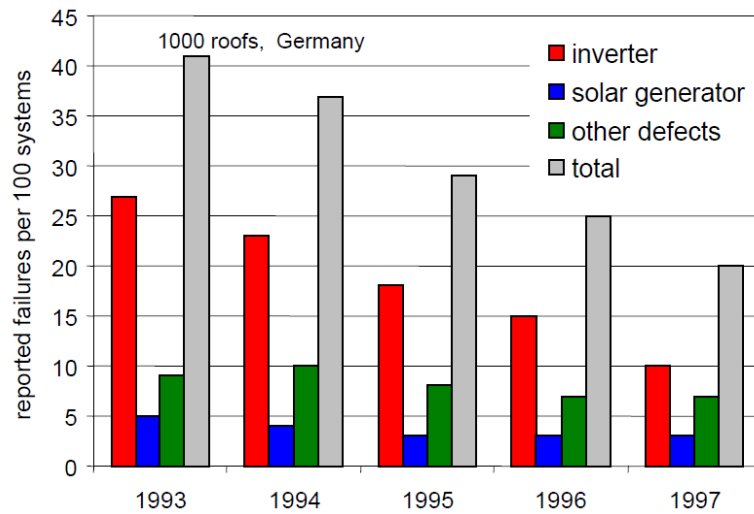


Figure I.10 : Failures by main component reported by owner under the German 1000 roofs program [PVPS'02]

Finally, when the PV system operates in degraded mode it does not necessarily mean that no energy is fed to the grid. The configurations that can continue to produce energy while having lost certain system components have higher continuity of service levels. The continuity of service should be taken into account in an extensive evaluation.

I.5.3. Investment costs

A decisive element to consider when planning to build a PV system is the investment cost. At present, the cost of a residential PV installation is principally driven by PV modules (55%), followed by installation materials (16%) and the power conversion units (13%) as shown on Figure I.11. Since power conversion units are expensive, the quantity of converters in the plant will highly affect the initial investment costs of the complete system. Nevertheless, the possible earnings, in the case of grid feed-in tariffs [TAL'10], made by supplementary energy produced with additional converters may reduce investment return rates.

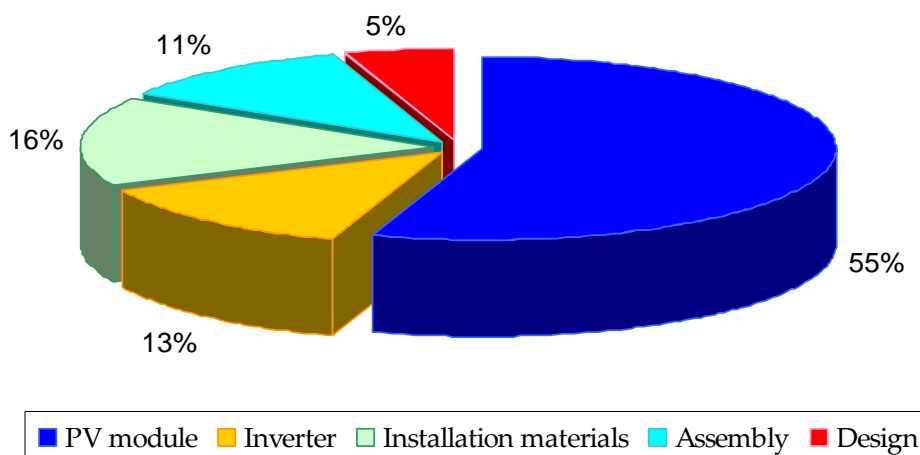


Figure I.11 : Distribution of PV system costs for residential applications [ANT'06]

The end of life cost of the entire system should also be included in this criterion. Topologies containing numerous components will not be advantaged in both initial and recycling costs, yet conducting a specific case study per installation to minimize investment costs can lead to the determination of the optimal number of converters to be used in the installation.

I.5.4. Upgradeability

PV systems are long term investments, with return on investments estimated between 10 and 20 years depending on the size and national incentive policies in effect. During the lifetime of the plant, upgrades may be necessary due to changing policies and customer needs. Upgradeable PV systems should be able to accept additional modules, to increase the plant's power rating, and future module technologies without disrupting normal operation. The upgradeability of topologies can be evaluated by detecting evolvable patterns that do not interfere with the overall operation. Furthermore, if modules need to be replaced during the plant's lifespan, an upgradeable installation must easily integrate new components without degrading its initial performance.

The expansion of grid-connected distributed generation will surely lead to changing grid codes as the number of installations increases. If ancillary service participation was required by grid system operators, the competitive topologies must be ready to fulfill these requirements with minimal changes on the installation [PIC'09].

The next section will present a review of topologies used in grid-connected installations. They will later be compared in Chapter V using the proposed evaluation criteria.

I.6. Review of grid-connected PV system topologies

Accompanying the expansion of grid-connected installations different arrangements of PV modules with their associated power converters have been developed to increase power production and reliability of the solar generators. The following system topologies that have been identified in scientific literature will be presented beginning with the centralized layouts and ending with the distributed ones.

I.6.1. Centralized inverter

The most widespread topology consists in using a single inverter to interface the utility-grid and the PV array. The PV array is set up into PV strings, which are series-connected PV modules to fit inverter voltage constraints, that are then connected in parallel in order to fit a desired plant power rating. Depending on the number of parallel strings, anti-feedback current diodes are inserted in each string to prevent the string to absorb current coming from an adjacent string, this may occur during shading of one entire string for example. Furthermore, the inverters considered in this work contain an integrated DC-DC voltage elevator level to enable current inversion on a larger array voltage range. A layout of the centralized inverter topology is presented on Figure I.12.

The principal advantages of the centralized inverter are the simplicity of the layout which leads to low cost, simple maintenance and monitoring of the plant [BAC'06]. However, the use of a single MPPT for the entire array does not guarantee maximal power extraction, especially when the plant is subject to partial shading as will be seen in Chapter IV. Moreover, cable losses can be important if the inverter is not installed close to the array which can be added to the losses in string diodes. The major drawbacks of this configuration are the lack of upgradeability and continuity of service. Indeed, if an owner decides to add PV modules to the array, the inverter must also be changed to fit the new array power ratings. Likewise, if the inverter is down, the plant cannot feed the grid until maintenance on the power converter is carried out. Both of these last aspects make the centralized inverter layout costly in such cases.

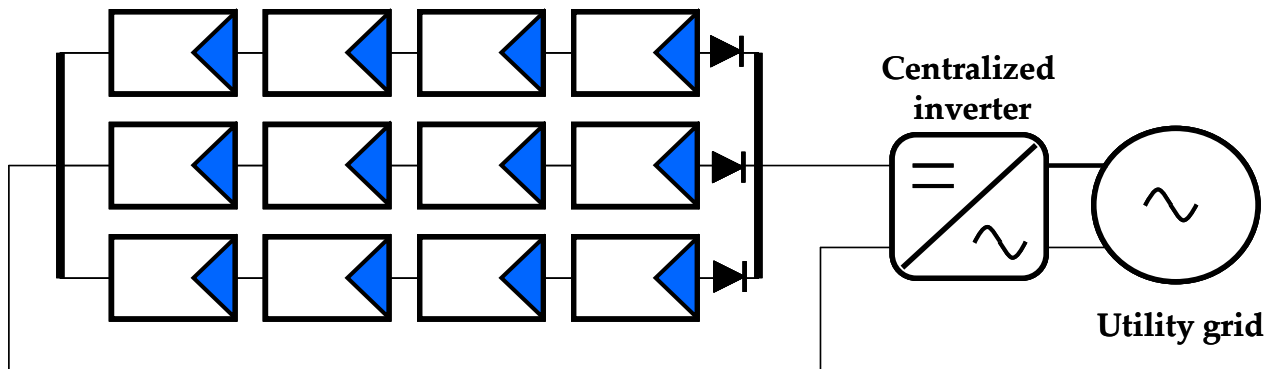


Figure I.12 : Centralized inverter

Meanwhile, this topology is widely adopted and will be considered a reference topology throughout this work. Recent studies show that using centralized inverters reduce by 60% the cost of power conversion units while losing only 1.5% in global conversion efficiency when compared to the string inverter topology [PAV'07]. This is why the centralized inverter is often presented as a simple low-cost solution.

I.6.2. Dynamic switching array

In the case of partial shading of an array, losses in power production can be considerable. To lower mismatch among modules of a same string, dynamic switches which reorganize the module interconnections have been designed. The topology is similar to the centralized inverter but differs by connecting each module to a connection box containing switches which are controlled independently from the inverter as shown on Figure I.13.

Control strategies for the switching matrix may differ either by choosing to simply choose to regroup modules which have similar incoming solar irradiance values [VEL'05] or enable module interconnections in between PV strings in order to reduce module mismatch [NGU'08] as will be seen in Chapter III. In large PV arrays, the cables linking each module to the connection box will imply greater conduction losses and necessary conductor oversize to limit voltage drop. Regardless of the applied control strategy, the use of a dynamic connection matrix adds complexity to the global PV system especially in terms of maintenance on the connection matrix.

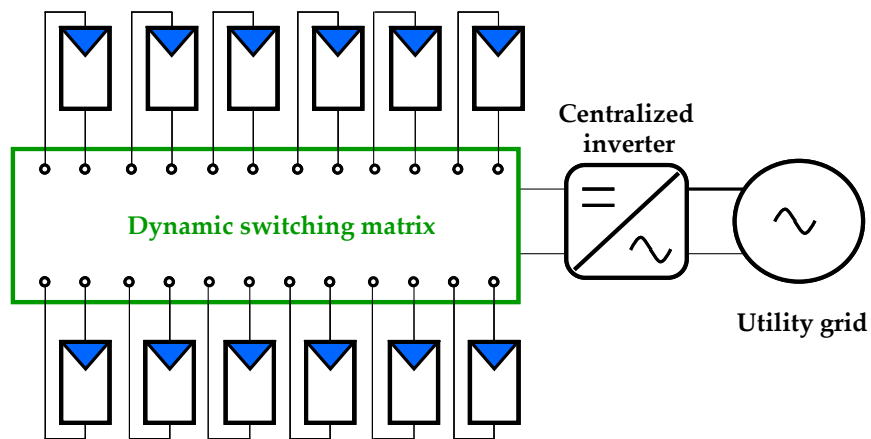


Figure I.13 : Dynamic switching array

The additional component may increase power production, by as much as 30% in certain cases [VEL'05], but does not address the lack of continuity of service and evolution of the centralized system. Furthermore, the initial cost of the system is greater than a centralized inverter configuration due to addition of the switching matrix.

I.6.3. String inverter

The string inverter topology consists in using one inverter per PV string of the array. The string inverters differ from centralized inverters only in the aspect that their power ratings are much lower. The inverters are then connected in parallel to the grid supply terminals as shown on Figure I.14. The use of several inverters increases the number of MPPT algorithms which control each PV string. If a string inverter is down, the other string inverters can continue to feed the grid. Additionally, the configuration can evolve by simply adding string inverters and connecting them to the grid supply terminals to increase the plant power rating.

However, there remain drawbacks to this topology. First, the initial cost of the system is greater than the traditional layout due to the additional inverters. Also, losses due to partial shading of modules within a same string can still mislead MPPT algorithms. Additionally, when the PV string power production is low, string inverters are less efficient. For example, at 5% load the efficiency of the inverter may decrease to 90% [BUR'09].

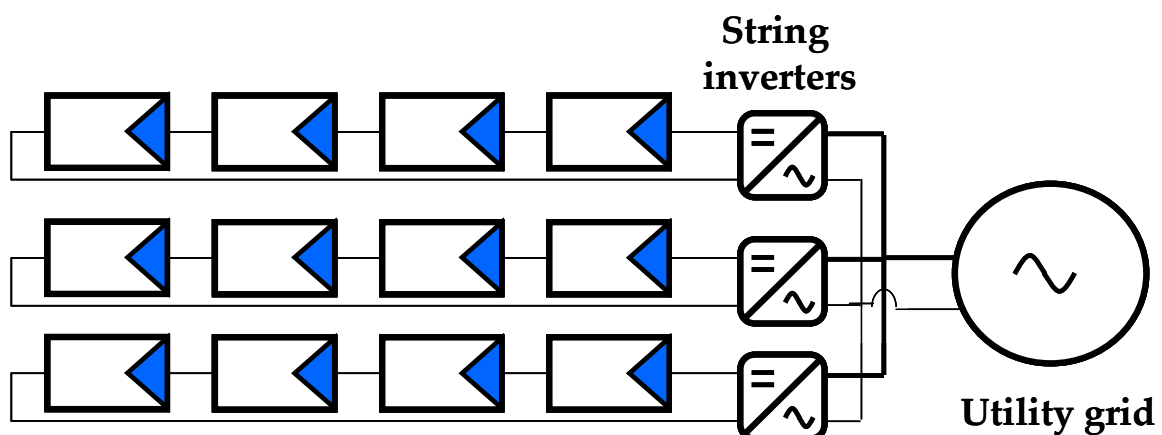


Figure I.14 : String inverter

In order to address this last point, certain commercial string inverters integrate a team concept, presented on Figure I.15, in which DC switches are implanted in between PV strings so that fewer string inverters operate when array power is low. In other words, the team concept can enable string inverters to operate as centralized inverters when solar irradiance is insufficient to elevate conversion efficiencies by coupling several strings together [MYR'03].

Studies have shown interest in using the string inverter topology, especially in partially shaded scenarios where up to 12% more power can be generated in comparison with a centralized inverter [PAV'07]. Furthermore, simulation results for the team concept show energy production increase by up to 4% [MYR'03]. Finally, experimental results on a 500 kW_p plant have shown that string inverters using the team concept have energy conversion efficiencies ranging between 92-98% with solar irradiances as low as 20 W/m² [CHO'06].

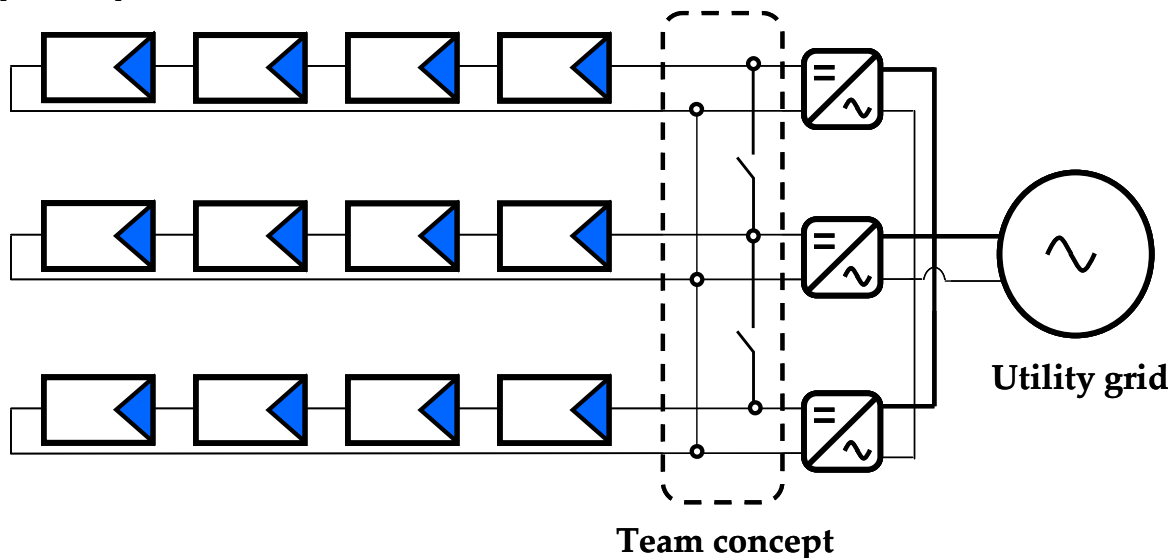


Figure I.15 : String inverter topology using the team concept

I.6.4. Multi-string inverter

In low voltage PV arrays, centralized and string inverters have two power conversion levels, one DC-DC voltage elevation level and an DC-AC inverting level in order to invert voltage to utility grid specifications, that is to say 230 V_{RMS} in European countries. Multi-string inverters, also known as multi-MPPT inverters, separate these two levels by implementing voltage elevating DC-DC converters per string which are linked to a common DC. One single inverter is used to invert the plant current as shown on Figure I.16. The multi-string topology is in reality a hybrid version of the centralized and string inverters by combining a MPPT per string while using fewer converters [MEI'00].

The cost of a multi-string inverter is lower than string inverters for an equivalent power rating. Indeed, this topology has similar functionalities as string inverters, such as using one DC-DC converters per string, but uses only one inverter for the entire array. This reduces the global cost of the system while conserving a power flow control per string. However, concerning continuity of service the single inverter remains the vulnerable

element as in the case of the centralized inverter. Indeed, although each string can be controlled independently, if the inverter fails no energy can be grid-fed.

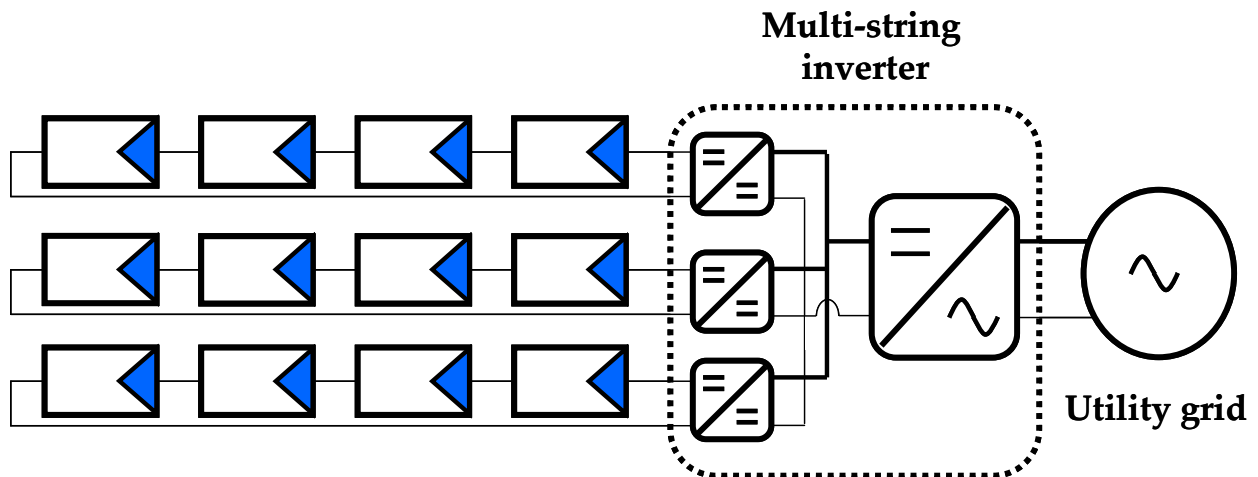


Figure I.16 : Multi-string inverter diagram

Although the single multi-string inverter eases maintenance procedures on the installation, any upgrade of the solar array using this topology is limited. Either a few modules can be added to the array if the power rating of the multi-inverter is sufficient, or for more significant upgrades the inverter must be replaced.

I.6.5. Parallel-connected DC-DC inverter

Parallel-connected DC-DC converters, also known as DC modules, use the same concept as multi-string inverters but applied to a module instead of a PV string. Each module is connected to an individual step-up DC-DC converter that elevates module voltage 30-80 V to a high voltage DC bus at approximately 400 V [YAO'09]. A centralized inverter is then connected to the DC bus for grid connection as presented on Figure I.17. The main advantages of this module integrated converter remains the optimal power use of each module, low sensitivity to module mismatch and a close monitoring of each module in the installation. Surely, the cost of such systems would remain lower than module inverters by regrouping the current inversion function.

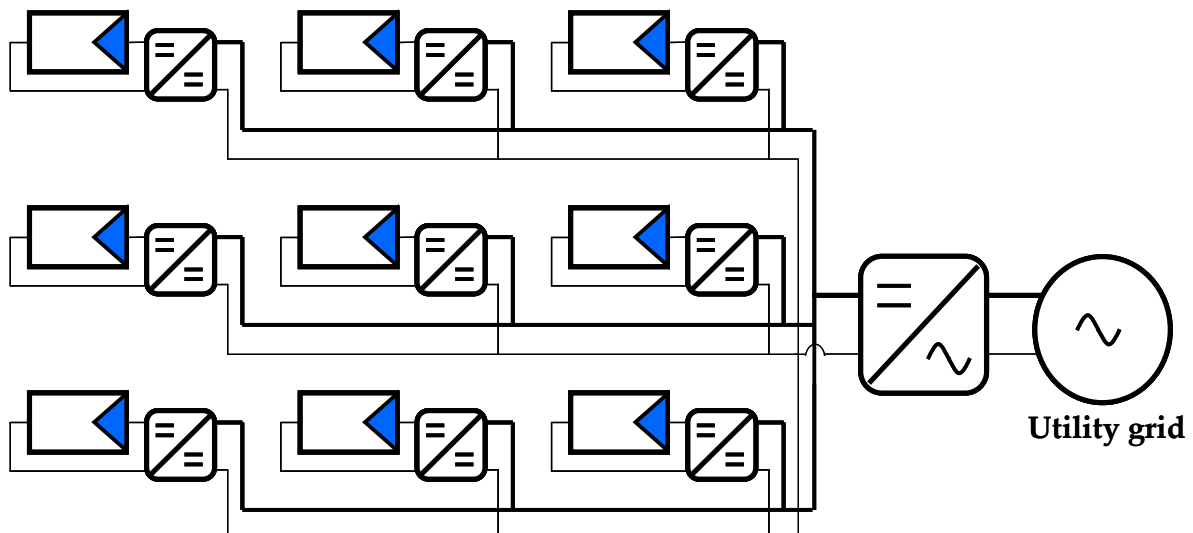


Figure I.17 : Parallel -connected DC-DC converters diagram

The global efficiency for these converters is lower than multi-string converters due to the high voltage elevation ratios, but remains in the 90-95% range. The Solution PV project has developed a double-boost converter able to elevate voltages from 40 V to 400 V using an intermediate DC bus stage with a voltage of 100 V. The DC bus stage voltage value has been chosen to optimize the conversion efficiency. The European efficiency of the developed double-boost converter reaches 95.45% [SAR'09].

Nevertheless, the upgradeability and continuity of service is degraded due to the presence of a centralized inverter. Indeed, in order to add more modules to the installation, one would be required to modify the power rating of the inverter for normal operation. Likewise, if the central inverter fails, the plant cannot feed energy into the grid until the inverter is repaired.

I.6.6. Series connected DC-DC converters

The series connection of modules in PV strings is convenient for obtaining high voltages used for grid connection. The series-connected DC-DC converter configuration, another type of DC module, uses DC-DC converters per module that are series connected in order to form DC module strings as presented on Figure I.18.

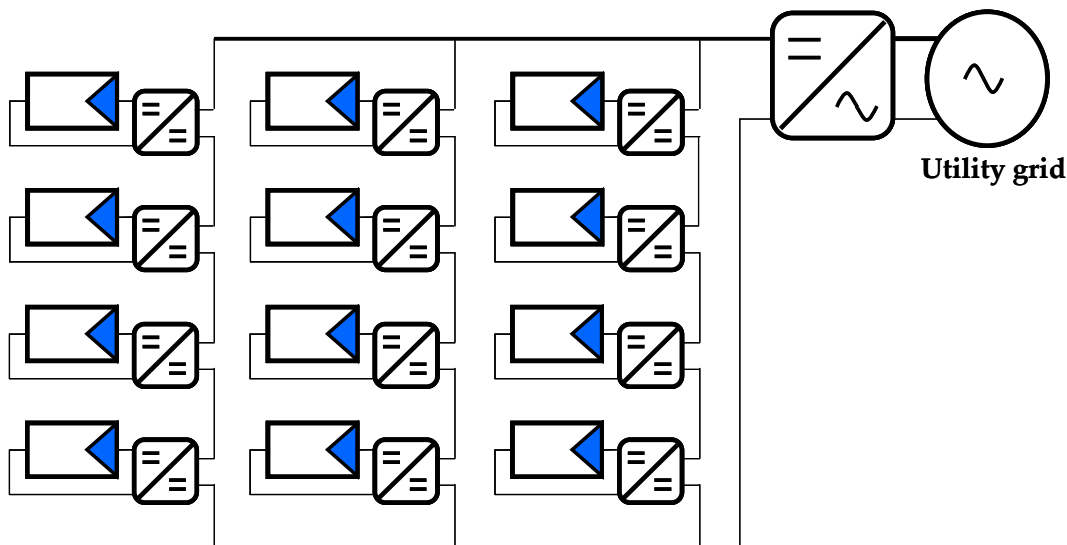


Figure I.18 : Cascaded DC-DC converter diagram

The advantage of series connecting the DC-DC converters is to have lower voltage elevation ratios ($V_{out}/V_{in} < 5$) than parallel-connected DC-DC converters layout, hence increasing power conversion efficiency [FER'06]. In this work, only step-up converters will be considered, however some manufacturers use Buck-Boost converters which can increase and decrease the output PV module voltage. The converters can perform maximum power extraction per module and use a bypass mechanism in case the module can not supply sufficient power. Another control strategy consists in using a supervisor system which could individually control the modules in two modes: maximum power extraction or output voltage limitation [BRA'09]. This PV system architecture keeps the qualities of the multi-module topology in terms of optimal power usage, monitoring capacities, and good continuity of service when one module converter is defective [WAL'04]. The main advantage

when compared to parallel connected DC-DC converters is the higher overall efficiency due to the lower voltage elevation ratios used for each chopper. The principal drawbacks remain the low upgradeability and continuity of service with respect to the central inverter.

A similar approach consists of series connecting both the PV modules and their associated DC-DC converter in series to control the current flow through the PV string as shown on Figure I.19. The principal benefits of the Generation Control Circuit (GCC) [SHI'01] is that each module voltage can be independently controlled by the power converter which operates at higher efficiency since most of the power will be transferred directly through the modules [VIG'10].

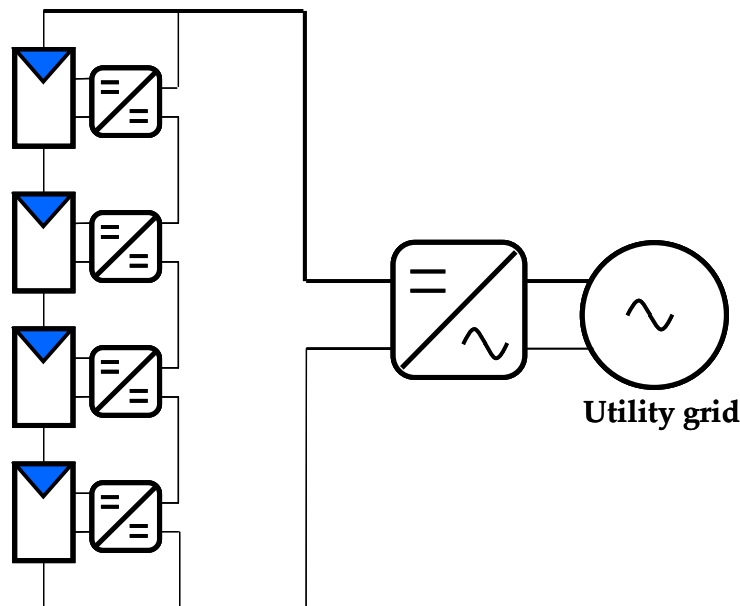


Figure I.19 : Generation control circuit diagram

The paralleling of GCC units on the DC side has not been addressed in the literature. However, parallel connections of multiple GCC units on the AC side at grid supply terminals would offer high global efficiency, continuity of service, as well as upgradeability. Indeed, the GCC unit appears similar to the string inverter layout but adds the individual module power optimization. Simulation results show that in the case two modules of a 6-module PV string are partially shadowed, the GCC can extract 14% more power than in a traditional configuration [SHI'03].

I.6.7. Module inverter

The closer the power converters are to each module, the less dependent the array will be to the different characteristics of each module. Module inverters, also known as AC modules, are directly connected to the each module junction box in the array as presented on Figure I.20. As other inverters, the module inverters considered have two power conversion levels. The first level elevates voltage from approximately 40 V to 400 V and the second level inverts voltage to fit grid codes.

Given the high voltage elevation ratios, the global efficiency of module inverters is lower than previous topologies 87-93% [WOY'03][CAR'06]. However, this topology has many advantages. First of all, the module power extraction is done optimally since each

module inverter has a MPPT algorithm. Secondly, each module is independent from each other due to the power electronics interface. Therefore, the impact of a mismatched module, due to shade or electrical faults, does not disturb the rest of the installation. This is not the case for the previously described system topologies. Thirdly, in case of module inverter failure only the power contribution of one module is lost: this is very promising in terms of continuity of plant power production. Moreover, the system is easily upgradeable by simply adding additional module inverters to the plant [KJA'05]. Finally, the monitoring of each module can be achieved using adapted communication networks such as powerline communications.

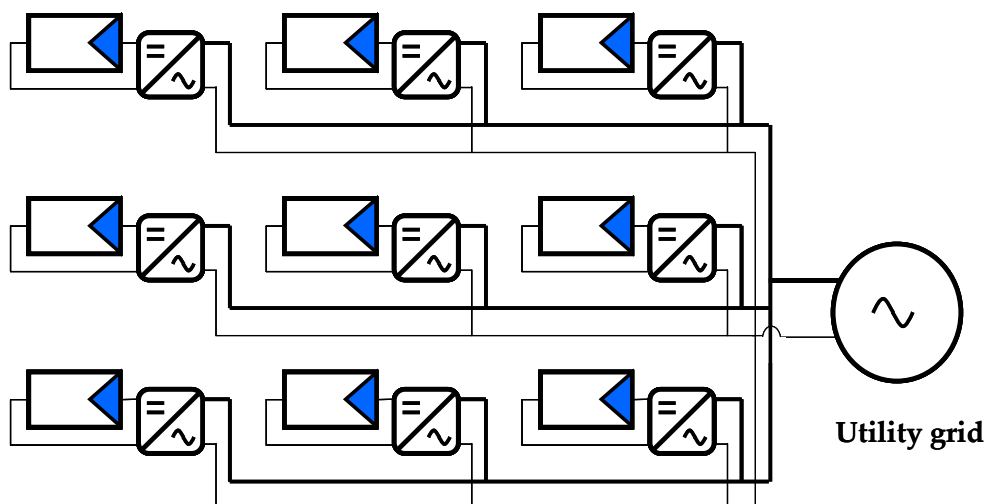


Figure I.20 : Module inverter diagram

Another module inverter concept uses a low-voltage inversion and adds a centralized transformer at the grid interface to elevate alternative voltage to grid requirements. The advantage of this later concept is that using low-voltages increases security and conversion efficiency, but leads to greater cable losses due to larger current values in between transmission cables from the module inverters to the transformer. Furthermore, the presence of a central transformer lessens the overall continuity of service of the plant.

I.6.8. Single cell inverter

The last system layout that can be found in scientific literature is the single cell inverter, also called AC-cells [PVPS'01]. The principal is to directly connect a single PV cell to the mains. This can be achieved by first using a voltage elevation level, with a ratio of approximately 200, connected to a 350 V DC bus followed by an inverter stage as presented on Figure I.21 [WUE'94].

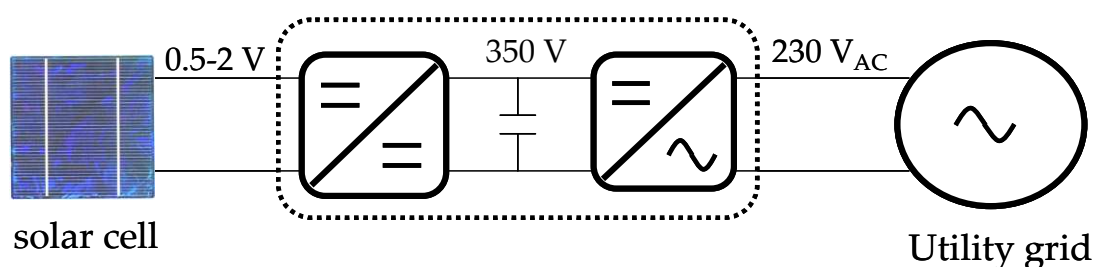


Figure I.21 : Single cell inverter

The main advantage is the reduction of shade induced and cell mismatch losses throughout the plant due to the proximity of the converter to the basic solar energy conversion element. Here again the single cell inverters give good results in terms of continuity of service and plant upgradeability. The monitoring of each solar cell can be carried out, which is helpful for fault detection but can lead to large amounts of information to process. Moreover, the maintenance of a plant containing modules of single cell inverters may prove to be costly in the long run in the event an inverter failure. The most important drawbacks of this solution are the elevated initial cost and the overall low efficiency (70-85%) of the solution.

Conclusion

Grid-connected PV systems have seen a tremendous development this last decade. This trend is expected to continue with lower growth rates. The estimated number of people living off PV grid-connected installations is believed to grow from 5.5 million in 2007 to over 1 billion people in 2030 [SGV'08]. PV systems comprise three main electrical components to perform secure power production: PV modules, power converters, and protection apparatus. Currently, PV systems principally employ crystalline silicon PV modules, but in the near future thin film technologies are expected to account for a quarter of the PV market. Several grid-connected PV system layouts have been reviewed going from centralized topologies to distributed plant topologies. The centralized configurations have the advantage of remaining simple and low cost whereas distributed technologies offer better upgradeability, continuity of service and monitoring services, but currently remain more expensive. As can be seen on Figure I.22, there is no overall optimal topology, the most adapted solution depends on the importance attributed to the evaluation criteria by PV system owner.

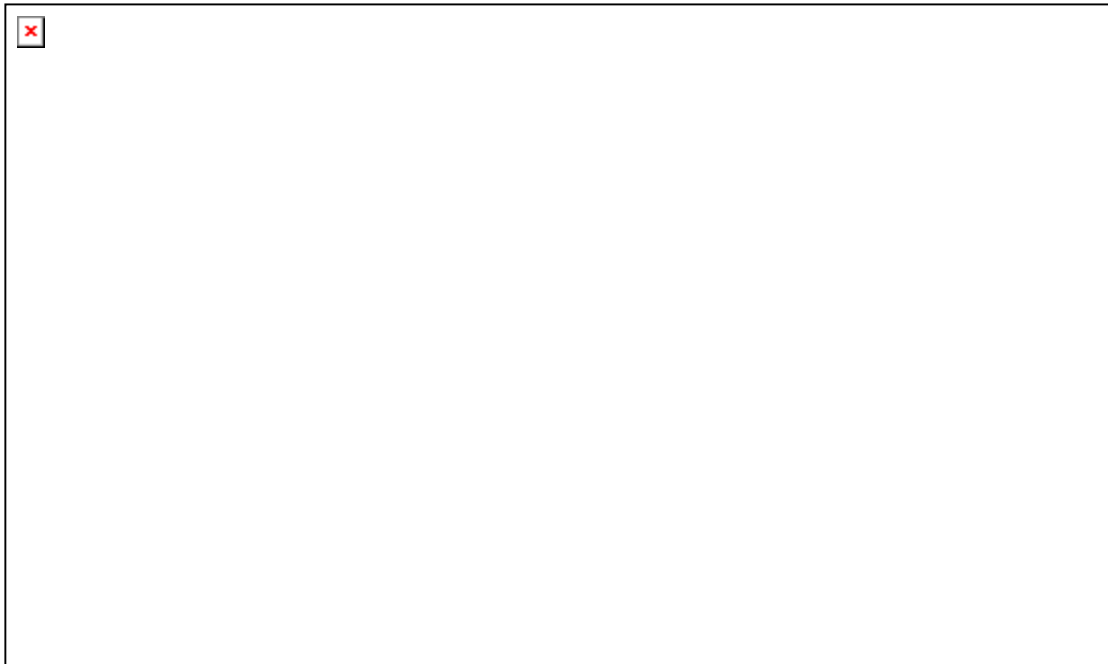


Figure I.22 : Comparison of PV system topologies according to evaluation criteria

The performance of PV systems is essentially determined by its capacity to deliver the most energy during its lifespan. Power production increase can be achieved by reducing power losses that occur in the PV generator and power conversion units. The next chapter will address PV array modelling in order to investigate new methods for decreasing solar generator losses.

Chapter II

Modelling photovoltaic arrays

Introduction

The development of photovoltaic plants throughout the world for both autonomous and grid-connected systems has required reliable modelling techniques for array power production forecast. The focus of this chapter is to describe how photovoltaic arrays are modelled going from the basic PV cell to large arrays using new developed models. Moreover, a method for extracting PV module parameters from experimental measurements will be presented. The environments in which the photovoltaic devices operate have great influence on the PV power production. The impact of incoming solar energy and module temperature on the power output of modules will be studied in order to develop methods to forecast power production in various meteorological conditions. Finally, the electrical equations describing the operation of PV arrays will be presented in order to build a valid power production forecast model for solar arrays.

II.1. Photovoltaic cell basics

The PV cell is the core element enabling the conversion of light induced photons into electrons through the photoelectric effect. In most cases, the conversion is done through a silicon P-N junction which captures photons and emits electrons with a conversion efficiency depending on the solar cell design. Silicon is widely used in the PV industry because of its high theoretical efficiency (25% for mono-crystalline technologies and up to 40% in multi-junction solar cells) and its availability on earth [AST'08]. This section will first describe the different operation states of the PV cell. Secondly, the elements used to ensure protection of the PV cell will be presented. The last section will deal with a brief state of the art of models used for PV cells and describe in detail the one-diode model.

II.1.1. Photovoltaic cell operation

The photovoltaic cell's current-voltage characteristic is similar to that of a Shockley diode and can operate in three current-voltage quadrants: power generator (zone I), overcurrent load (zone II) and backfeed-current load (zone IV), as shown on Figure II.1 [ABE'90]. In nominal operation, the PV cells are used as power generators with typical open-circuit voltages (V_{oc}) of 0.6 V for crystalline technologies and short-circuit currents (I_{sc}) of several amps depending on the surface size and technology of the cell.

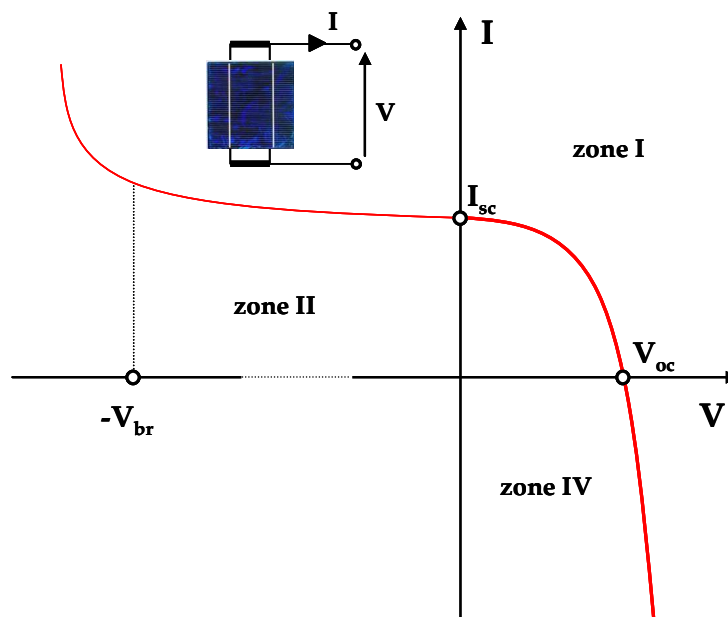


Figure II.1 : Current-voltage characteristic of a photovoltaic cell

The PV cell can also operate in overcurrent or backfeed current zones leading to irreversible cell damage. Indeed, when the PV cell is submitted to reverse voltage there exists a breakdown voltage (V_{br}), typically between 10 V and 15 V for crystalline technologies [HER'97], where the current flowing through the cell increases exponentially leading to excessive thermal stress. Moreover, the cell may be subject to absorb current when it is submitted to voltages greater than its open-circuit voltage. In the case of backfeed current values greater than five times the open-circuit current (in absolute value), the solar cell may be considerably be deteriorated [WIL'98].

In order to ensure safe operation of the PV cell in the power generation zone, protection mechanisms have been implanted in cells or cell sub-strings.

II.1.2. Photovoltaic cell protection apparatus

In commercial PV modules, devices are implanted in the modules to protect the PV cells from electrical degradation due to overcurrents. Other devices are used to protect PV modules from absorbing current from other power generation sources, they are better known as backfeed protection devices. Both overcurrent and backfeed current protection for PV modules will be overviewed in this subchapter.

II.1.2.1. Overcurrent protection

Overcurrent protection apparatus are used to prevent PV cell operation in zone II. For currents higher than the short-circuit current, the cell must operate with reverse voltage. In such conditions, the PV cell generator becomes a load. At high reverse voltages, when the current density surpasses a critical limit a shunt path in the cell is formed by thermal breakdown, this phenomenon is also known as hot-spot formation. Hot-spots cause overheating of the cell and cause irreversible damage. In order to prevent such a process, bypass diodes have been implanted on each cell, almost exclusively for space applications, and more commonly in cell sub-strings for commercial applications.

The bypass diode operation principle consists in limiting reverse voltage of cells among a sub-string. In other words, the bypass diode prevents overcurrents by short-circuiting the cell sub-string. Most commercial modules use one bypass diode per 18 cell sub-strings, as shown on Figure II.2(a).

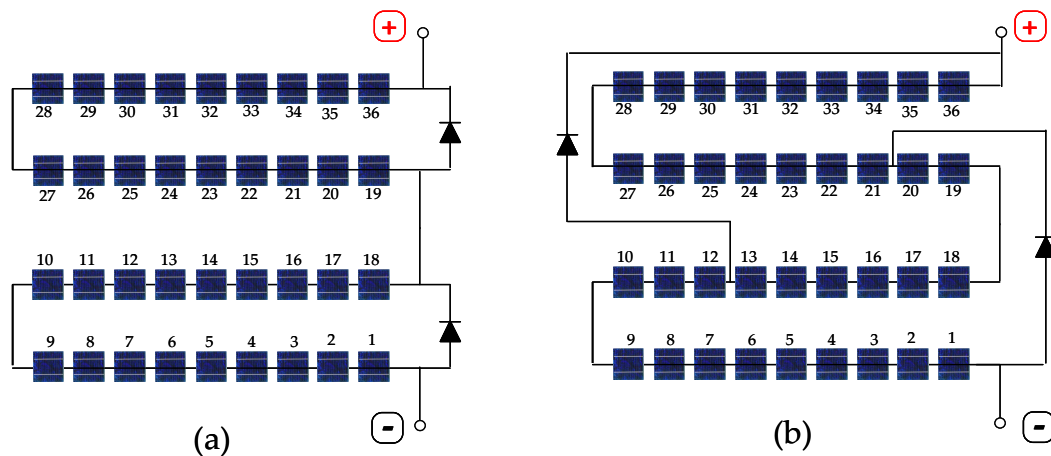


Figure II.2 : (a) 18 cell sub-string with its associated bypass diode; (b) bypass diodes implanted with overlapped solar cells (13-20)

This rule adheres to Hermann's precept of using at most 20 cells per sub-string for one bypass diode in order to prevent thermal overload [HER'97]. Moreover, in certain cases commercial PV modules bypass diodes are placed in order to overlap solar cells as shown on Figure II.2(b). When a cell is shadowed in the non-overlapped region (cells 1-12 and 21-36), the power output is the same as in the previous implementation. However, power output is slightly increased when a shadow is cast on the overlapped solar cells (cells 13-20) at low-voltages [SIL'09].

Other solutions have been proposed to prevent reverse-voltage such as PV cells with integrated bypass diodes [YOS'96][DAN'97] and bypass batteries [NASA'07]. However, none of these later solutions are currently employed in commercial applications.

II.1.2.2. Backfeed current protection

Blocking diodes have been used for years in stand alone applications to prevent batteries from feeding current back to PV arrays during the night hours [WIL'98]. This problem has also been noticed in high-voltage arrays having multiple strings in parallel. In order to prevent such operation, fuses and blocking diodes can be used to protect PV modules, hence cell sub-strings, from backfeed currents as shown on Figure II.3. Backfeed current protection apparatus are generally employed on each string of series-connected PV modules.

Comparisons between these two protection apparatus have not led to unanimous conclusions. On the one hand, blocking diodes seem more reliable since they resist surges better than fuses. Yet, diodes induce greater power losses and voltage drop than fuses. In any case, it has been established that systems without backfeed protection are subject to extensive damage in ground fault situations [WIL'97].

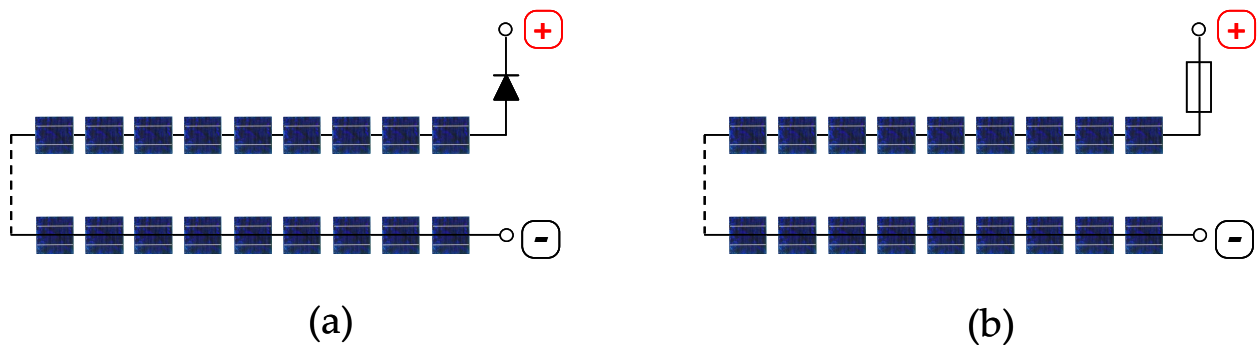


Figure II.3 : 18 cell-substring using a (a) blocking diode and (b) fuse as backfeed current protection

In conclusion to this part, overcurrent and backfeed current protections are necessary to ensure safe operation of PV cells. They are generally employed in commercial PV modules. However, it should be noticed that protection apparatus are added components to the array which add complexity to the system in terms of maintenance and reliability.

II.1.3. Photovoltaic cell modelling

Several models have been proposed throughout the past in order to simulate PV cells operating in various conditions. In essence, each model is an improvement of the ideal model which contains a current source, representing the incoming solar power, and a diode, representing the P-N junction. Additional elements are added to increase the behavior description of the solar cell in certain operating quadrants. The most common models are presented and compared on Table II.1.

The one-diode model is the most widespread model used for PV cells and PV modules due to its low complexity and good accuracy in the power generating quadrant. Evolutions of the one diode model have led to more precise models, such as Bishop's model which describes reverse bias behavior of a solar cell [BIS'88]. The two-diode model improves

the one-diode model by considering both recombination processes in the structure of the material and at its surface [PET'08]. Furthermore, dynamic models have been proposed by introducing a capacitance in order to model the PV cell's dynamic behavior [UJI'02]. The complexity of the models follows the number of parameters to be identified.

The application aimed in this work is to model PV modules. As seen previously in II.1.2, PV modules are equipped with bypass diodes, which means that reverse bias behavior is not considered in our application. The one-diode model has been withheld in this work for its good balance between complexity and precision.

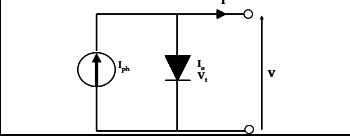
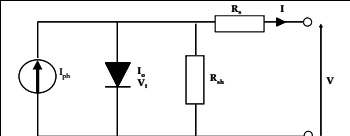
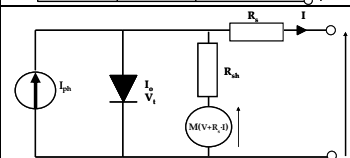
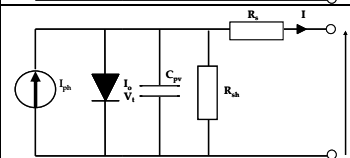
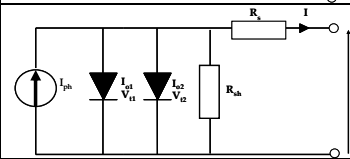
Model	Electrical Scheme	Number of parameters	Accuracy	References
ideal model		3	low	[PIPS'08]
one-diode model		5	good	[KEN'69]
Bishop's model		8	good with reverse bias	[BIS'88]
one-diode dynamic model		6	good with dynamic behavior	[UJI'02]
two-diode model		7	very good	[CHA'87]

Table II.1: Synopsis of widely used models for PV cells

The one diode model leads to the transcendental current-voltage relation expressed in equation II.1 [SER'07][PAT'08]. This expression contains five characteristic parameters enabling PV cell identification. Similar models can be derived from expression by considering the shunt resistance (R_{sh}) infinite, also known as the 4-parameter model, or by considering the series resistance (R_s) negligible with respect to the shunt resistance, but both models will not be considered in this work.

$$I = I_{ph} - I_o \cdot \left(e^{\frac{V+R_s \cdot I}{V_t}} - 1 \right) - \frac{V+R_s \cdot I}{R_{sh}} \quad \text{II.1}$$

In order to properly understand the physical meaning of the model a brief description of each parameter will be carried out next.

□ Light induced current, I_{ph}

The light induced current represents the current generator value in the electrical scheme at a given irradiance. This parameter, also called photocurrent, is created by incoming solar photons and thus varies in accordance with solar irradiance. In PV cell curve fitting, it is common to assimilate the short-circuit current (I_{sc}) to the photocurrent as it has been observed that they both depend linearly with solar irradiance and temperature [DES'04]. This will be further detailed in Chapter III.

□ Diode reverse saturation current, I_0

The diode reverse saturation current is a well-known parameter in diode modelling. The reverse saturation current is independent of the diode voltage and its value depends on numerous factors including: intrinsic semiconductor concentration, cell transverse area, type of material, minority carrier's lifetime and the lengths of depletion layers for type P and N semiconductors [MAT'07]. In brief, this parameter depends mainly on cell temperature, semiconductor characteristics, and the number of PV cells in series (when used for PV module modelling).

□ Thermal voltage, V_t

The thermal voltage considered in equation II.1 takes into account: the cell temperature T , the diode ideality factor n (also known as emission coefficient), the number of cells in series N_s (when applied to PV module modelling) and physical constants such as Boltzmann constant k_b and the elementary charge q , as shown in equation II.2

$$V_t = \frac{N_s \cdot n \cdot k_b \cdot T}{q} \quad \text{II.2}$$

The thermal voltage parameter is convenient to use in PV cell parameter identification because it combines both the ideality factor and cell temperature into one variable [KAR'07]. This parameter is dependent of PV cell technology and temperature.

□ Series resistance, R_s

The series resistance in PV cells results from the resistances located at cell solder bonds, emitter and base regions, cell metallization, cell-interconnect bus bars and resistances located at PV cell terminals [MEY'04]. It has been observed that this parameter depends on solar irradiance and cell temperature, and influences the position of the maximum power point on the current-voltage characteristic.

□ Shunt resistance, R_{sh}

The shunt resistance represents any high-conductivity paths through the solar cell or on the cell edges due to crystal damage and impurities in and near the P-N junction giving rise to a shunt current [MEY'04]. The value of the shunt resistance being much higher than the series resistance, it is occasionally supposed infinite, as in the 4-parameter model. The shunt resistance can however be directly linked to the derivative of the current-voltage

characteristic near the short-circuit current, and therefore has an impact on the slope of the I-V curve close to null voltages.

Annex 1 presents simulation results showing the influence of each parameter on the current voltage characteristic of a PV cell. The following section deals with PV module modelling using the single diode model and introducing an explicit expression of PV module current-voltage.

II.2. Photovoltaic module modelling

Photovoltaic modules consist of a group of cell sub-strings connected in series that are protected by bypass diodes. The number of PV cell sub-string length varies from 8 to 24 PV cells per bypass diode, but the most widely spread design uses one bypass diode per 18 PV cell-string. The number of cell-strings inside a PV module depends on the application. Commercial modules typically have 2 to 4 cell-substrings connected in series, making their maximum power voltages varying between 15-55 V. Cell sub-strings are convenient to model because the presence of the bypass diode eliminates cell sub-string operation in the reverse current zone II (cf. II.1.1.). The one-diode model is convenient in the sense that reverse operation of PV modules is nonexistent due to the presence of bypass diodes. The PV cell model can be adapted to PV modules by modifying parameter values I_{ph} , I_o , R_s , R_{sh} , and V_t . The single diode model leads to a transcendental equation shown in equation II.1, which can be solved by numerical determination using iterative algorithms such as Newton-like methods [YAM'00].

However, prior research in the electronics field has shown interest in solving a similar expression referred to the generalized diode equation. In the 1990's, an approximate analytical solution was proposed by Fjeldly [FJE'91] using explicit continuous trial functions separating current and voltage of the circuit. Later, various trial functions were proposed [ABU'92], with some incorporating the shunt resistance [ORT'92] in order to reduce errors in the approximation. The exact analytical solution to the partial generalized diode equation, omitting the shunt resistance, was proposed by Banwell [BAN'00] by applying the Lambert W-function. Almost a decade later, researchers developed an analytical solution for the photovoltaic cell in order to study photovoltaic cell parameters [DIN'08], determine them [JAI'05], and simulate PV cell arrays [JAI'06][PET'07].

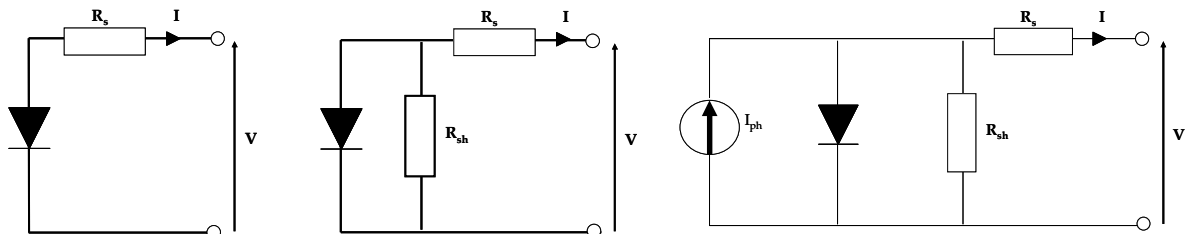


Figure II.4 : Equivalent electrical scheme of the generalized diode equation (a), generalized diode equation with shunt resistance (b) and single diode model for PV modules (c)

The single diode model equation can be put into the form $y = x + b \cdot e^x$ as it will be detailed in paragraphs II.2.2. and II.2.3. This type of equation can be solved by using the Lambert W-function and explicitly expresses x as a function of y . The interest in explicitly

expressing the PV module current/voltage as a function of voltage/current facilitates both computation and analytical calculation of the influence of parameters on PV module operation. In this section both PV module current and voltage expressions will be presented.

II.2.1. Analytical Lambert W-function

In 1758, J.H. Lambert solved the trinomial equation $x = q + x^m$ by determining a series development solution; this later solution was transformed by L.P. Euler and led to the now called Lambert W-function which will be described more thoroughly in this section [COR'96]. Furthermore, E.M. Wright contributed to developing the computation of complex values of the Lambert W-function which helps to explain the current name of the function [WRI'59].

II.2.1.1. Definition

The Lambert W-function, also known as Omega function, is defined by as the inverse of the function $W^{-1} : x \rightarrow x \cdot e^x$ and is commonly noted $W(x)$. Although the Lambert W-function is also defined for complex numbers, we will limit our study for real values on the principal branch, known as W_0 , which has values $-1 \leq W(x)$. The principal branch is an increasing monotonic function therefore a positive real number will have a unique solution in the set of positive real numbers.

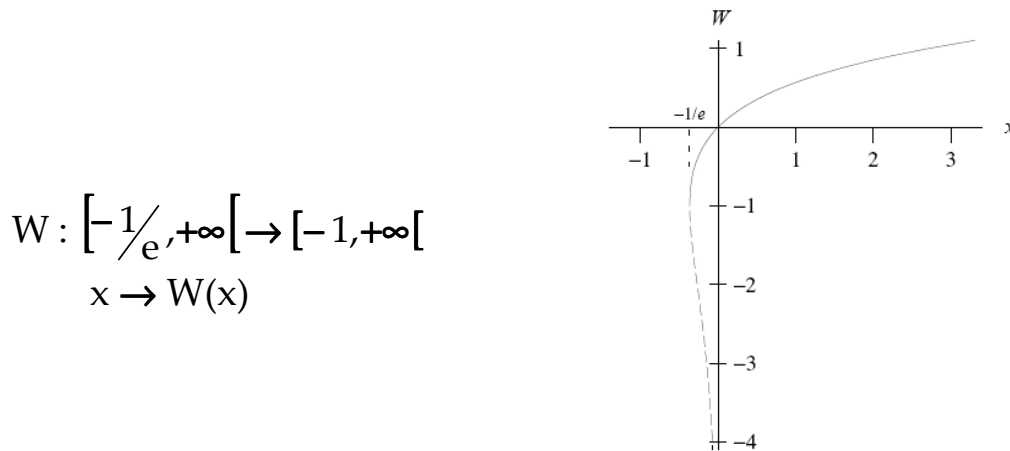


Figure II.5 : Graphic plot of Lambert W-function for real values

Interest in this function consists in resolving an equation of the form II.3, equation II.1 can be transformed into such a form as will be seen further on.

$$y = x + b \cdot e^x \tag{II.3}$$

By applying several simple transformations of equation II.3, an explicit solution of x as a function of y using the Lambert W-function is obtained, as shown in II.4

$$\begin{aligned} y &= x + b \cdot e^x \\ (y-x) \cdot e^{-x} &= b \\ (y-x) \cdot e^{y-x} &= b \cdot e^y \\ y-x &= W(b \cdot e^y) \end{aligned}$$

$$x = y - W(b \cdot e^y) \quad \text{II.4}$$

As shown in the previous expression, the computation of x for large values of y will require a calculation of Lambert W -function values for close to infinity inputs, given the exponential expression. For this reason, it will be convenient to use the asymptotic expression of $W(x)$ which is detailed next.

II.2.1.2. Infinity asymptote expression

The Lambert W -function computation uses a series expansion. The series expansion has the advantage of having rapid computation time, yet for high input values of the Lambert W -function this method can lead to errors. In order to overcome this problem, the use of the asymptotic expression has proven to be useful. As shown in equation II.4 the input value is exponential. This quickly leads to large values, making a simple asymptote expression necessary.

Let $z = b \cdot e^y$ with $b > 0$, which leads to $z > 0$.

Moreover, let

$$W(z) = \log(z) + u \quad \text{II.5}$$

By applying the definition of the Lambert W -function, equation II.6 is obtained.

$$\begin{aligned} z &= [\log(z) + u] \cdot e^{\log(z)+u} \\ z &= [\log(z) + u] \cdot z \cdot e^u \\ 1 &= [\log(z) + u] \cdot e^u \end{aligned} \quad \text{II.6}$$

If $\log(z) \gg u$ when $z \rightarrow +\infty$ (hypothesis 1), relation II.7 is deduced.

$$e^u \approx \frac{1}{\log(z)} \quad \text{II.7}$$

In the case $\log(z) > 0$ (hypothesis 2), II.7 can be rewritten as II.8.

$$u \approx -\log[\log(z)] \quad \text{II.8}$$

Now, coming back to our application, $\log(z)$ can directly be expressed as shown below.

$$\log(z) = \log(b) + y \quad \text{II.9}$$

Therefore, by substituting y in II.9 into equation II.4 the following expression is obtained:

$$W(z) = \log(z) - \log(b) - x \quad \text{II.10}$$

If $u = -\log(b) - x$, equation II.5 can be recognized.

Hence, the determination of the infinity asymptote for our application by using equations II.8 and II.9 can continue.

$$\begin{aligned} -\log(b) - x &= -\log(\log(b) + y) \\ x &= \log(\log(b) + y) - \log(b) \end{aligned} \quad \text{II.11}$$

This asymptote expression will be used in calculations of high values of y , for further results on using the Lambert W-function refer to [COR'96]. In conclusion to this part, equation II.4 can be substituted by expression II.11 when $y \rightarrow +\infty$.

The photovoltaic module contains two main variables: current and voltage. The next part of this chapter will successively present the analytical expression of module current as a function of the voltage followed by the expression of module voltage as a function of the current.

II.2.2. Analytical expression of photovoltaic module current

II.2.2.1. PV module current expression

The expression of PV module current as function of voltage may be useful for determining the current flowing through modules whose voltage is imposed, like in an array of parallel connected modules as shown on Figure II.6.

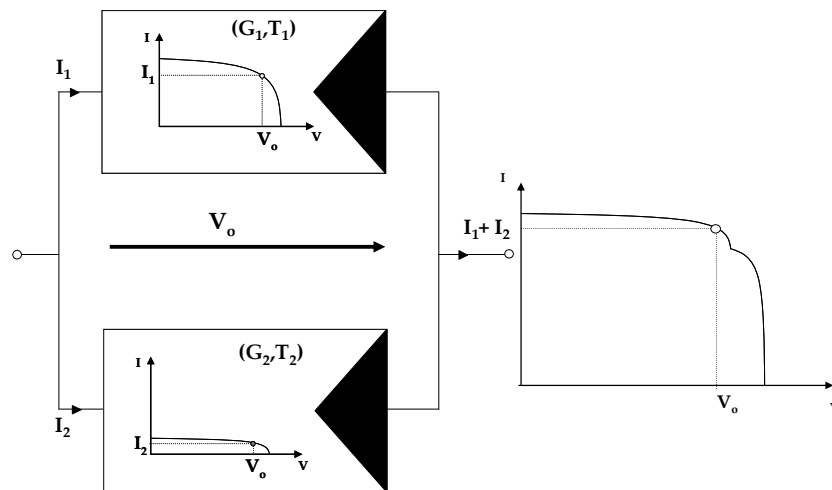


Figure II.6 : Parallel connected module operation diagram with different I-V characteristics

Direct expression of module current is obtained by transforming and manipulating expression II.1 which leads to the equation presented below.

$$\frac{R_s \cdot R_{sh}}{(R_s + R_{sh}) \cdot V_t} \cdot (I_{ph} + I_o) = \frac{V \cdot \left(\frac{R_s}{R_s + R_{sh}} \right) + R_s \cdot I}{V_t} + \frac{R_s \cdot R_{sh} \cdot I_o}{(R_s + R_{sh}) \cdot V_t} \cdot e^{\frac{V \cdot R_{sh}}{V_t \cdot (R_s + R_{sh})}} e^{\left(\frac{V \cdot \left(\frac{R_s}{R_s + R_{sh}} \right) + R_s \cdot I}{V_t} \right)}$$

By defining the following variables:

$$\begin{aligned} y &= \frac{R_s \cdot R_{sh}}{(R_s + R_{sh}) \cdot V_t} \cdot (I_{ph} + I_o) && \text{function of constant parameters} \\ x &= \frac{V \cdot \left(\frac{R_s}{R_s + R_{sh}} \right) + R_s \cdot I}{V_t} && \text{function of V and I} \end{aligned}$$

$$b = \frac{R_s \cdot R_{sh} \cdot I_o}{(R_s + R_{sh}) \cdot V_t} \cdot e^{\frac{V \cdot R_{sh}}{V_t \cdot (R_s + R_{sh})}} \quad \text{function of } V$$

The previous form of equation II.3 is obtained, which leads to the solution II.4 where the module current is expressed as a function of the module parameters and voltage.

$$I = \frac{V_t}{R_s} \cdot [y - W(b \cdot e^y)] - \frac{V}{R_s + R_{sh}} \quad \text{II.12}$$

II.2.2.2. Verification of mathematical solution existence

In order to verify that a mathematical solution exists, it must be proven that $b \cdot e^y > 0$.

Yet $\square b = \frac{R_s \cdot R_{sh}}{(R_s + R_{sh}) \cdot V_t} \cdot e^{\frac{V \cdot R_{sh}}{V_t \cdot (R_s + R_{sh})}} > 0$ for $V \in \mathbb{R}$, since all parameters have strictly positive values.

$$\square e^y > 0 \text{ for any } y \in \mathbb{R}.$$

Therefore, $W(b \cdot e^y)$ exists for all values of module voltage.

II.2.2.3. Usage of infinity asymptote expression

In order to use expression II.11, the validation of both hypotheses in section 2.1.2 must be checked.

Let $z = b \cdot e^y$ and $u = -\log(b) - x$ using expressions in section 2.2.1.

\square **Hypothesis 1** : $\log(z) \gg u$ when $z \rightarrow +\infty$

Using the previous expressions the difference between $\log(z)$ and u can be calculated. Given the expression of y , which is a finite number with given constant parameters, it can be seen that z evolves as does b when approaching infinity.

Therefore, given expression II.13 the hypothesis is validated.

$$\log(z) - u = 2 \cdot \log(b) + y + x \xrightarrow{z \rightarrow +\infty} +\infty \quad \text{II.13}$$

\square **Hypothesis 2** : $\log(z) > 0$

The verification of the solution existence showed that $b > 0$ and $y > 0$ which proves the existence of $\log(z)$. Since $\log(z) = \log(b) + y$, there remains to prove that $\log(b) > -y$. An analysis of the possible values of the parameters would be necessary. The choice not to pursue the mathematical analysis of possible parameter values was taken in order to focus more on other work. It will be supposed that this condition is true and will be validated experimentally. From a pragmatic point of view, the real parameters of PV modules usually satisfy the hypothesis.

The asymptotic value of the current can be obtained by using formula II.10 and is expressed as follows:

$$I = \frac{V_t \cdot [\log(\log(b) + y) - \log(b)] - V \cdot \left(\frac{R_s}{R_s + R_{sh}} \right)}{R_s} \quad \text{II.14}$$

After having presented the expression of the PV module current, the complementary formula for PV module voltage will be addressed.

II.2.3. Analytical expression of photovoltaic module voltage

II.2.3.1. PV module voltage expression

The determination of the module voltage is similar to the previous method and differs only in the values of x , y , and b . Interest in using voltage as function of current can be found in describing the effect of module mismatch in PV strings since the current flow is the same for each module as shown on Figure II.7.

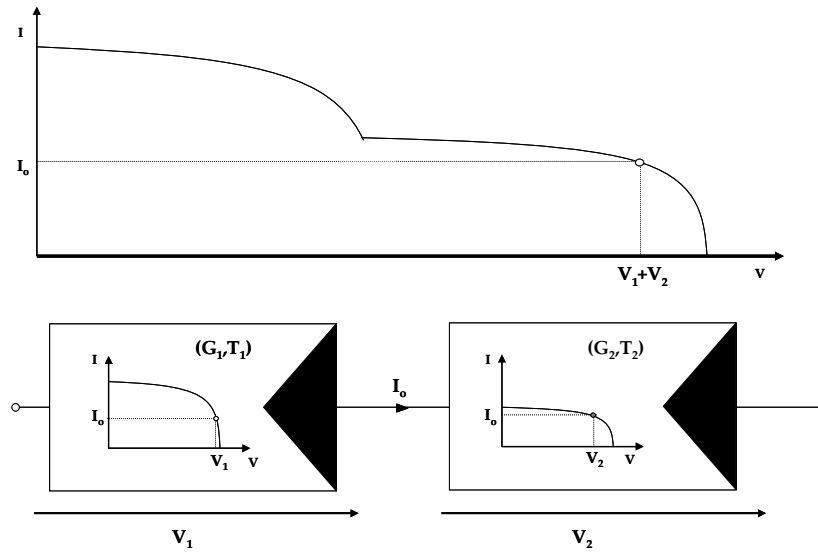


Figure II.7 : Series connected module operation diagram with different I-V characteristics

The transcription of relation II.1 leads to the following expression:

$$\frac{R_{sh}}{V_t} \cdot (I_{ph} + I_o - I) = \frac{R_{sh} \cdot I_o}{V_t} \cdot e^{\frac{V + R_s \cdot I}{V_t}} + \frac{V + R_s \cdot I}{V_t}$$

where

$$y = \frac{R_{sh}}{V_t} \cdot (I_{ph} + I_o - I) \quad \text{function of } I$$

$$x = \frac{V + R_s \cdot I}{V_t} \quad \text{function of } V \text{ and } I$$

$$\text{and} \quad b = \frac{R_{sh} \cdot I_o}{V_t} \quad \text{function of constant parameters}$$

The term x is the only variable that includes the module voltage, therefore the previous equation can be rewritten to isolate V using II.3, which leads to II.15

$$V = V_t \cdot \left[\frac{R_{sh}}{V_t} \cdot (I_{ph} + I_o - I) - W \left(\frac{R_{sh} \cdot I_o}{V_t} \cdot e^{\frac{R_{sh} \cdot (I_{ph} + I_o - I)}{V_t}} \right) \right] - R_s \cdot I \quad \text{II.15}$$

II.2.3.2. Verification of mathematical solution existence

As for the previous relation, $b \cdot e^y > 0$ must be verified for the solution to exist for positive real values of current.

In this case, b is a positive constant for a given PV module. The exponential term always being positive, the existence of a unique voltage for a given input current can be deduced. The proof for the existence is the same as in section II.2.2.2. Therefore $W(b \cdot e^y)$ exists for all values of module voltage.

II.2.3.3. Usage of infinity asymptote

The term $b \cdot e^y$ approaches infinity when the module absorbs large amounts of current ($I < 0$, ie. when $I \rightarrow -\infty$), in order to use the asymptote relation hypotheses 1 and 2 of section II.2.1.2 must be verified.

As previously, $z = b \cdot e^y$ and $u = -\log(b) - x$.

□ **Hypothesis 1:** $\log(z) \gg u$ when $z \rightarrow +\infty$

In this case, substitution of u and z is necessary in order to determine if the difference between $\log(z)$ and u is positive.

$$\log(z) - u = 2 \cdot \log(b) + y + x = 2 \cdot \log(b) + \frac{R_{sh}}{V_t} \cdot (I_{ph} + I_o) + \frac{V}{V_t} + \frac{R_s - R_{sh}}{V_t} \cdot I$$

Furthermore, the common approximation $R_s \ll R_{sh}$ can be used in order to facilitate asymptotic behavior.

$$2 \cdot \log(b) + \frac{R_{sh}}{V_t} \cdot (I_{ph} + I_o) + \frac{V}{V_t} - \frac{R_{sh}}{V_t} \cdot I \xrightarrow{I \rightarrow -\infty} +\infty$$

Hence, the first hypothesis is proven.

□ **Hypothesis 2:** $\log(z) > 0$

Given the expression of $\log(z) = \log(b) + y$ with these new values of $b > 0$ and $y > 0$, an analysis on the parameters R_s , R_{sh} , V_t , I_o , I_{ph} to verify for which values $\log(z) \leq 0$ would need to be conducted. Again, it is supposed that the hypothesis is true and will be verified *a posteriori*.

The asymptotic value of the voltage can be obtained by using formula II.10 and is expressed as follows:

$$V = V_t \cdot [\log(\log(b) + y) - \log(b)] - R_s \cdot I \quad \text{II.16}$$

In order to reduce the complexity of the both PV module current and voltage expressions a simplified expression of these has been established

II.2.4. Simplified expressions of PV module current and voltage

The five parameter model for PV modules can be simplified by using approximations between series and shunt resistances. Indeed, there is an order of magnitude of at least 100 between the series and shunt resistance [KAU'03][KIR'08]. Such approximations can be very useful to ease computation.

Some models completely exclude the shunt resistance by considering the value infinite, as in the 4 parameter model [DES'04][MAT'07]. In the 4 parameter model, the voltage drop caused by the series resistance is therefore completely omitted. In this study, we will consider $R_s \ll R_{sh}$, which disregards the current flow through the shunt resistance with respect to the current flow through the series resistance. This approximation will simplify the previous expressions of module current and voltage. It should be noticed that the assumption $R_s \ll R_{sh}$ remains true for different module irradiance and temperature values. In the case of module degradations this hypothesis should be reconsidered.

$$I = \frac{V_t}{R_s} \cdot \left[\frac{R_s \cdot (I_{ph} + I_o)}{V_t} - W \left(\frac{I_o}{V_t} \cdot R_s \cdot e^{\frac{V}{V_t}} \cdot e^{\frac{R_s \cdot (I_{ph} + I_o)}{V_t}} \right) \right] - \frac{V}{R_{sh}} \quad \text{II.17}$$

$$V = V_t \cdot \left[\frac{R_{sh}}{V_t} \cdot (I_{ph} + I_o - I) - W \left(\frac{R_{sh} \cdot I_o}{V_t} \cdot e^{\frac{R_{sh} \cdot (I_{ph} + I_o - I)}{V_t}} \right) \right] - R_s \cdot I \quad \text{II.18}$$

In the analysis of module mismatch in an array, it has been chosen to use equation II.17 expressing the current as a function of module voltage for better numerical precision. Indeed, between short-circuit current (I_{sc}) and maximum power point current (I_{mpp}), a large interval of voltage values is crossed for a small interval of current values, as shown on Figure II.8(a).

Therefore in order to raise precision on current values between I_{sc} and I_{mpp} , the choice of using module voltage as an input was preferred throughout this work. If higher precision between open-circuit voltage (V_{oc}) and maximum power voltage (V_{mpp}) is favored, then equation II.18 should be considered as shown on Figure II.8(b).

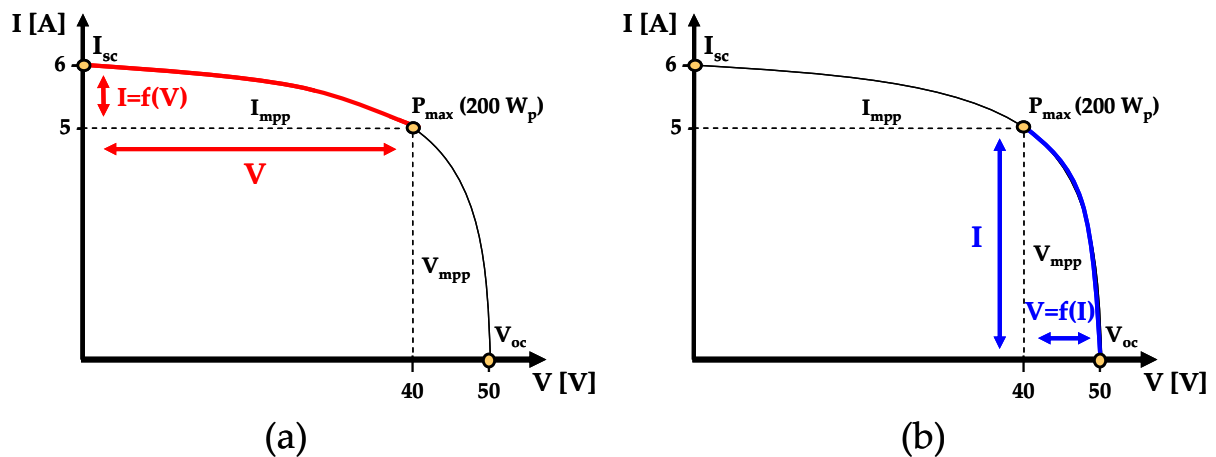


Figure II.8 : Influence of chosen module function on precision of output values ; (a) high precision of module current at low voltage (b) high precision of voltage at low current . Numerical values have been taken from a 200 W_p commercial crystalline-silicon module

The following section will present resolution methods used to solve non-linear problems. Newton-Raphson and Halley's method will be presented, compared, and applied to PV modules.

II.2.5. Numerical calculation of PV module characteristics

The resolution of algebraic equations has brought much interest throughout the years in order to make faster and more accurate algorithms to solve problems. The most well-known procedure was proposed by Newton in 1669 and Raphson in 1690, nowadays referred to the Newton-Raphson method. The main advantage of this method is its wide-range field of applications in the sense that it can be used to solve both linear and non-linear problems. The quadratic convergence makes this method attractive to use. Unfortunately, the Newton-Raphson method remains sensitive to the initial guess beginning the iterative process. This initial guess must verify certain convergence theorems in order to guarantee the procedure's convergence [YAM'00].

Since then, many Newton-like methods have been developed bringing higher orders of convergence and smaller asymptotic errors [BAB'06]. An interesting variant of the Newton-Raphson method is Halley's method, named after the famous astronomer and mathematician, which has the advantage of being less sensitive to the initial guess and has cubic convergence [KAN'07].

Comparative results between both methods are presented in Table II.2.

Iterative Method	Order of Convergence	Information Efficiency	Initial Guess Sensitivity
Newton-Raphson	2	1,41	sensitive
Halley	3	1,44	less sensitive

Table II.2. : Comparison of iterative methods for numerical analysis

Information efficiency is defined using the order convergence of the method q , and the information usage d (which represents the number of new pieces of information required per iteration) as shown in equation II.19 [BAB'06].

$$EFF = q^{1/d} \quad \text{II.19}$$

This indicator helps to compare methods in information efficiency use. The comparison has oriented our choice to use Halley's method for determining current-voltage characteristics of modules because of the higher order of convergence, information efficiency, and sensitivity to initial guess.

II.2.5.1. General presentation of Halley's Method

The iterative Newton-like methods proposed to find the roots of a function $f(x)$ have global similarities in their processes. As Babajee points out [BAB'06], the determination of the root begins with an initial guess x_0 and uses an iterative process. Halley's method uses a Taylor series expansion, also used in the Newton-Raphson method, of the function f around

x_0 but continuing to the second order [KAN'07]. The iterative process is described in equation II.20

$$x_{k+1} = x_k + \frac{f(x_k)}{D(x_k)} \quad \text{II.20}$$

where

$$D(x_k) = f'(x_k) \quad \text{in the Newton-Raphson method}$$

$$D(x_k) = f'(x_k) - \frac{f(x_k) \cdot f''(x_k)}{2 \cdot f'(x_k)} \quad \text{in Halley's Method} \quad \text{II.21}$$

The iterative process stops when the difference between steps is smaller than the precision ε desired by the user, as shown below.

$$|x_{k+1} - x_k| < \varepsilon$$

After presenting the process used in Halley's method, we shall apply it to the PV module in order to calculate the values of the Lambert W-function.

II.2.5.2. Halley's method applied to the PV module

Considering equation II.17, the evaluation of current requires elementary operations (addition, multiplication) and Lambert W-function value. Hence, determination of the Lambert W-function value will be carried out using numerical calculation with Halley's Method and the asymptote equation II.14 when necessary. The function defined in II.22 will be used to determine the value of x , which corresponds to the image of z using the Lambert W-function.

$$f(x) = x \cdot e^x - z \quad \text{II.22}$$

The iterative process to do so takes the form of equation II.21. [COR'96].

$$x_{k+1} = x_k + \frac{x_k \cdot e^{x_k} - z}{\frac{(x_k + 2) \cdot (x_k \cdot e^{x_k} - z)}{2 \cdot x_k + 2} - e^{x_k} \cdot (x_k + 1)} \quad \text{II.23}$$

The method proposed to calculate current-voltage characteristics conserves accuracy and increases the convergence rate compared to the traditional resolution method. These two last points are discussed in the next section.

II.2.5.3. Comparison between Newton-Raphson and Halley's method applied to photovoltaic modules

In scientific literature concerning photovoltaic modelling, the Newton-Raphson method is frequently used for solving the one-diode model equation [CHA'95][GAU'01][KAW'03]. The proposed model has two main advantages in comparison with traditional methods: explicit expression of module current as a function of voltage and

accelerated calculation speed. As seen previously, the one-diode model equation can be expressed using the transcendental equation or use the Lambert W-function, which dissociates current and voltage analytically. This point is interesting for further calculations, such as analytical maximum power point coordinates determination or parameter extraction, which will be investigated later on. The transcendental equation is then solved by using the Newton-Raphson method, whereas the expression using the analytical solution uses Halley's method to calculate Lambert W-function images.

Both methods have been implanted in MATLAB© software for simulation and comparison. The Newton-Raphson method uses MATLAB© embedded function *fsolve* from the Optimization Toolbox™ to solve the transcendental equation II.1 The proposed method uses the same software and equation II.17 to determine module current. The Lambert W-function numerical calculation is done with an algorithm written by P.Getreur [GET'06] using an embedded Hayley's method. The initial guess x_0 , recommended by Getreur, used for both algorithms is a linear function of the input value x where e is Euler's number, as shown in equation II.24.

$$x_0 = \sqrt{2 \cdot (1 + e \cdot x)} \quad \text{II.24}$$

It should be acknowledged that the Newton-Raphson method is not optimized possibly making its convergence slower than an optimal convergence. However, in order to correctly compare both methods the initial guesses of both algorithms have been set equally.

Five sets of module currents have been calculated using a voltage vector containing 100, 500, 1000, 1500 and 2000 points. The current-voltage characteristics were determined using parameters for a 200 W_p module ($I_{ph}=3.83$ A, $I_0=3.4e-10$ A, $R_s=1.16$ Ω , $R_{sh}=1000$ Ω , $V_t=2.97$ V), the computation times for each scenario are presented on Figure II.9. The left axis (in blue), expressed in milliseconds, is attributed to the Lambert W method whereas the right axis (in red), expressed in seconds, is attributed to the Newton-Raphson computation time results.

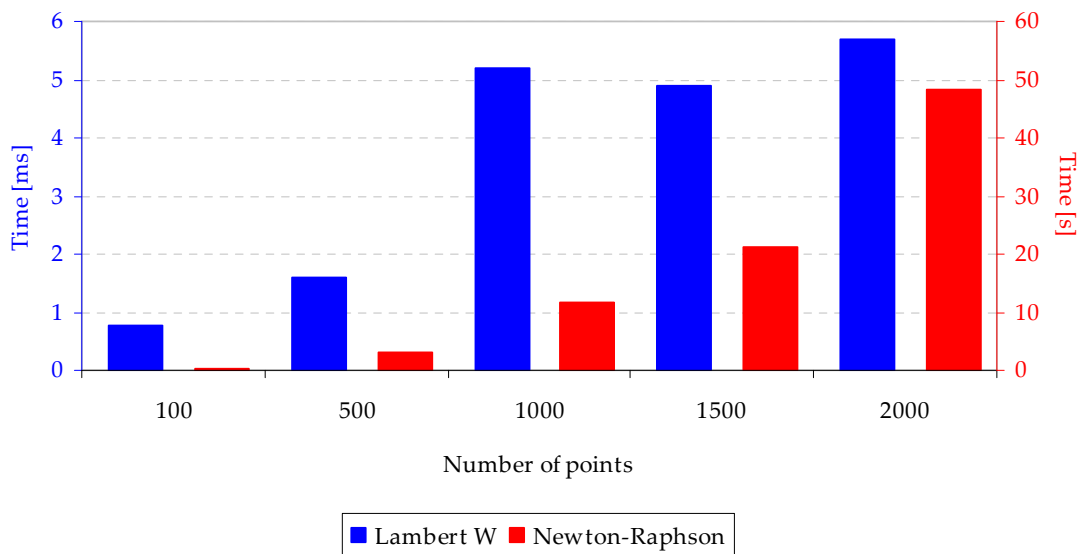


Figure II.9 : I-V characteristic simulation times using Newton-Raphson and Lambert W method

Results show that the Lambert W method is approximately 1000 times faster than the Newton-Raphson method. Furthermore, a final test with 10000 points was initially intended, yet where the Lambert W algorithm was capable of giving an answer in 33 ms, the Newton-Raphson algorithm was incapable of finalizing computation do to memory saturation. This last point may not be significant in the practice for PV module I-V characteristic simulations, yet shows another interest in using the Lambert W algorithm for very large calculations.

In conclusion, we have seen that photovoltaic modules can be modelled by using the PV cell model with modified parameters. The transcendental equation governing current-voltage values can be transformed analytically in order to express module current as a function of voltage (or vice versa) using the Lambert W-function. The advantage of using this approach is the dissociation of current and voltage, which is interesting for analytically determining specific points on the current-voltage characteristic and accelerated calculation time in comparison with traditional methods.

II.3. PV module parameter identification

The aim of this section is to determine the single-diode model parameters values that fit experimental I-V characteristics of photovoltaic modules. In order to accomplish this, the least square curve fitting procedure is applied to the PV module model and experimental curves. Both the methodology and validation, based on several measurements, of the proposed method will be addressed in this part.

II.3.1. Least square curve fitting

The least square curve fitting technique minimizes the error between the simulation curve and experimental curve. The module function is inspired from equation II.17, but adds the 5 module parameters as inputs, as shown on equation II.25.

$$g(x, V) = \frac{V_t}{R_s} \cdot \left[\frac{R_s \cdot (I_{ph} + I_o)}{V_t} - W \left(\frac{I_o}{V_t} \cdot R_s \cdot e^{\frac{V}{V_t}} \cdot e^{\frac{R_s \cdot (I_{ph} + I_o)}{V_t}} \right) \right] - \frac{V}{R_{sh}} \quad II.25$$

where $x = [R_s, R_{sh}, V_t, I_{ph}, I_o]$

More precisely, the least square fitting procedure consists in determining module fitting parameters by minimizing the sum of the squares of the offsets of the experimental curve data points. In other words, for a given set of experimental voltages V_i and currents I_i , the least square fitting procedure will end the iterative process when the sum of offset squares are minimal, this is done through the calculation of the residual R^2 as shown in equation II.26.

$$R^2 = \sum_i [I_i - g(x, V_i)]^2 \quad II.26$$

The minimum of the residual is determined when its derivative with respect to the parameter x is zeroed [WEI'10]. The MATLAB software provides an embedded least square

fitting algorithm, named *lsqcurvefit* in the Optimization Toolbox. To begin the iterative process an initial guess is needed. The outcome of the procedure is very sensitive to the initial guess that is why module datasheet values can be useful to initialize the process.

II.3.2. Parameter initialization using datasheet values

Datasheets of PV modules detail three specific points of the current-voltage characteristic: short-circuit (I_{sc}), maximum power point (P_{MPP} , V_{MPP} , I_{MPP}), and open-circuit (V_{oc}) values, as shown on Figure II.10. They will be used to initialize the least square curve fitting procedure.

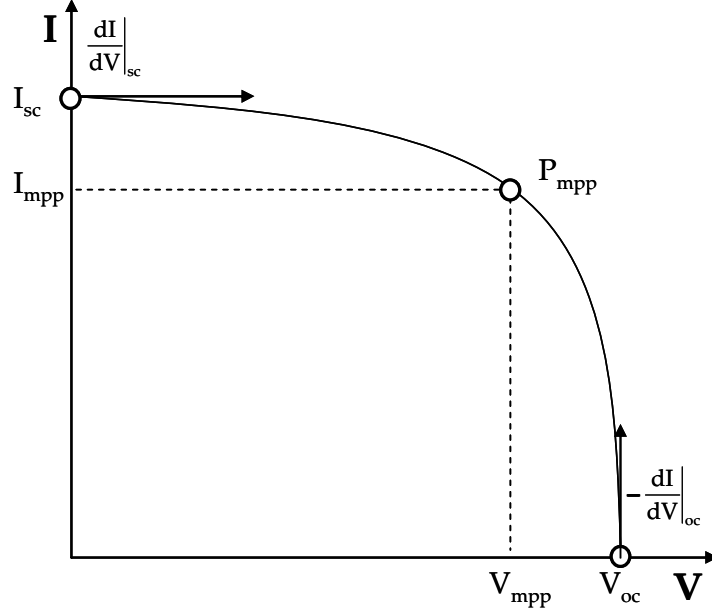


Figure II.10 : PV module I-V characteristic with datasheet specified points

By applying the one-diode model expression (cf. equation II.1) at short-circuit and open-circuit conditions equations II.27 and II.28 are obtained.

$$I_{sc} = I_{ph} - I_o \cdot \left(e^{\frac{R_s \cdot I_{sc}}{V_t}} - 1 \right) - \frac{R_s \cdot I_{sc}}{R_{sh}} \quad \text{II.27}$$

$$0 = I_{ph} - I_o \cdot \left(e^{\frac{V_{oc}}{V_t}} - 1 \right) - \frac{V_{oc}}{R_{sh}} \quad \text{II.28}$$

Considering the shunt resistance infinite and the reverse saturation current negligible with respect to the light-induced current, equations II.27 and II.28 can be rewritten to determine initial values of I_{ph} and I_o as shown in equations II.29 and II.30. These later expressions are approximate values of the parameters, given the assumptions that were made, but are useful for initializing the identification process given simplicity of the expressions.

$$I_{ph} = I_{sc} \quad \text{II.29}$$

$$I_o = I_{sc} \cdot e^{\frac{-V_{oc}}{V_t}} \quad \text{II.30}$$

Moreover, by deriving equation II.1 we obtain the expression of the current derivative with respect to voltage as shown in equation II.31.

$$\frac{dI}{dV} = - \frac{\frac{I_o}{V_t} \cdot e^{\frac{V+R_s \cdot I}{V_t}} + \frac{1}{R_{sh}}}{1 + R_s \cdot \left(\frac{I_o}{V_t} \cdot e^{\frac{V+R_s \cdot I}{V_t}} + \frac{1}{R_{sh}} \right)} \quad \text{II.31}$$

By applying the derivative expression at open-circuit and short-circuit conditions, series and shunt resistance values can be determined as presented in equations II.32 and II.33

$$\left. \frac{dI}{dV} \right|_{oc} = - \frac{1}{R_{sh}} \quad \text{II.32}$$

$$\left. \frac{dI}{dV} \right|_{sc} = - \frac{1}{R_s} \quad \text{II.33}$$

These later results assume three hypotheses:

- series resistance is negligible compared to shunt resistance

$$R_s \ll R_{sh}$$

- exponential term is negligible in short-circuit conditions

$$\frac{I_o}{V_t} \cdot e^{\frac{R_s \cdot I_{sc}}{V_t}} \ll 1$$

- exponential term is major in open-circuit conditions

$$\frac{I_o}{V_t} \cdot e^{\frac{V_{oc}}{V_t}} \gg 1$$

The first approximation is commonly used and validated in Annex 2, however the last two hypotheses have been deduced from order of magnitude analysis and numerical calculations.

Finally, the last parameter to initialize is the thermal voltage. By using equation II.1, II.29 and II.30 at the maximum power point, equation II.34 can be deduced:

$$I_{MPP} = I_{sc} - I_{sc} \cdot e^{\frac{-V_{oc}}{V_t}} \cdot \left(e^{\frac{V_{MPP} + R_s \cdot I_{MPP}}{V_t}} - 1 \right) - \frac{V_{MPP} + R_s \cdot I_{MPP}}{R_{sh}}$$

by considering $e^{\frac{V_{MPP} + R_s \cdot I_{MPP}}{V_t}} \gg 1$

$$I_{MPP} = I_{sc} - I_{sc} \cdot e^{-\frac{V_{MPP} + R_s \cdot I_{MPP} - V_{oc}}{V_t}} - \frac{V_{MPP} + R_s \cdot I_{MPP}}{R_{sh}}$$

$$\frac{V_{MPP} + R_s \cdot I_{MPP} - V_{oc}}{V_t} = \log \left(\frac{I_{sc} - I_{MPP} - \frac{V_{MPP} + R_s \cdot I_{MPP}}{R_{sh}}}{I_{sc}} \right)$$

$$V_t = \frac{V_{MPP} + R_s \cdot I_{MPP} - V_{oc}}{\log \left(\frac{I_{sc} - I_{MPP} - \frac{V_{MPP} + R_s \cdot I_{MPP}}{R_{sh}}}{I_{sc}} \right)}$$

by considering $R_s \ll R_{sh}$

$$V_t = \frac{V_{mpp} + R_s \cdot I_{mpp} - V_{oc}}{\log \left(\frac{I_{sc} - I_{mpp} + \frac{V_{mpp}}{R_{sh}}}{I_{sc}} \right)} \quad \text{II.34}$$

Thus the initialization for parameter extraction can be conducted using datasheet values. Concerning the series and shunt resistance, the use of values read on the datasheet I-V characteristic are necessary for determining the derivative values at open-circuit and short-circuit conditions.

II.3.3. PV module parameter extraction validation

The proposed parameter extraction method has been applied to experimental I-V characteristics of I-106 modules manufactured by Isofóton. The experimental curves were obtained using the PVPM 2540C curve tracer which measures 100 operating points of the module, represented as blue dots on Figure II.11.

The previously described least square curve fitting method was then applied in order to extract module parameters. The simulation curve, represented in red, was then plotted using the extracted parameters and single-diode model. The four I-V characteristics presented on Figure II.11 come from different modules at various irradiance and temperature conditions.

Results show the high precision between measurement and simulation in various conditions. However, practical experience has shown that in certain cases the parameter initialization described in part II.3.2 was not always sufficiently accurate for the least square curve fitting algorithm to converge. In such cases, an empirical tuning was used. Further work would consist in finding a global method for parameter extraction of any type of PV modules. Moreover, it should be acknowledged that given the procedure, the single-diode

parameters that are calculated are a mathematical set of parameters that correspond to an I-V characteristic. These fitting parameters should not be mistaken with the physical parameters of the single diode model, but rather valid mathematical parameters used for PV module simulations.

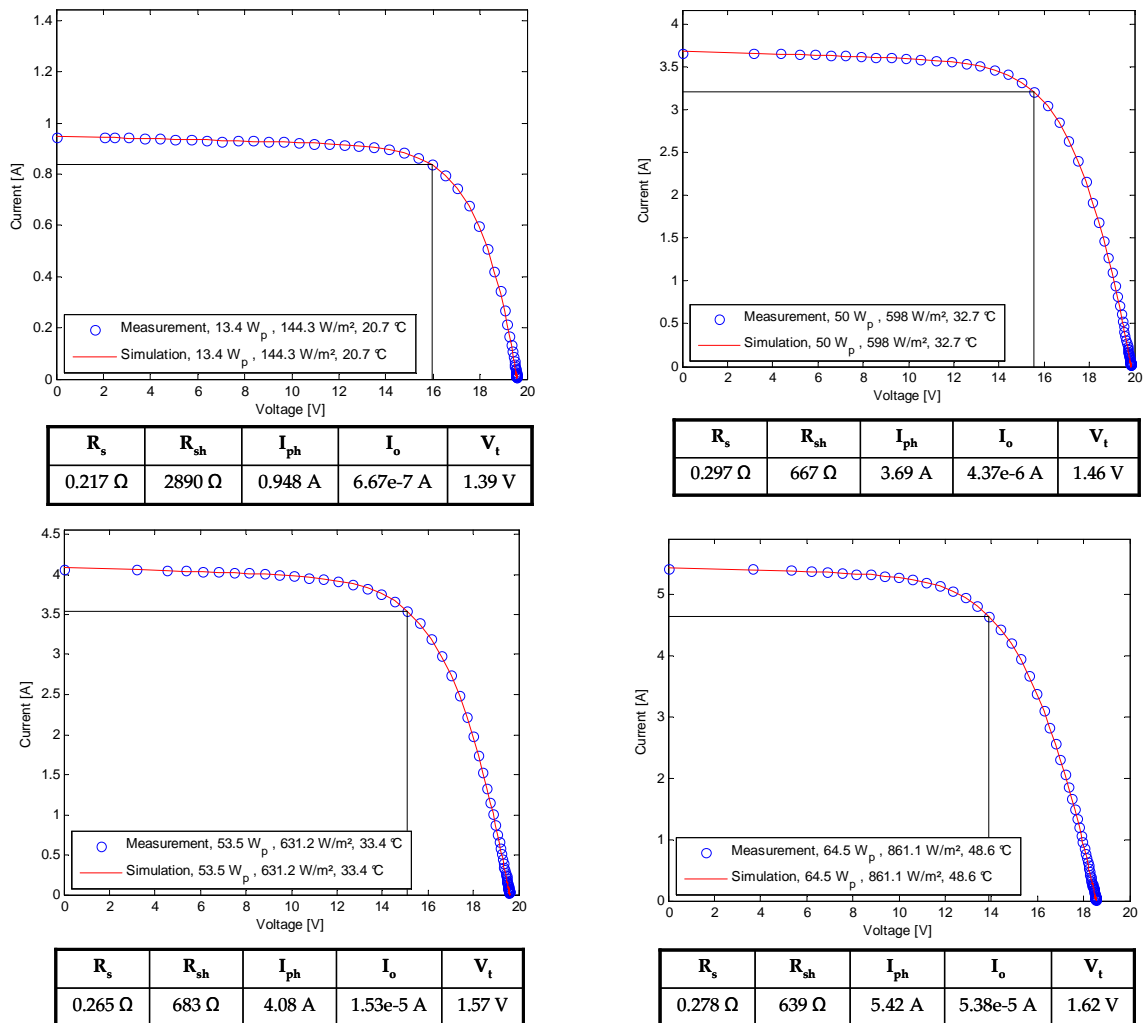


Figure II.11: Experimental and simulation results of parameter extraction

II.4. Module parameter environmental condition translation method

Module peak power ratings are given at standard test conditions (STC) in datasheets that is to say with $1000 W/m^2$ solar irradiance, $25^{\circ}C$ module temperature and 1.5 air mass ratio. These test conditions, carried out in solar simulators, are useful for determining the efficiency of modules. This procedure enables the comparison of module performances between manufacturers and photovoltaic technologies. However, in field operating conditions all three STC conditions are rarely achieved especially given the low temperature level at such high irradiance, since the intense solar power also tends to warm the PV modules up to around $50^{\circ}C$ on days with a clear sky. The need to compare manufacturer ratings with field test results has led to the development of forecasting module characteristics in other environmental conditions than STC conditions.

II.4.1. I-V curve translation method

In the 1990's, research on translating I-V curves from outdoor measurement conditions to standard test conditions has been studied [BLA'88]. The principle of the extrapolation method consists in calculating new values of short-circuit current and open-circuit voltage at desired conditions (G_2, T_2) using values determined in reference conditions (G_1, T_1). The reference I-V curve is then translated using equations containing the newly calculated values. A summary of proposed translation methods are presented in Table II.3.

Each of the presented methods use correction factors that are determined for each PV module: temperature correction factor for current (α), temperature correction factor for voltage (β) and irradiance correction factor for voltage (δ). Since module short-circuit current evolves linearly with incoming solar irradiance, the ratio between reference condition irradiance G_1 and desired condition irradiance G_2 are used to translate current values. The influence of air mass used in the STC definition, which considers the effect of the atmosphere on the sunlight's path and intensity, has not been taken into account in these translation methods. By considering the irradiances G_2 and G_1 to be the effective irradiance received by the module rather than the solar irradiance, the notion of air mass can be disregarded. This methodology has been adopted in this work, therefore the effect of air mass will not be considered throughout the study.

Method	Translation Equations	Validity interval
Blaesser [BLA'88]	$I(G_2, T_2) = I(G_1, T_1) + I_{sc}(G_1, T_1) \cdot \left(\frac{G_2}{G_1} - 1 \right) + \alpha \cdot (T_2 - T_1)$ $V(G_2, T_2) = V(G_1, T_1) - R_s \cdot (I(G_2, T_2) - I(G_1, T_1)) + \beta \cdot (T_2 - T_1)$	Irradiance : 100-1000 W/m ²
Anderson [AND'96]	$I(G_2, T_2) = \frac{I(G_1, T_1)}{[1 + \alpha \cdot (T_1 - T_2)]} \cdot \frac{G_1}{G_2}$ $V(G_2, T_2) = \frac{V(G_1, T_1)}{[1 + \beta \cdot (T_1 - T_2)] \cdot \left[1 + \delta \cdot \ln \left(\frac{G_1}{G_2} \right) \right]}$	Irradiance : 100-1000 W/m ² Temperature : 25-75°C
Marion [MAR'02]	$I(G_2, T_2) = I(G_1, T_1) \cdot \frac{G_2}{G_1} \cdot [1 + \alpha \cdot (T_2 - T_1)]$ $V(G_2, T_2) = V(G_1, T_1) \cdot [1 + \beta \cdot (T_2 - T_1)] \cdot \left[1 + \delta \cdot \ln \left(\frac{G_2}{G_1} \right) \right]$	Irradiance : 100-1200 W/m ² Temperature : 0-80°C

Table II.3 : Review of I-V curve translation methods from environmental conditions (G_1, T_1) to (G_2, T_2) using temperature correction factors α, β , and irradiance correction factor δ .

Moreover, the translation equations are valid in certain intervals of environmental conditions. The closer the desired conditions are to the reference condition, the higher the precision of the translation results are. Furthermore, the precision of the translation depends mostly on the correction factor values. Hence, determining specific values for a certain module, rather than the technology of modules can increase precision, that is why certain

authors propose methods to calculate these correction factors from measurements [MAR'02].

These translation methods have the advantage of forecasting module performances in outdoor conditions, but lack to show the influence of environmental conditions variations on the one-diode model parameters of modules.

II.4.2. Module parameter translation method

The module parameter translation method has been developed in order to accelerate the process consisting in observing the influence of irradiance and temperature on module parameters. The original process for parameter translation contained two steps: translating experimental I-V curves to desired conditions and extracting the parameters of the translated I-V characteristic. In order to reduce the number of steps, and thus reduce the cumulated errors in the process, an analytical link between parameters in reference conditions and desired conditions has been developed. The Marion method [MAR'02] was used in the process for the simplicity of I-V curve translation method and its large validity interval.

Indeed, by referring to the calculations of open-circuit voltage and short-circuit current in the desired conditions, a linear relationship between module current at (G_1, T_1) and (G_2, T_2) conditions can be deduced, as shown on equations II.35. Similarly, a relation between module voltages in both conditions is presented in equation II.36.

$$I(G_2, T_2) = \frac{I_{sc}(G_2, T_2)}{I_{sc}(G_1, T_1)} \cdot I(G_1, T_1) = \frac{G_2}{G_1} \cdot [1 + \alpha \cdot (T_2 - T_1)] \cdot I(G_1, T_1) \quad \text{II.35}$$

$$V(G_2, T_2) = \frac{V_{oc}(G_2, T_2)}{V_{oc}(G_1, T_1)} \cdot V(G_1, T_1) = [1 + \beta \cdot (T_2 - T_1)] \cdot \left[1 + \delta \cdot \ln\left(\frac{G_2}{G_1}\right) \right] \cdot V(G_1, T_1) \quad \text{II.36}$$

By supposing that each module parameter is a function dependent of effective irradiance and module temperature, we can use the one-diode model equation applied at (G_2, T_2) conditions to identify dependencies of parameters with environmental conditions. In order to simplify notation, the parameters expressed at (G_x, T_x) conditions are indexed with the term x.

At conditions (G_2, T_2) , equation II.1 gives:

$$I_2 = I_{ph_2} - I_{o_2} \cdot \left(e^{\frac{V_2 + R_{s_2} \cdot I_2}{V_{t_2}}} - 1 \right) - \frac{V_2 + R_{s_2} \cdot I_2}{R_{sh_2}}$$

By replacing the current and voltage values at conditions (G_2, T_2) with equations II.35 and II.36, we obtain :

$$I_1 = \frac{I_{sc1}}{I_{sc2}} \cdot I_{ph_2} - \frac{I_{sc1}}{I_{sc2}} \cdot I_{o_2} \cdot \left(e^{\frac{V_1 + R_{s_2} \cdot \frac{I_{sc2} \cdot V_{oc1} \cdot I_1}{I_{sc1} \cdot V_{oc2}}}{\frac{V_{oc1} \cdot V_{t_2}}{V_{oc2}}}} - 1 \right) - \frac{V_1 + R_{s_2} \cdot \frac{I_{sc2}}{I_{sc1}} \cdot \frac{V_{oc1}}{V_{oc2}} \cdot I_1}{\frac{I_{sc2}}{I_{sc1}} \cdot \frac{V_{oc1}}{V_{oc2}} \cdot R_{sh_2}} \quad \text{II.37}$$

The previous expression can be related to the one-diode model equation for conditions (G_1, T_1) . By identification, we can deduce the relationship between parameters at (G_2, T_2) and (G_1, T_1) conditions, as presented on equations II.38-II.42

$$I_{ph}(G_2, T_2) = \frac{I_{sc2}}{I_{sc1}} \cdot I_{ph}(G_1, T_1) = \frac{G_2}{G_1} \cdot [1 + \alpha \cdot (T_2 - T_1)] \cdot I_{ph}(G_1, T_1) \quad \text{II.38}$$

$$I_o(G_2, T_2) = \frac{I_{sc2}}{I_{sc1}} \cdot I_o(G_1, T_1) = \frac{G_2}{G_1} \cdot [1 + \alpha \cdot (T_2 - T_1)] \cdot I_o(G_1, T_1) \quad \text{II.39}$$

$$V_t(G_2, T_2) = \frac{V_{oc2}}{V_{oc1}} \cdot V_t(G_1, T_1) = [1 + \beta \cdot (T_1 - T_2)] \cdot \left[1 + \delta \cdot \ln\left(\frac{G_2}{G_1}\right) \right] \cdot V_t(G_1, T_1) \quad \text{II.40}$$

$$R_s(G_2, T_2) = \frac{I_{sc1}}{I_{sc2}} \cdot \frac{V_{oc2}}{V_{oc1}} \cdot R_s(G_1, T_1) = \frac{[1 + \beta \cdot (T_2 - T_1)] \cdot \left[1 + \delta \cdot \ln\left(\frac{G_2}{G_1}\right) \right]}{\frac{G_2}{G_1} \cdot [1 + \alpha \cdot (T_2 - T_1)]} \cdot R_s(G_1, T_1) \quad \text{II.41}$$

$$R_{sh}(G_2, T_2) = \frac{I_{sc1}}{I_{sc2}} \cdot \frac{V_{oc2}}{V_{oc1}} \cdot R_{sh}(G_1, T_1) = \frac{[1 + \beta \cdot (T_2 - T_1)] \cdot \left[1 + \delta \cdot \ln\left(\frac{G_2}{G_1}\right) \right]}{\frac{G_2}{G_1} \cdot [1 + \alpha \cdot (T_2 - T_1)]} \cdot R_{sh}(G_1, T_1) \quad \text{II.42}$$

The identification process determines new single diode model parameters that fit the translated I-V curve. As mentioned previously, these translated parameters are mathematical parameters that do not necessarily have a relationship with the physical parameters of the PV module or the initial parameters were used for the translation. Thus, the evolution of module parameters with irradiance and temperature cannot be studied using this process. However, the parameter translation method has proven to be practical in the forecast of module power production in various environmental conditions. The parameter translation equations have been confronted to experimental results in Annex 3.

II.5. PV array with modifiable interconnections modelling

Photovoltaic arrays are composed of interconnected PV modules designed to fit certain voltage and power constraints. Traditionally, PV arrays are made up of several PV strings, exclusively series-connected modules, containing the necessary number of module to fit voltage constraints. These PV strings are then connected in parallel in order to meet PV plant power requirements. As will be seen in Chapter III, the traditional method of designing PV plants has been reconsidered in order to reduce mismatch losses in solar arrays by adding interconnections in between modules of distinct PV strings.

This section aims to model PV array operation with various module interconnection schemes for PV plant production forecast. The specific case of series-parallel arrangements will first be studied in depth in order to understand the different relations binding on modules. In the second section, a general model taking into account interconnections between PV strings will be examined.

II.5.1. Traditional photovoltaic array model

Historically, PV plants were designed to fit two constraints: voltage and power. The voltage of the plant is determined by appropriately choosing the number of modules (M) that make up a PV string. In the case of grid-connected plants, the number of modules per string is determined in order to fit inverter input voltage specifications. The number of PV strings (N) is determined in order to fit desired power specifications for an application. Therefore, the array voltage depends on the module voltage, as shown in equation II.43, and the array power depends on the module current, as shown in equation II.44. The nominal values used for module voltage and current correspond to the module's maximum power point values since MPPT algorithms are intended to operate at maximum power.

$$V_{\text{array}} = M \cdot V_{\text{module}} \quad \text{II.43}$$

$$P_{\text{array}} = N \cdot I_{\text{module}} \cdot V_{\text{array}} \quad \text{II.44}$$

The operation point of each module within the array can be determined by using electrical relations resulting from the array layout. In the case of conventional designed arrays, more commonly referred to as a series-parallel (SP) arrangement, the interconnections in between PV strings are exclusively made at their extremities as shown on Figure II.12.

In an array containing $M \cdot N$ modules, with N strings of M modules per string, we can identify $(M-1) \cdot N$ nodes, represented by dots on Figure II.12. Each module $M_{i,j}$ in the array has its attributed voltage $V_{i,j}$ and current $I_{i,j}$.

The electrical relations describing module operation within the array can be distinguished into three categories: current laws, voltage laws, and the DC-bus voltage law.

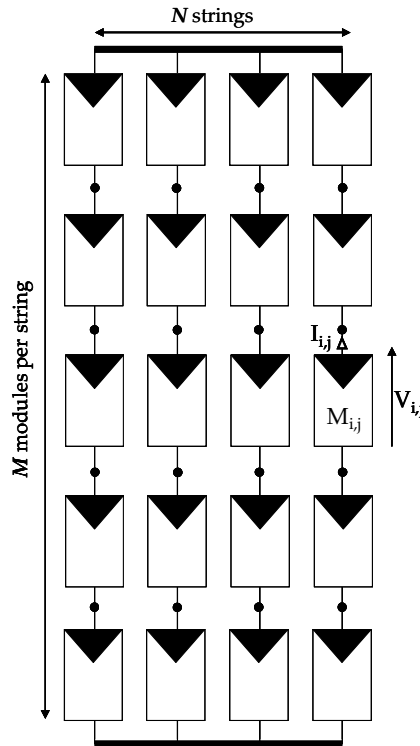


Figure II.12 : Series-parallel array diagram containing $M \cdot N$ PV modules

II.5.1.1. Current Laws

The current laws describe current flow through modules of the array using Kirchhoff's current laws at nodes. In the case of the SP topology, the current flowing through two consecutive modules of a same string is equal, as shown in II.45

$$\forall i \in [1, M-1], \forall j \in [1, N], I_{i,j} - I_{i+1,j} = 0 \quad \text{II.45}$$

In the case of partial shading of a PV string, which primarily affects module current, we can perceive that the module with the least current will influence the entire string due to the unique current flow and therefore lower the production of the entire string. This phenomenon, which is essential to mismatch loss generation, will be further examined in Chapter III.

The current laws result in $(M-1) \cdot N$ equations describing current flow at each node.

II.5.1.2. Voltage Laws

The voltage laws describe the voltage equalities that lie between single modules or strings of modules connected in parallel. Indeed, two parallel connected modules have the same voltage. In the case of the SP topology, $(N-1)$ strings of M modules are connected to the first string in parallel, which leads to equation II.46.

$$\forall j \in [2, N], \sum_{i=1}^M V_{i,1} - \sum_{i=1}^M V_{i,j} = 0 \quad \text{II.46}$$

The first string (ie. $N=1$) will be chosen as a reference string for determining the array voltage for commodity. However, it should be noticed that the reasoning is similar by choosing any of the PV strings as a reference string.

The voltage laws bring $(N-1)$ additional equations to our PV array model.

II.5.1.3. DC-bus voltage law

The PV plant operates at a given voltage which is imposed by the load. In the case of grid-connected systems, the array voltage is maintained by the inverter in a certain interval. Hence, the array voltage is imposed and must be equal to the DC bus voltage, as shown in equation II.47

$$\sum_{i=1}^M V_{i,1} - V_{\text{bus}} = 0 \quad \text{II.47}$$

II.5.1.4. Mathematical formulation of PV arrays

The aim of this section is to determine the current-voltage characteristic of a series-paralleled array as well as the operating point of each module of a PV array. To do so, we must determine each module current and voltage. In other words, the equation system contains $2 \cdot M \cdot N$ unknowns: $M \cdot N$ module currents and $M \cdot N$ module voltages.

In part II.2, we have seen that PV module current can be expressed as a function of module voltage with equation II.17. Therefore, our equation system can be reduced to a M·N sized system by using the relation presented in equation II.48, where $I_{i,j}$ represents the current of module $M_{i,j}$, $V_{i,j}$ represents the voltage of module $M_{i,j}$ and the index k is used for identifying modules with different parameters $R_{s_k}, R_{sh_k}, I_{ph_k}, I_{o_k}$ and V_{t_k} .

$$I_{i,j} = f_k(V_{i,j}) = \frac{V_{t_k}}{R_{s_k}} \cdot \left[\frac{R_{s_k} \cdot (I_{ph_k} + I_{o_k})}{V_{t_k}} - W \left(\frac{I_{o_k}}{V_{t_k}} \cdot R_{s_k} \cdot e^{\frac{V_{i,j} + R_{s_k} \cdot (I_{ph_k} + I_{o_k})}{V_{t_k}}} \right) \right] - \frac{V_{i,j}}{R_{sh_k}} \quad \text{II.48}$$

In addition, the combination of current, voltage, and array voltage laws, add up to M·N independent equations. Therefore, given the number of equations and unknowns, our equation system can be solved and admits a unique solution. The procedure used to solve the system will be detailed in section II.5.3, once the influence of module interconnections on current and voltage laws have been investigated.

II.5.2. Photovoltaic arrays with modifiable interconnections

Recent research in module design has shown interest in modifying PV cell interconnection schemes for reducing mismatch losses within PV modules [GAUE'02][GAUSE'02][KAU'03][WAN'09]. Alternative interconnection schemes have also been proposed and simulated using dedicated algorithms for each topology. This has brought interest in customizing interconnection schemes of modules within a PV plant in order to simulate its effect in various shade scenarios. Our work proposes a global method to automatically generate modified sets of equations corresponding to any interconnection layout, that is to say one single algorithm for various configurations.

As seen in the previous section, an array composed of N strings of M modules per string contains $(M-1) \cdot N$ nodes. Considering that a module interconnection is a lateral connection established in between two nodes of adjacent strings, we can identify $(M-1) \cdot (N-1)$ possible module interconnections, represented by green squares in Figure II.13.

Referring to the traditional array layout as a basis for building our equation system, the aim is to modify the equation system by taking into account node interconnections. A diagram showing node interconnection between modules is presented on Figure II.14 and can be referred to illustrate the modifications made in current and voltage laws between adjacent modules.

II.5.2.1. Current law fusion

The junction between nodes $N_{i,j}$ and $N_{i,j+1}$ implies changes in current flow between modules $M_{i,j}, M_{i,j+1}, M_{i-1,j}, M_{i-1,j+1}$. By applying Kirchhoff's current law applied to node $ConMat_{i,j}$, as shown in equation II.49, it can be observed that this new relation results from the addition of two current laws, previously presented in equation II.45, applied to the joined nodes.

$$I_{i-1,j} - I_{i,j} + I_{i-1,j+1} - I_{i,j+1} = 0 \quad \text{II.49}$$

Thus, in the case of module interconnection at node $\text{ConMat}_{i,j}$, the two current laws of nodes $N_{i,j}$ and $N_{i,j+1}$ fuse to generate equation II.49. Therefore, for each interconnection established, the equation system loses one independent equation.

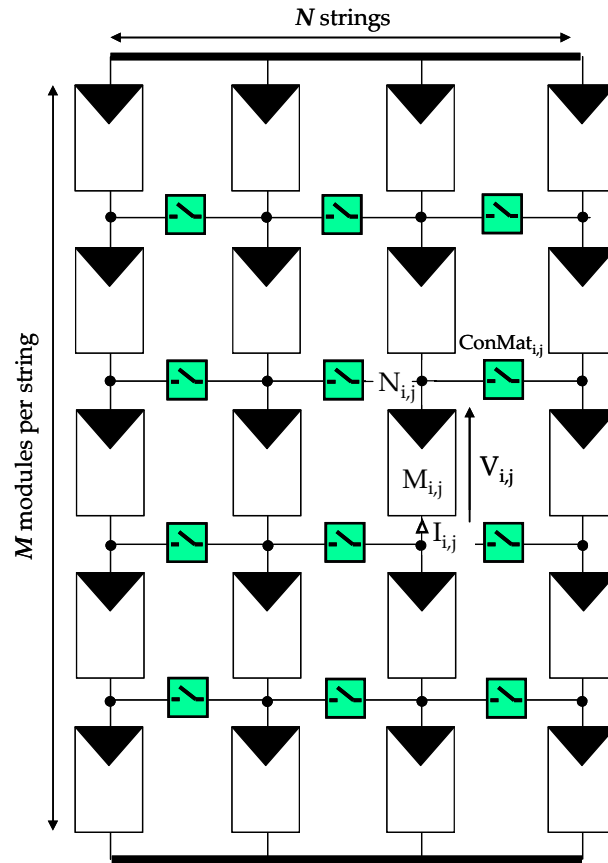


Figure II.13 : Solar array with modifiable module interconnections

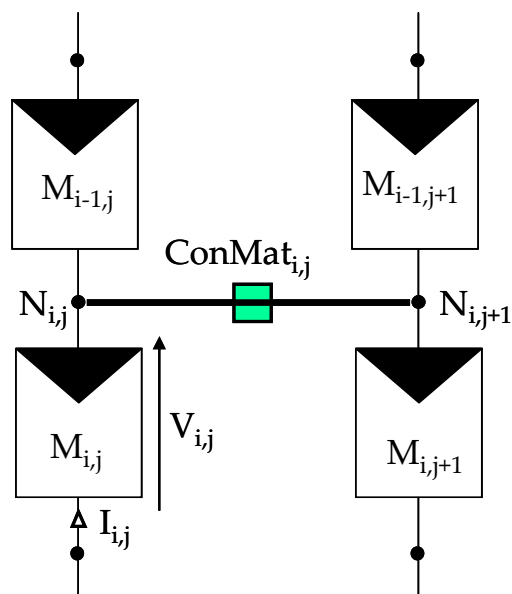


Figure II.14 : Impact of module interconnection on current and voltage laws

II.5.2.2. Voltage law creation

Voltage laws are also modified when a link between modules is created. Indeed, as shown on Figure II.14, the potentials of nodes $N_{i,j}$ and $N_{i,j+1}$ must be equal, in other words the sum of voltages of up to $ConMat_{i,j}$ must be equal, as shown in equation II.50

$$\sum_{k=1}^{i-1} V_{k,j} - \sum_{k=1}^{i-1} V_{k,j+1} = 0 \quad \text{II.50}$$

Consequently, a parallel module-module link establishment brings a supplementary equation to our initial series-parallel equation system.

In conclusion, the junction of two nodes within a PV array leads to two consequences: fusion of two current laws and creation of a voltage law. Therefore, no matter how many interconnections are established the equation system always contains always $M \cdot N$ equations.

II.5.3. Calculating photovoltaic array characteristics

Photovoltaic arrays are characterized by their current-voltage curve, which is used by MPPT algorithms in order to extract maximum power. The aim of this section is to determine the current-voltage curve of a PV array provided that the parameters of each module within the array are known. To do so, it has been chosen to find the current supplied by the array at a given DC bus voltage. Using the relations established in II.4.1. and II.4.2., we will first determine the operating point, that is to say module voltages and currents, and deduce the corresponding array voltage and current. This will be done by resolving matrix equation II.51.

$$Y = F(X) \quad \text{II.51}$$

Where Y is the residual vector to be zeroed and F is the array operation function describing current flow and voltage relations in between modules of the array. The unknown vector X represents the module voltage values to be determined.

A similar reasoning can be used by choosing to solve for module currents as the unknown vector, in such a case the array operation function must be adapted and the function linking module current and voltage (ie. equation II.18) must be used.

The following sections will first describe the processes to interpret module interconnection schemes, then deal with the creation of the array operation function in order to determine PV array current-voltage characteristic.

II.5.3.1. Interpreting module interconnections: Connection Matrix

The layout of a PV array reminds us that PV modules can be associated to values representing their state arranged in a matrix array. Such modelling has been done throughout the past in order to forecast PV modules power production [CHA'95][KAU'03], given that a PV module is an array of solar cells. Likewise, later work has used matrix

models to study PV array production in cases of module mismatch [PET'07][CHO'09].

As stated in section II.4.2, in order to use a global algorithm to simulate PV arrays with customized interconnection schemes, the introduction of a connection matrix was considered. Indeed, in an array composed of $M \cdot N$ PV modules, we can define a connection matrix ConMat containing $(M-1)$ rows with $(N-1)$ columns. If an interconnection between nodes $N_{i,j}$ and $N_{i,j+1}$ is established, then $\text{ConMat}_{i,j}$ value is set to 1, otherwise the value is set to 0.

The example presented on Figure II.15 shows how the connection matrix helps to interpret how the PV modules within an array are linked. The non-null values of the connection matrix determine which current laws will be fused and to which modules the additional voltage laws will be attributed.

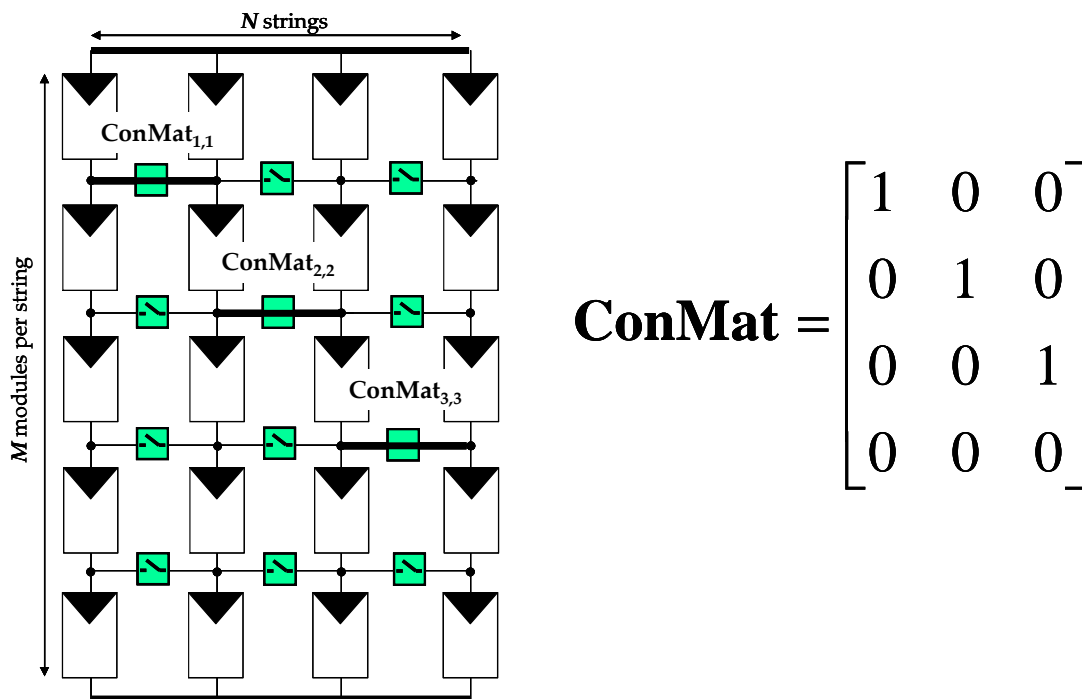


Figure II.15 : Example of connection matrix with a given interconnection scheme for a 5x4 PV array

As will be discussed in the next section, the connection matrix will be useful in automatically generating the array law matrixes.

II.5.3.2. Creating the array law matrixes

The operation of modules within the array can be determined by using the current, voltage and array voltage laws presented previously. The procedure adopted for creating the corresponding matrixes to these laws consists in initializing them with a traditional series-parallel array scheme and then modifying them in order to take into account new interconnections.

The first step is to transform the voltage matrix into a voltage vector. This is done by using the relationship presented in Figure II.16.

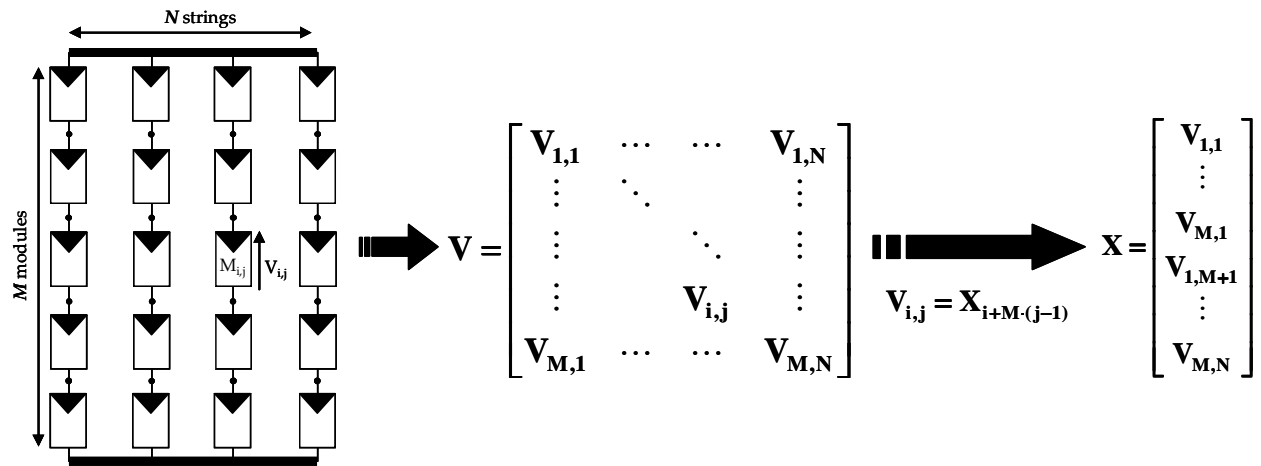


Figure II.16 : Link between PV module voltages and unknown vector

□ **Current law matrix : FCmat**

The initial current law matrix is the one corresponding to the series-parallel array arrangement, that is to say having a null connection matrix. When an interconnection is established, the current law matrix FCmat is modified, depending on where the interconnection is established, by fusing two lines together as shown on Figure II.17. In the example, the link between nodes $N_{2,1}$ and $N_{2,2}$ leads to the fusion of lines 2 and 4 in the current law matrix.

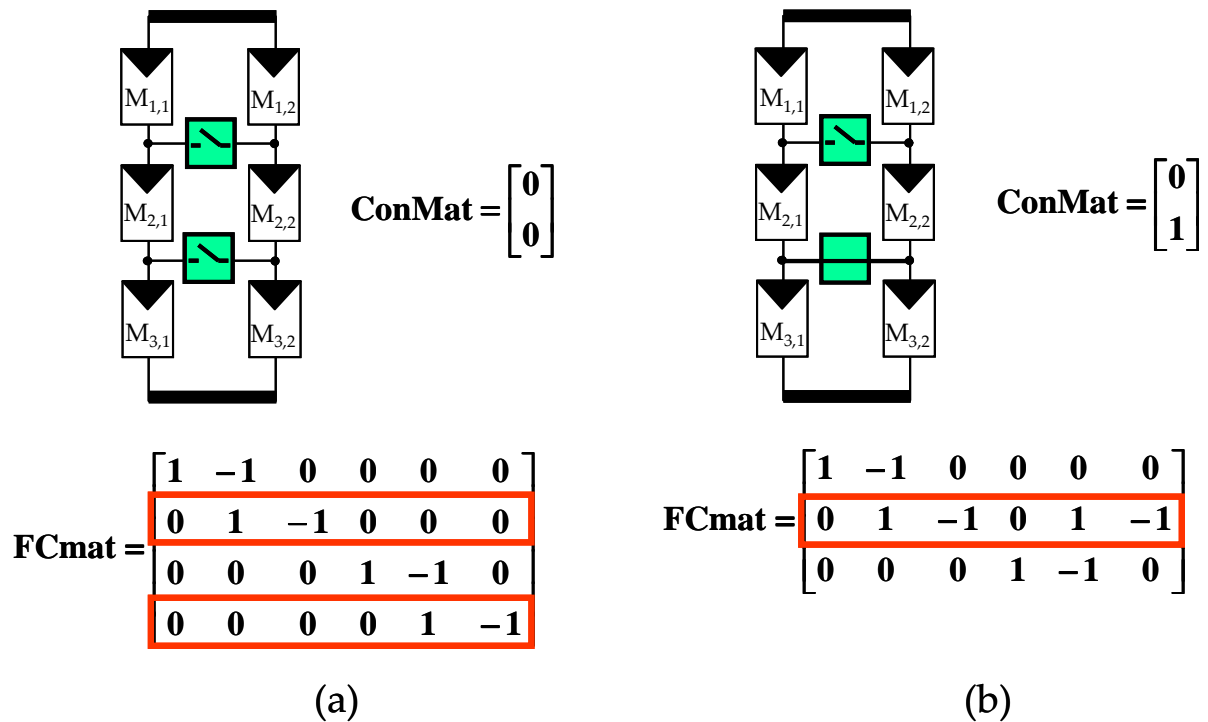


Figure II.17 : Evolution of current law matrix FCmat on a 3x2 array; (a) series-parallel arrangement (b) module interconnection of nodes $N_{2,1}$ and $N_{2,2}$

To carry out the line fusion, the connection matrix is analyzed line by line in order to evaluate adjacent nodes that are interconnected. Once the lines concerned with the fusion are identified, they are then combined and the exceeding lines are removed.

□ Voltage law matrix : FVmat

As in the current law matrix, the voltage law matrix FVmat is initialized for a series-parallel array. The junction of two nodes leads to the creation of a new voltage relationship between modules connected to the node as well as other modules in the PV strings, as illustrated on Figure II.18. Here, the link between nodes $N_{2,1}$ and $N_{2,2}$ creates a new voltage relation linking modules $M_{1,1}$, $M_{2,1}$, $M_{1,2}$ and $M_{2,2}$.

Here again, the procedure consists in analyzing the connection matrix and determining which modules are involved in the additional voltage law resulting from the interconnection. However, the FVmat matrix evolution process consists in adding lines rather than removing specific lines as in FCmat, which is much easier to implement.

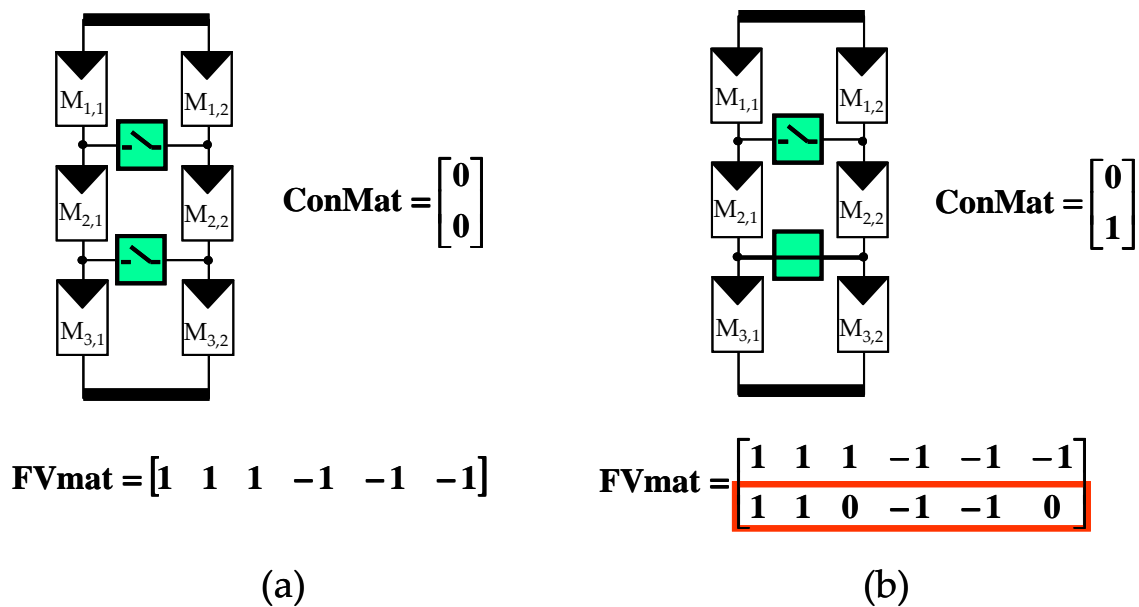


Figure II.18 : Evolution of voltage law matrix FVmat on a 3x2 array; (a) series-parallel arrangement (b) module interconnection at node $N_{2,1}$

The final law to implement concerns the array voltage.

□ DC-bus law vector: FDCbusVect

The array voltage vector is the last relation in our M·N equation system that helps to describe PV array operation. As stated earlier, it has been chosen to attribute array voltage V_{bus} to the first string of the PV array. Interconnections of modules have no influence on the array voltage vector since the voltage of the PV string depends entirely on the voltage imposed by the DC bus. In the case of the previous example using a 3x2 array, Figure II.19 shows how the array voltage vector takes shape.

The law matrixes FCmat, FVmat and FDCbusVect will be used to generate the array operation function F , presented in II.51. The next section will describe how the law matrixes are used to solve the system and determine the current-voltage characteristic of the array.

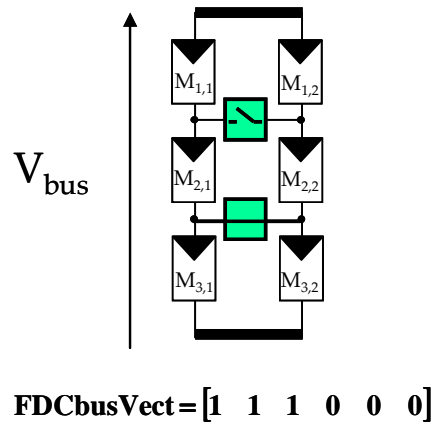


Figure II.19 : Expression of the array voltage vector in the case of a 3x2 array

II.5.3.3. Solving the PV array equation system

The solution to the equation system is determined by using the Newton-Raphson method for matrix equations. The creation of the residual vector can be seen as a function taking a single input vector X . The resolution consists in finding the root of the array operation function F defined in equation II.52, where matrixes A , B , C , and the Φ function are defined next.

$$\mathbf{F}(\mathbf{X}) = \mathbf{A} \times \mathbf{X} + \mathbf{B} + \mathbf{C} \times \Phi(\mathbf{X}) \quad \text{II.52}$$

In order to consider each module independently, the parameters of each module are taken into account in the Φ function as shown in Figure II.20. The index k , is used for each module in order to determine their corresponding current at voltage x_k with parameters R_{s_k} , R_{sh_k} , I_{ph_k} , I_{ok} , and V_{tk} as defined in equation II.48

$$\Phi(\mathbf{X}) = \Phi \left(\begin{bmatrix} x_1 \\ \vdots \\ x_k \\ \vdots \\ x_{M \cdot N} \end{bmatrix} \right) = \begin{bmatrix} f_1(x_1) \\ \vdots \\ f_k(x_k) \\ \vdots \\ f_{M \cdot N}(x_{M \cdot N}) \end{bmatrix}$$

 Figure II.20: Construction of Φ function using subfunctions f_k

Furthermore, the law matrixes are used to determine matrixes A , B , and C as shown on Figure II.21.

$$\mathbf{F}(\mathbf{X}) = \underbrace{\begin{bmatrix} 0 \\ \mathbf{FVmat} \\ \mathbf{FDCbusVect} \end{bmatrix}}_{\mathbf{A}} \times \mathbf{X} + \underbrace{\begin{bmatrix} 0 \\ 0 \\ -V_{bus} \end{bmatrix}}_{\mathbf{B}} + \underbrace{\begin{bmatrix} \mathbf{FCmat} \\ 0 \\ 0 \end{bmatrix}}_{\mathbf{C}} \times \Phi(\mathbf{X})$$

 Figure II.21 : Array operation function using unknown voltage vector X and current, voltage and array voltage matrixes

The Newton-Raphson method is then applied to the array operation function F in order to determine the root. To do so, the inverse of the jacobian matrix of the F function must be calculated, and the iteration process in matrix format is presented in II.53. Further explanations on the jacobian matrix calculation can be found in Annex 4.

$$\mathbf{X}_{k+1} = \mathbf{X}_k + \mathbf{J}^{-1}[\mathbf{X}_k] \times \mathbf{F}[\mathbf{X}_k] \quad \text{II.53}$$

The initial guess has been chosen by supposing that all modules participate equally in maintaining the DC bus voltage. The process is then stopped once the norm of the residual is sufficiently small; in our case, the precision has been chosen to be 10^{-6} .

Once the process has converged to a solution, each module voltage is known for a given DC bus voltage. The corresponding currents are determined using the Φ function, as seen in Figure II.22. In theory, given the conservation of current throughout the array, each row of the current matrix should have the same sum. In practice however, numerical errors may occur in which the current conservation law is not verified. In order to address this issue, the array current value is calculated as the arithmetic mean of the array currents in each array row (in red on Figure II.22).

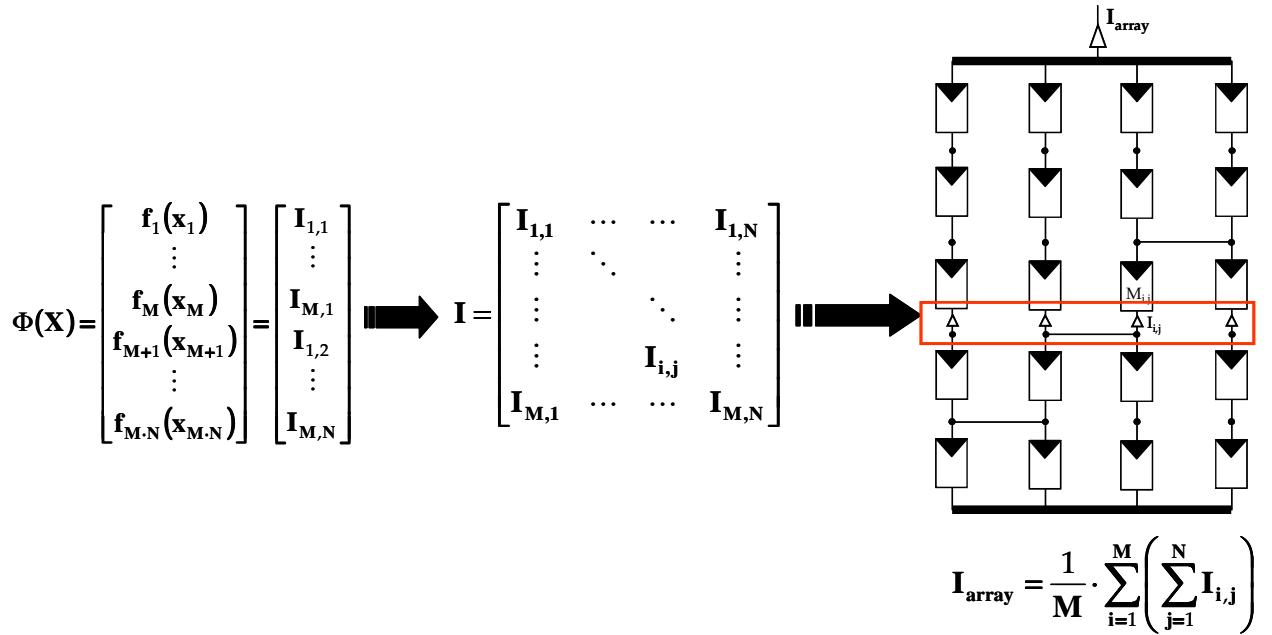


Figure II.22 : Determination of array current using the voltage matrix

Given the DC bus voltage vector and the corresponding array current vector, the current-voltage characteristic of the array can be plotted. The precision of the current-voltage curve depends on the number of points constituting the input dc-bus voltage vector. An example of the I-V characteristic construction using a 5x4 array is presented on Figure II.23 where the array voltage vector contains 100 points.

In the example, a static shade is set on modules $M_{1,1}$ and $M_{1,2}$ reducing the incoming irradiance by 40%. The module parameters used in the simulation correspond to a commercial monocrystalline 200 W_p module. The PV array model requires three inputs: module parameters, PV array parameters and the connection matrix in order to determine

the I-V characteristic of the array. Furthermore, the operating state of each module at a given DC bus voltage can be displayed. In the example, the voltages and currents of the modules at maximum power point (red lines) are featured. In the next chapter, the PV array model will be used in various scenarios in order to show power production benefits by using alternative module interconnection schemes.

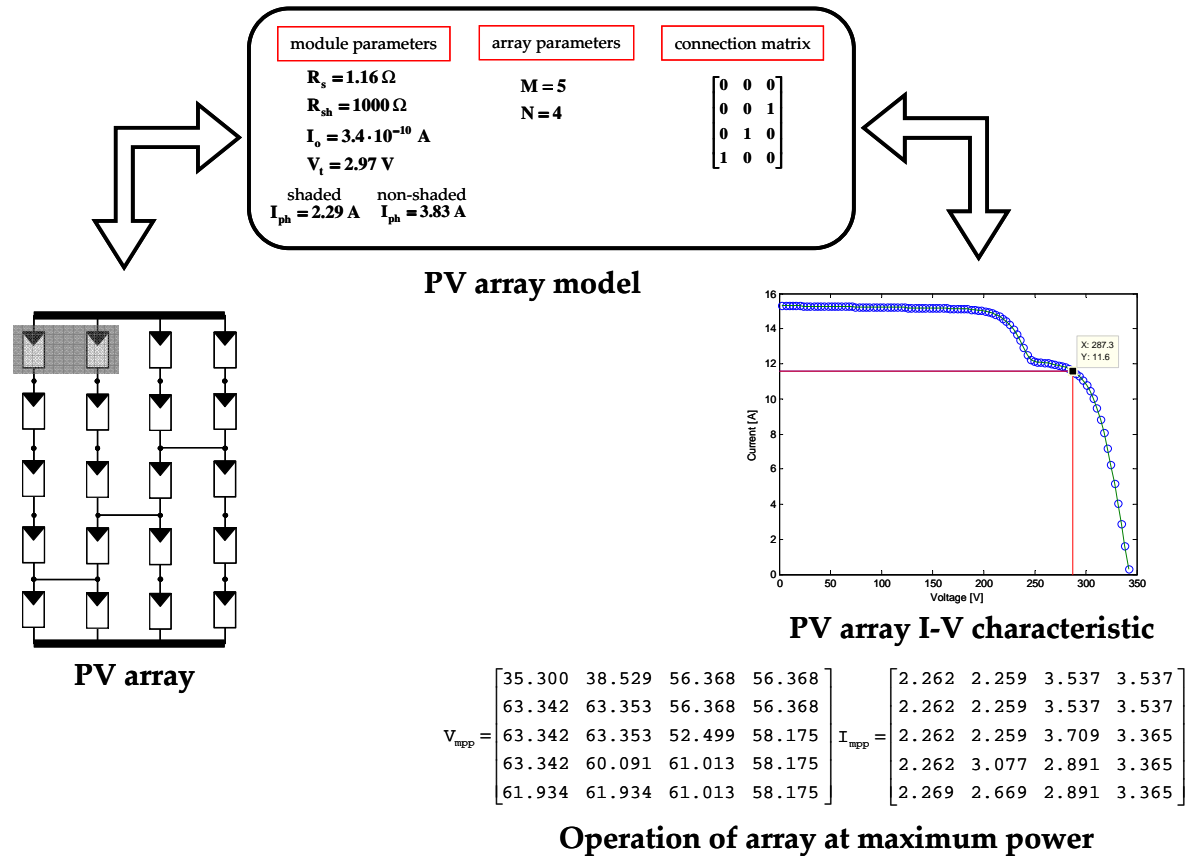


Figure II.23 : Example of I-V characteristic construction using proposed PV array model

Conclusion

In this chapter, the operation of PV arrays has been addressed from cell-to-array. The electric behavior as well as existing protection apparatus for PV cells has been overviewed. Furthermore, a review of existing PV cell models has been presented which has led to the choice of using the one-diode model for its precision and simplicity. Analytical expressions of PV module current and voltage have been obtained by using the Lambert W-function. Simulation results have shown that both the tracing of module I-V characteristics and module parameter extraction using analytical expressions increase performances. Indeed, the proposed method accelerates computing time while conserving the one-diode model precision.

The construction of PV array characteristics has also been discussed. The proposed model takes into account PV arrays with both traditional and alternative module interconnection layouts. The electrical laws governing voltage relations and current flow of the array have been detailed and transcribed into mathematical formulation. A procedure for determining I-V characteristics of PV arrays with modifiable interconnection schemes by

matrix equation solving has been explained. The next chapter will introduce the mismatch loss phenomenon that occurs in PV arrays and present how to reduce such losses by using alternative array interconnection schemes.

Chapter III

Reducing mismatch losses with alternative array interconnection schemes

Introduction

Accompanying the development of terrestrial applications for photovoltaic cell networks, field experience has brought to light the incapacity of arrays to completely extract the available power from solar cells. These losses, also known as mismatch losses, are caused by solar cell heterogeneity in the array. In this chapter, the different causes of module mismatch will be addressed. By the means of a developed simulation tool, simulation results will reveal how mismatch losses affect a traditional series-parallel connected array. Furthermore, the impact of modifying PV array interconnections on reducing mismatch losses will be presented. Experimental results confronted to simulated power production forecasts will be analyzed in order to validate the PV array model exposed previously. Finally, further simulation results comparing the performances of alternative array interconnections with the traditional array design will be provided in order to choose the best adapted interconnection scheme.

III.1. Mismatch losses in photovoltaic arrays

Throughout the years of monitoring photovoltaic fields, it has been brought to light that PV arrays may produce less power than their rated power. The difference between the maximum power of the array and the sum of the maximum powers of each module is referred to as mismatch losses [BUC'79][CHA'95][GAUE'02][KAU'03]. Mismatch losses are essentially caused by the dispersion of modules electrical characteristics in an array. Indeed, generally modules within an array do not have the exact same electrical properties, because of intrinsic module parameters or heterogeneous environmental conditions, which lead to mismatch loss apparition. Certain authors have identified mismatch losses as being one of the most important factors of power losses in PV applications [CHO'09], and usually count for 10% of a PV system's losses [MEY'04][CHO'09][QUA'96]. Other studies have shown that when only one solar cell in a PV module is totally shadowed these losses can attain a 30% power loss [SIL'07].

The causes of mismatch losses can be separated into two categories: those induced by the PV module's intrinsic electrical properties and those linked to its surrounding environment during operation.

III.1.1. Intrinsic photovoltaic module mismatch

III.1.1.1 Causes of intrinsic PV module mismatch

Modules composing an array usually have different characteristics even though they have the same manufactured power rating. Indeed, manufacturer's tolerance values in module maximum power output are in the $\pm 5\%$ range. Chamberlin showed that even within a batch of a given product, module parameters can have large dispersion values as shown in Table III.1 [CHA'95].

P_{max}	R_s	R_{sh}	V_t	I_{ph}
2.1 %	33%	48%	18%	1.3%

Table III.1 : Variation of module parameters tested on 192 Arco Solar M75 modules [CHA'95]

Aside from manufacturing defects, degradation of the PV cells in the modules occurs during their lifetime. A module may endure discoloration of the encapsulating material due to ultra violet exposure, temperature or humidity, which results in the yellowing of the encapsulating material therefore modifying module properties. Cell degradation may also occur after physical deterioration of the cell. For example, hail impacts or vandalism on a module can lead to cell cracking. Furthermore, hot-spot formation leads to irreversible decrease of shunt resistance values. Moreover, commercial PV modules have anti-reflective coating on the surface of the module, reducing the reflectivity of bare silicon from 35% to approximately 3%. The degradation of the anti-reflective coating will reduce the number of photons that can be absorbed by the PV cells, hence reducing the power production. Furthermore, during the photoelectric conversion process the energy released by electron-hole pair recombination in the P-N junction can break some of the weak Si-Si bonds in the PV

cell. This degradation is often referred to light-induced degradation, or Staebler-Wronski effect [MEY'04], which deteriorates the quality of the PV cell and thus its performance. Finally, module mismatch is frequently caused by module soiling. The accumulation of dust, dirt, leaves, bird droppings, or other matter on the module's top surface reduces the incident energy received by the PV cell and is referred to as front-surface soiling. Although this effect is very common for PV plants, the self-cleaning of the modules do to wind and rain make this mismatch cause often temporary.

All of the above causes produce either temporary or permanent effects on module performance, but generally produce permanent alterations on PV cell structure that reduce the solar energy conversion efficiency.

III.1.2. Effect of intrinsic PV module mismatch on array performance

Modules can be assembled in two manners: in series or in parallel. The purpose of this section is to show the impact of assembling modules on the module arrangement power output. To do so, an example based on simulation results using three modules with different characteristics is taken; an analysis of their assembly in series and in parallel will be studied using the simulation tools developed in Chapter II. As shown on Figure III.1, the modules used have similar rated powers, especially for modules 1 and 3, yet have different positions of maximum power point (MPPs), depicted by circles on the figure. Moreover, module 2 has undergone damage consequently decreasing shunt and series resistances and reducing the MPP value. As can be observed both current and voltage values at the MPP are dispersed: maximum power voltage ranges from 52 to 58 V whereas current varies between 3.2 and 3.7 A. This heterogeneity in MPP voltage and current will have a major influence on mismatch loss generation.

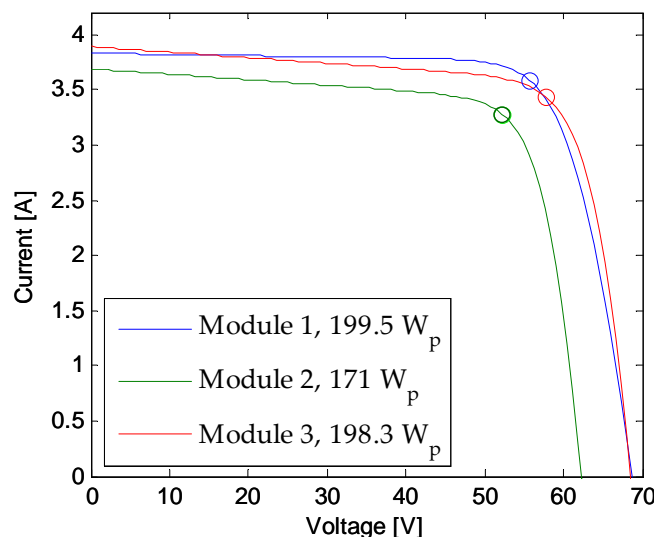


Figure III.1. : Simulated I-V characteristics of three modules with different characteristics, maximum power points are depicted by circles

The interconnection of these modules can be done in series or parallel, as shown on Figure III.2, leading to different results on module mismatch. The ideal case would consist in delivering the maximum power for each module. In other words, if mismatch losses did not

occur during module interconnection, one would expect the array to deliver a maximum power of 568.8 W.

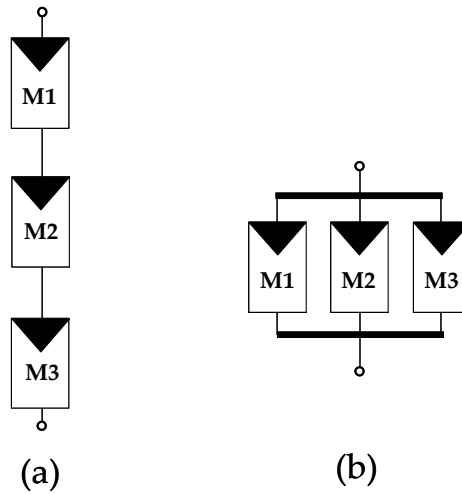


Figure III.2. : Diagram with (a) series connection of modules and (b) parallel connection of modules

□ **Series connection**

In series-connected modules, the current flowing through each module is the same. In the case of a partially shaded string, the modules that cannot provide the string current are short-circuited by bypass diodes to enable proper string current flow and protect the shaded modules from operating in reverse bias voltages. In our case, the power-current curve of the three series connected modules has been plotted on Figure III.3(a). The maximum power extractable from the PV string is of 562.4 W, that is to say 1.12% less power than our ideal case.

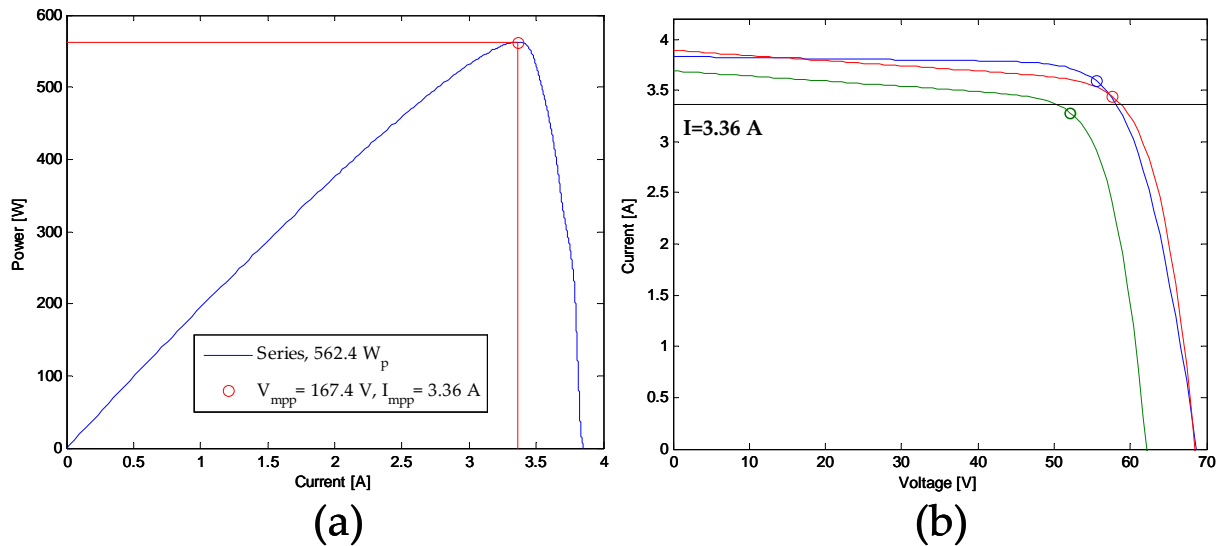


Figure III.3. : (a) power-current characteristic of series connected modules; (b) I-V characteristic of individual modules with series-connected maximum power operating current (in black)

In order to understand the power loss, it should be noticed that the maximum power current, common to all modules, does not coincide with the maximum power current of each individual module, as shown on Figure III.3(b). In a case where each module maximum power currents are the same, the mismatch losses in series connected modules would be null.

□ **Parallel connection**

In parallel-connected modules, the voltage is common to each module. Simulation results of the three parallel connected modules are presented on Figure III.4. In this case, the local power peaks are less visible at high voltages than in the series-connected case. However, the maximum output power of the parallel-connected modules reaches only 559.9 W, that is to say 1.57% less power than in our ideal case. The power loss can be observed on Figure III.4(b), since the maximum power voltage of the array does not line up with the maximum power voltage of each module. Generally, losses due to PV module mismatch leads to low loss levels (<2%), however those provoked by the environment surrounding the array can considerably degrade power production.

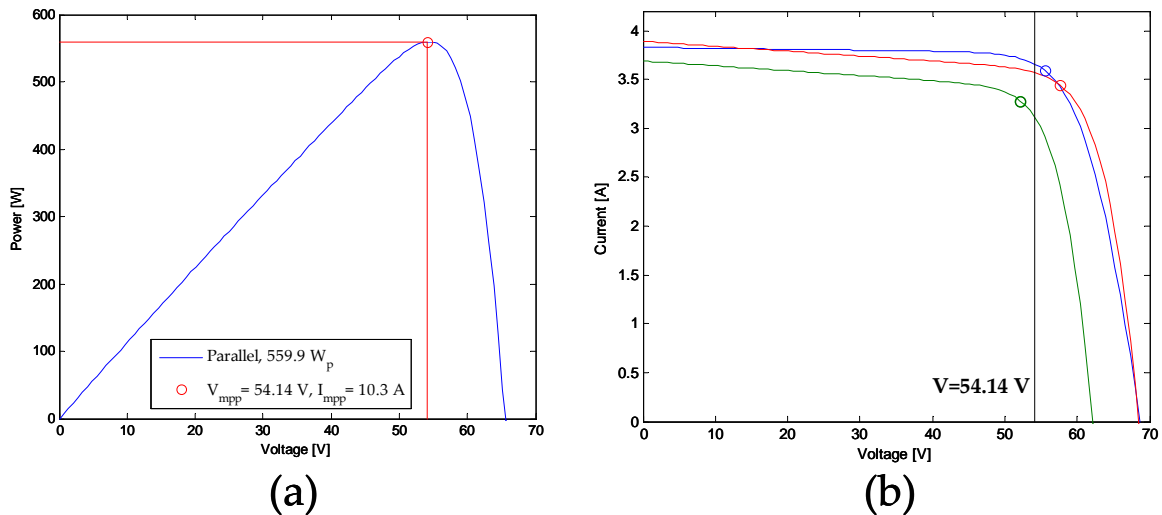


Figure III.4. : (a) p-v characteristic of parallel connected modules; (b) I-V characteristics of each module with parallel-connected maximum power voltage (in black)

III.1.2. Environmental mismatch

III.1.2.1. Causes of environmental mismatch

Photovoltaic module performance varies with the incident solar irradiance and module temperature as shown on Figure III.5. Although the decrease in maximum power is similar for temperature (-0.3 %/°C) and irradiance (-0.2%/W·m²) variations, the effect of irradiance is generally predominant due to the wider range of possible values. Indeed, solar irradiance tends to vary between 0 to 1300 W/m² during the year, whereas module temperature typically varies between 0 and 75°C. During the day, each module of the array is subject to varying solar irradiance and temperature. If each module is supposed identical and submitted to the same conditions module mismatch does not occur. However, shadows may be projected onto a portion of the array due to nearby trees, passing clouds, buildings, antennas or other objects. Partial shadowing of an array, also known as the shadow problem [KAU'05][FEL'81], leads to power loss percentage much greater than the shadowed area portion of the array [RAU'71]. In the German 1000-Solar-Roofs program, half of the PV plants were submitted to partial shadowing leading to a non-negligible annual loss in performance. For some systems, this loss attained 10% [QUA'96]. Another author reported

that in BIPV applications, shading of arrays accounted for output energy losses reaching 25% [NOR'10]. Moreover, in utility-sized plants, it has been reported that snowfall on modules can lower the annual yield of plants by up to 3% [BEC'06]. Similar effects can be found in arrays having modules with different tilt angles, such as in certain BIPV applications [NOR'10]. In this case, modules of the array do not receive the same direct solar irradiation which leads to module mismatch.

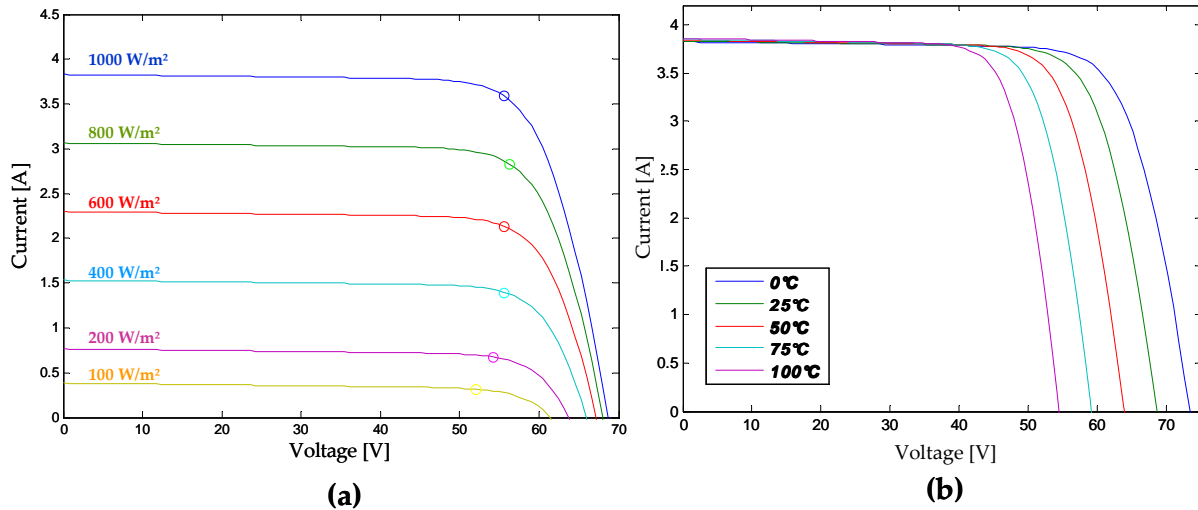


Figure III.5: Influence of (a) solar irradiance @25°C and (b) temperature @1000W/m² on c-Si module I-V characteristics

Partially shaded modules also tend to have lower temperatures than non-shaded modules leading to the combination of the lower irradiance and temperature effect. In some cases the temperature distribution among modules of an array can be unequal due to nearby heat sources, like PV inverters, or differences in module ventilation. This causes modifications in the module I-V characteristics as shown previously, and hence generating module mismatch.

III.1.2.2. Impact of environmental mismatch on array performance

In order to show the differences between intrinsic PV module mismatch (due to internal parameters dispersion) and environmental induced mismatch losses, the example in section III.1.1.2. has been revisited. The three previous modules (§2.1.2) have been used for this example, however Module 3 is submitted to a 60% shade in both series and parallel connection schemes, as shown on Figure III.6. Furthermore, the effect of module shading on module temperature has been taken into account in order to simulate more realistic situations. In other words, modules 1 and 2 are at conditions (1000 W/m², 50°C) whereas Module 3 is at (400 W/m², 25°C) using the beforehand mentioned notation. In this case Module 3 has reduced its maximum output power down to 82.5 W. In this scenario, the maximum theoretical power deliverable by the array reaches 453 W. This value will be referred to as the ideal case in the following paragraphs.

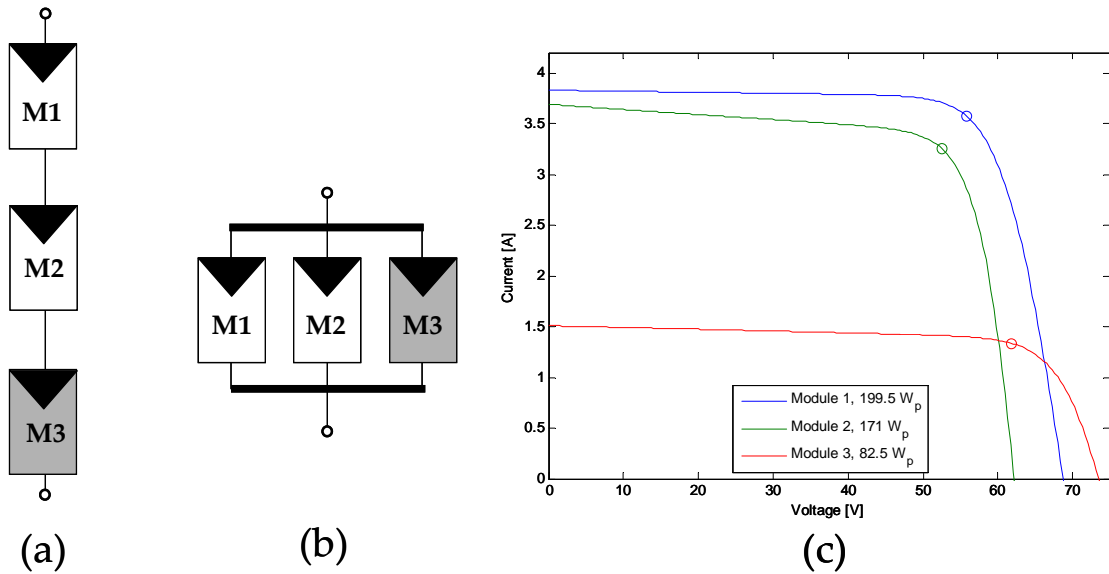


Figure III.6. : (a) Diagram of series connected modules, and (b) parallel connected modules, and (c) I-V characteristics of modules where maximum power points are denoted by circles.

□ **Series connection**

In the case of series-connected modules, the multi-power peaks are clearly visible on Figure III.7. The presence of these peaks is due to the operation of the bypass diode in Module 3. Diodes become active when the string current is higher than the current that the shaded module can supply.

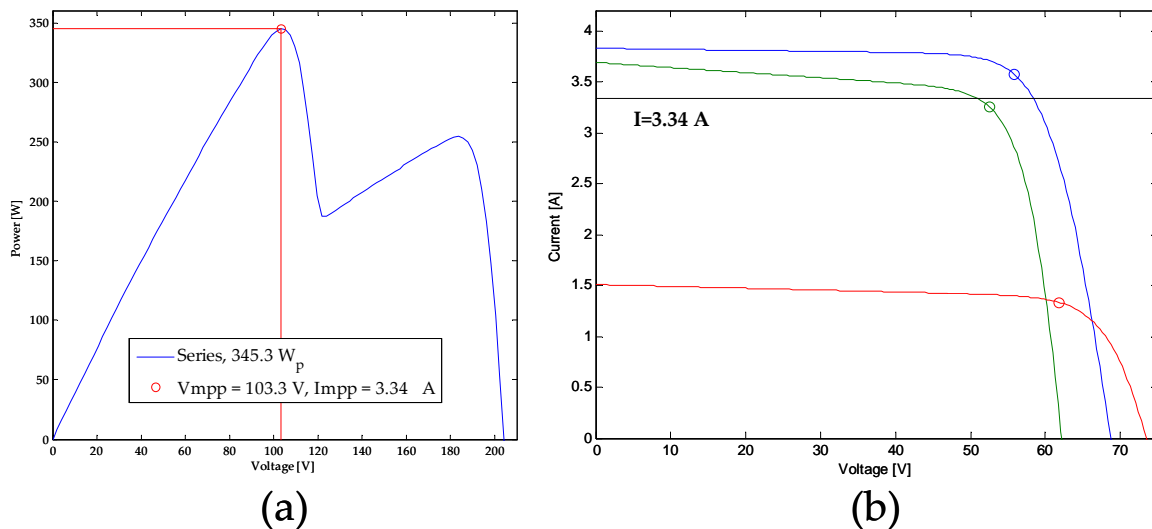


Figure III.7. : (a) Power-current characteristic of series connected modules; (b) I-V characteristic of individual modules with series-connected maximum power operating current (in black)

The maximum power extractable from the PV string is of 345.3 W, that is to say 24% less power than in the ideal case. Figure III.7(b) helps to understand why these losses are so ample by showing that the MPP current delivered by Module 3 is below those of Modules 1 and 2. Module 3 is bypassed when the maximum power of the string is obtained. The power pit, located at approximately 120 V on power-voltage curve (a), marks the deactivation of the bypass diode. From there on, Module 3 is able to participate in the power production. Here, the dispersion in MPP current values is much greater than in the intrinsic PV module

mismatch case, thus leading to greater losses.

□ **Parallel connection**

In the parallel-connected scenario, the effect of shade on the array is much less visible. The multi-peak phenomenon is imperceptible as shown on Figure III.8(a). The maximum extractable power adds up to 442.7 W which leads to a 2% power reduction with respect to the ideal case. This is due to a lower dispersion in MPP voltage values as can be seen on Figure III.8(b).

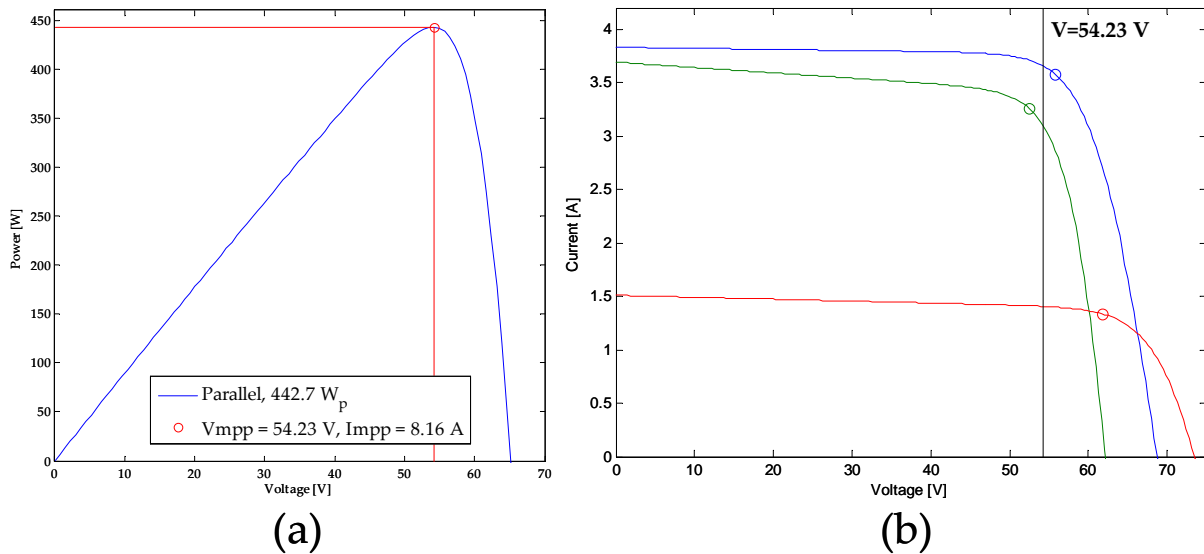


Figure III.8. : (a) p-v characteristic of parallel connected modules; (b) I-V characteristics of each module with parallel-connected maximum power voltage (in black)

In conclusion to this section, we have seen that module mismatch can be classified into two categories: intrinsic PV module mismatch and environmental mismatch. The first category refers to losses induced by inherent electrical properties of the module whereas the second designates losses due to heterogeneous environmental conditions (irradiance and temperature) among modules of an array. Furthermore, the influence of series and parallel connections for these two mismatch loss types has been analyzed. Figure III.9 presents the calculated mismatch losses for the four previously described scenarios. In the case of partial shading, mismatch losses can be considerable for series connected modules.

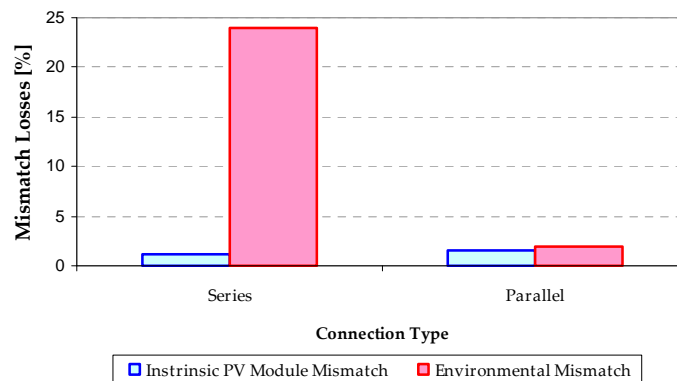


Figure III.9 : Analysis of both types of mismatch losses in the studied scenarios

The next section will describe more in depth mismatch loss phenomenon in series-parallel connected arrays based on experimental and simulation results.

III.2. Study of mismatch losses in series-parallel connected arrays

The traditional design procedure for PV arrays consists in determining the number of modules per string to fit inverter specifications, followed by the necessary number of strings in parallel to fit power needs by the load as presented in Chapter II. During the installation of the array, the modules are disposed in several parallel connected strings of modules as shown in Figure III.10. The purpose of this subchapter is to study the impact of shade-induced mismatch losses in the series-parallel (SP) using both experimental and simulation results.

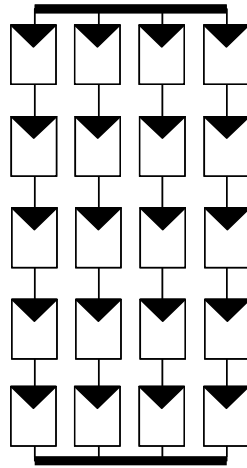


Figure III.10 : Diagram of the traditional series-parallel topology

Partial shading of arrays can be characterized by the shade's size, intensity and location on the solar generator. These three independent factors are directly linked to the quantity of generated mismatch losses. In this work, shade intensity is described by the means of a shade factor which translates the decrease in incoming solar irradiance due to an obstacle [QUA'96]. The shade factor is defined as the ratio between the solar irradiance received by the shaded module (G_{shaded}) and the non-shaded module ($G_{\text{non-shaded}}$) as shown in equation III.1.

$$SF = 1 - \frac{G_{\text{shaded}}}{G_{\text{non-shaded}}} \quad \text{III.1}$$

Since, solar irradiance can directly be linked to the short-circuit current of the module (cf. Chapter II.4) the shade factor literally impacts the short-circuit value of the module. In modelling terms, the parameter affected by shade is the light-induced current.

III.2.1. Preliminary validation of simulation model using experimental results

In order to forecast mismatch losses in an existing installation, the first step is to determine the maximum power extractable from each PV module within the array. The

principal difficulty in determining this is to carry out measurements at fixed environmental conditions. The measurement of a plant is carried out under constant solar irradiance G and module temperature T . Supposing that each module in the array receives the same irradiance and is at the same temperature as the solar and temperature sensors, which is a common approximation, one can calculate the theoretical maximum power extractable from the array. The difference between the theoretical maximum extractable power, sum of maximum powers of each module, and the measured array maximum power represent the module mismatch losses given that all measurements are done under (G,T) conditions. Mismatch losses of the array are then calculated using equation III.2.

$$MML = 1 - \frac{P_{\max\text{ARRAY}}}{\sum_{i=1}^{M \cdot N} P_{\max i}} \quad \text{III.2}$$

In practice, this later constraint is difficult to achieve given the time span necessary to connect each module to the I-V curve tracing device, carry out each module measurement, and then the array measurement. For this reason, the simulation tool described in Chapter II, concerning PV array forecasting has been applied. The software, named Toposolver, can translate measured I-V characteristics from existing modules from environmental conditions (G_1, T_1) to the array measurement conditions (G_2, T_2) in order to predict mismatch losses. An overview of the developed software is presented in Annex 5. Since the results depend on the accuracy of the forecasting tool, the validation of the model is necessary beforehand.

III.2.1.1. Field measurements of 2.2 kW_p plant at Jaén University campus

Collaboration with Jaén University has made possible experimental measurements on a 2.2 kW_p plant located on a rooftop. The PV array is part of the UNIVER (UNIVERSIDAD VERde) project consisting of a 200 kW_p grid-connected PV installation which is separated into four arrays: two 70 kW_p solar parking generators, a 40 kW_p façade installation, and a 20 kW_p pergola installation [DRI'07] as shown on Figure III.11. The array used for the measurement campaign is part of the pergola installation, on the roof of the inverter building shown on Figure III.11(c). This 2.2 kW_p array, referred to as Pergola 5, is composed of twenty Isofotón I-106 modules of monocrystalline silicon technology. Datasheet values of these modules can be found in Annex 6.



Figure III.11 : Views of (a) solar parking 1 & 2 PV arrays, (b) facade PV installation, and (c) pergola installation [PER'07]

The experimental procedure consisted in measuring the I-V characteristics of each module and the entire array using an I-V curve tracer. The module characteristics, taken at conditions (G_1, T_1) were then translated to the array measurement environmental conditions (G_2, T_2) using the developed Toposolver software presented in Chapter II. An example of the translation procedure is presented on Figure III.12. Once each module I-V curve is translated to the array measurement conditions, the program is used to predict the output of the array using the SP topology.

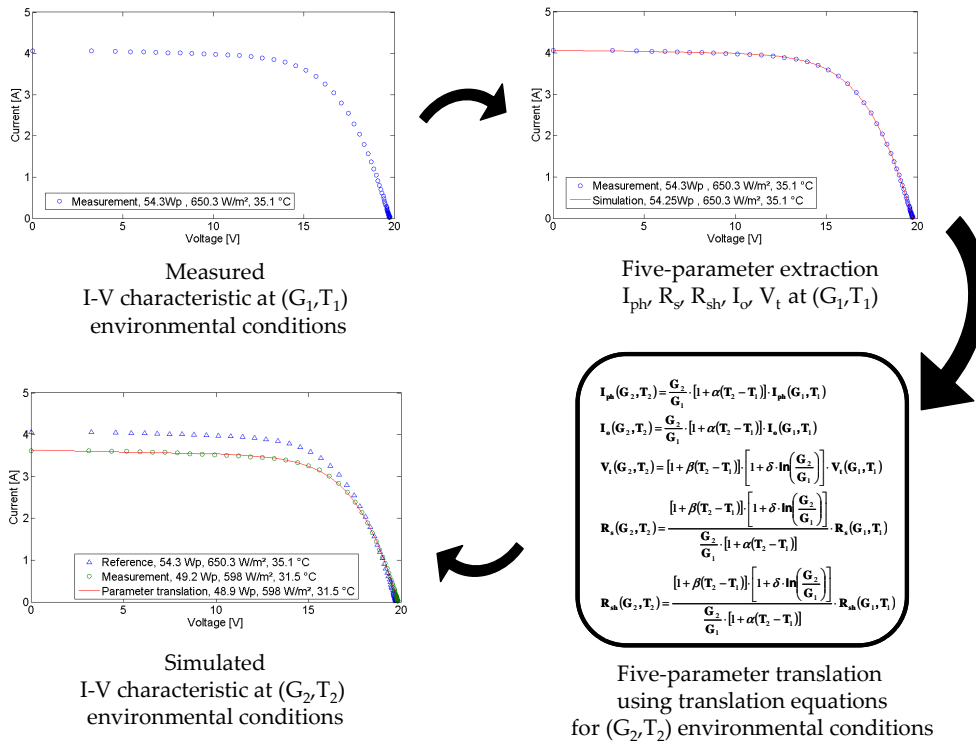


Figure III.12 : I-V curve translation procedure for one module starting from module measurement conditions (G_1, T_1) to array measurement conditions (G_2, T_2)

III.2.1.2. Non-shaded Pergola 5 array

The module measurements have been carried out using a connection box, detailed in Annex 7, in order to rapidly connect and disconnect modules from the I-V curve tracer. The I-V characteristics for each module composing the Pergola 5 array have been reported on Figure III.13. The environmental conditions are similar with solar irradiance ranging from 597.1-599.1 W/m² and module temperatures from 31.2-33°C. By considering the effect of the environmental conditions negligible on the output power given there small dispersion range, we can see that manufacturer tolerances lead to a variation in maximum power output ranging from 47.8-51.7 W_p.

The I-V characteristic of the SP array, arranged in 4 strings with 5 modules per string, was taken at environmental condition (581 W/m², 29.3°C) which was not in adequacy with the module I-V curve readings. Hence, the module I-V curves were translated to the SP array recording environmental conditions using Toposolver.

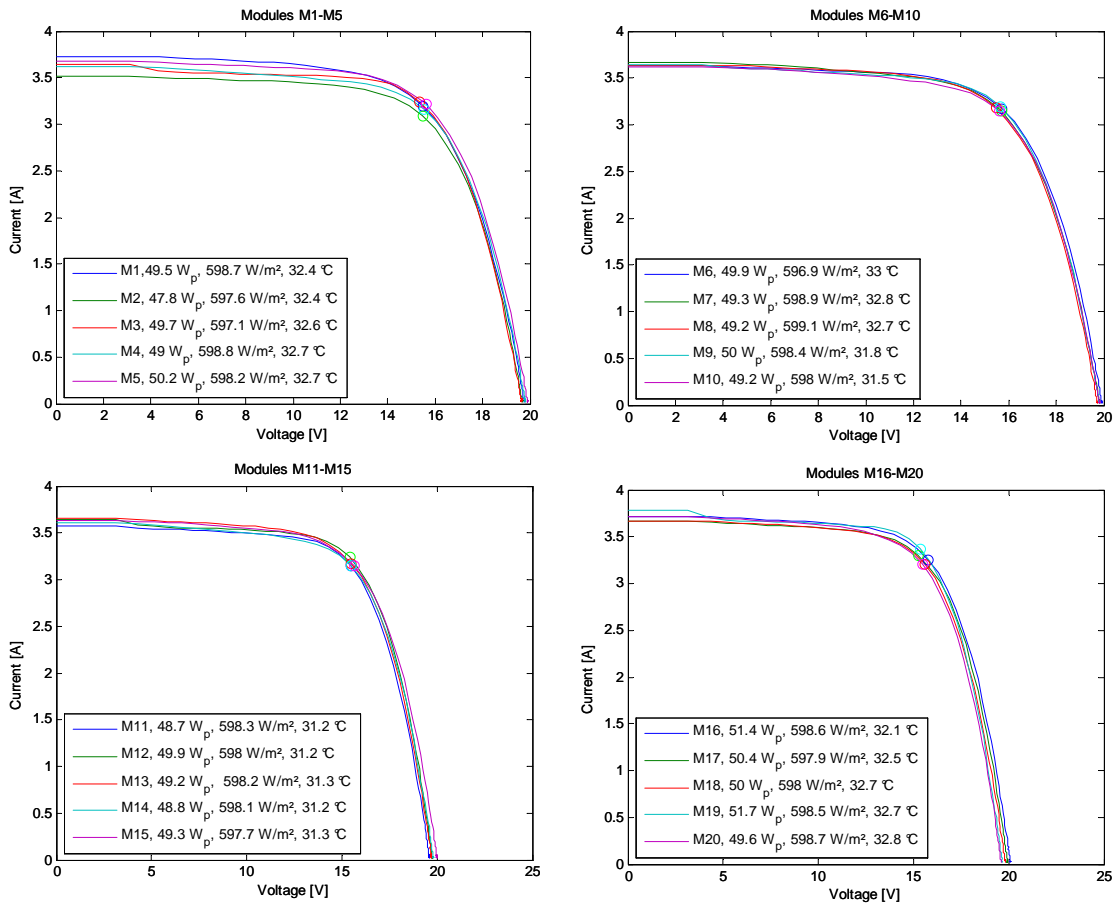


Figure III.13 : I-V characteristics of each module in the non-shaded Pergola 5 array

Results presented on Figure III.14 show high concordance between the simulation model and the experimental results. In the non-shaded 2.2 kW_p array only a 2 W difference between simulation and experimental maximum power output is observed, that is to say an 0.2% precision in terms of maximum power output.

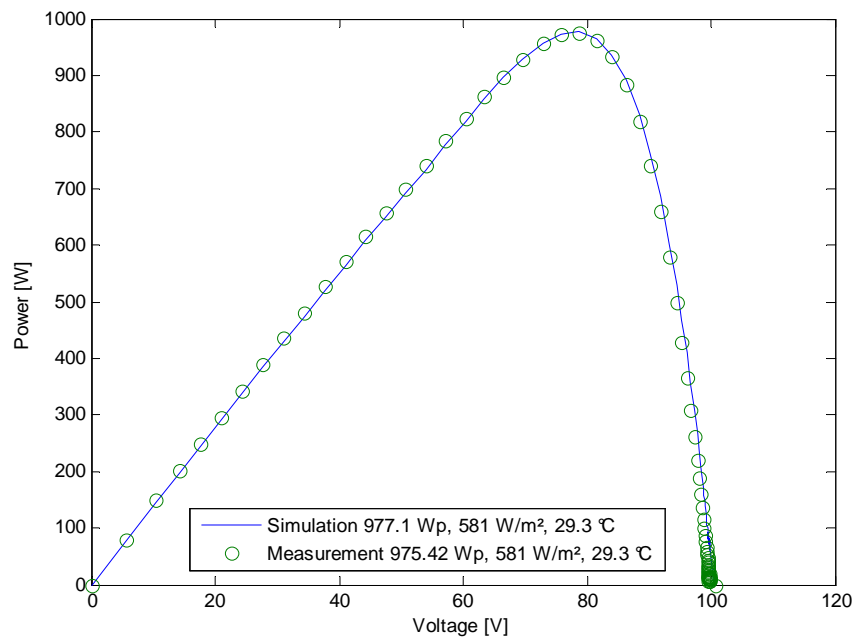


Figure III.14 : Comparison between experimental and simulation results

III.2.1.2. Partially-shaded Pergola 5 array

In the case of a partially shaded PV array, the experimental procedure was identical to the before mentioned experiment. In order to reproduce the effect of shade on a PV array, a plastic film has been placed on the module surface as shown on Figure III.15(b). Depending on the incoming irradiance the shade factor induced by the plastic film varied slightly. For this reason, module I-V curve readings and array readings were carried out in a short time span.

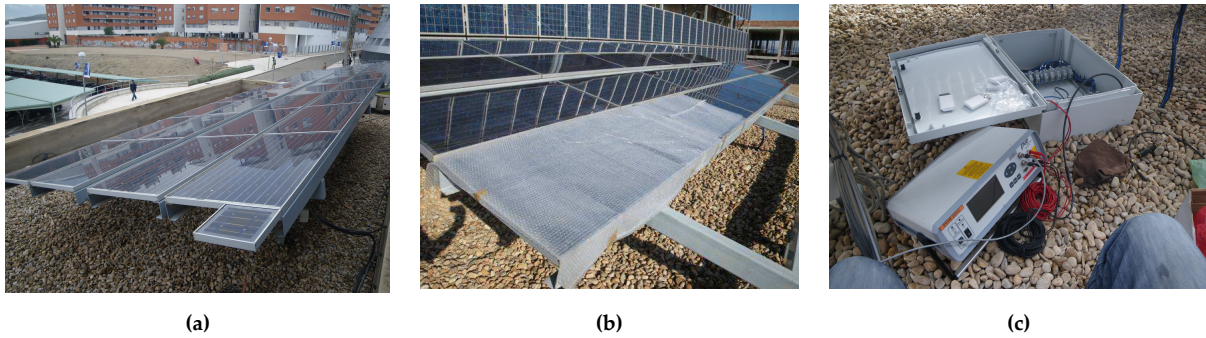


Figure III.15 : Views of (a) entire Pergola 5 plant with irradiance sensor in the foreground, (b) artificial shade on modules M1 & M2, (c) I-V curve tracer PVPM 2540C with connection box

In the partially shaded scenario S1, where M1 and M2 are artificially shaded by the bubble-wrap, the short circuit current was reduced by roughly 40% as can be seen on Figure III.16. Since short-circuit current varies linearly with incoming solar irradiance, we can deduce that the artificial shade reduces the incoming irradiance by 40% on modules M1 and M2.

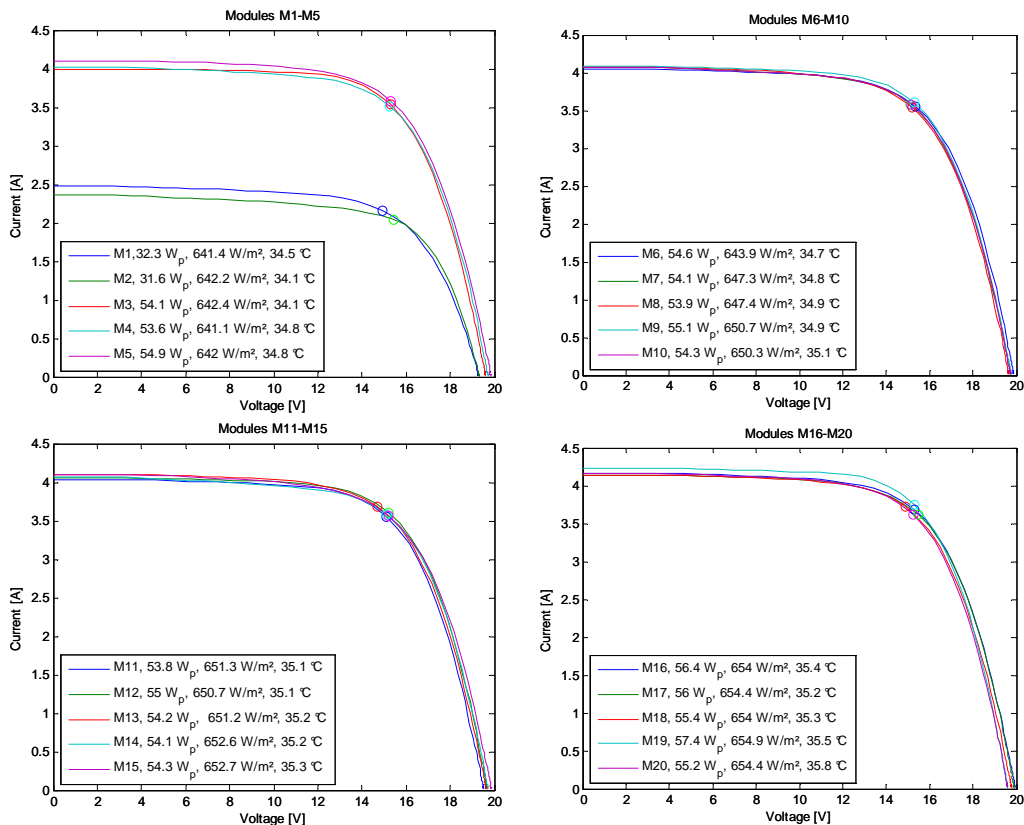


Figure III.16 : I-V characteristics of Pergola 5 modules with shade scenario S1

The comparison between simulation and experimental results of this scenario are presented on Figure III.17. First, we can observe a discrepancy between forecast and measurement in the 20-40V range. This is mainly due to the bypass diodes which are activated at low voltages. The bypass diode model considered in Toposolver uses quasi-ideal diode model which is not entirely compatible with the real diodes used in the I-106 modules. In order to obtain more accurate results, a curve-fitting of the real bypass diodes should be conducted to determine diode parameters.

Secondly, the general trends of the I-V curve are correctly restituted both in shape and with acceptable open-circuit and short-circuit values. Finally, the maximum power output of the simulated partial shaded array has a 24 W difference with the experimental value, that is to say the model has an error of 2.2% with reference to the experimental results.

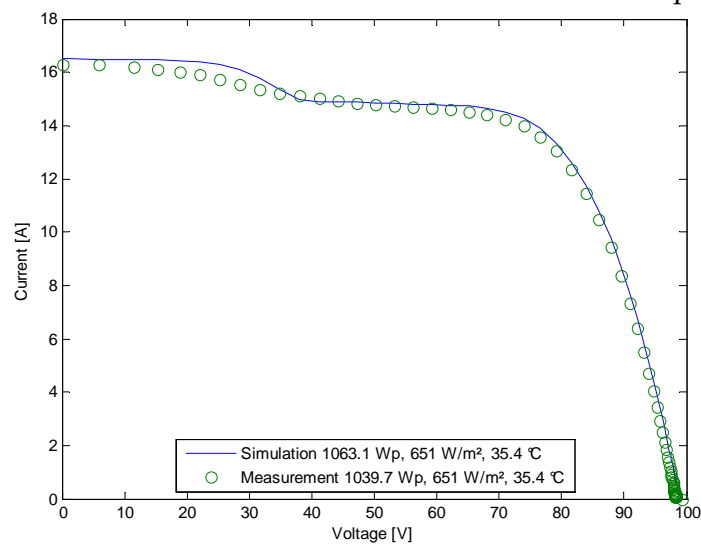


Figure III.17 : I-V characteristic of partially shaded Pergola 5 using scenario S1

These preliminary results show the accuracy of the Toposolver software in forecasting PV array maximum power. Other model validations will be addressed in section III.3 when alternative array topologies will be presented.

III.2.2. Mismatch losses in a 2.2 kW_p based on experimental data

The Pergola 5 installation has been submitted to six shade scenarios and environmental conditions in order to determine mismatch losses due to both PV module property dispersion and heterogeneous environmental conditions. The experimental procedure consists in measuring the I-V curve of each module at conditions (G_1, T_1), then measuring the array characteristic at environmental conditions (G_2, T_2) for the different scenarios. The I-V curves of each module are later translated to conditions (G_2, T_2) and the maximum extractable power of each module is recorded.

The first three scenarios N1, N2, and N3 are used to determine the mismatch losses due to module property dispersion under various environmental conditions presented on Table III.2. The last three shade scenarios S1, S2, and S3 use artificial shade placed in different locations as can be seen on Figure III.18.

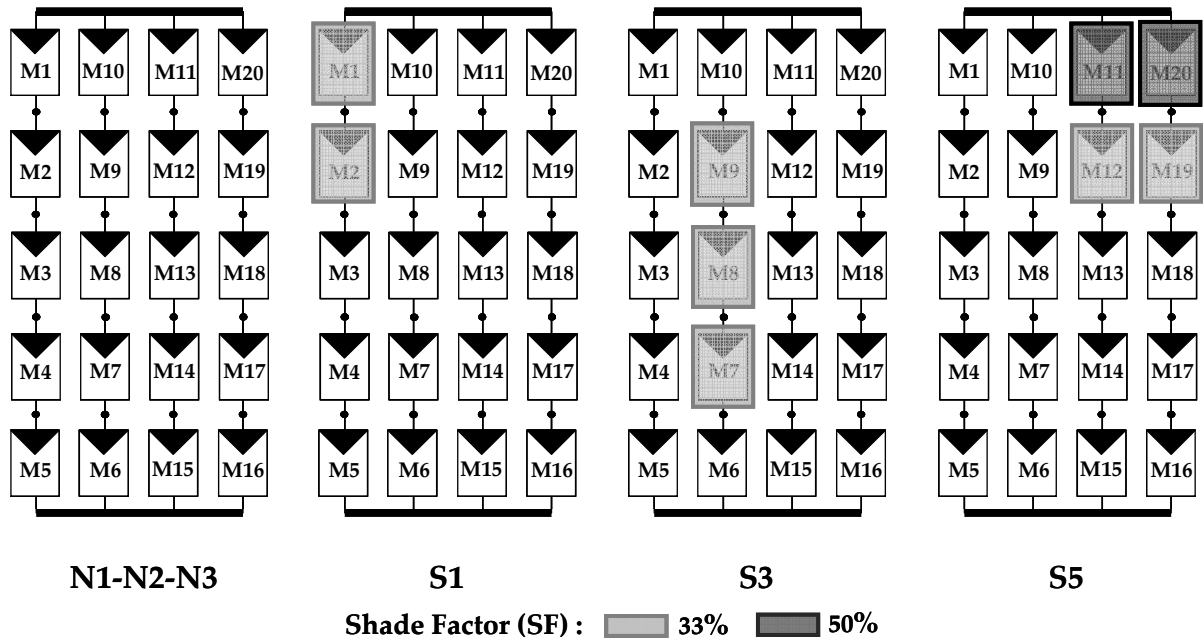


Figure III.18 : Shade scenarios used on Pergola 5 array

The shade factors have been deduced by measuring the short-circuit current of the non-shaded and artificially shaded module. Since the short-circuit current varies linearly with irradiance, the ratio between shaded and non-shaded module short-circuit currents and irradiance are conserved. In shade scenario S1, modules M1 and M2 have 33% less incoming irradiance, whereas in S2 modules M7, M8, and M9 of the same string are partially shaded by 33%. In scenario S5, modules M11 and M20 are shaded by 50% whereas modules M12 and M19 are shaded by 33%.

Since these measurements have been carried outdoors, the environmental conditions were not controlled as can be seen on Table III.2. For the non-shaded scenarios, this is very interesting in order to establish the impact of solar irradiance and temperature on mismatch losses. However, in the shaded scenarios S1, S3, and S5 both the impact of shade and environmental conditions are combined.

N1	N2	N3	S1	S3	S5
107 W/m ²	581 W/m ²	633 W/m ²	650 W/m ²	847 W/m ²	810 W/m ²
17,3 °C	29,3 °C	33,2 °C	35,5 °C	47,5 °C	45,4 °C

Table III.2 : Pergola 5 array measurement values of solar irradiance [W/m²] and module temperature [°C] for the proposed shade scenario

The mismatch losses of the Pergola 5 array in the previously mentioned shade scenarios are presented on Figure III.19. Results show that when the array is non shaded, mismatch losses remain under 2% and tend to increase with solar irradiance and temperature. In partially shaded scenarios, mismatch losses range between 2.4-12.8%.

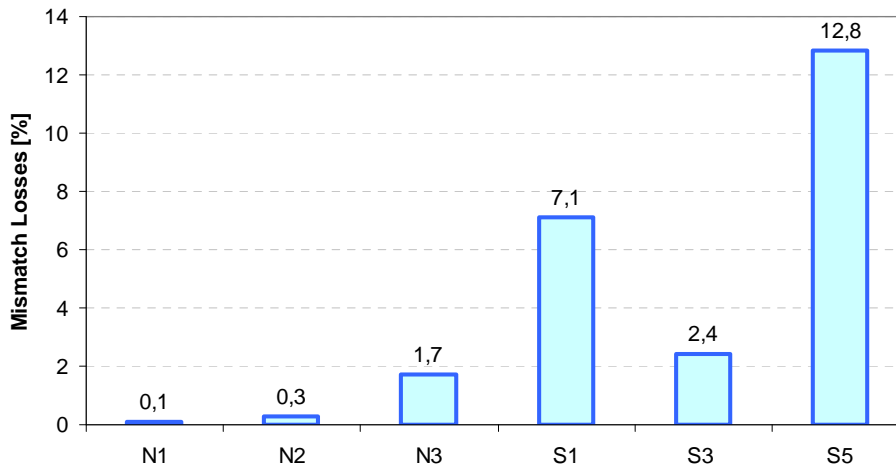


Figure III.19 : Mismatch losses obtained in the proposed shade scenarios

First of all, we can see that mismatch losses are greater when the array is partially shaded.

Secondly, when comparing S1 and S3, we can see that the more a PV string contains shaded modules, the lower the mismatch losses. Indeed, in scenario S1 only two modules of a same string are shaded whereas in scenario S3 three modules are shaded. At first this may seem surprising, yet since mismatch losses represent the dispersion in power outputs of interconnected modules, a string containing more shaded modules will have lower mismatch losses. For example, a totally shaded string will have no mismatch losses. This point will be detailed further in the next section.

Finally, results show that the location of the shaded modules has an important impact on the value of mismatch losses. When comparing results between scenarios S1 and S5, despite the fact that the shade factor is slightly greater for the last scenario, we can see that mismatch losses in scenario S5 are almost twice those of scenario S1. Indeed, when shaded modules are located on several strings the mismatch losses tend to increase.

After having seen that mismatch losses induced by partial shading are predominant over module property dispersion, the next section will further develop the module mismatch phenomenon when submitted to partial shading.

III.2.3. Mismatch losses in partially shaded series-parallel arrays

The purpose of this part is to analyze mismatch losses in various shade scenarios to better understand the phenomenon. To do so, the developed simulation tool has been applied to a 4x3 array, 3 strings of 4 modules per string, in all possible shade scenarios with identical PV modules. The series-parallel topology has the advantage of having much symmetry in terms of shade scenarios. When one module is shaded in a PV string, the power loss is independent of the position of the shaded module in that PV string. Likewise, when one module is shaded on a 4x3 array, the power loss is independent of the string number in which the module is located. Considering these symmetry properties, shade positions indicating the number of shaded modules per string can be used to reduce the number of

shade scenarios. In the following simulations, the number of shaded modules is gradually increased and for each shade position the maximum power output of the array is recorded. Shade positions are noted using the following code $n_1-n_2-\dots-n_N$, where N is the number of strings in the array and n_X is the number of shaded modules on string X . For example, in the case where three modules are shaded, as presented on Figure III.20, there are three equivalent shade scenarios.

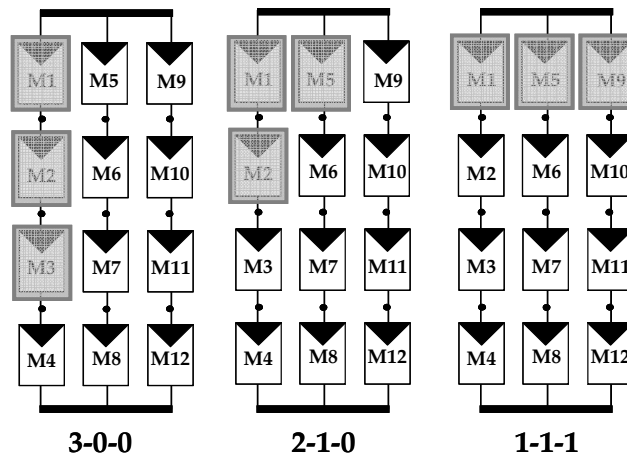


Figure III.20 : Possible shade scenarios for a 4x3 array with 3 shaded modules. The shade position is specified underneath each scenario.

The PV modules in the array used for the simulations are all identical and inspired from commercial 200 W_p modules. At standard test conditions, the PV module has a maximum power of 199.5 W_p , further information on the module can be found in Annex 8.

The following simulation results have been carried out by Luiz Lavado Villa during his Master of Science in Electrical Engineering internship at the G2Elab [LAV'10] under the supervision of B. Raison and myself.

The first simulation consisted in calculating the mismatch losses, expressed in absolute value, of a single PV string of a 4x3 array. The modules of the array were progressively shaded using a 0.2 shade factor. Results with their associated shade position are presented on Figure III.21, they show that the amount of mismatch losses of a single string tend to decrease linearly as the number of shaded modules increases. The line formed by these mismatch losses will now be referred to as *mismatch lines*.

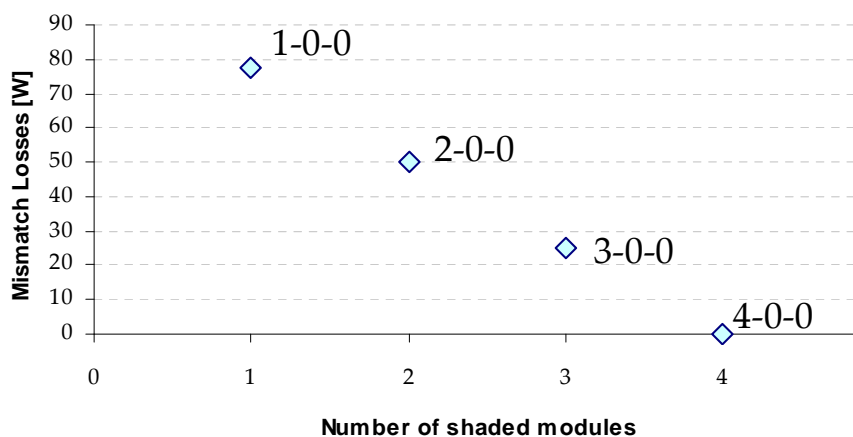


Figure III.21 : Mismatch losses of a single PV string, without bypass diodes, in a 4x3 array depending on the shade position.

A second set of simulations have been carried out on a 4x3 array by taking into account all the possible shade positions and using the same shade factor. The mismatch losses expressed in both absolute and relative values are presented on Figure III.22. As can be seen below, several shade positions are possible for a given number of shaded modules : 1 shade position (1-0-0) for 1 shaded module, 2 shade positions (2-0-0 and 1-1-0) for 2 shaded modules, 3 shade positions (3-0-0, 2-1-0, and 1-1-1) for 3 shaded modules and so on.

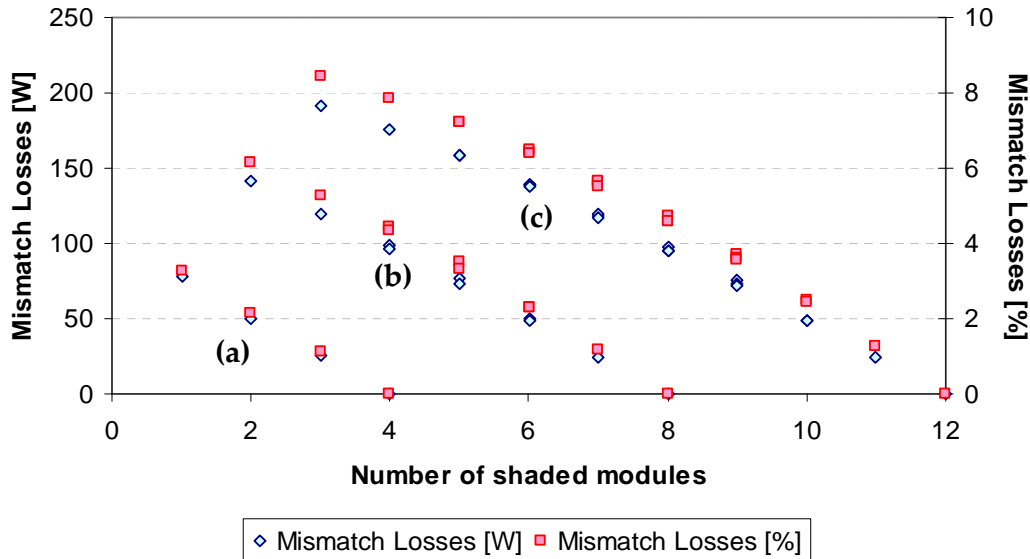


Figure III.22 : Impact of the number of shaded modules, without bypass diodes, on power and mismatch losses in a 4x3 array with (a) one partially shaded string (b) two partially shaded strings, and (c) three partiallaly shaded strings.

Results show that mismatch losses and power losses have the same trends: three sets of lines that decrease as the number of shaded modules in the array increases. The worst case scenario is obtained for three shaded modules in the array. After having analyzed the shade position corresponding to each point, as has been highlighted in the previous subsection, the worst case scenario corresponds to shade position 1-1-1. In other words, when each string contains a 20% shaded module, mismatch losses are expected to rise to 8.5%. This represents a power loss of 191 W, which approximately represents the maximum power of one module at STC conditions.

Furthermore, the mismatch lines are linked to the shade position. Indeed, each mismatch line contains points corresponding to identical number of strings being subject to shade. For instance, the mismatch line (a) corresponds to the shade positions in which only one string is partially shaded (ie. 1-0-0, 2-0-0, 3-0-0, and 4-0-0). When one string is entirely shaded, mismatch losses are null. This explains the null values when 4, 8, and 12 modules are shaded. The simulation results show three mismatch lines coinciding with partial shade affecting one string (a), two strings (b), and three strings (c).

Moreover, further simulations have shown that mismatch lines tend to be linear when considering absolute power losses and non-linear when considering the relative value of power losses. For this reason, the following analysis will use the absolute power loss indicator to interpret the evolution of mismatch losses.

III.2.3.1. Influence of the number of modules per string

The second set of simulations consisted in modifying the number of modules per string. Since traditional power plants tend to have many modules per string (typically 5 to 10 modules for residential power ratings) in order to fit input inverter voltage specifications, the study of the influence of adding modules to a string has been investigated. Three arrays have been considered: 6x3 array, 5x3 array and 4x3 array using the same procedure as in the previous paragraph, that is to say by taking into account all the possible shade scenarios.

As can be seen on Figure III.23, the mismatch lines have been drawn to ease comprehension of the string length. Since the considered arrays each contain three strings, three mismatch lines can be observed for each array configuration. The mismatch losses tend to increase as do the number of modules per string.

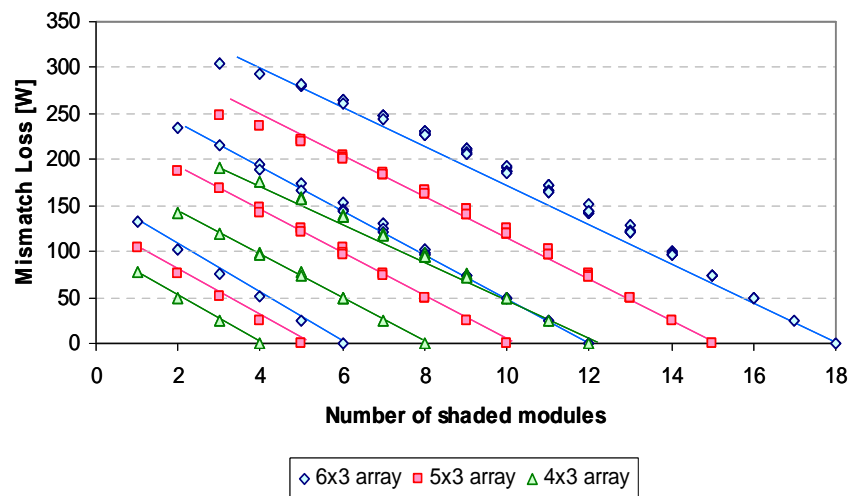


Figure III.23 : Evolution of mismatch losses with the number of modules per string. . The PV modules are not equipped with bypass diodes.

In graphical terms, the mismatch lines tend to shift upwards as modules are added to the strings. In the case one module in the array is shaded by 20%, a 4x3 array will have half the mismatches losses than a 6x3 array. In the worst case scenario (ie. shade position 1-1-1), mismatch losses will represent 142 W (6.1 %) in a 4x3 array, whereas the losses increase to 248 W (8.6%) and 305 W (8.8 %) for a 5x3 array and 6x3 array respectively. The mismatch losses increase both in power and percentage when the array strings contain more modules.

In conclusion: the longer the string, the greater the mismatch losses for a given shade scenario at low shade intensity.

III.2.3.2. Influence of the number of strings in an array

In PV array design, once the number of modules per string is determined the number of strings in the array is calculated to fit desired power specifications. A third set of simulations were carried out to understand the influence of the number of strings on mismatch losses. To do so, three arrays that differ by the number of parallel-connected strings: 5x4 array, 5x3 array, and 5x2 array have been simulated. The results presented on Figure III.24 confirm the correlation made between the number of mismatch lines and the

number of strings in the array. Furthermore, the gap in between the same set of mismatch lines is relatively small. For example, in the case of two strings subject to shading, see (a) on Figure III.24, the mismatch losses between the three arrays are similar. In mismatch lines (a), the maximum losses are evaluated at 165 W (8.6%), 188 W (6.5%), and 199 W (5.1%) for the 5x2 array, 5x3 array and 5x4 array respectively. Mismatch losses tend to decrease as strings are added to an array when expressed in percentage of power loss as can be seen on Figure III. 25.

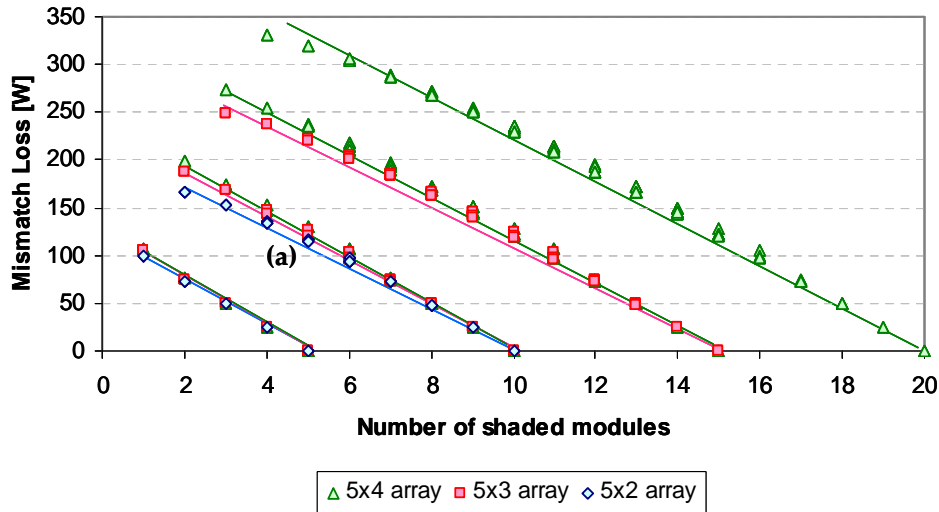


Figure III.24 : Evolution of mismatch losses with the number of strings. The PV modules do not have bypass diodes.

However, the worst case scenario power losses differ for each array configuration and increase with the number of strings. In each array, the greatest mismatch losses are attained when each string is shaded. The worst case scenario (WCS) mismatch losses represent 165 W (8.6%), 248 W (8.6 %) and 273 W (7%) for the 5x2 array, 5x3 array, and 5x4 array respectively. However, mismatch losses expressed in percent of total extractable power are reduced when modules are added to the strings.

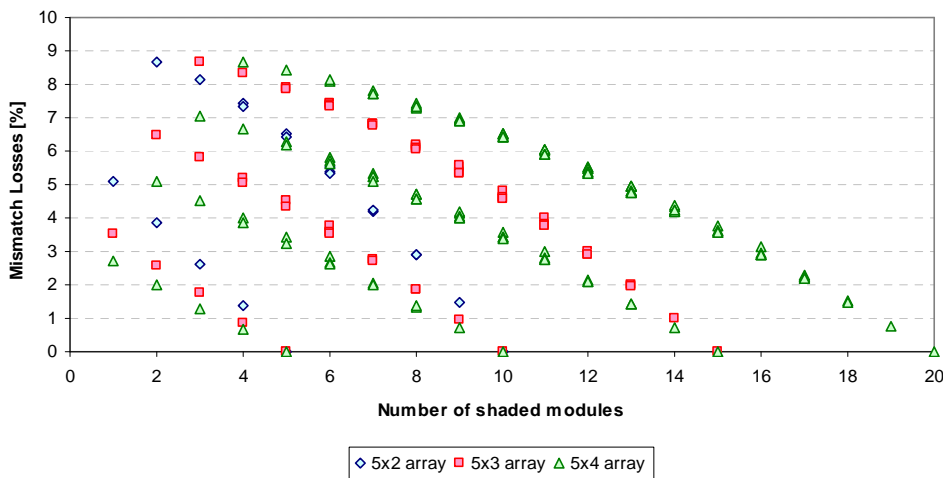


Figure III. 25 : Evolution of mismatch losses with the number of strings expressed in percentage of power. The PV modules do not have bypass diodes.

In conclusion: the more strings are added to an array, the lower the mismatch losses with respect to the portion of extractable power.

III.2.3.3. Influence of shade intensity

After having seen the impact of the shade position on module mismatch, the influence of shade intensity will be studied in this paragraph. Indeed, shade induced by a passing cloud and an opaque obstacle differ depending on the distance of the obstruction from the solar generator. The albedo of the surrounding environment may compensate to some extent the decrease of incoming solar irradiance. In order to study the effect of the shade intensity, simulations on a 4x3 array have been carried out using three shade factors: 0.2, 0.5, and 0.9. In this simulation, the bypass diodes have been removed in order to later understand their impact on mismatch loss generation.

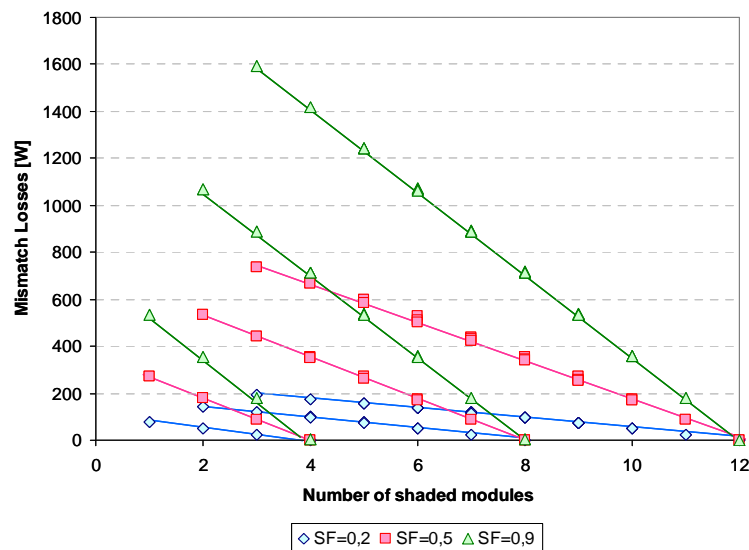


Figure III.26 : Impact of shade factor on mismatch loss generation in a 4x3 array with removed bypass diodes

Simulation results presented on Figure III.26 show that mismatch lines conserve their parallelism; therefore shade intensity has a homogeneous effect on mismatch loss generation. Results show that mismatch losses increase with the shade factor. For shade factors of 0.2, 0.5, and 0.9 the steepness of the mismatch lines are approximately worth 26, 93, and 178 W per shaded module. Therefore, when one module is shaded on a string, the power losses can rise considerably in a nonlinear manner. In the extreme cases, when the shade factor varies from 0.2 to 0.9, that is to say the shade factor is 4.5 times greater, the steepness increases by 670%.

The worst case scenario (WCS) is also affected disproportionately with the shade factor. Indeed, WCS mismatch losses total 191 W (8%), 736 W (35%), and 1593 W (86%) for shade factors 0.2, 0.5, and 0.9 respectively. Both the absolute and proportional power losses increase considerably with the shade factor.

Yet, it should be noticed that some of these simulation results may not have physical meanings. Indeed, when bypass diodes are removed, the PV modules may operate in reverse bias, that is to say as power consumers rather than producers. In reality, some of the cells may be destroyed by thermal stress when approaching the thermal overcurrent value, as mentioned in chapter II.1.2. Nevertheless, the impact of shade intensity on mismatch

generation can be better understood using these simulations.

In conclusion: mismatch losses increase non-linearly with the shade intensity when considering a PV array without bypass diodes.

III.2.3.4. Influence of shade intensity with bypass diode-equipped modules

The main purpose of bypass diodes in cell-strings is to prevent deterioration of solar cells by bypassing current through a diode rather than operating in reverse-voltage. Incidentally, bypass diodes also reduce mismatches by preventing the shaded modules to impose the operation point to the PV string or array. Simulation results of a 4x3 array with bypass diodes are presented on Figure III.27.

The first outstanding result, when compared to PV modules without bypass diodes, is the disappearance of mismatch lines. At low shade factors, the mismatch lines remain, but the points tend to scatter as the shade factor and number of shaded modules increase. This can be explained by the added non-linearity of the bypass diodes in the electrical system. When a diode is active, a point shifts downwards from its original mismatch line. The mismatch lines drawn on Figure III.27 correspond to those of modules without bypass diodes in order to clearly identify which points have shifted. The most discernable point-shifts are obtained for a shade factor of 90% in which none of the mismatch lines are entirely intact.

Secondly, a considerable decrease of mismatch losses in the WCS can be observed. In severe shade conditions, the highest amount of mismatch losses (WCS) are roughly three times lower when using a bypass diode per module when compared to modules without one, as can be seen on Table III.3. Furthermore, the WCS shade position has been changed due to the presence of bypass diodes. The WCS is no longer obtained when a module on each string is shaded, i.e. with shade position 1-1-1, but depends on the shade factor as can be seen on Table III.3. In the case SF=0.9, the WCS does not have shaded modules scattered on each string, but only two strings are partially shaded.

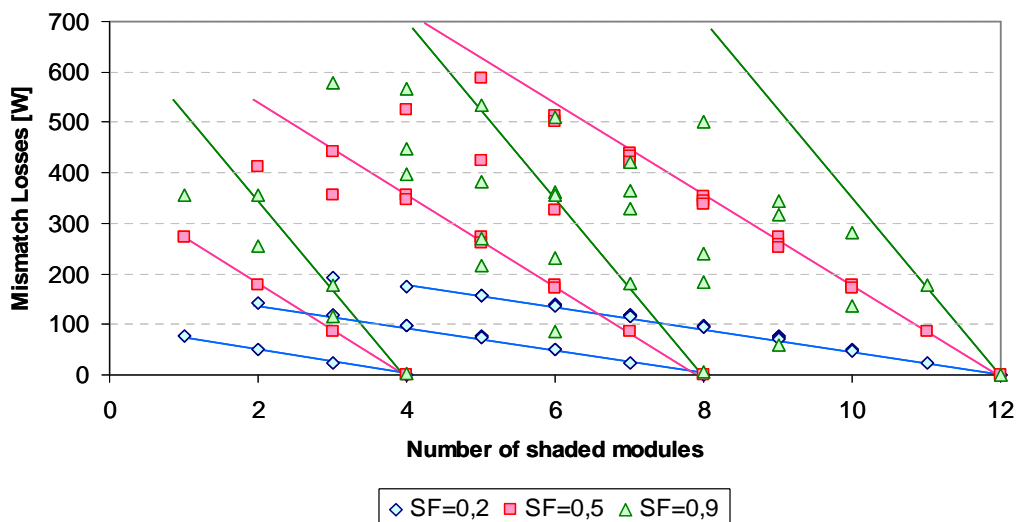


Figure III.27: Impact of shade factor on mismatch loss generation in a 4x3 array with bypass diodes

Finally, the bypass diodes reduce considerably the percentage of mismatch losses and seem to set a 30% threshold of maximum power losses regardless of the shade factor. This last point may be linked to the number of modules constituting the array and the maximum power rating of each module. Further investigation on the interdependence in between maximum mismatch losses and the array design should be carried out to better comprehend the phenomenon.

Shade Factor	Removed bypass diode			Connected bypass diode		
	WCS Mismatch Losses		Shade position	WCS Mismatch Losses		Shade position
0,2	191 W	8%	1-1-1	191 W	8%	1-1-1
0,5	736 W	35%	1-1-1	586 W	31%	2-2-1
0,9	1593 W	86%	1-1-1	578 W	31%	2-1-0

Table III.3 : Mismatch losses in worst case scenario (WCS) with both removed and connected bypass diodes

In conclusion, the presence of bypass diodes reduces mismatch losses in partially shaded arrays. Mismatch lines can be used to predict the quantity of mismatch losses in an array under different shade conditions by using the mismatch line properties. However, mismatch loss prediction is more complex when considering modules equipped with bypass diodes due to the added non-linearity of these overcurrent protection devices.

An approach to reduce mismatch losses consists in modifying the module interconnection scheme within the array. The next section will present experimental and simulation results to quantify the impact of alternative interconnection schemes on mismatch loss generation.

III.3. Alternative array interconnection schemes

The study of the impact of shade on photovoltaic cell arrays has been investigated accompanying the development of terrestrial applications. Studies have been carried out throughout the past to reconsider how solar cell arrays may be designed to lower mismatch losses. One solution proposed for solving the shadow problem in PV modules has consisted in quasi-randomly organizing PV cells [FEL'81]. In other words, Feldman proposed to distribute the shadowed cells throughout the strings of the solar cell array by organizing cell interconnections based on the position of shadowed cells. Quasi-random cell organization simulation results showed power output improvements of 20-30%. Another solution was to statically modify PV cell interconnections within modules by series-parallelizing them which adds redundancy in the electrical circuit [GAU'01]. Gautam proposed two interconnections schemes: total-cross tied (TCT) and bridge-link (BL) configurations which proved to reduce shade-induced mismatch losses in PV modules when compared to the series-parallel (SP) configuration by up to 15%. Recently, the honey-comb (HC) configuration was brought to light which showed better results than the TCT and BL configurations in certain shade scenarios [WAN'09]. The previously mentioned interconnection patterns are presented on

Figure III.10 on a 5x4 array.

Simulation results obtained in literature have brought the need for experimental verification of mismatch loss reduction using alternative interconnection schemes. For this reason, further measurements have been carried out on the Pergola 5 plant (cf. chapter III.2).

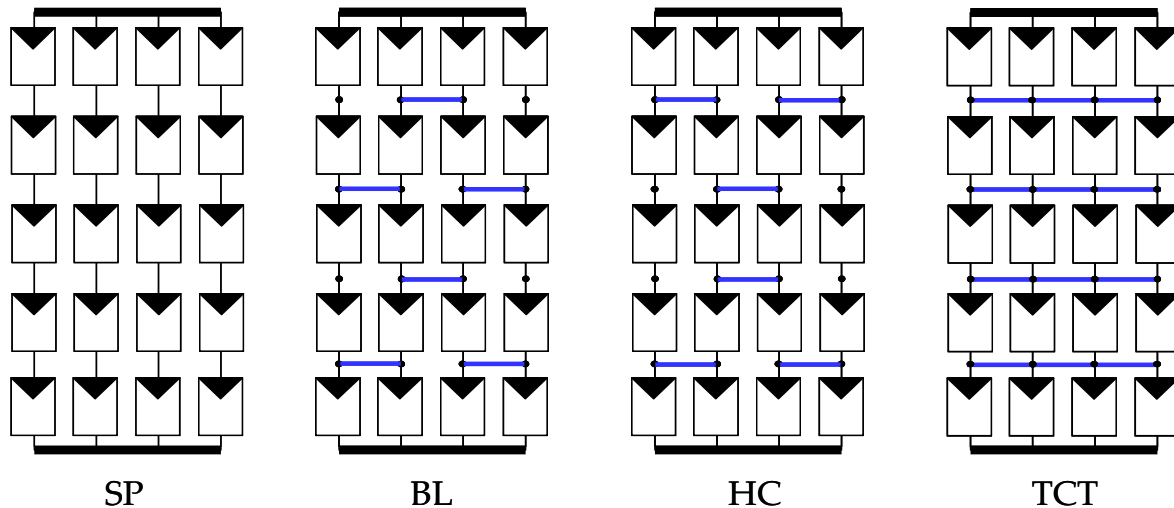


Figure III.28 : Diagram of series-parallel (SP), bridge-link (BL), honey-comb (HC), and total-cross tied (TCT) interconnection schemes.

III.3.1. Experimental results of Pergola 5 array using alternative interconnection schemes

The Pergola 5 plant was originally connected in the traditional series-parallel configuration consisting of two strings of ten modules due to grid-tied inverter voltage requirements. In order to understand the effect of modifying the array interconnections, the Pergola 5 array needed to be modified to examine the TCT and BL patterns experimentally. The HC pattern has not been tested experimentally. The withheld solution consisted in reorganizing the array into a 5x4 array disconnected from the grid. Array interconnection schemes (SP, TCT, and BL) were changed using the connection box previously described in III.2.1.2. Each module terminals were brought to the connection box fuse terminals. The fuse outputs were connected to MultiContact plugs to rapidly and safely reorganize the array interconnections. For further information on the connection box refer to Annex 7.

The experimental procedure consisted in first measuring the I-V characteristic of the three proposed array interconnection schemes (SP, TCT, and BL) and then each individual module of the array at similar environmental conditions. Five shade scenarios were investigated on the Pergola 5 plant, certain views of the shade scenarios are shown on Figure III.29. The influence of modifying string lengths has also been studied, which leads to the eight different scenarios presented on Figure III.30.



Figure III.29 : Views of Pergola 5 plant with shade scenarios N2, S2-S3, and S4-S5

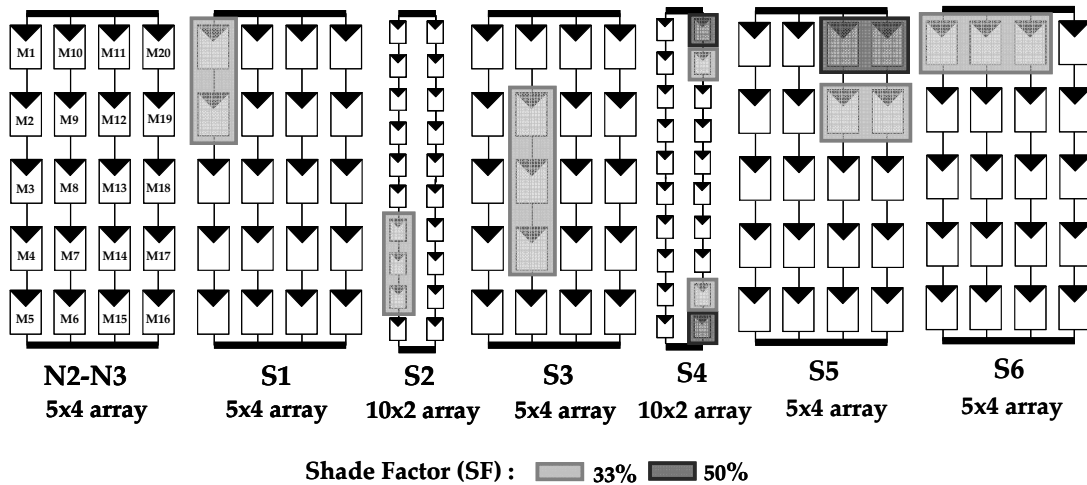


Figure III.30 : Shade scenarios for Pergola 5

The environmental conditions in which the experiments were carried out can be found on Table III.2. Experimental results, presented on Table III.4, show that in each case the alternative interconnection schemes produce more power than the traditional SP configuration. In normal operating conditions, the power output of the different arrays is similar with under 2% differences in maximum power output when compared to the SP configuration.

	SP	TCT		BL	
	[W]	[W]	[%SP]	[W]	[%SP]
N2	975,42	988,5	1,3%	995,1	2,0%
N3	1087,5	1089,9	0,2%	1090,2	0,2%
S1	1001,2	1039,7	3,7%	1025,0	2,4%
S2	1149,2	1201,7	4,4%	1191,8	3,7%
S3	1196,2	1215,2	1,6%	N/A	N/A
S4	999,04	1055,8	5,4%	1047,4	4,8%
S5	957,08	1009,8	5,2%	N/A	N/A
S6	607,61	627,7	3,2%	N/A	N/A

Table III.4 : Maximum power of Pergola 5 array using alternative topologies in different shade scenarios

However, in the partially shaded S4 scenario, the power output of the TCT and BL arrays are 5.4% and 4.8% greater than the SP measured power. Considering the use of the experimental procedure, the additional cable losses due to module interconnections are negligible given the short distances of the MultiContact plugs. Cable losses may be greater in a fixed TCT or BL configuration, but should remain small since the cable length joins two adjacent module junction boxes.

The calculation of mismatch loss in the arrays has been carried out as previously exposed in section III.2. using Toposolver, results are presented on Figure III.31.

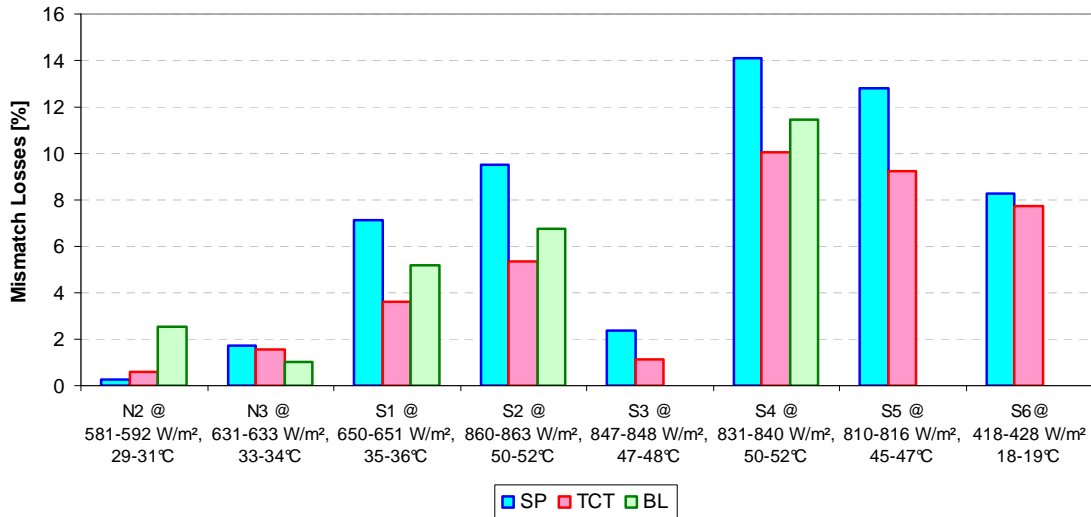


Figure III.31: Mismatch losses of Pergola 5 array using alternative topologies in different shade scenarios

Besides scenario N2, the alternative topologies reduce considerably mismatch losses in the PV array. In scenarios S1, S2, and S3 the mismatch losses in the TCT topology are half of those in the SP arrangement. Likewise, the BL interconnection scheme systematically has lower mismatch losses than the traditional SP array design.

Concerning the results of scenario N2, we can see that the SP topology performs best. This is in contradiction with all the other measurements. Since mismatch losses are calculated using a simulation of the theoretical extractable power, errors in the determination of this value lead to mismatch loss prediction errors. Since parameter translation equations are less accurate in low irradiance and temperature ranges, the simulated maximum extractable power may be inaccurate.

Moreover, the impact of array design has an impact on the amount of generated mismatch losses. In scenarios S2 and S3 the exact same shade scenario is applied to the array, only module connections are modified into 4x3 and 10x2 arrays. The experiment shows that for a same shade position on an array the manner in which these are connected can affect the output power and mismatch losses. In this case, more power is produced when the array is connected in 5x4, likewise mismatch losses are five times lower in scenario S3 than in S2.

In conclusion, experimental results carried out on the 2.2 kW_p array show that alternative interconnection schemes produce more power than traditional series-parallel

connected arrays. The highest power increase is obtained using the TCT pattern with partial shade scenario S4 in which 5.4% more power is extracted from the solar generator. Furthermore, the influence of array design on power and mismatch loss generation has been evaluated. PV arrays submitted to partial shade should take into account the design of the array with respect to the shade position in order to increase the power output, albeit in using series-parallel or alternative interconnection schemes.

III.3.2. PV array forecasting tool validation using experimental results

The PV array power production forecasting tool has been used in the previously described shade scenarios. In order to validate the model, maximum power values of experimental and simulation results have been compared and are presented on Figure III.32 and Table III.5.

Results show that most of the simulation results are within the 5% error threshold when compared to experimental results. Considering that the measurement device has a precision of 5% on recorded power values, the simulation results stay in the same range and are compatible with measured results. Detailed results of these simulations can be found in Annex 9. However, certain sources of errors have been brought to light especially in the case of scenario S5-TCT in which the simulation error reaches 9.2%.

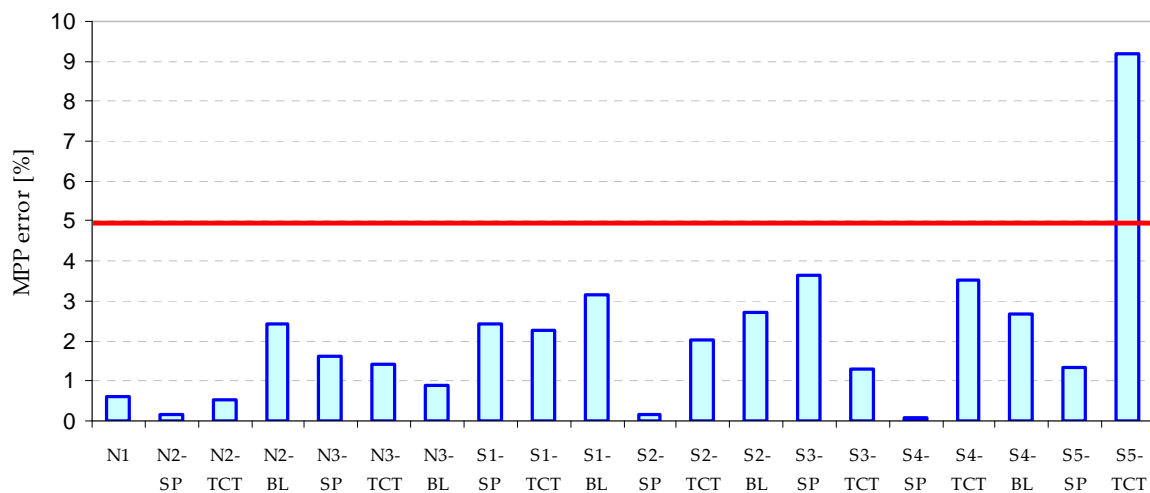


Figure III.32 : Relative error between simulation and experimental results

First of all, the single-diode model is not always adapted to partially shaded modules. When the module does not have a homogeneous shade the one-diode model is no longer adapted to the module current-voltage characteristic, as can be seen on Figure III. 33, since it considers the module as a single large solar cell and thus disregards the power flow inside the cells of a module. On Figure III. 33(c), even though the variation of module maximum power remains low, the shape of the characteristic will not be adequate at low array voltages due to modelling errors. On the I-V curve of shade scenario S5, presented on Figure III.34, this error is visible at low voltages and near the maximum power point. A more complex

model which takes into account these I-V curve shapes, such as Bishop’s model, by considering a module as a combination of elementary solar cells rather than a large unique solar cell would highly increase forecast precision in such scenarios.

Shade Scenario		MPP		MPP error	
		Measurement	Simulation		
N1	SP	199,5 W	198,3 W	1,2 W	0,6%
N2	SP	975,4 W	977,1 W	1,7 W	0,2%
	TCT	988,5 W	993,8 W	5,3 W	0,5%
	BL	995,1 W	1019,3 W	24,2 W	2,4%
N3	SP	1087,5 W	1105,0 W	17,5 W	1,6%
	TCT	1089,9 W	1105,4 W	15,5 W	1,4%
	BL	1090,2 W	1100,0 W	9,8 W	0,9%
S1	SP	1001,2 W	1025,7 W	24,5 W	2,4%
	TCT	1039,7 W	1063,1 W	23,4 W	2,3%
	BL	1025,0 W	1057,2 W	32,2 W	3,1%
S2	SP	1149,2 W	1147,4 W	1,8 W	0,2%
	TCT	1201,7 W	1226,2 W	24,5 W	2,0%
	BL	1191,8 W	1224,2 W	32,4 W	2,7%
S3	SP	1149,2 W	1107,1 W	42,1 W	3,7%
	TCT	1201,7 W	1186,2 W	15,5 W	1,3%
S4	SP	999,0 W	1000,0 W	1,0 W	0,1%
	TCT	1055,8 W	1093,2 W	37,4 W	3,5%
	BL	1047,4 W	1075,4 W	28,0 W	2,7%
S5	SP	957,1 W	944,3 W	12,8 W	1,3%
	TCT	1009,8 W	1102,4 W	92,6 W	9,2%

Table III.5 : Experimental and simulation results of PV power production forecasting tool

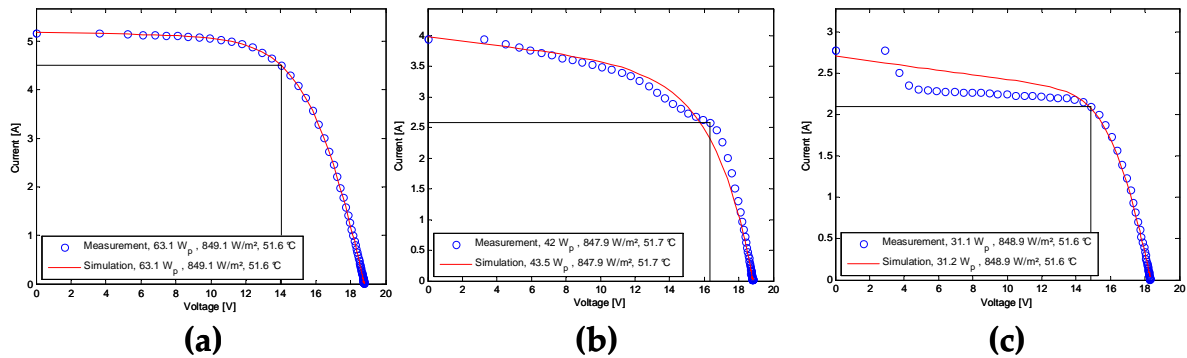


Figure III. 33: Current-voltage characteristics of (a) non shaded module M13, (b) partially shaded module M12, and (c) partially shaded module M20 in shade scenario S5

Secondly, the bypass diode plays a considerable role on I-V characteristics of partially shadowed arrays. The activation of these diodes leads to multiple power peaks on the power-voltage curves, as can be seen on Figure III.34. In the simulation tool, the bypass diodes were modelled using the diode equation III.3 with reverse saturation current $I_0=10^{-4}$ and thermal voltage $V_t=0.6$ V. The activation of the diodes in the simulation model are not clearly visible on Figure III.34(right) whereas the multiple power peaks at 62 V and 75 V can be seen on the experimental results. This standard diode model may not be adequate to those used in the junction boxes of the Isotofón I-106 modules. Unfortunately, the characteristics of the real diodes have not been obtained in order to compare them with the diode model.

$$I_D = I_o \cdot \left(e^{-\frac{V_D}{V_i}} - 1 \right) \quad \text{III.3}$$

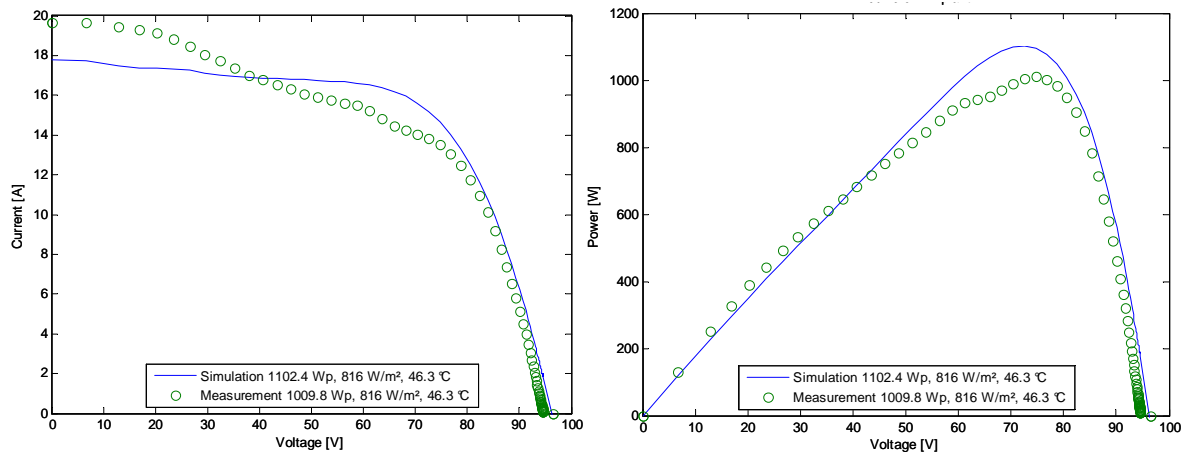


Figure III.34 : Experimental and simulated I-V characteristic (left) and P-V characteristic (right) of Pergola 5 array in shade scenario S5-TCT.

Finally, the last expected source of error is obtained during the translation of environmental conditions. Even though the method has been proven to be efficient when the initial and final conditions differ by up to 200 W/m² and 10°C at most, forecasted power error ratings greater than 5% have been observed for larger solar irradiance and module temperature values. In shade scenario S5, although the environmental conditions remain within the 200 W/m² and 10°C range, some parameter translation error may contribute to the differences in between measured and forecasted results.

In conclusion, the power production tool gives satisfactory results in 19 of the 20 cases studied. However, the interpretation of simulation results may trespass the 5% precision threshold when modules are shaded heterogeneously throughout the array due to inadequacy of the one diode model, bypass diode modelling and parameter translation related discrepancies.

III.3.3. Comparison of alternative topologies

A performance comparison of the series-parallel, total cross-tied, bridge-link and honey-comb topologies has been carried out using simulation results of Pergola 5 installation. The measured current-voltage characteristics of each non-shaded module of the array have been used to extract module parameters which have been later translated to environmental conditions (650 W/m², 35.5°C). The study has been carried out for each topology by progressively shading all modules in order to determine their mismatch lines using a shade factor of 0.33. It should be noticed that in the cases of the SP and TCT topologies all shade scenarios have been envisaged due to shade symmetries, however this is not the case for BL and HC topologies because of the lack of symmetry in the interconnection scheme. The shade factor and environmental conditions are identical to shade scenario S1, therefore some previously described results will be recognized in these new simulation results.

The mismatch losses for each topology are presented on Figure III.35. For more clarity, the mismatch lines have separately been presented on Figure III.36 for each topology. A linear regression, illustrated by a solid line, has been applied to each mismatch line in order to compare the performances of the interconnection schemes.

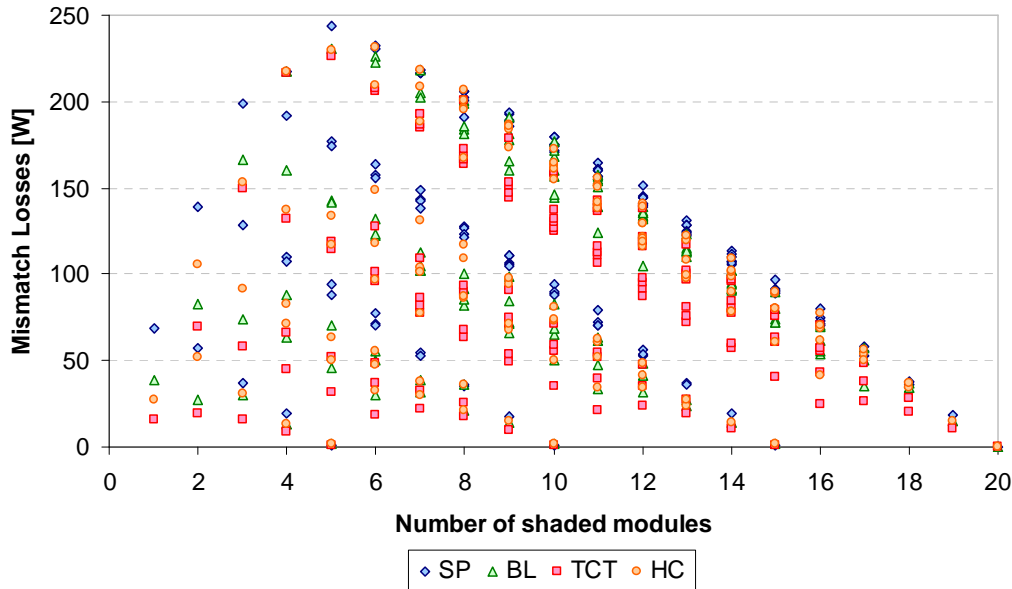


Figure III.35 : Evolution of mismatch losses in Pergola 5 array with the number of shaded modules

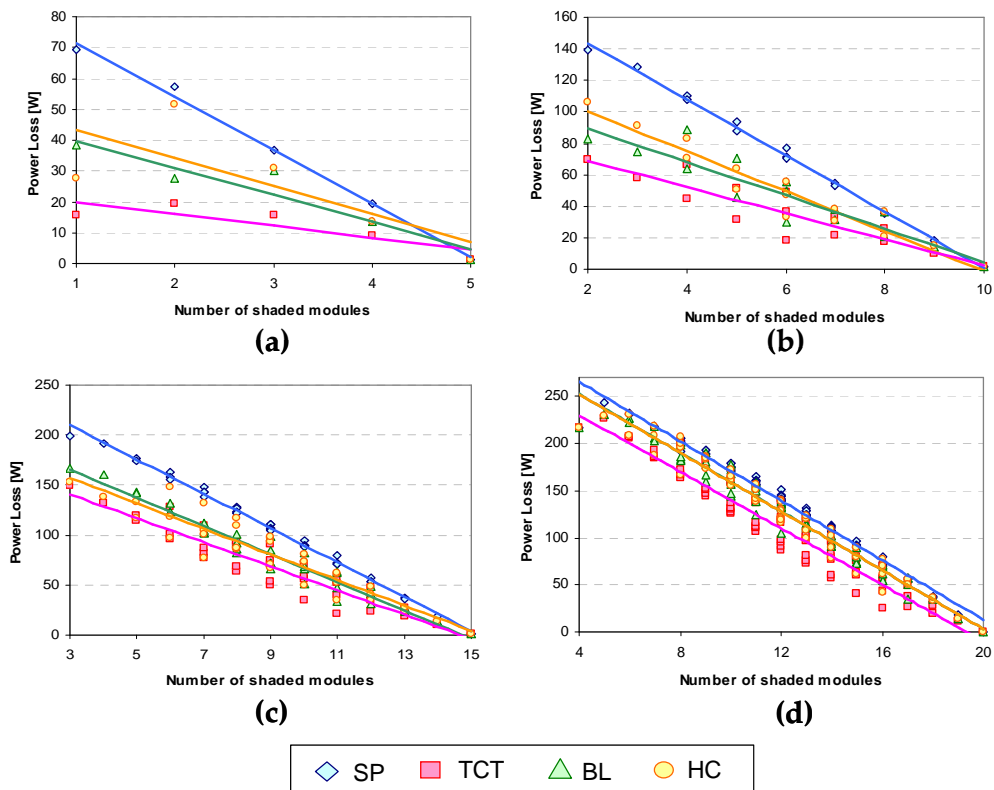


Figure III.36 : Simulation results for Pergola 5 array with linear regression of mismatch losses by mismatch lines (a) 1 shaded string, (b) 2 shaded strings, (c) 3 shaded strings, and (d) 4 shaded strings

First of all, results show that the total cross-tied topology performs best in reducing mismatch losses in the Pergola 5 array whereas the SP topology has the most losses. In the worst case scenario, when 5 modules are shaded in four 4 strings, mismatch losses account

for 24 % (243 W), 22.5% (230 W), 22.3% (229 W), and 22 % (226 W) of the total extractable power for the SP, BL, HC and TCT topologies respectively.

Secondly, the performance of BL and HC topologies is variable depending on the shadow position. In some shade positions, the BL arrangement will have higher mismatch losses than HC as shown in Figure III.36(c). However, when one or two strings are shaded the HC topology generally has higher mismatch losses than BL.

Finally, results show that mismatch losses with homogeneous shading on a string are under 2 W. This can be seen by the points located on the abscise axis when 5, 10, 15 and 20 modules of the array are shaded. In other words, the principal cause for large values of mismatch losses are due to partial shading which attain 24% whereas PV module mismatch accounts only for 0.2%.

Conclusion

Mismatch losses in photovoltaic arrays are induced by the heterogeneity of PV modules composing the array. Sources of mismatch can be classified into two groups: intrinsic PV module and environmental mismatches. Intrinsic PV module mismatch refers to inherent or acquired electrical differences between modules from their manufacturing process to their end of life. Environmental mismatch is caused by the surrounding environment of the module and is principally concerned by partial shading and temperature differences that may exist within the array. Through experimental and simulation results, alternative interconnection schemes have proven to be more efficient than the traditional series-parallel array layout in reducing mismatch losses when considering mild shade factors. Additional circuit redundancy caused by module interconnections leads to higher power production when the array is subject to partial shading. Experimental results have proved that alternative topologies can increase power by up to 5% with regards to a traditional module arrangement through mismatch loss reduction. In severe shading conditions, the activation of bypass diodes distorts the mismatch lines, thus making the performance of alternative array topologies irregular with respect to power output of the traditional design. The solar array power forecasting tool has been validated by correctly predicting power of nineteen different experimental results within a 5% error margin. Finally, simulation results applied to an existing PV array showed that mismatch losses may attain 24% in the worst case scenario. In conclusion, modifying module interconnection schemes can reduce mismatch losses in an array therefore producing more solar generated power. The next chapters will address another manner to reduce mismatch losses by inserting power converters in the array.

Chapter IV

Mismatch loss reduction using energy flow control via power converters

Introduction

The introduction of power electronic devices within the solar arrays is another method for module mismatch compensation. Power electronic devices have the advantage of adding a degree of freedom in the power flow management, yet generate power conversion losses in exchange. The aim of this chapter is to present the models for conventional power electronic converters dedicated to PV systems. In order to facilitate the computation without decreasing their accuracy, some classical averaged models are reduced using mode separation. Average and reduced average models of power converters with their associated conversion loss calculations will be addressed. Furthermore, photovoltaic power converters require adapted control strategies due to the specificity of the current-voltage characteristics. For this reason, the maximum power point tracking and single-phase inverter controls used in this work will be exposed. Lastly, the specific control strategy for the series-connected DC-DC converter topology will be detailed.

IV.1. Average models of power converters

Power converter operation is commonly described using an exact model which takes into account the switching operation behaviors. However, the output power of the systems is carried out by the fundamental component in alternative current circuits and by the average value in direct current circuits, for this reason average modelling techniques are used. The average modelling of power electronic devices consists in limiting the study by omitting the harmonics due to power switches. The averaged model has the advantage of reducing simulation time, which is interesting to use in complex systems such as grid-connected photovoltaics, while conserving accuracy and is easy to use for power converter control design [BACH'06]. The reduced-average modelling consists in further reducing the original average model by considering the time dynamics of the fast variables to be instantaneous. In this section, the classical and reduced-averaged models for the inverter and DC-DC converter will be exposed. These models will later be used in the Simulink environment, therefore the Simulink models will also be presented in this chapter. Finally, the losses generated during the power conversion will be addressed in the last section.

IV.1.1. Averaged modelling of a single phase grid-connected inverter

Grid-connected photovoltaic systems can be linked to the grid using a single phase or three-phase inverter depending on the power of the installation and grid codes. Generally, grid-interactive power production units consider the grid as an ideal AC voltage source ($230V_{RMS}$ -50Hz) with an associated impedance, in this case consisting of a series connected inductance (L_{GRID}) and resistance (R_{GRID}), as can be seen on Figure IV.1.

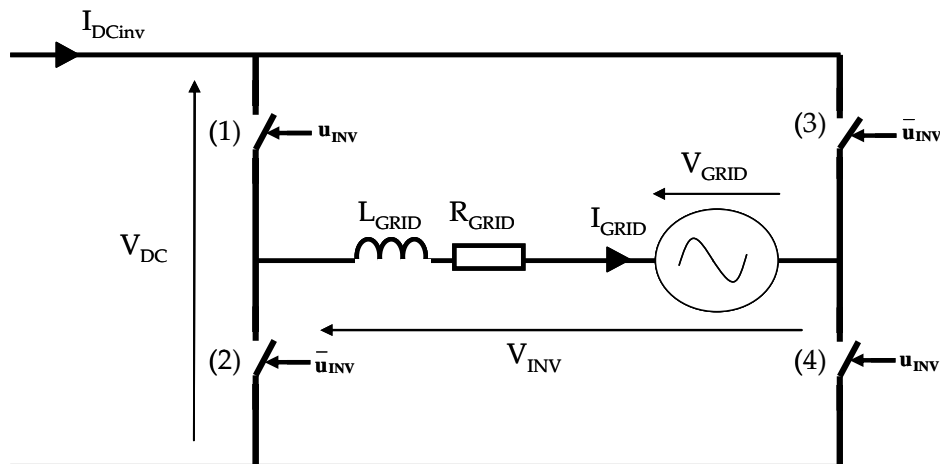


Figure IV.1 : Electrical scheme of a single phase grid-connected inverter

In this work, a single phase inverter using an H-bridge topology consisting of four ideal switches will be considered. The power losses generated during the switching and conduction will be calculated separately. An electrical diagram of the single-phase inverter is presented on before mentioned figure. The binary commutation function u_{INV} controls each switch by taking the value 1 when the switch is closed and -1 when the switch is open. The

top-left and bottom-right switches of the inverter are controlled by u_{INV} , whereas the two remaining switches are controlled by its complementary \bar{u}_{INV} in order to correctly invert the input DC voltage (V_{DC}) and current (I_{DCINV}). The switches are controlled with a duty cycle β_{INV} taking values in the $[-1,1]$ range, its explicit expression is presented on equation IV.1. The positive values of β_{INV} refer to operation of switches (1) and (4) while negative values are obtained when (2) and (3) operate simultaneously.

$$\beta_{INV} = \frac{1}{T_{PWM}} \cdot \int_{t-T_{PWM}}^t u_{INV}(\tau) \cdot d\tau \quad IV.1$$

Where, u_{INV} is the switch commutation function taking values in $\{-1,1\}$ and T_{PWM} is the pulse-width modulation period.

The average model equation describing the operation of the single phase inverter is presented on equation IV.2 where V_{DC} is the input voltage, V_{GRID} is the grid voltage, and I_{GRID} is the grid-fed current.

$$L_{GRID} \cdot \frac{dI_{GRID}}{dt} + R_{GRID} \cdot I_{GRID} = \beta_{INV} \cdot V_{DC} - V_{GRID} \quad IV.2$$

The grid inverter implementation into Simulink was achieved by using the Laplace transformation of the grid side filter. Hence, the grid-fed current can be expressed as a function of the duty cycle β_{INV} , the input voltage V_{DC} , the grid voltage V_{GRID} and grid impedance parameters L_{GRID} and R_{GRID} . The corresponding Simulink model is presented on Figure IV.2.

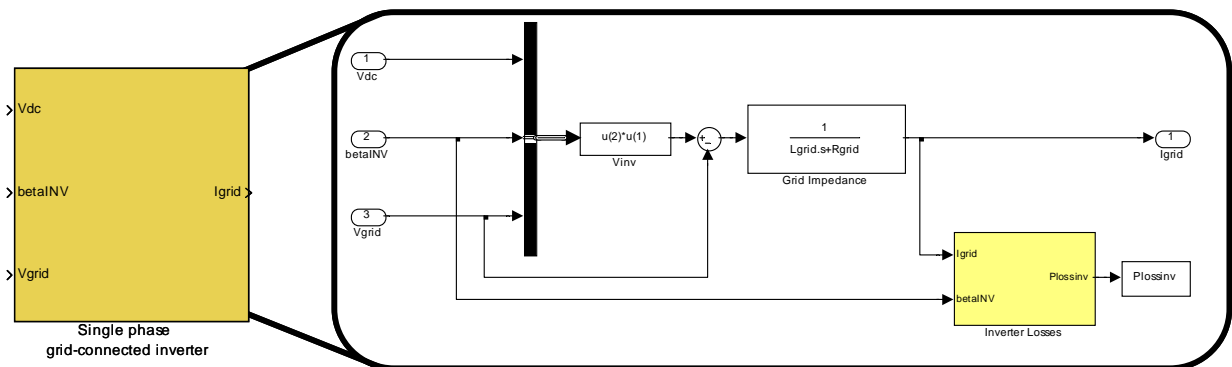


Figure IV.2 : Single phase grid-tied inverter Simulink model

An example comparing the exact and average inverter model is presented on Figure IV.3. In this example, the inverter operation has been simulated over one period. The grid-current average model, in red, corresponds to the average values of the exact model, in blue. The advantage of the average model is clearly visible by reducing the influence of the current harmonics to its fundamental component. Simulation results show that both the accuracy and dynamic behavior of the grid-fed current are conserved.

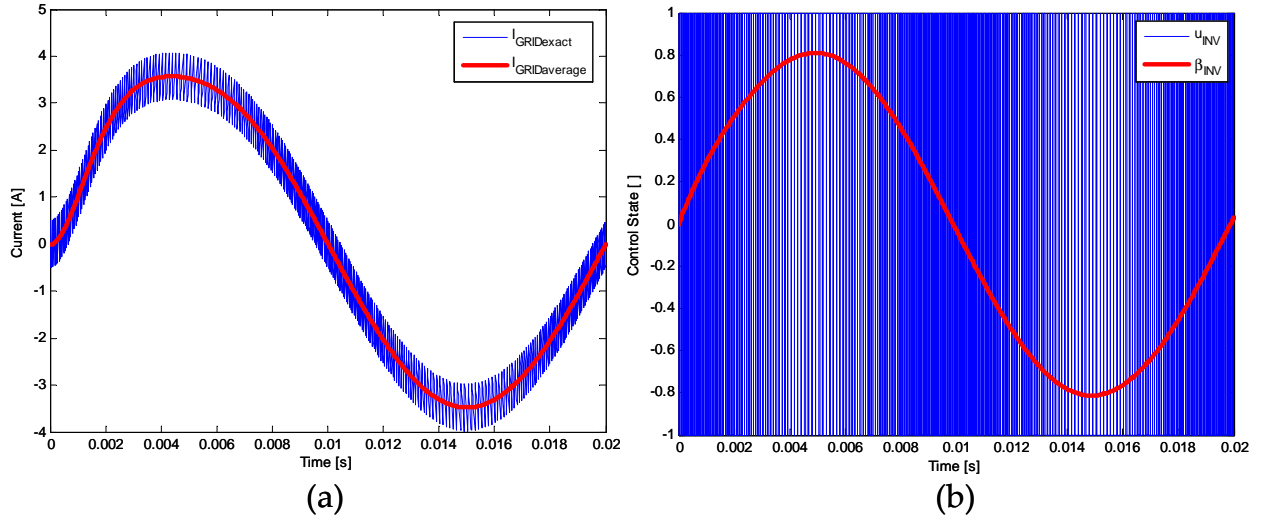


Figure IV.3 : (a) Exact and average models of single-phase inverter current and their (b) associated control

The following section will describe the DC-DC converter models used in this work: series-connected Boost, parallel-connected Boost, and Double Boost converters.

IV.1.2. Reduced average modelling of the DC-DC converter

The DC-DC converters concerned in this study are step-up voltage converters known as Boost converters. The Boost converter, presented on Figure IV.4, contains only one switch which is controlled by the commutation function u_{DC} taking values in the $\{0,1\}$ set depending on the switch conduction state. As in the inverter average model, the electrical switch of the Boost converter uses a duty cycle α_{DC} . However, in this case the duty cycle is strictly positive in the $[0,1]$ range.

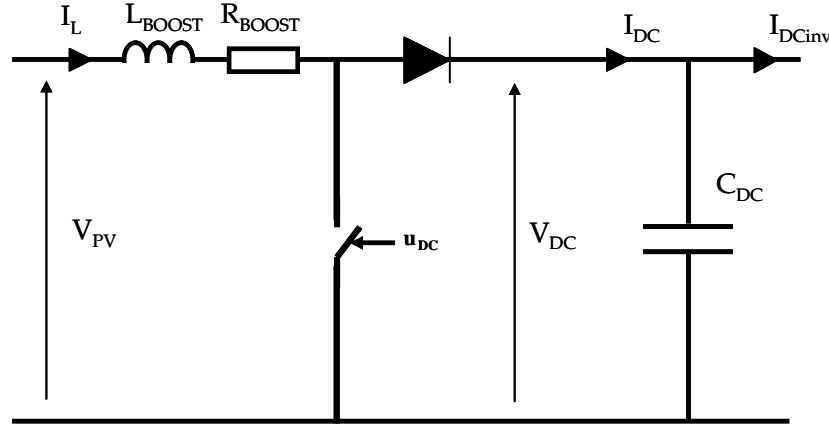


Figure IV.4 : Electrical scheme of Boost converter

The average modelling equations of the Boost converter are presented on equations IV.3 and IV.4

$$L_{BOOST} \cdot \frac{dI_L(t)}{dt} + R_{BOOST} \cdot I_L(t) = V_{PV}(t) - (1 - \alpha_{DC}(t)) \cdot V_{DC}(t) \quad IV.3$$

$$C_{DC} \frac{dV_{DC}(t)}{dt} = (1 - \alpha_{DC}(t)) \cdot I_L(t) - I_{DCinv}(t) \quad IV.4$$

By considering the control of the input current I_L to have a fast response time, the

previous equations can be simplified into equations IV.5. Indeed, by supposing the control rapid with respect to the other physical units of the converters, the current value I_L can be assimilated to the reference value I_L^* . For this reason, the Boost converter model is referred to a reduced average model.

$$R_{\text{BOOST}} \cdot I_L^*(t) = V_{\text{PV}}(t) - (1 - \alpha_{\text{DC}}(t)) \cdot V_{\text{DC}}(t) \quad \text{IV.5}$$

$$C_{\text{DC}} \frac{dV_{\text{DC}}(t)}{dt} = (1 - \alpha_{\text{DC}}(t)) \cdot I_L^*(t) - I_{\text{DCinv}}(t) \quad \text{IV.6}$$

Using equation IV.6, the Boost converter duty cycle can be expressed as a function of the PV array voltage V_{PV} , DC bus voltage V_{DC} , and the reference input current I_L^* as shown on equation IV.7. Thus, by replacing this last expression in equation IV.6, the DC bus voltage can be expressed as a function of the PV array voltage, reference input current, and the output current I_{DCinv} , as can be seen in equation IV.8. The DC bus voltage expression has been reduced to a first order system using the reduced average model.

$$\alpha_{\text{DC}}(t) = 1 - \frac{V_{\text{PV}}(t) - R_{\text{BOOST}} \cdot I_L^*(t)}{V_{\text{DC}}(t)} \quad \text{IV.7}$$

$$C_{\text{DC}} \cdot \frac{dV_{\text{DC}}(t)}{dt} = \frac{V_{\text{PV}}(t) - R_{\text{BOOST}} \cdot I_L^*(t)}{V_{\text{DC}}(t)} \cdot I_L^*(t) - I_{\text{DCinv}}(t) \quad \text{IV.8}$$

The Boost converter can either be connected in series or in parallel with other converters. The combination of the previous equations can lead to two modelling strategies when implemented in the simulation software depending on the desired output of the converter. When considering the series connected Boost converters, the input current is the same for each converter in the converter-string, therefore the voltage will be chosen as the output.

- **Series-connected Boost converter Simulink model**

As seen above, the output voltage of the Boost converter can be expressed as a function of the input voltage V_{PV} , the input current I_L , and the output current as presented in equation IV.9.

$$V_{\text{DC}} = \frac{1}{C_{\text{DC}}} \cdot \frac{1}{T} \cdot \int_0^T \left(\frac{V_{\text{PV}} - R_{\text{BOOST}} \cdot I_L^*}{V_{\text{DC}}} \cdot I_L^* - I_{\text{DCinv}} \right) dt \quad \text{IV.9}$$

Where V_{DC} is the output voltage, C_{DC} and R_{BOOST} are the Boost converter capacitor and resistance, T the computation period, and I_L and I_{DCinv} the input and output currents respectively. The corresponding Simulink model of the series-connected Boost converter is presented on Figure IV.5.

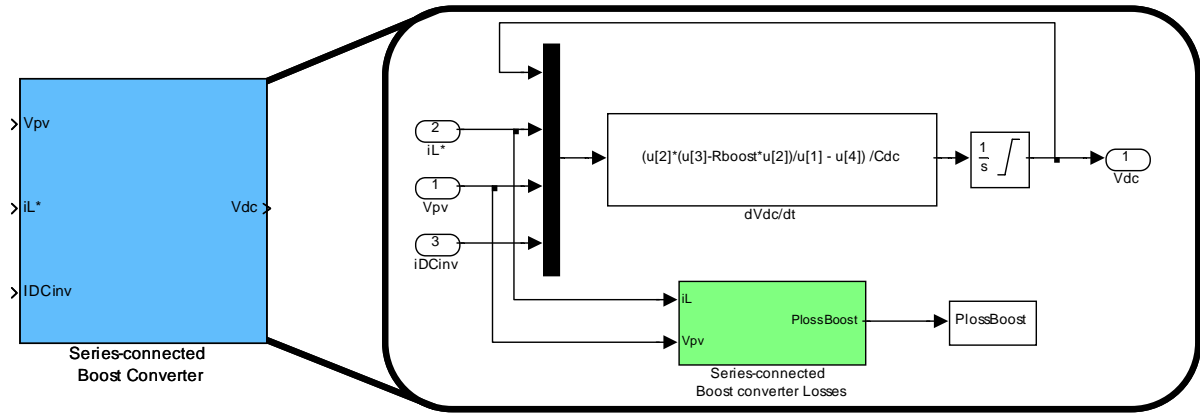


Figure IV.5 : Simulink model of series-connected Boost converter

▪ **Parallel-connected Boost converter Simulink model**

Contrary to series-connected boost converters where the output current is common to each converter within the same string, parallel-connected converters share the same output voltage. Therefore, the model must be adapted by considering an input DC bus voltage and an output DC bus current.

The output current of the Boost converter can be expressed as a function of the input voltage V_{PV} , the input current I_L^* and the output voltage V_{DC} as shown in equation IV.10.

$$I_{DCinv} = \frac{V_{PV} - R_{BOOST} \cdot I_L^*}{V_{DC}} \cdot I_L^* - C_{DC} \cdot \frac{dV_{DC}}{dt} \tag{IV.10}$$

The corresponding Simulink model to the previous equation is presented on Figure IV.6. Power conversion losses remain calculated in the same manner as previously, since only the converter input values are required.

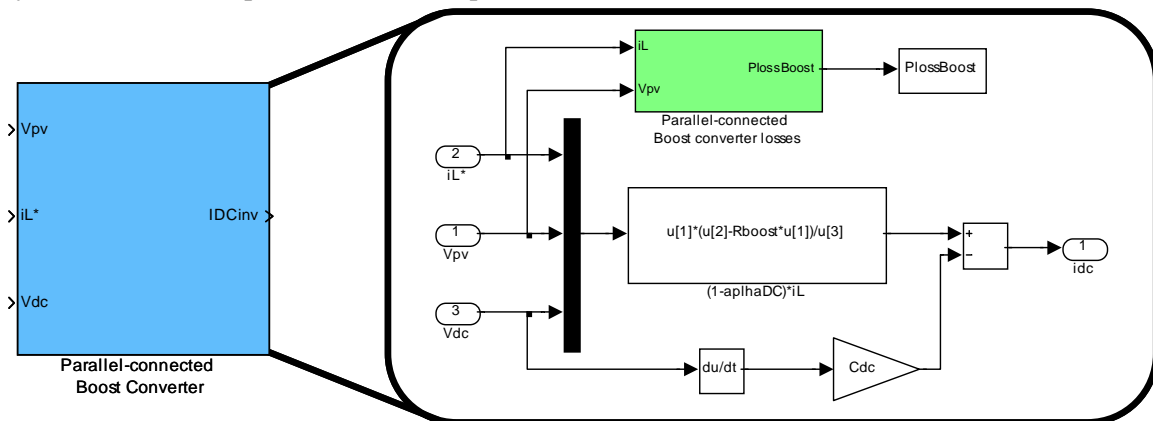


Figure IV.6 : Simulink model of parallel-connected Boost converter

▪ **Double Boost converter Simulink model**

Module inverter and multi-module topologies require a high voltage elevation ratio. For instance, the ratio may reach up to eight, considering modules with maximum power point voltages at 50 V and an output voltage of 400 V to correctly meet voltage inversion requirements. Since real Boost converters cannot attain such ratios in one single stage with

acceptable losses (ie. less than 2%), a Double Boost converter has been used to fulfill this task. A double-boost converter consists in using two consecutive Boost converters as shown in Figure IV.7.

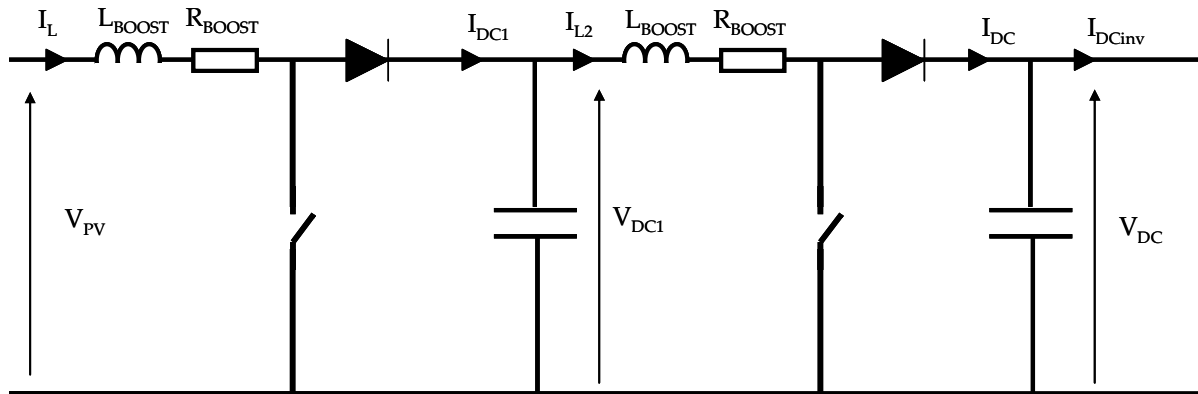


Figure IV.7 : Electrical scheme of Double Boost converter

Following laboratory internal studies, the maximum efficiency is reached for an intermediate bus voltage (V_{DC1}) which has been set to 100 V. The Simulink models previously described remain valid since the reduced average model does not take into account the voltage ratio limits. However, the power losses in the Double Boost converter must be adapted. The power losses are determined by adding the losses of both Boost converters and taking into account their different voltage and current ratings. These will be presented in the next section.

IV.1.3. Power conversion losses modeling

The losses in power converters are generated by switching devices, diodes and passive components. In this study, commercial power electronic products have been selected for the topologies that will be studied: centralized inverter, string inverter, multi-string inverter, module inverter, parallel-connected and series-connected DC-DC converter. The power electronic components sizing has been carried out for a 3 kW_p PV array. A synoptic table of the components used in each topology is presented Table IV.1. The corresponding datasheet values of these components have been transcribed in Annex 10.

The calculation of power losses for power electronic components depends on the nature and technology of the component, in our case three components are employed: IGBT switches, MOSFET switches and diodes.

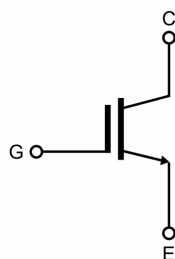
The power supply required for the control circuit in each converter has been considered constant, accounting for 5 W, based on an analysis of several commercial inverter datasheets. The average control circuit consumption ranges from 1 W, in standby operation, up to 20 W in normal operation depending on the power rating of the inverter. However, energy losses due to inductances have not been taken into account.

PV System Topology	Power Rating	Device	Component	Product	Max. Voltage [V]	Max. Current [A]
Centralized Inverter	30 kW	Boost Converter	Switch	IGBT-SKM 195GB066D	600	150
			Diode	150K60	400	150
		Inverter	Switch	IGBT-SKM 195GB066D	600	150
	3 kW	Boost Converter	Switch	IGBT-IRGB4062DPbF	600	24
			Diode	15ETH06	400	15
		Inverter	Switch	IGBT-IRGB4062DPbF	600	24
String Inverter	30 kW	Boost Converter	Switch	IGBT-IRGB4060DPbF	600	8
	3 kW		Diode	15ETH06	400	15
		Inverter	Switch	IGBT-IRGB4060DPbF	600	8
Multi-String Inverter	30 kW	Boost Converter	Switch	IGBT-IRGB4060DPbF	600	8
			Diode	15ETH06	400	15
	30 kW	Inverter	Switch	IGBT-SKM 195GB066D	600	150
	3 kW	Inverter	Switch	IGBT-IRGB4062DPbF	600	24
Parallel-connected DC-DC converters	30 kW	Double-Boost Converter 1st level	Switch	MOSFET-SiHF640	200	11
			Diode	MBR10200CT	200	10
	3 kW	Double-Boost Converter 2nd level	Switch	IGBT-IRGB4060DPbF	600	8
			Diode	15ETH06	400	15
	30 kW	Inverter	Switch	IGBT-SKM 195GB066D	600	150
	3 kW	Inverter	Switch	IGBT-IRGB4062DPbF	600	24
Series-connected DC-DC converters	30 kW	Boost Converter	Switch	MOSFET-SiHF640	200	11
			Diode	MBR10200CT	200	10
	30 kW	Inverter	Switch	IGBT-SKM 195GB066D	600	150
	3 kW	Inverter	Switch	IGBT-IRGB4062DPbF	600	24
Module Inverter	30 kW	Double-Boost Converter 1st level	Switch	MOSFET-SiHF640	200	11
			Diode	MBR10200CT	200	10
	3 kW	Double-Boost Converter 2nd level	Switch	IGBT-IRGB4060DPbF	600	8
			Diode	15ETH06	400	15
		Inverter	Switch	IGBT-IRGB4059DPbF	600	4

Table IV.1 : Components used for power converter loss calculations

IV.1.3.1. Power losses in IGBT switches

Insulated Gate Bipolar Transistor (IGBT) switches have been used in power converters requiring high voltage ratings. IGBTs are composed of three connection terminals: gate, collector and emitter. As in all switches, two types of power losses are generated during operation: conduction and switching losses.



Parameter	Physical Unit
$V_{CE0} (@0 A)$	[V]
R_{CE}	[Ω]
E_{ON}	[J]
E_{OFF}	[J]
V_{REF}	[V]
I_{REF}	[A]

Figure IV.8: (left) electrical scheme of IGBT and (right) parameters for power loss calculations obtained in datasheets

Conduction losses are caused by switch voltage drop and resistance of the closed switch, whereas switching losses refer to those produced during the transition between open and closed states of the switch. The parameters permitting the calculation of mismatch losses

can be directly read from the component datasheet or can be deduced from them (such as V_{CE0}).

The conduction losses are determined by modelling the closed switch as a voltage source (V_{CE0}) with a series connected resistance (R_{CE}). The power dissipated by conduction over one cycle is presented in equation IV.11 [DAN'06][GRA'09].

$$P_{IGBTcond} = \frac{1}{T} \int_0^T (V_{CE0}(t) \cdot I_{SW}(t) + R_{CE} \cdot I_{SW}^2(t)) \cdot dt = V_{CE0} \cdot I_{SWEFF} + R_{CE} \cdot I_{SWRMS}^2 \quad IV.11$$

where I_{SW} is the current flowing through the switch, V_{CE0} is the collector-to-emitter saturation voltage, R_{CE} is the collector-to-emitter resistance, and T the computation period.

In the case of inverter, power losses can be expressed as a function of the duty cycle (β_{INV}) and the RMS grid current (I_{GRID}) as shown in equation IV.12.

$$P_{IGBTcond} = |\beta_{INV}| \cdot (V_{CE0} \cdot I_{GRID} + R_{CE} \cdot I_{GRID}^2) \quad IV.12$$

In the case of Boost converter, power losses can be expressed as a function of the duty cycle (α_{DC}) and the input current (I_L) as shown in equation IV.13.

$$P_{IGBTcond} = \alpha_{DC} \cdot (V_{CE0} \cdot I_L + R_{CE} \cdot I_L^2) \quad IV.13$$

Switching losses in IGBTs are calculated using dissipated energy values during both on and off phases of the switching. Datasheets provide both dissipated energy values (E_{ON} and E_{OFF}) at given voltage (V_{REF}) and current (I_{REF}) ratings. These values depend on the voltage at the switch terminals (V_{SW}). By considering the energy dissipation to vary linearly with the power flow and switching frequency (f), we obtain equation IV.14 [BAS'01].

$$P_{IGBTsw} = (E_{ON} + E_{OFF}) \cdot \frac{(V_{SW} - V_{CE0}) \cdot I_{SW}}{V_{REF} \cdot I_{REF}} \cdot f \quad IV.14$$

In the case of inverter, power losses can be expressed as a function of the DC bus voltage (V_{DC}), and the RMS grid current (I_{GRID}) as shown in equation IV.15.

$$P_{IGBTsw} = (E_{ON} + E_{OFF}) \cdot \frac{(V_{DC} - V_{CE0}) \cdot I_{GRID}}{V_{REF} \cdot I_{REF}} \cdot f \quad IV.15$$

In the case of Boost converter, switching losses can be expressed as a function of the duty cycle (α_{DC}), the DC bus voltage (V_{DC}) and the input current (I_L) as shown in equation IV.16.

$$P_{IGBTsw} = (E_{ON} + E_{OFF}) \cdot \frac{(V_{DC} - V_{CE0}) \cdot \alpha_{DC} \cdot I_L}{V_{REF} \cdot I_{REF}} \cdot f \quad IV.16$$

As can be seen on Figure IV.8, the IGBT packs contain reverse diodes. The power losses calculation of these diodes will be dealt with later in this section.

IV.1.3.2. Power losses in MOSFET switches

Metal Oxide Semiconductor Field Effect Transistors (MOSFETs) use a different technology than the previously described systems and were chosen to be implemented for lower voltage power conversion. MOSFETs contain three terminals for power flow and switch state control: drain, gate and source as presented on Figure IV.9

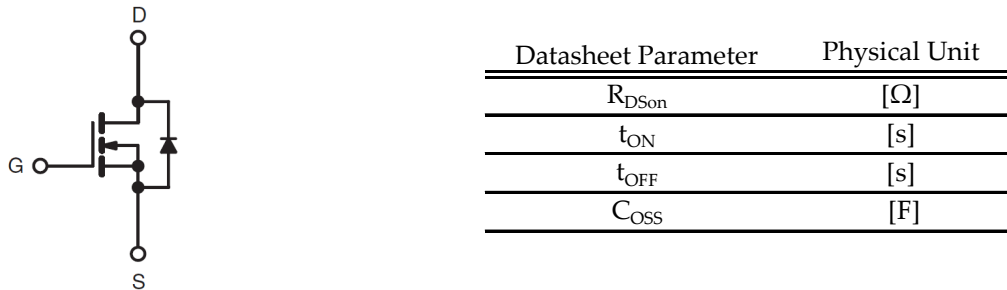


Figure IV.9: (left) electrical scheme of MOSFET and (right) parameters for power loss calculations obtained in datasheets

In this study the MOSFET switches are used in the low-voltage elevation for series Boost chopper and the 1st stage of the Double Boost chopper. Conduction losses can be expressed as a function of the drain-to-source resistance (R_{DSon}), the chopper duty cycle (α_{DC}), and the input current (I_L) as seen on equation IV.17 [GRA'06].

$$P_{MOSFETcond} = R_{DSon} \cdot \alpha_{DC} \cdot I_L^2 \quad IV.17$$

The switching losses in a MOSFET switch are calculated considering the reverse diode to be of Schottky technology, this prevents current overlap [DAN'06] during the transition between on and off states. Hence, switching losses can be expressed as a function of the voltage of output voltage (V_{DC1}), current flowing through the switch (I_{SW}), the switching frequency (f) and parameters available on component datasheets..

$$P_{MOSFETsw} = f \cdot \left(\frac{V_{DC1} \cdot I_{SWon} \cdot t_{on}}{2} + \frac{V_{DC1} \cdot I_{SWoff} \cdot t_{off}}{2} + \frac{C_{oss} \cdot V_{DC1}^2}{2} \right) \quad IV.18$$

In the case of the Boost converter, the expressions of I_{SWON} and I_{SWOFF} depend on the input current I_L , the duty cycle α_{DC1} , the input voltage V_{PV} , the inductance (L_{BOOST}) and the switching frequency, as can be seen in equations IV.19 and IV.20 [GRA'06].

$$I_{SWon} = I_L + \frac{\alpha_{DC1} \cdot V_{PV}}{f \cdot L_{BOOST}} \quad IV.19$$

$$I_{SWoff} = I_L - \frac{\alpha_{DC1} \cdot V_{PV}}{f \cdot L_{BOOST}} \quad IV.20$$

The last source of losses in power electronic devices is diodes that can be used alone or in association with IGBT.

V.1.3.3. Power losses in diodes

The diodes considered in this study are mostly Schottky diodes that prevent current overlap during the on and off switch states. Therefore, the switching losses are considered negligible and will not be calculated in this work. Conduction losses in diodes can be determined using the parameters from datasheets, as shown on Figure IV.10.

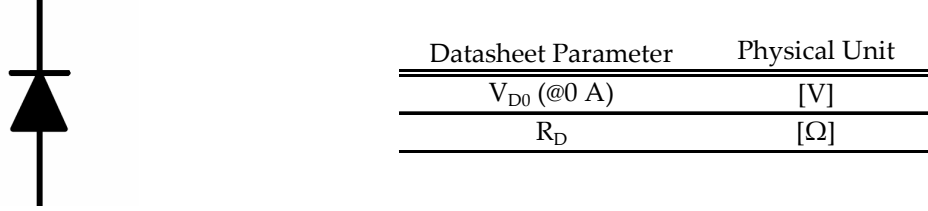


Figure IV.10: (left) electrical scheme of diode and (right) parameters for power loss calculations obtained in datasheets

In the case of the Boost converter, conduction losses for diodes can be expressed as functions of the duty cycle (α_{DC}), the input current (I_L), and datasheet parameters [BAS'01].

$$P_{D_{cond}} = V_{D0} \cdot (1 - \alpha_{DC}) \cdot I_L + R_D \cdot (1 - \alpha_{DC}) \cdot I_L^2 \quad IV.21$$

The power losses are then calculated for each converter depending on their type, inverter or DC-DC converter and rated power using the equations previously presented. The Simulink blocksets for each converter have been built to determine the power loss values considering: the switch technology, quantity of switches used per converter, duty cycle, current values and datasheet parameters.

After having presented the power converter models and their associated power losses that will later be used in Chapter V, the control strategies of the power conversion units of PV systems need to be described.

IV.2. Control strategies for PV power converters

The photovoltaic energy conversion chain consists in converting the DC power from the solar array into AC power that fulfills grid requirements such as: voltage, frequency, grid-fed power, and total harmonic distortion levels. The first conversion stage uses a DC-DC converter to extract the maximum power from the solar array through maximum power point tracking (MPPT) algorithms. The extracted DC power is then converted into AC power by the means of an inverter. A synoptic diagram of the entire power conversion chain is presented on Figure IV.11.

In this work, the energy from the PV array is entirely fed to the grid, power losses aside, the DC-DC converter's task consists in extracting the PV array maximum power current regardless of the DC bus voltage V_{DC} . The DC bus voltage is controlled by the inverter through the continuous current $I_{DC_{inv}}$ that is withdrawn from the DC bus capacitor C_{DC} . Additionally, the inverter must inject sinusoidal current I_{GRID} to the utility-grid, with an RMS value corresponding to an image of the continuous input current. A reactive component may also be added to the grid-fed current, however in this work only active power is transmitted to the utility-grid. The reactive power feeding function is

completely dissociated from the continuous power level and should be implemented in the current inversion control stage.

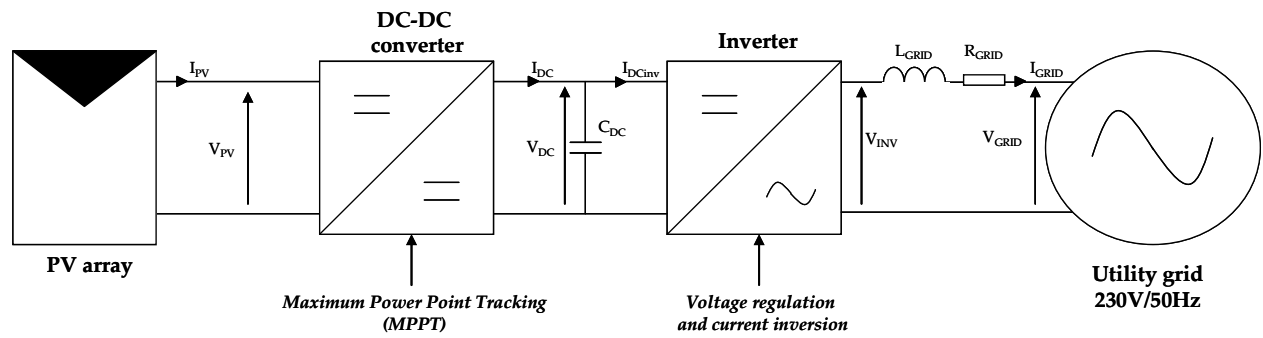


Figure IV.11 : Diagram of grid-connected PV plant

The control strategy for PV conversion must fulfill three main functions: current inversion, DC bus voltage regulation, and MPPT. The dynamics of the multiple converter system must also be taken into account in order to ensure correct operation of the global PV system. The control strategy proposed in this study will be presented starting from the system with the fastest response time to the slowest one.

IV.2.1. Inverter control

The proposed inverter control strategy fulfills two functions: DC bus regulation and current inversion. In order to guarantee the stability of the system, the current must be inverted faster than the DC bus voltage. The DC bus voltage (V_{DC}) value is dependent of the amount of DC bus current to be extracted (I_{DCinv}). The inverter input current is then alternated using the power switches to meet grid code requirements. If the DC bus voltage had a faster dynamic than the current inversion process, the inverter would not be able to alternate the direct current by ensuring low harmonic distortion values.

IV.2.1.1. Current inversion control

The current inversion process is controlled by the means of a proportional-integral (PI) corrector for its simplicity of use and adaptable response time. The transfer function of the inverter and the PI controller loop are presented on Figure IV.12. In this stage, the DC bus voltage may be considered constant, and fixed to its reference value, since the dynamic of the current inversion control is much faster than the DC bus voltage control.

The parameters of the PI controller are determined using the grid impedance values and a desired time constant $\tau_i=10^{-5}$ s. The detailed calculations of the PI controller parameters K_i and K_{i1} can be found in Annex 11. An example of the controller performance is shown on Figure IV.13 in which the reference RMS grid current is subject to a step of 1 A at time 0.1 s. Simulation results show that the inverter current control adapts to its reference value accordingly.

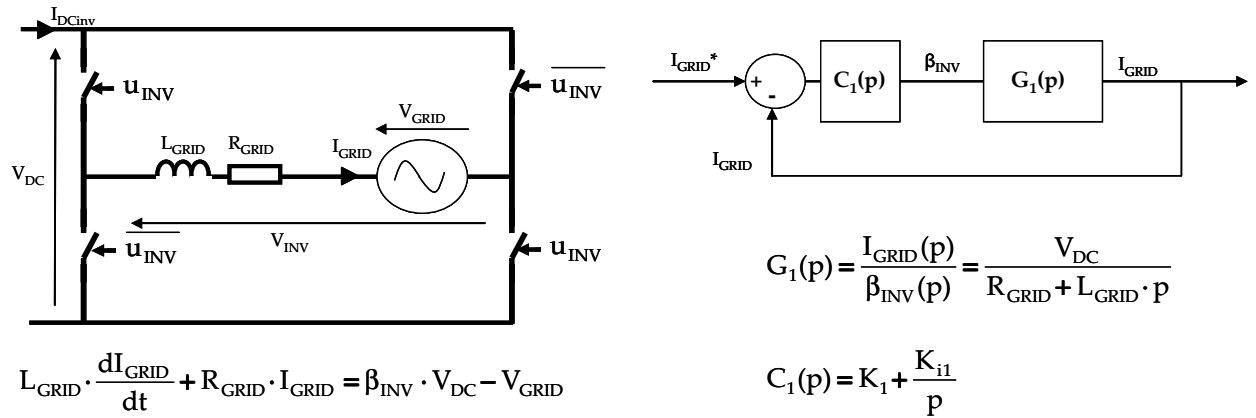


Figure IV.12 : (left) Electrical scheme of inverter with equations expressed in the time domain and (right) transfer function model of the inverter with its associated PI controller

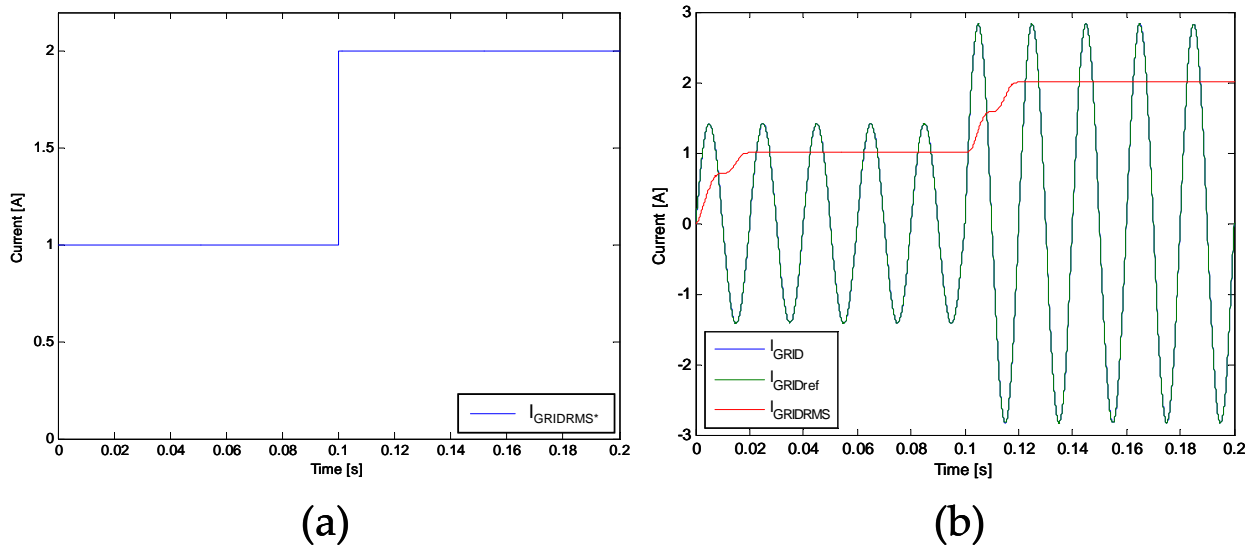


Figure IV.13 : Example of (a) increase of inverter input current and (b) grid-fed current I_{GRID} responding to a step in reference grid current I_{GRID}^* and its associated

Following the current inversion process, the second task of the grid-connected inverter is to control the DC bus voltage.

IV.2.1.2. DC bus voltage control

The strategy for controlling the DC voltage consists in modifying the value of the reference inverter input current to maintain the DC bus voltage at a reference voltage $V_{DC}^* = 400V$. This is achieved by determining the inverter input current (I_{DCinv}^*) to maintain the DC bus voltage at the reference value using PI controller C_2 , as shown on Figure IV.14. As detailed in Annex 11, the inverter response time is faster than the DC voltage bus control, therefore the closed-loop transfer function ($CLTF_1$) can be assimilated to a unitary gain.

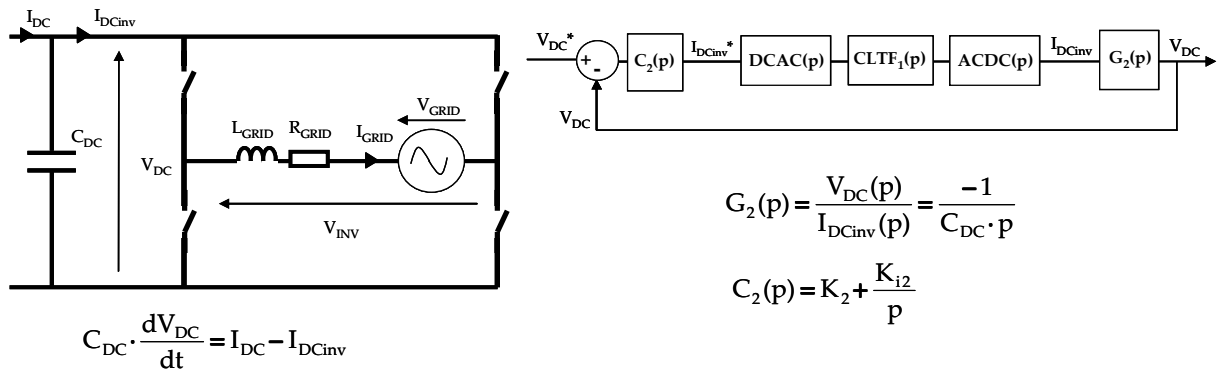


Figure IV.14 : (left) Electrical scheme of DC bus and inverter with equations expressed in the time domain (right) Transfer function modelling of the DC bus capacitor with its associated PI controller

As can be seen on Figure IV.14, an additional transfer function DCAC transforms the inverter input current reference into the grid-fed inverter reference current. This is done by using a Phased Locked Loop (PLL), which detects the grid phase, and power conservation equations. Inversely, the ACDC bloc uses the RMS value of the grid current while applying power conservation equations. The complete inverter control scheme, in Simulink format, is presented on Figure IV.15.

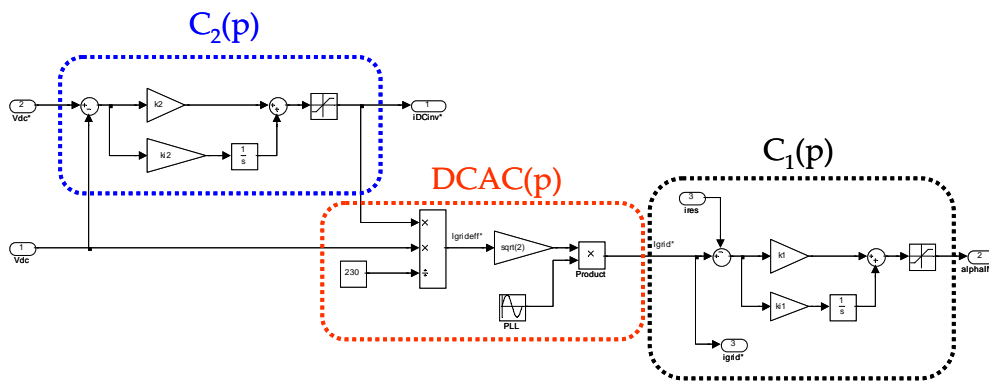


Figure IV.15 : Inverter control scheme fulfilling both DC bus and current inversion control

The DC bus voltage control strategy has been applied to the inverter using step DC bus voltage reference of 400 V that varies to 420 V at 0.25 s. Simulation results presented on Figure IV.16 show that the DC bus voltage quickly reaches its reference value with a small overshoot of approximately 3 V, well under the 5% threshold.

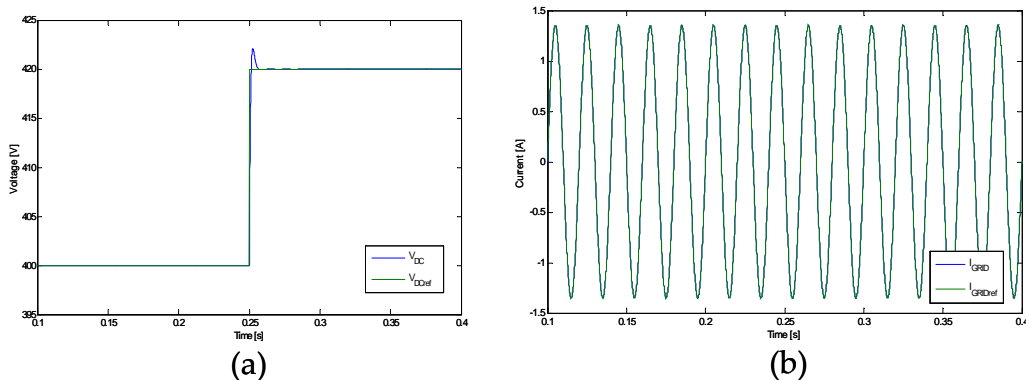


Figure IV.16 : (a) DC bus voltage control response to a DC bus voltage reference and the (b) corresponding grid-fed current

Furthermore, the grid-fed current is not affected by the DC bus voltage value modification, neither in amplitude nor in harmonic distortion. The performance of the inverter control for disturbance rejection can be seen on Figure IV.20. The DC bus voltage disturbances induced by the maximum point tracking algorithm due to the step reference voltage change are quickly rejected, these are visible on the figure by the impulses on the DC bus voltage on Figure IV.20(b).

IV.2.2. DC-DC converter control

The DC-DC converter control strategy consists in extracting the maximum power of the PV array by determining the optimal input voltage reference. The voltage reference is set by using a MPPT algorithm which tracks the evolution of the PV array power in order to find the optimal voltage reference.

Several MPPT algorithms can be found in literature: constant voltage tracking (CVT), perturb-and-observe (P&O) or hill-climbing, incremental conductance (INC), and extremum seeking control (ESC) methods [BRA'09][LI'09]. The most widespread method remains the P&O method where the derivative of the PV array power with respect to array voltage is compared until a sign change is detected. This method is also called the hill-climbing method since the MPPT algorithm acts like a climber on the power-voltage curve hill.

An example of the P&O MPPT is applied to a 3 kW_p array, the power-voltage curve and evolution of the PV array voltage can be seen on Figure IV.17. In this example, the algorithm is initiated at open-circuit voltage and progressively converges towards the power peak. The MPPT attains the maximum power point (MPP) of the array approximately ten seconds after the initial step. Once the MPP is attained, the PV array voltage oscillates around the MPP voltage. In this work, the MPPT algorithm used in all simulations will be P&O technique.

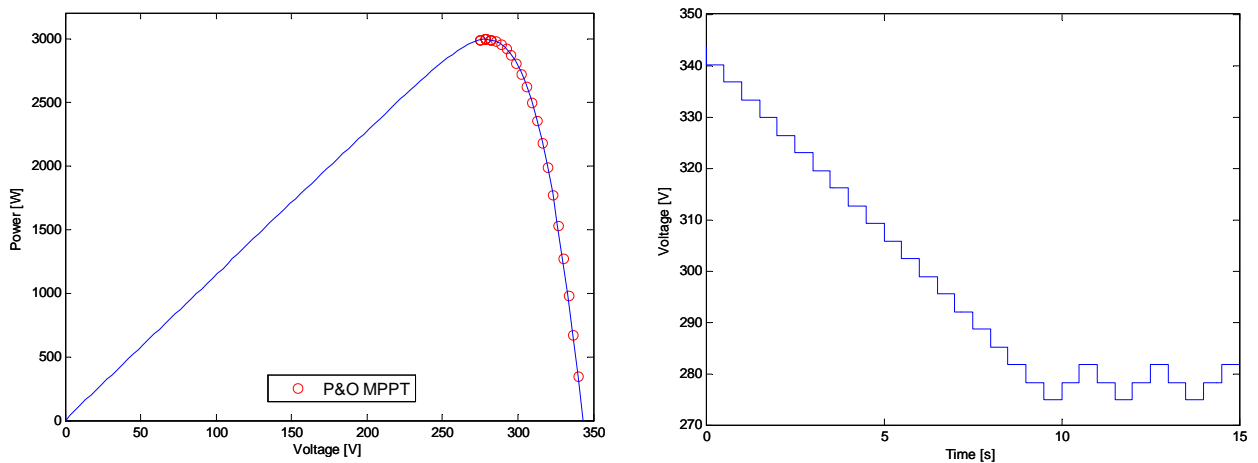


Figure IV.17 : (left) Power-voltage characteristic of a 3 kW_p array with P&O MPPT (right) evolution of P&O MPPT voltage

IV.2.2.1. Maximum Power Point Tracking implementation

The reduced-average model of the DC-DC converter assumes the dynamics of the input current (I_L) control to be instantaneous, hence its value is directly assimilated with the input reference current (I_L^*). The control scheme is therefore directly linked to the control of the input voltage (V_{PV}) as can be seen on Figure IV.18. Since, the Boost converter model contains the only dynamic that has been supposed instantaneous, as shown in equation (3), the Boost transfer function appears as a constant gain. Indeed, considering the dynamics of the system, the DC bus voltage control has a faster response time than the MPPT algorithm. Therefore, the DC bus voltage V_{DC} can be seen as a constant value with respect to the Boost converter control dynamics. The corrector coefficient calculations are detailed in Annex 11.

The entire DC-DC converter control strategy in Simulink model format is presented on Figure IV.19.

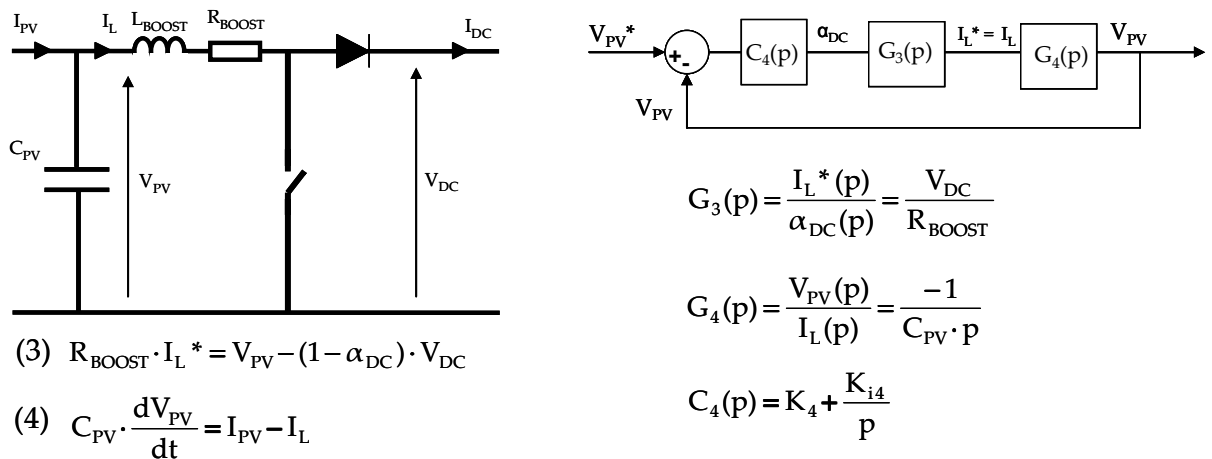


Figure IV.18 : (left) Electrical scheme of Boost converter with equations expressed in the time domain and (right) transfer function model of the Boost converter with its associated PI controller

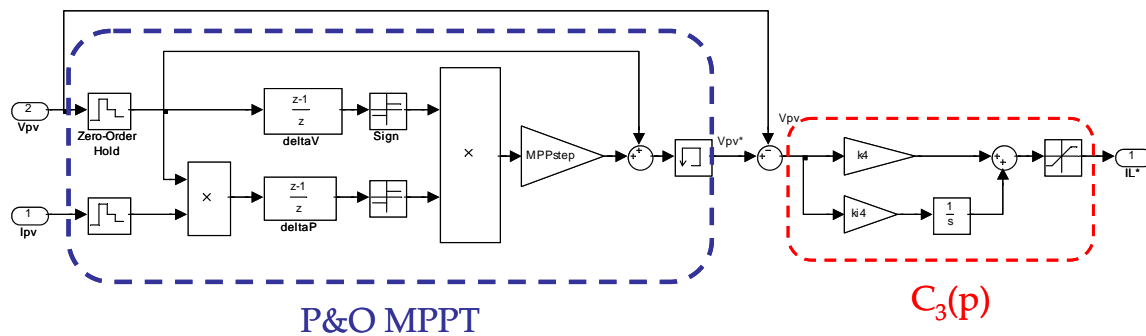


Figure IV.19 : Simulink model of DC-DC converter control scheme

The control scheme has been simulated on a grid-connected 3 kW_p array. Simulation results, presented on Figure IV.20, show the progressive increase of grid-fed current as the MPPT algorithm attains the PV array's maximum power point. Although the voltage reference variations are sharp, due to the non-linearity of the employed P&O MPPT algorithm, the DC bus voltage varies within an acceptable range of ± 1 V.

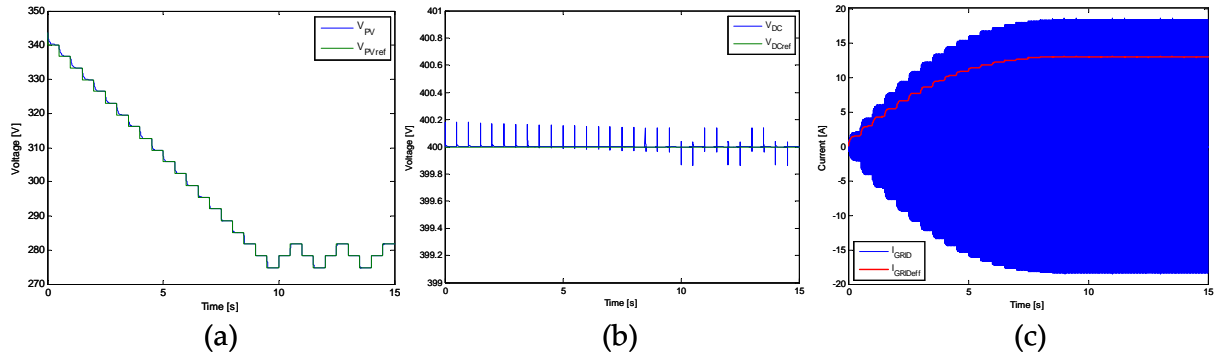


Figure IV.20 : Evolution of (a) PV array voltage, (b) DC bus voltage, and (c) grid-fed current of a 3 kW_p grid-connected PV plant

IV.2.2.2. Efficiency of MPPT algorithms

The efficiency of an MPPT algorithm can be defined as the ratio between the maximum power that can be extracted by the MPPT with respect to the maximum available power in the array. The purpose of this brief study is to show the importance of the precision of the algorithm and some drawbacks of traditional P&O method. The P&O MPPT is an iterative method which modifies the operation point of the PV array by analyzing the power derivative with respect to voltage at each iteration. Hence, the value of the voltage step can significantly impact the efficiency of the algorithm. A set of simulations on a 3 kW_p array, in three different shade scenarios, using three P&O tracking algorithms with different voltage steps ($0.01 \cdot V_{oc}$, $0.05 \cdot V_{oc}$, and $0.1 \cdot V_{oc}$) have been compared. The voltage steps have been chosen to be expressed in percentage of the open-circuit voltage (V_{oc}) in order to extrapolate results to arrays with different power ratings. The MPPT has been tested in non-shaded scenario mppt1 and partially shaded conditions: scenarios mppt2 and mppt3. The PV array considered in these simulations contains fifteen 200 W_p modules arranged in a 5x3 array. In shade scenario mppt2, one module of each string is shaded by 20%, whereas in shade scenario mppt3 the same modules are shaded by 80%. The P&O algorithm used initiates the process at a pre-determined voltage ($0.8 \cdot V_{oc}$) making it a hybrid version of traditional P&O algorithms and the constant voltage tracking (CVT) algorithm. Results of the MPPT algorithms in scenarios mppt1, mppt2, and mppt3 are presented on Table IV.2. The open-circuit (V_{oc}), maximum available power (P_{MAX}) from the array, and efficiency of the MPPT extraction have been added to the table for better comprehension.

	mppt1			mppt2			mppt3		
V_{oc} [V]	343,6			342,9			338,6		
P_{MAX} [W]	2991,8			2623,6			2327,7		
MPPT voltage step [V]	$0,01 \cdot V_{oc}$	$0,05 \cdot V_{oc}$	$0,1 \cdot V_{oc}$	$0,01 \cdot V_{oc}$	$0,05 \cdot V_{oc}$	$0,1 \cdot V_{oc}$	$0,01 \cdot V_{oc}$	$0,05 \cdot V_{oc}$	$0,1 \cdot V_{oc}$
MPP [W]	2991,8	2986,1	2986,1	2621,3	2618,7	2494,4	677,8	677,4	677,4
Efficiency	100,0%	99,8%	99,8%	99,9%	99,8%	95,1%	29,1%	29,1%	29,1%

Table IV.2 : Influence of MPPT voltage step in three different shade scenarios

In non-shaded conditions, the voltage step size does not significantly impact the efficiency of the algorithm. As expected, the smallest step size extracts the most power whereas the larger step sizes suffer losses, but are capable of extracting 99.8% of the PV array power. But, in partially shaded scenarios mppt2 and mppt3, the efficiency of the P&O MPPT can considerably decrease. In scenario mppt2, step sizes $0.01 \cdot V_{oc}$ and $0.05 \cdot V_{oc}$ obtain high efficiencies whereas for a step size of $0.1 \cdot V_{oc}$ only 95% of the PV array power can be extracted. In scenario mppt3, all three algorithms have poor efficiencies attaining 29.1%. To better understand these last results, the MPPT voltage evolution and associated power-voltage curve containing MPPT operating points for scenario mppt1 are presented on Figure IV.21 mppt1(a) and mppt1(b) respectively. Likewise, the power-voltage curves for scenarios mppt2 and mppt3 are displayed on the same figure.

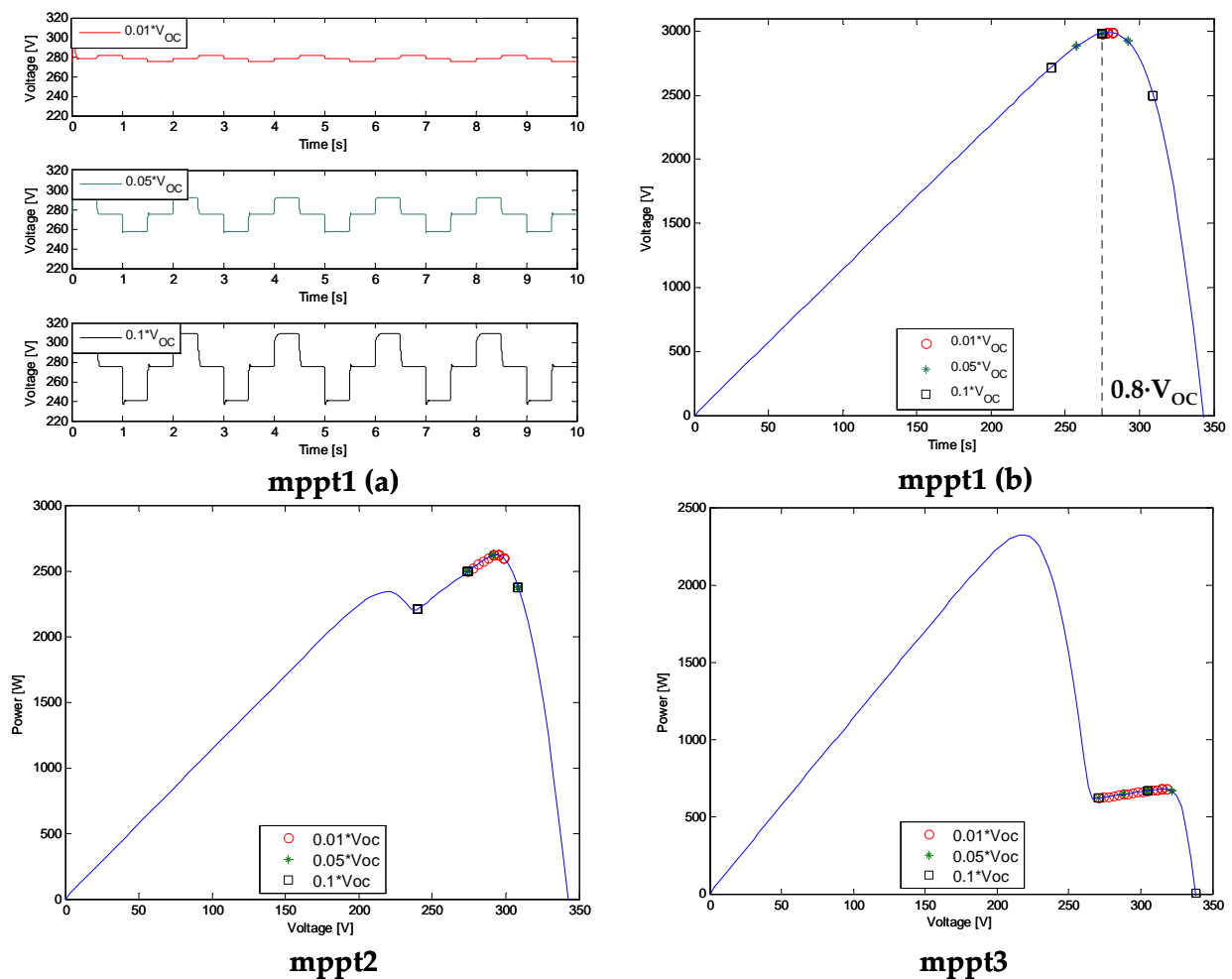


Figure IV.21 : Power-voltage characteristics for each scenario with the evolution of the PV array operating point for each MPPT step size

In scenarios mppt2 and mppt3, the P-V characteristics contain multiple peaks due to the partial shading of the array. In scenario mppt2, the global maximum is reached by the MPPT algorithm, yet for step-size $0.1 \cdot V_{oc}$ the peak summit is not reached due to its low precision, instead the algorithm oscillates around the peak. In scenario mppt3, the P&O MPPT reaches a local maximum, due to the initial voltage of the MPPT algorithm, rather than the global maximum. Consequently, low efficiencies are obtained regardless of the

voltage step value. Similar results may appear when an array is subject to abrupt environmental changes leading to slow response times to reach a new maximum.

As shown in the above results, high precision MPPT algorithms perform best. However, as precision rises the convergence speed decreases when considering a discrete system with a fixed time step. Another remaining problem is the wrong directionality in which the hill-climbing technique takes, as in scenario mppt3, resulting in convergence towards local maxima rather than the global maximum. Current research aims to solve these two defects by using variable step sizes [KAZ'09]. However, most of the existing PV systems are still equipped with P&O tracking systems making them vulnerable to partial-shading of the array.

These control strategies are directly applied to most of the system topologies that have been presented in Chapter I: centralized inverter, string and multi-string inverters, as well as parallel-connected DC-DC converters and module inverters. However, the control strategy for a series-connected DC-DC converter must dealt with separately.

IV.2.3. Series-connected DC-DC converter control strategy

The series-connected DC-DC converter system topology is composed of Boost converters that are assembled in strings and connected to a DC voltage bus, as presented below. Proper operation of such a configuration requires a unique current flow through the Boost converter string while maintaining a sufficient DC bus value in order to fit inverter requirements. To fulfill these conditions, the Boost converters need two operation modes: MPPT and DC bus voltage regulation. Moreover, several strings may be connected in parallel to the DC bus capacitor. In this study, a single series-connected DC-DC converter string will be described.

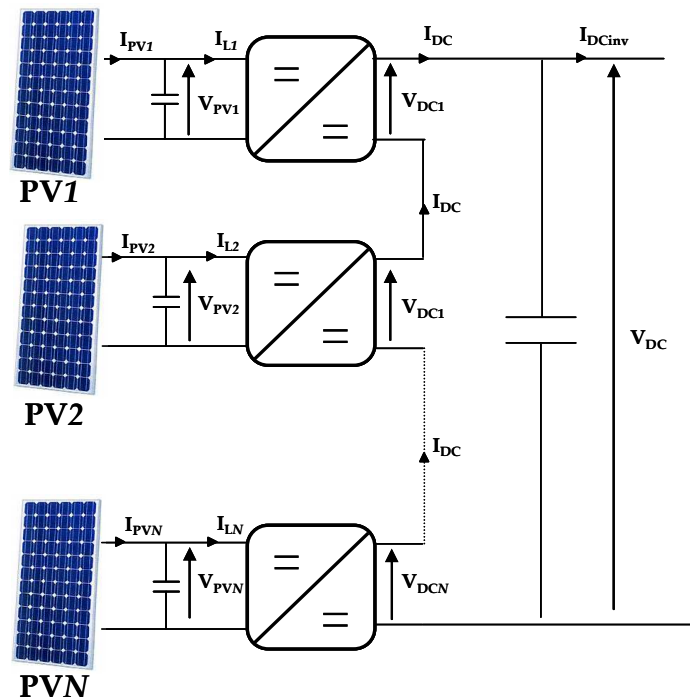


Figure IV.22 : Electrical scheme of series-connected DC-DC converter

The number of series-connected converters is directly linked to the required Boost voltage ratio in order to maintain a decent DC bus voltage. In normal operation, they participate equally to the string voltage. Hence, the output voltage of each Boost converter is V_{DC}/N . Consequently, the more converters are placed per string, the lower is the voltage ratio for each converter. Considering normal operation of the PV system, the Boost converters can fulfill both MPPT and maintain a sufficient DC bus voltage. However, in degraded mode operation (ie. partially shaded strings) the output voltage of the Boost converters may require an additional control strategy in order to limit over-voltage [BRA'10]. One way of managing degraded mode operation is to use an independent control strategy for each DC-DC converter. In this work, the Boost converters will use both MPPT and Output Voltage Control (OVC) as shown on Figure IV.23. The output voltage control limits the output voltage of the DC-DC converter to prevent over-voltages. The operation mode management is performed by a switch that triggers to OVC mode when the output voltage surpasses the $0.95 \cdot V_{DClim}$ threshold, otherwise the Boost converter operates in MPPT mode.

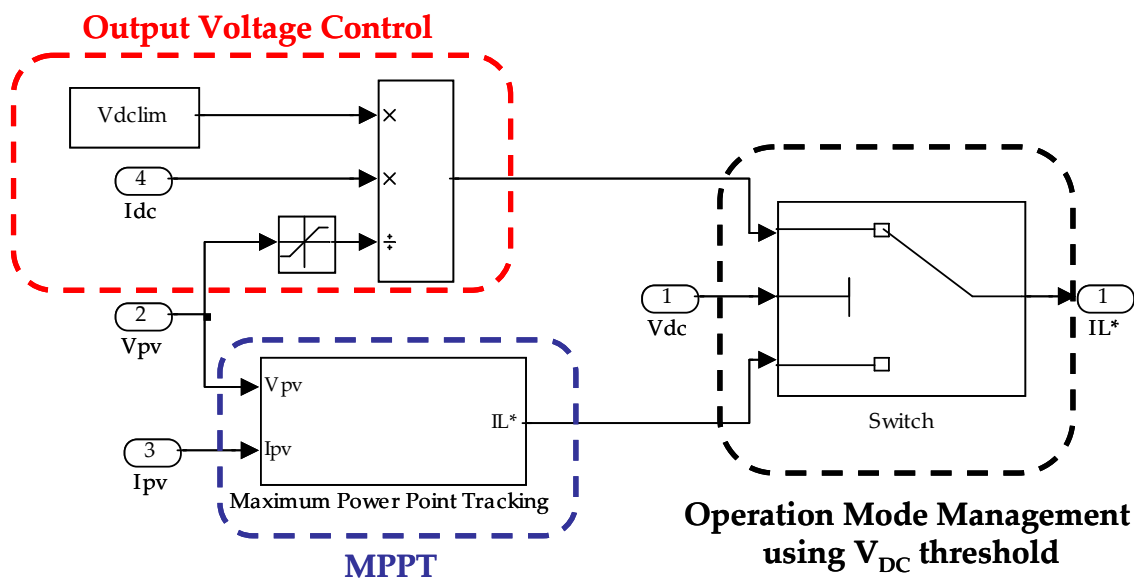


Figure IV.23 : Series-connected DC-DC converter control strategy

Although the independent control strategy is simple to implement, its efficiency is poor in degraded mode operation. The modules with the most available power, i.e. those which are non-shaded, will be the first to operate using the output voltage control. Since the available DC output power is directly proportional to the PV module power for each DC-DC converter and that the converters see the same output current flow, therefore the output voltage can be directly linked to the PV module power. Hence, PV modules with the most power will first be subject to voltage limitation.

Recent research on this configuration has lead to the development of a more optimal control strategy in which a supervisory algorithm is used to decide which operation mode is best suited for the DC-DC converters, while fitting voltage constraints, in order to extract the most power from the Boost converter string [BRA'10].

IV.2.3.1. Normal Operation Mode

In normal operating conditions, the PV modules are submitted to identical environmental conditions. The number of Boost converters per string has been determined in order to have small voltage transformation ratios for greater conversion efficiency. In this case, five converters have been inserted per string which leads to transformation ratio of 1.45 when the PV module operates at MPP (55 V) and the DC bus voltage is set to its nominal value of 400 V.

The simulation results presented below show that the MPPT algorithm progressively extracts more power from the modules, labelled PV1 to PV5, while maintaining the reference DC bus voltage. Normal operating conditions do not use the output voltage control. Therefore, all modules participate equally in maintaining the DC bus voltage. However, in degraded mode operation the output voltage limitation is necessary to prevent material over-voltage and to maintain grid-feeding conditions.

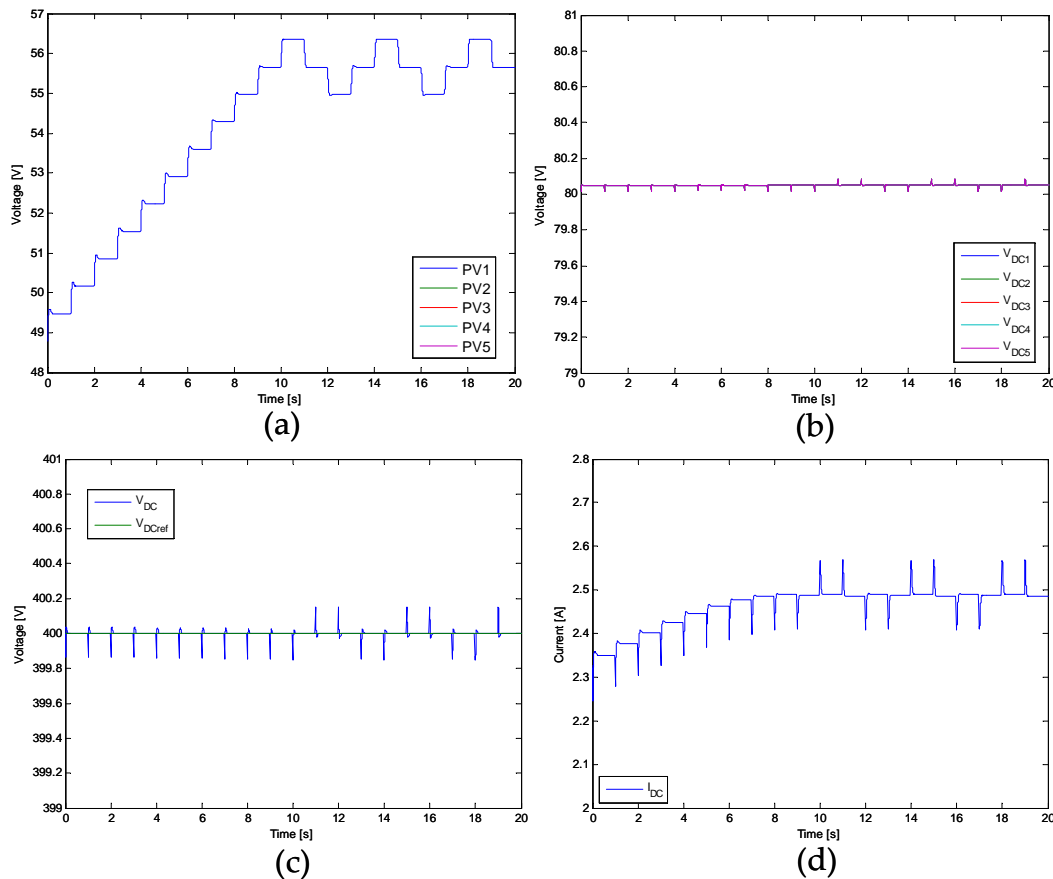


Figure IV.24 : Normal operation mode of series-connected DC-DC converter : (a) PV module voltages, (b) Boost converter output voltages, (c) DC bus voltage, and (d) Boost converter output current

The module-to-grid efficiency of the system reaches 95.8% in steady state conditions, which is greater than the multi-module topology, as will be seen in Chapter V. Indeed, the series connection of converters lessens the voltage ratio for each converter, thus lowering power conversion losses.

IV.2.3.2. Degraded Operation Mode

Occasionally, the PV array may be subject to heterogeneous environmental conditions leading to imbalances in the power delivered by each converter in the string. In such conditions, the MPPT control of the Boost converters may not be able to sustain the DC bus voltage to adequate levels for the inverter. Here, the DC-DC converter string is now submitted to partial shading, in which three PV modules PV1, PV2, and PV3 are shaded by 80%. These severe shade conditions enable both control strategies to operate simultaneously. As described earlier, the modules with the most available power (PV4 and PV5) are the first to switch to output voltage control, as can be seen on Figure IV.25(a), limiting the output voltage of the Boost converters to 120 V.

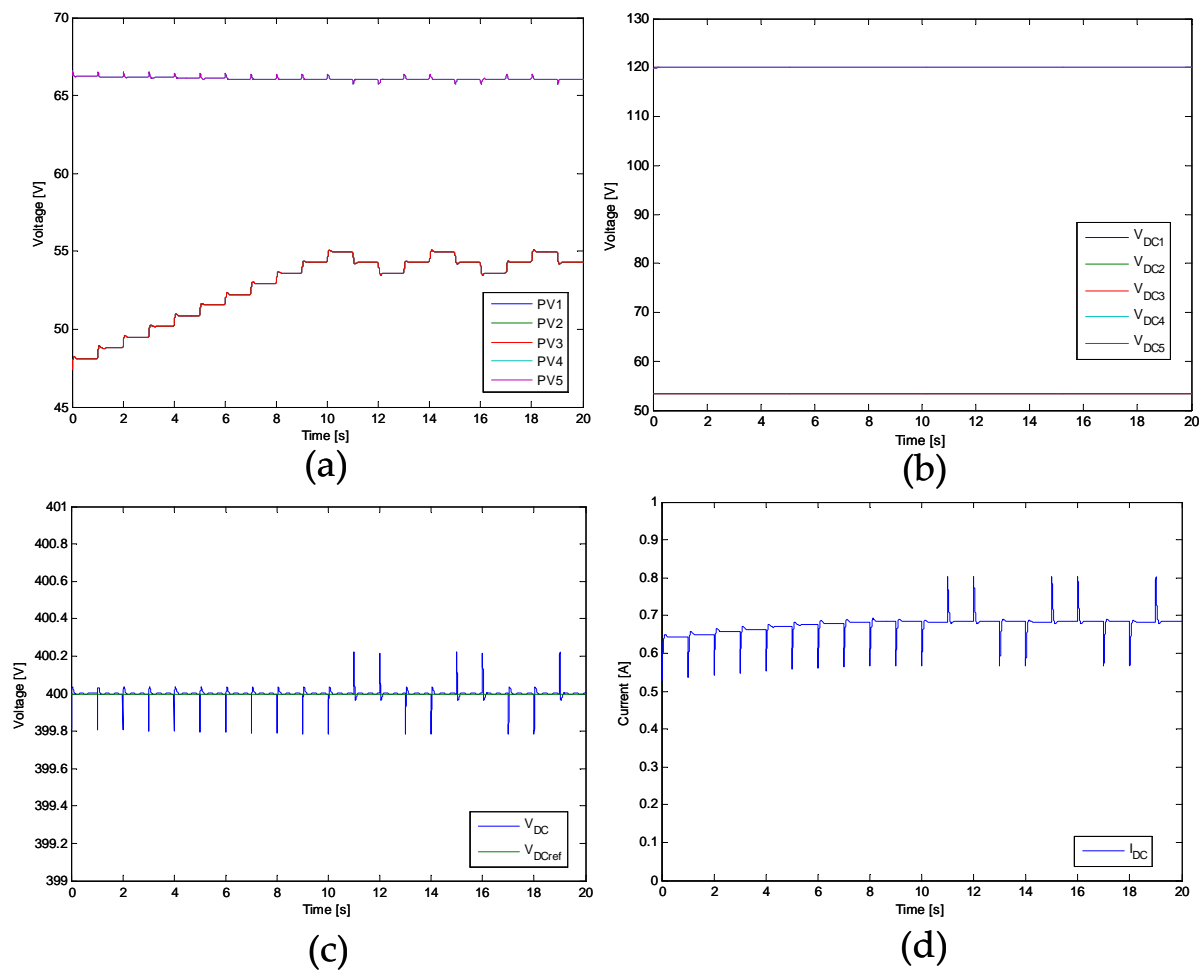


Figure IV.25 : Degraded operation mode of series-connected DC-DC converter : (a) PV module voltages, (b) Boost converter output voltages, (c) DC bus voltage, and (d) Boost converter output current

Using this dual operation mode control, the PV modules may continue to feed the grid in severe shade conditions. However, the overall efficiency of the system attains 50.9%. More intelligent systems, such as using a supervisor, could decide which converter switches to output voltage control in order to use the MPPT control for modules with the most power, rather than those with the least.

Conclusion

Average models of photovoltaic power conversion systems have been built to evaluate the performances of the proposed system topologies. Both inverter and DC-DC converter average models presented in this chapter will be used next for grid-fed power production comparison. Furthermore, the reduced average model of a Boost converter has been introduced in order to design control strategies by disregarding switching dynamics. A method for calculating power conversion losses in common power electronic devices based on real component datasheet values has been presented. Finally, the control strategies for photovoltaic power conversion units have been developed for each system topology.

In the next chapter, these power converter models and their associated control strategies will be applied to residential and commercial-sized PV arrays to evaluate their performances for reducing mismatch losses.

Chapter V

Analysis of PV system topologies

Introduction

During the design phase of grid-connected PV systems, several factors must be taken into account to choose the best suited topology such as power rating specifications and investment costs. Depending on the surrounding environment of the PV installation, the forecasted power production may be lower than expected when partial shading of the array occurs periodically. In this chapter, the impact of implementing power converters in the array to increase the power production in partially shaded scenarios will be studied and performances will be compared. Aside from power production, PV installation designers must take into account the investment costs, degraded mode operation performance and upgradeability of their systems to determine the optimal solar plant design. An evaluation tool, named topology grading method, that takes into account these later aspects has been developed to assist designers by attributing grades to topologies which best fulfill their needs. Finally, the topology grading method will be applied to residential and commercial-sized arrays in two exemplary cases.

V.1. Power production performance

The power converter models and their associated control strategies have been implemented into Simulink simulation software to study six system topologies: centralized inverter, string inverter, multi-string inverter, parallel-connected DC-DC converters, series-connected DC-DC converters and module inverter. In order to evaluate the interest of using alternative PV array topologies, both the SP and TCT array configurations will be considered in these simulations.

The power production of a residential (3 kW_p) and commercial (30 kW_p) grid-connected PV plant will be compared for six shade scenarios. The residential array is organized in a 5x3 array using 200 W_p modules, whereas the commercial one is arranged in a 5x30 configuration. Larger sized arrays (>200 kW_p) are not considered in this study for two main reasons: low probability of significant partial shading and prohibitive installation costs of multiple converters in utility-sized arrays.

The 3 kW_p and 30 kW_p PV arrays have been submitted to both non-shaded and partially-shaded conditions in order to determine the most performant PV system topology. In this first section, the performance of the array will be evaluated by the amount of grid-fed power for each topology. In the following sections, the overall performance will take into account the additional factors presented in Chapter I.

The new shade scenarios, shown on Figure V.1, illustrate mild and severe shading of the array.

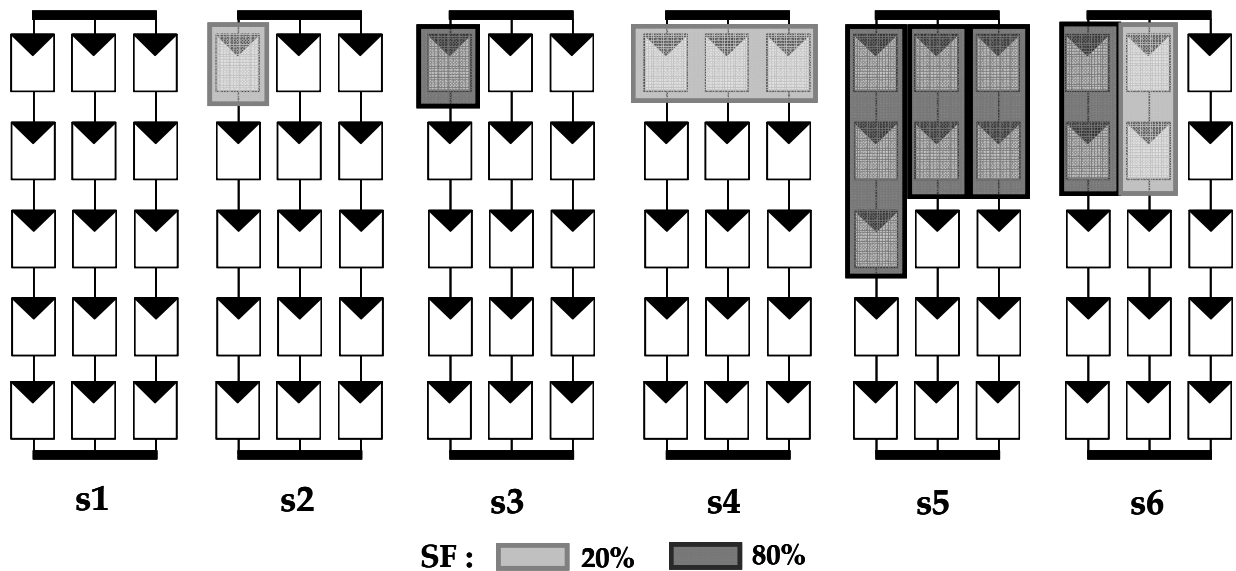


Figure V.1 : Diagram of shade scenarios for PV system topology comparison for a residential 3kW_p array.

In shade scenarios s2 and s3, one module per string is shaded on one third of the total number of strings in the array. In other words, the residential installation will have one shaded module, whereas the commercial plant will have 10 shaded modules scattered onto 10 different strings. These last scenarios differ by the intensity of the shaded module: 20% shade factor for s2 and 80% shade factor for s3. The reason for using a different number of shaded modules for the 3 kW_p and 30 kW_p is to compare them using equivalent shade

scenarios with respect to the shaded portion of the array. Should one module be shaded in both arrays, the impact of the shaded module in the commercial array would be insignificant considering the power rating. Shade scenarios s4 and s5 represent the worst case scenario for mismatch losses (cf. §III.2.3.3.) for a shade factor of 20% and 80% respectively. Finally, shade scenario s6 contains two-shaded modules per string on two-thirds of the total number of strings. Two different shade factors have been used to illustrate the effect of object shading, where modules close to an object are severely shaded, while modules far from the opaque object have lower shading factors. Although, this last shade scenario is more appropriate for residential installations, due to a nearby chimney, tree, or house, it may apply to commercial arrays due to nearby building shadows. Furthermore, in the following simulation results the MPPT algorithms have been optimized in order to extract the most available power, i.e. the additional losses due to MPPT inefficiency have not been considered in this work.

V.1.1 Residential PV systems

The portion of grid-connected PV power originating from residential installations is disparate throughout the world and can be closely linked to national renewable energy policies. In France, the majority of grid-connected systems have power ratings under 3kW_p , as it can be seen on Figure V.2, representing approximately 40% of the installed PV power. Residential installations are the most vulnerable to partial shading due to unmovable objects from the surrounding environment that induce shade (nearby trees, antennas, chimney, etc.).

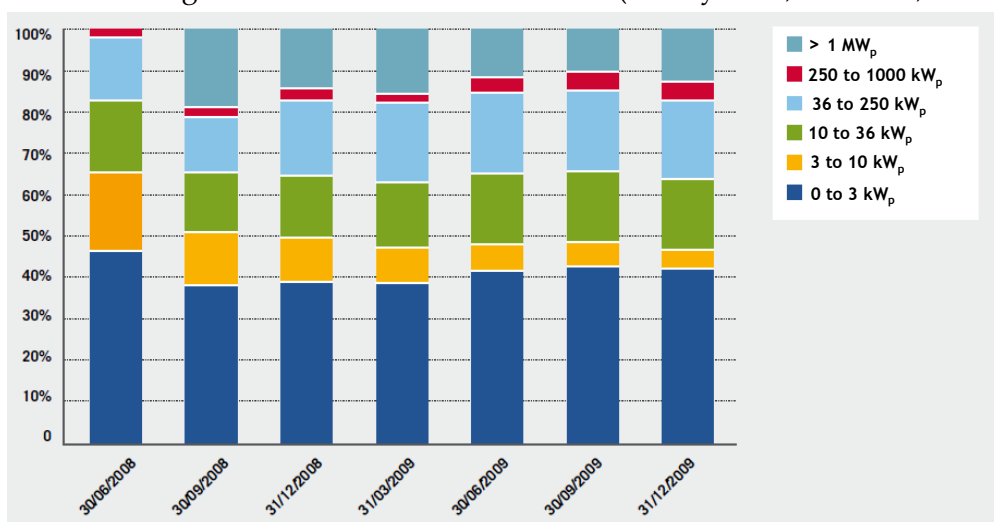


Figure V.2 : Distribution of grid-connected PV installations according to power rating in France [SER'10]

For this reason, the performances of alternative PV system topologies have been compared in the previously described shade scenarios; results are presented on Figure V.3.

In shade scenario s1, the centralized and string inverter topologies obtain the best results since power losses due to PV power extraction and transformation are lower in large power conversion units than in modular converters. Hence, centralized topologies should be favoured when arrays are mostly subject to normal operating conditions. However, in shade scenario s2 the power production gap between centralized and modular topologies decreases. In severe shaded conditions, the order is inverted and modular configurations are able to produce more power despite the low efficiencies of the system. The string oriented

systems obtain the best performances when a small portion (here 1/3 of the total array surface) is mildly and severely shaded.

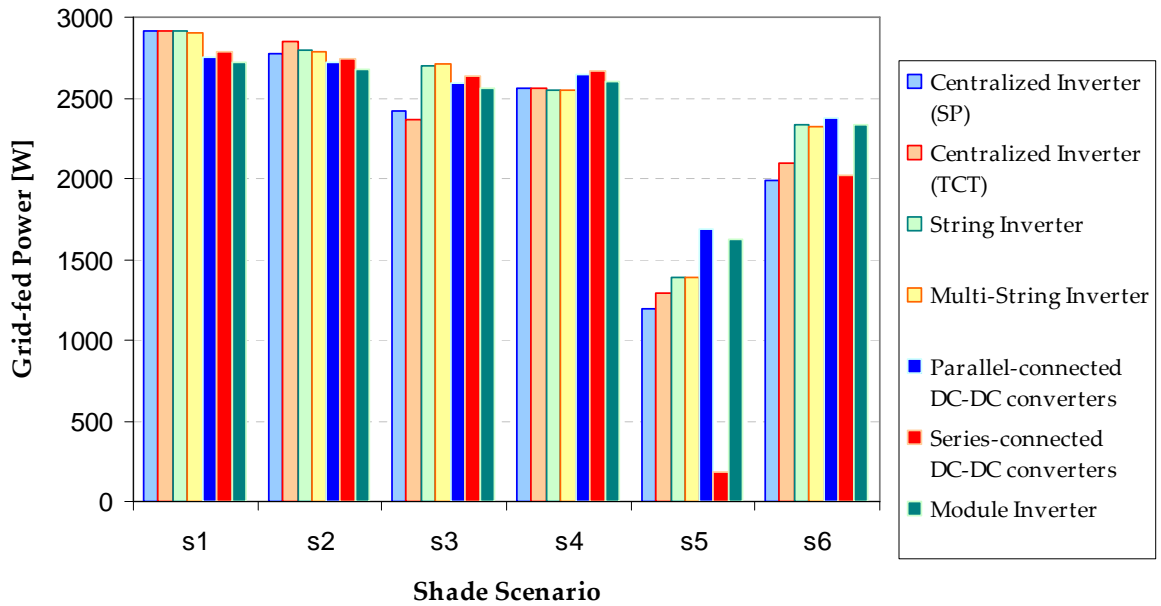


Figure V.3: Grid-fed power of the 3 kW_p PV system topologies in different shade scenarios

In shade scenario s6, the effectiveness of module-oriented topologies is clearly visible. Indeed, these system topologies are able to extract all the available power from the PV modules, while the centralized inverters can only extract 2047.2 W (79% of the available power) and 2158 W (83% of the available power) for the SP and TCT configurations respectively. Consequently, more power is grid-fed even though the conversion efficiency is lower as can be seen on Table V.1. The string and module-oriented plant configurations produce between 17% and 19% more power than the traditional centralized inverter with an SP array interconnection scheme.

	Centralized Inverter (SP)		Centralized Inverter (TCT)		String Inverter		Multi-String Inverter		Parallel-connected DC-DC converters		Series-connected DC-DC converters		Module Inverter	
	Available Power [W _p]	System Efficiency	Available Power [W _p]	System Efficiency	Available Power [W _p]	System Efficiency	Available Power [W _p]	System Efficiency	Available Power [W _p]	System Efficiency	Available Power [W _p]	System Efficiency	Available Power [W _p]	System Efficiency
s1	2991,8	97,4%	2991,8	97,4%	2991,8	97,4%	2991,8	96,9%	2991,8	92,1%	2991,8	93,0%	2991,8	90,8%
s2	2847,2	97,4%	2921,9	97,4%	2869,1	97,4%	2869,1	97,0%	2951,9	92,0%	2951,9	93,0%	2951,9	90,7%
s3	2489,0	97,2%	2435,4	97,2%	2770,5	97,3%	2770,5	97,7%	2829,0	91,8%	2829,0	93,0%	2829,0	90,5%
s4	2623,6	97,3%	2623,6	97,3%	2623,6	97,3%	2623,6	97,0%	2871,9	92,0%	2871,9	93,0%	2871,9	90,6%
s5	1228,0	96,8%	1329,7	96,8%	1442,1	96,0%	1442,1	96,3%	1851,6	91,0%	1851,6	9,9%	1851,6	87,8%
s6	2047,2	97,4%	2158,0	97,4%	2402,1	97,1%	2402,1	96,9%	2586,1	91,8%	2586,1	78,0%	2586,1	90,1%

Table V.1 : Maximum available power from PV modules and system efficiency of PV system topologies

In shade scenario s5, the series connected DC-DC converter system has the poorest results due to the ineffective control strategy discussed in Chapter IV. However, it is interesting to note that this topology has the highest system efficiency of all module-oriented layouts, in mildly shaded scenarios. An improvement of the control strategy in degraded mode operation to prevent the voltage limitation of the most powerful modules could considerably make this solution attractive.

Lastly, the DC-DC and DC-AC power conversion losses of each system topology in normal operating conditions (scenario s1), presented on Figure V.4, shows differences in the distribution of these losses. In the centralized and string-oriented topologies, the majority of power losses are caused by the current inversion process, whereas module-oriented topologies have greater losses during the DC-DC conversion and due to control circuit supply. This last point may be interesting to further examine PV systems for power loss optimization by concentrating on the conversion stages that are the least efficient.

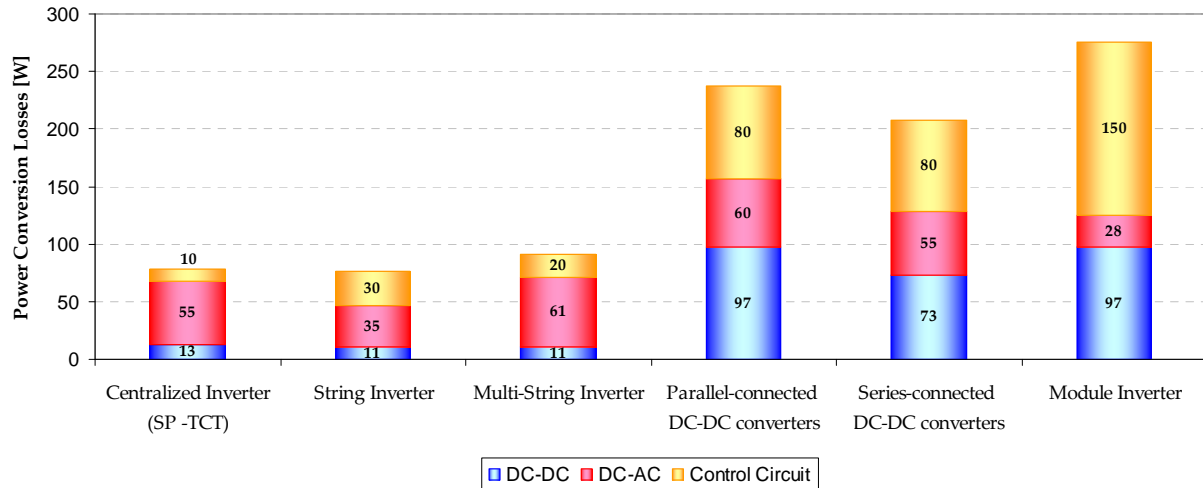


Figure V.4 : Power conversion losses of PV system topologies for a 3 kW_p array for scenario s1

In conclusion to this study, interest in using a centralized inverter topology with a TCT interconnection scheme for non-shaded and mildly shaded residential arrays has been brought to light. However, in residential arrays often subject to partial shading, the implementation of module-oriented topologies (parallel-connected DC-DC converter, series-connected DC-DC converter and module inverter) is beneficial in terms of power production. In order to observe the influence of the array power-rating on the PV system topology performance, simulation results on a commercial-sized array have been carried out and are presented in the following section.

V.1.2. Commercial-sized PV systems

The predominance of residential PV installations connected to the utility grid is not the case everywhere. For example in Spain, most PV installations have power ratings in the 5-100 kW_p range, as showed on Figure V.5. Such installations may be installed on large area rooftops or solar parkings (such as the one at Jaén University §III.2.1) with few obstacles in their surrounding environment.

Although less common than in residential systems, partial shading may still occur on these large installations. Indeed, in arrays that occupy large surfaces the partial shading due to passing clouds is more frequent than on smaller arrays in which the cloud entirely covers the surface. In the interest of examining the performance of large systems, the previous shade scenarios have been applied to a 30 kW_p plant.

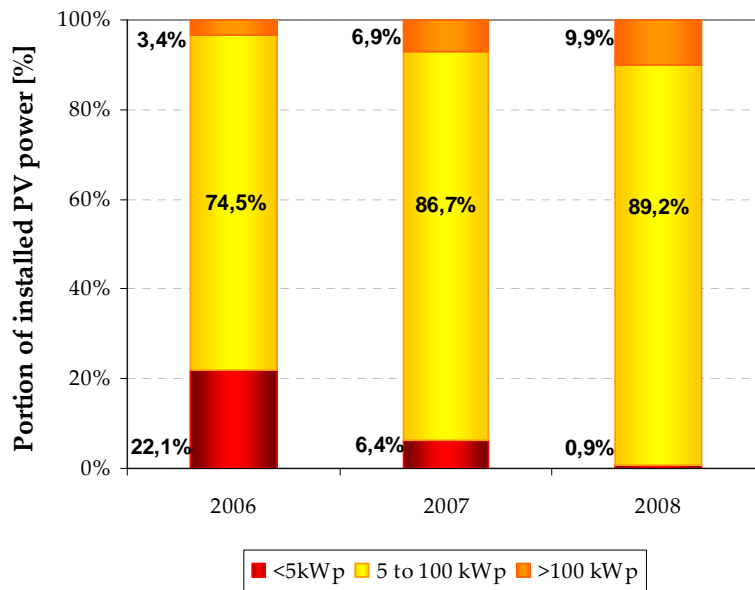


Figure V.5: Distribution of grid-connected PV systems according to power rating in Spain [ASIF'09]

The simulation results presented on Figure V.6 show similar performances to those of residential PV systems. The main difference lies in the system efficiency variations of certain topologies, as can be seen on Table V.2. In normal operating conditions, the centralized inverter layout has decreased its efficiency by 0.5 points, whereas multi-string, multi-module, and series-connected DC-DC converter topologies have gained 0.3 points. String and module inverters remain at identical efficiency levels since the addition of strings in the array has not modified the portion of power losses in the complete system with respect to the 3 kW_p plant.

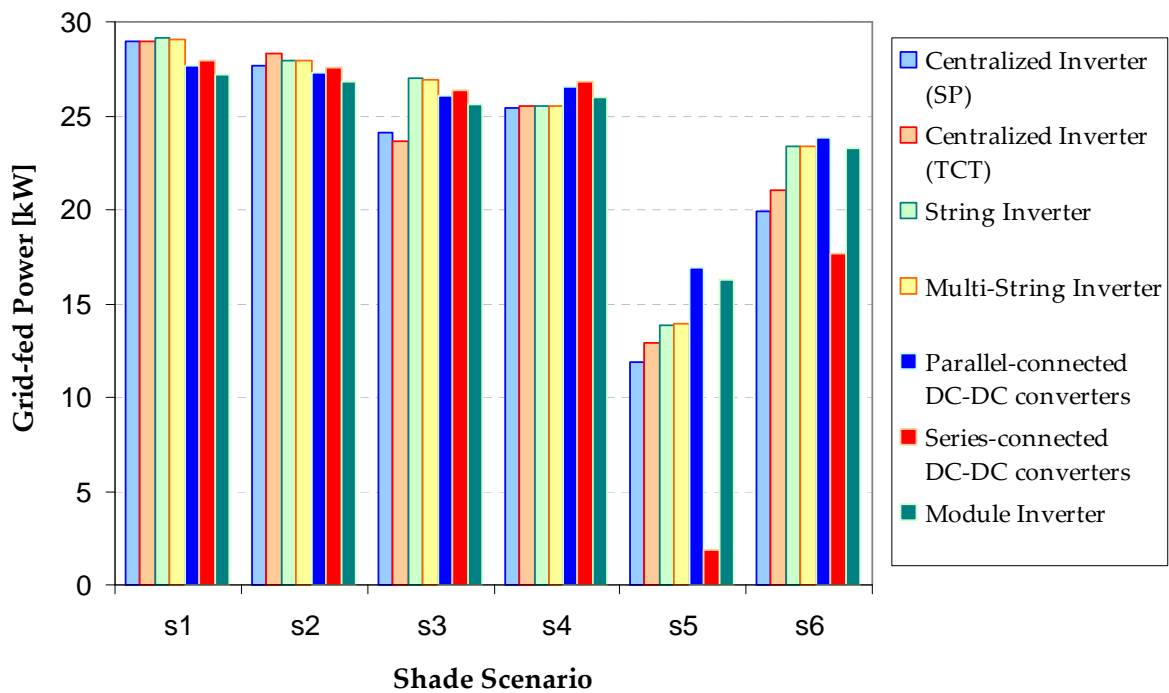


Figure V.6 : Grid-fed power of the 30 kW_p PV system topologies in different shade scenarios

	Centralized Inverter (SP)		Centralized Inverter (TCT)		String Inverter		Multi-String Inverter		Parallel-connected DC-DC converters		Series-connected DC-DC converters		Module Inverter	
	Grid-fed Power[W]	System Efficiency	Grid-fed Power[W]	System Efficiency	Grid-fed Power[W]	System Efficiency	Grid-fed Power[W]	System Efficiency	Grid-fed Power[W]	System Efficiency	Grid-fed Power[W]	System Efficiency	Grid-fed Power[W]	System Efficiency
s1	28978	96,9%	28978	96,9%	29154	97,4%	29092	97,2%	27632	92,4%	27911	93,3%	27164	90,8%
s2	27618	97,0%	28330	97,0%	27951	97,4%	27900	97,2%	27254	92,3%	27534	93,3%	26785	90,7%
s3	24095	96,8%	23681	97,2%	26967	97,3%	26931	97,2%	26106	92,3%	26362	93,2%	25607	90,5%
s4	25465	97,1%	25491	97,2%	25528	97,3%	25526	97,3%	26517	92,3%	26781	93,3%	26018	90,6%
s5	11874	96,7%	12864	96,7%	13841	96,0%	13943	96,7%	16911	91,3%	1886	10,2%	16262	87,8%
s6	19947	97,4%	21016	97,4%	23335	97,1%	23358	97,2%	23834	92,2%	17661	68,3%	23290	90,1%

Table V.2 : Maximum available solar array power and system efficiency results according to system topology

The distribution of power losses presented on Figure V.7 shows that those do not vary linearly for all topologies considered. The hybrid topologies (multi-string, parallel-connected and series-connected DC-DC converter) see the losses associated to the control circuit decrease as the array power rating increases. Moreover, DC-AC conversion losses in multi-string and multi-module topologies are lower than in the residential scenario considering the power rating increase.

Lastly, the DC-DC conversion related losses in the centralized topology are proportionally much higher than in the residential case. This is linked to the higher current flow through the Boost converter switch during the conversion process. In this case, losses may be lower by eliminating the DC-DC conversion stage and directly realizing the MPPT by modifying the inverter control scheme. The input current reference value (I_{DCinv}^*) could directly be imposed by an MPPT algorithm rather than the DC voltage regulation presented in Chapter IV. However, if this later solution is adopted, additional PV modules should be integrated in the strings in order to guarantee that the maximum power point voltage is higher than the minimal voltage inversion value (approximately $V_{GRIDRMS} \cdot \sqrt{2}$).

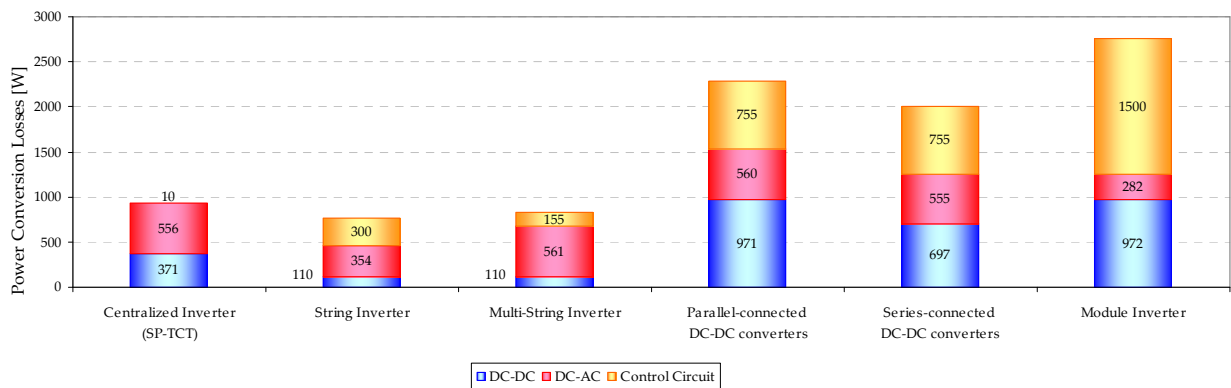


Figure V.7: Distribution of the system topologies power losses in shade scenario s1 with values expressed in watts

In conclusion, the implementation of power electronics in PV arrays can considerably decrease the quantity of mismatch losses in partially shaded arrays. The ability of module-oriented topologies to extract all the available power shows that it is the best suited for mismatch loss reduction. Nevertheless, the capacity to extract more power from PV modules is compensated by low efficiencies of these later topologies. Consequently, in normal operating conditions centralized and string inverters obtain the best performances. The PV array interconnection scheme modification to TCT has proven to have a positive impact on power production of residential and commercial-sized arrays in most cases, yet in severe localized shade conditions the SP topology gives better results. In partially shaded

conditions, especially in severe shade conditions, the module-oriented PV systems become competitive. The most promising of these topologies appears to be the series-connected DC-DC converter which attains best module-to-grid efficiencies, but simulations presented in Chapter IV have shown that smarter control strategies should be developed in order to prove the viability of this later system in severely shaded arrays. Following the study of solar resource degradation of PV systems, it is important to evaluate the performances of topologies when subject to the degradation of power converters.

V.2. Degraded mode management evaluation

The organization of a PV system contributes to its effectiveness in normal and degraded mode operation. In normal mode operation the PV system is designed to operate in nominal operating conditions, thus making the power production and system efficiency the most important indicators. However, when a system component fails to operate correctly, the dependencies between system components and their effect on power production becomes important. PV system topologies that are able to mitigate component dependencies are the ones that will be able to continue to feed energy to the grid while part of the system is defective.

The evaluation of component dependencies is done through an analysis of power flow paths, in other words by analyzing components in the module-to-grid power flow in which the malfunction of a system component may affect all modules. To quantify the dependence of a module with the DC-DC and DC-AC conversion units an indicator has been developed. The converter dependency (CD) indicator, whose expression is presented on equation V.1, aims to identify the PV system topologies that contain power flow knots by determining the number of modules that are affected by each DC-DC and DC-AC converter fault in an MxN array.

$$CD = \frac{N_{DC-DC} + N_{DC-AC}}{M \cdot N} \quad V.1$$

Where N_{DC-DC} is the number of modules that depend on the DC-DC converter, N_{DC-AC} is the number of modules that depend on the inverter, M the number of modules per string, and N the number of strings in the array.

The CD indicator value ranges from 0 to 2. The zero value is an unattainable minimum, but values lower than one can be interpreted as low dependability of power electronics on the PV system's continuity of service. For CD values higher than one, the presence of at least one power flow knot is revealed making each module in the array dependent of the same power converter. Indeed, considering feasible values with physical significance of M and N, the parameters N_{DC-DC} and N_{DC-AC} must fulfill conditions (a) and (b) expressed in equation V.2.

$$\begin{aligned} 0 &\leq N_{DC-DC} \leq M \cdot N & (a) \\ 0 &< N_{DC-AC} \leq M \cdot N & (b) \end{aligned} \quad V.2$$

Therefore, a CD value higher than one indicates that at least one parameter of N_{DC-DC} and N_{DC-AC} has reached its maximum value. That is to say that each module in the array depends on the at least one of the conversion processes, albeit DC-DC or DC-AC.

Now, when considering the six studied PV system topologies, whose CD indicators are presented on Table V.3, two assertions can be made. The first consists in noticing that centralized inverter, multi-string inverter, parallel-connected and series-connected DC-DC converters have CD values surpassing the unity. In each case, the power flow knot detected is the unique inverter which is the critical element for power injection into the grid.

	Centralized Inverter		String Inverter		Multi-String Inverter		Parallel-connected DC-DC converters		Series-connected DC-DC converters		Module Inverter	
	DC-DC	DC-AC	DC-DC	DC-AC	DC-DC	DC-AC	DC-DC	DC-AC	DC-DC	DC-AC	DC-DC	DC-AC
Number of dependent modules in a MxN array	M·N	M·N	M	M	M	M·N	1	M·N	1	M·N	1	1
Converter Dependency	2		$\frac{2}{N}$		$1 + \frac{1}{N}$		$1 + \frac{1}{M \cdot N}$		$1 + \frac{1}{M \cdot N}$		$\frac{2}{M \cdot N}$	

Table V.3: Expression of module dependency indicator for different PV module topologies

The second element is that both string and module inverters have low CD indicators, regardless of the values of M and N. Furthermore, their dependency decreases as PV strings are longer and as the number of PV strings increases. In other words, as the size of the PV array increases, the impact of one defective component on the grid-fed power production decreases.

The CD indicators have been calculated for the previously described 3 kW_p and 30 kW_p arrays; they are presented on Figure V.8.

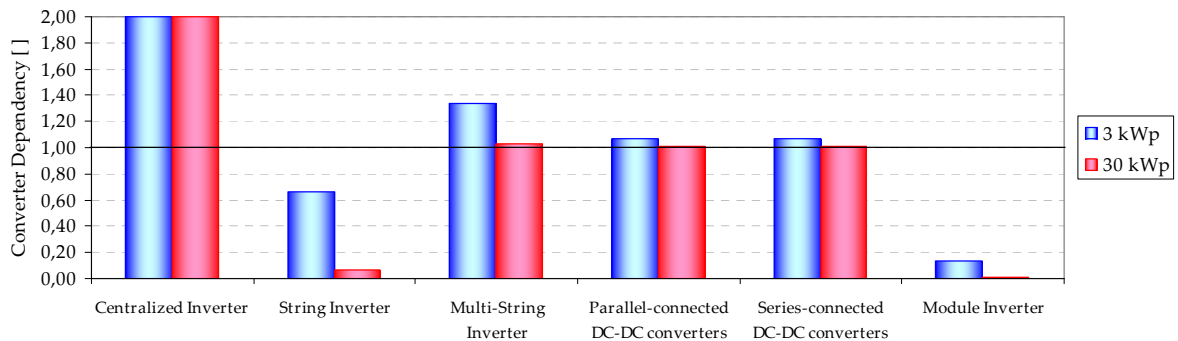


Figure V.8: Converter dependency indicator values applied to 3kW_p and 30 kW_p array for each studied PV system topology

The power rating of the array can have a considerable impact on its converter dependency. This is best illustrated in the case of the multi-string inverter topology in which the CD value approaches 1 as the array size increases. The parallel-connected and series-connected DC-DC converter topologies have a similar behavior since as the number of modules increases, the impact of a DC-DC converter failure on the rest of the system decreases. However, in all cases a failure from the centralized inverter would prohibit any power production to the grid. For this reason, their CD values are necessarily higher than one.

The CD indicator could be improved by integrating reliability indicators, mentioned in Chapter I, such as the MTBF. By doing so, the CD indicator could deliver information on

the mean time in which continuity of service is guaranteed. Because of the lack of data on the reliability indicators of converters for the studied system topologies, the development of the improved indicator has not been carried out in this work.

An indicator for evaluating the capacity of PV system topologies to continue to feed the utility-grid in degraded mode operation of converters has been developed. Using this indicator, the best results are obtained for module inverters and string inverters respectively. While the centralized inverter is capable of transforming solar power efficiently, its design is the most sensitive to power converter failure. The converter dependency is convenient to use for analyzing the continuity of service of an installation, but does not take into account another important aspect: the investment costs.

V.3. Investment costs

A major factor to consider when comparing PV systems is the investment costs. This section will aim to estimate the total investment costs of the six studied systems for both residential and commercial PV arrays. The approach consists in estimating the price per watt for: PV modules, converters for each system topology, and additional costs (installation, assembly and design). Once the price per watt for each PV system is achieved, they will be applied to a 3 kW_p and 30 kW_p array.

First, the PV module prices have been considered using a mean value of module retail prices with peak power values of 125 W_p and higher. The cost per watt has been volume weighted to take into account the disparities in power rating of the PV module market. The evolution of PV module prices over the last two years up until June 2010 is presented on Figure V.9 [SOL'10].

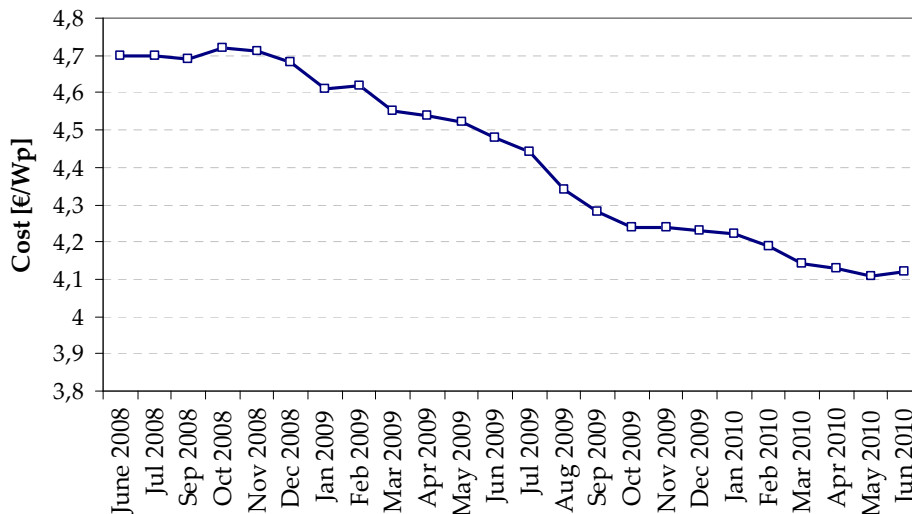


Figure V.9: Price of PV modules from June 2008 to June 2010; expressed in €/W_p [SOL'10]

The continuous decrease of the price over time and by considering the decrease to continue slightly, the PV module price value used in the cost simulation was fixed at 4.1 €/W_p. The total cost of the modules for a PV array with a rated power P_{PV} is expressed in equation V.3.

$$C_{\text{MODULES}} = P_{\text{PV}} \cdot C_{\text{PVMODULE}} \quad \text{V.3}$$

Where C_{MODULES} is the total cost for PV modules, P_{PV} the power rating of the array and C_{PVMODULE} is the unitary price for one module

Secondly, PV system topology prices have been estimated using a similar index. As in all cost predictions, prices vary with respect to several factors such as the quantity ordered, the manufacturer, the technology, and the different available options (PV monitoring, energy storage management, etc.). The costs of the PV system topologies used in this work are presented on Table V.4. These prices have been determined using available retail prices of inverters (centralized, string and multi-string) in the 1-10 kW range. The prices of module-oriented topologies have been determined in a similar manner, when the information was available or based on market previsions.

	Centralized Inverter	String Inverter	Multi-String Inverter	Parallel-connected DC-DC converter	Series-connected DC-DC converter	Module Inverter
Cost [€/W]	0,5	0,7	0,6	0,95	1	1,2

Table V.4 : Estimated prices of PV system topologies expressed in €/W

The total converter cost can be determined using equation V.4.

$$C_{\text{CONVERTERS}} = P_{\text{PV}} \cdot C_{\text{TOPOLOGY}} \quad \text{V.4}$$

where $C_{\text{CONVERTERS}}$ is the total converter cost, P_{PV} the PV array power rating, and C_{TOPOLOGY} is the unitary price for a PV system topology

Finally, the extra costs linked to the design, installation, and assembly of the PV system components has been considered. To estimate the price of these additional costs, the distribution of PV system costs for residential applications, presented in Chapter I (§I.5.3), has been used. Indeed, these auxiliary costs add up to 32% of the total price of a residential PV system. Based on the assumption that PV modules account for 55% of the total cost, additional costs can be calculated by determining the total cost of the system through the price of PV modules as shown on equation V.5.

$$C_{\text{ADDITIONAL}} = \frac{0,32}{0,55} \cdot C_{\text{MODULES}} \quad \text{V.5}$$

where $C_{\text{ADDITIONAL}}$ the total additional costs and C_{MODULES} the total cost of PV modules.

The total installation costs have been estimated by adding the module, converter and additional cost estimates. Results for residential and commercial-sized systems are presented on Table V.5 and Figure V.10.

	Centralized Inverter	String Inverter	Multi-String Inverter	Parallel-connected DC-DC converter	Series-connected DC-DC converter	Module Inverter
3 kWp [k€]	20,96	21,56	21,26	22,31	22,46	23,06
30 kWp [k€]	209,56	215,56	212,56	223,06	224,56	230,56

Table V.5 : Cost estimation of PV system topologies for a 3kWp and 30 kWp installation

First of all, given the cost determination method one can easily see that the prices vary linearly with the power rating of the array. In reality, cost savings may be achieved due

to mass production and large purchases, however these economies of scale have not been considered in this work. The cost estimates show that the low-cost solution is the centralized inverter topology. For a residential-sized installation, the most expensive solution accounts for a 10% price increase when compared to the centralized inverter topology. In a commercial-sized system the module inverter cost overrun would most probably be higher when compared to the centralized inverter.

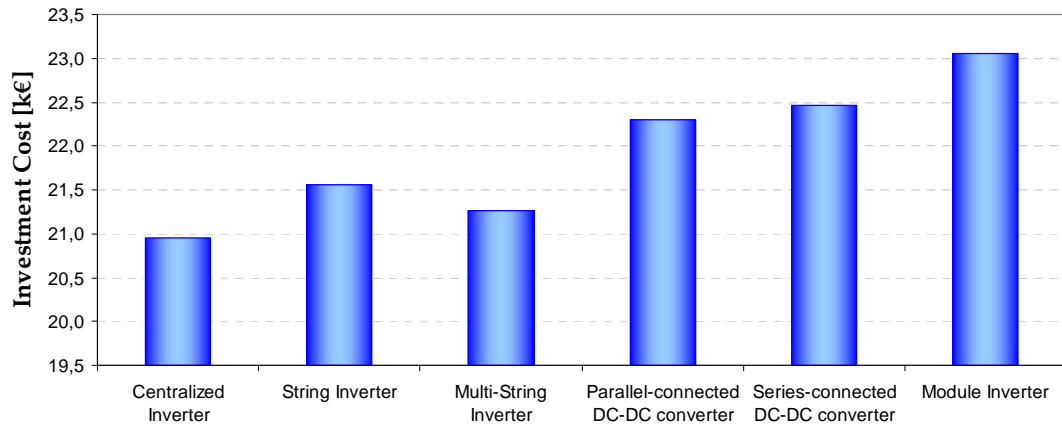


Figure V.10 : Cost estimation of 3kW_p PV installation in k€ for the studied PV system topologies

Additionally, to carry out a return on investment evaluation, which has not been considered in this work, the income from feed in tariffs should be included. This later parameter varies significantly depending on the national policies of each country, the power rating and type of installation (ground-mounted, roof-mounted, or BIPV).

The last aspect to consider when evaluating PV system is its ability to evolve with future technologies and upgrades.

V.4. Upgradeability

During the lifespan of a PV installation, the system may evolve from its initial state due to repair or replacement of components. The upgradeability of an installation refers to the ability of a system topology to incorporate new components in the plant. Such components may be needed to increase the PV installation's power rating, replace defective modules (different from the original ones), or introduce novel components (such as energy storage or monitoring systems).

To evaluate the upgradeability of a PV system topology a grading scale has been developed by considering the distinctive patterns in topologies. Indeed, all topologies are organized by multiplying a characteristic pattern, containing PV modules and power conversion units, which will be referred to as the *topology pattern*. For example, the centralized inverter is organized in several PV strings connected in parallel and linked to a unique centralized inverter. In this case, since the inverter is common to the plant and cannot be subdivided to form a pattern, the topology pattern is a PV string. Now considering the string inverter topology, one can see that the PV system layout can be seen as an assembly of PV strings with their associated inverter, as shown on Figure V.11.

Moreover, the topology pattern is made up of more basic components that are

assembled together; these will be referred to as the *internal pattern*. In the case of the multi-string inverter, the topology pattern is constituted of a PV string with its associated DC-DC converter. Hence, the internal pattern of string topologies is a PV module. In the case of module inverters, the internal pattern refers to the PV module with its associated inverter.

A distinction is made between both topology and internal pattern to illustrate the importance of the system modification. In the case of a minor evolution, the upgradeability results for the internal pattern should be considered, whereas for major modifications the topology pattern results are more suitable.

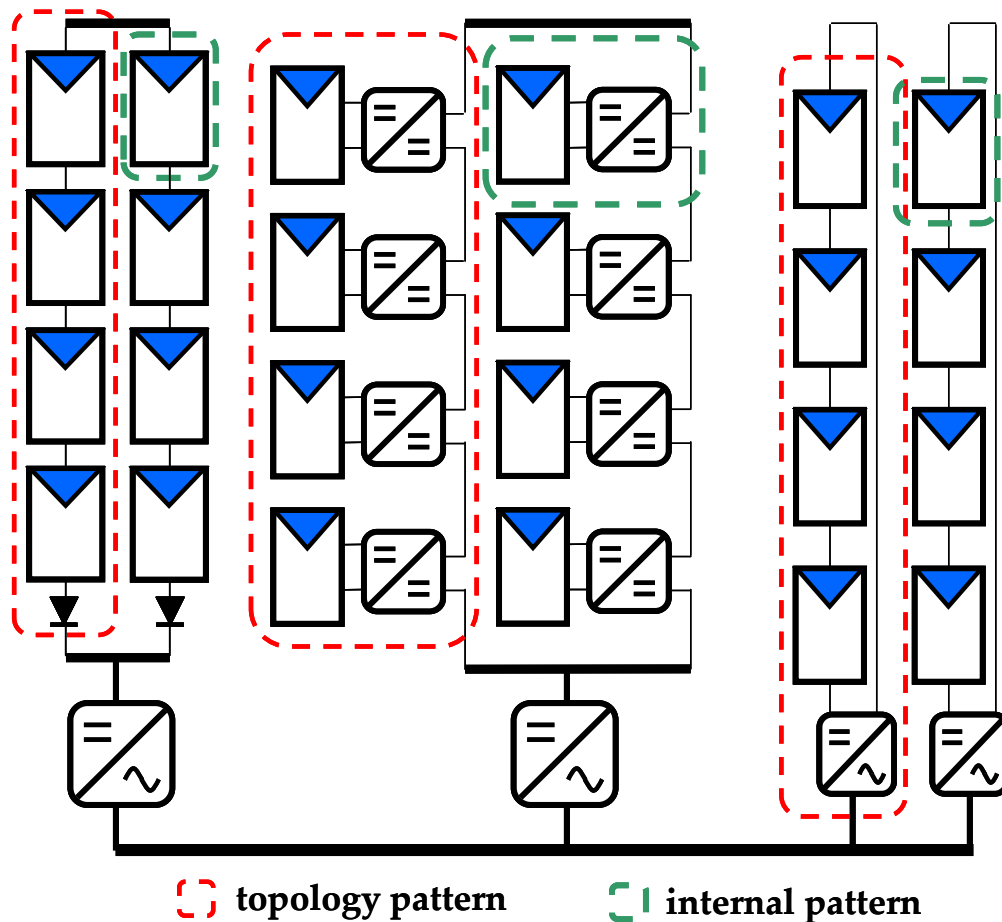


Figure V.11: Topology and internal patterns in PV system topologies

Upgradeability evaluation is carried out by introducing an additional pattern in the system topology and concluding on its impact for correct operation. A grade is then attributed to the system topology with values ranging from 1 to 3, as presented on Table V.6. Low grade values indicate topologies which cannot operate correctly when an additional pattern is introduced into the system. System topologies that integrate patterns without needing component changes obtain the highest grades. Finally, the intermediate values are attributed to system topologies which do not necessarily require other component upgrades to ensure correct operation. Topologies with intermediate grades have may be upgraded, but within limited ranges. The upgradeability results for the six studied system topologies are presented on Table V.7.

GRADE	SIGNIFICATION
1	A pattern upgrade <i>inevitably requires</i> further modifications
2	A pattern upgrade <i>may require</i> further modifications (depending on inverter/DC-DC converter specifications)
3	A pattern upgrade <i>does not</i> require modifications

Table V.6 : Upgradeability evaluation grading scale

The centralized inverter is the least upgradeable since adding a PV string to the array may imply the replacement of the inverter in order to deliver the maximum array power. In the case the internal pattern is upgraded, ie. a module is added to the PV string, the array voltage is unbalanced thus, the longest string will not have the same maximum power voltage as the other PV strings in the array. The most upgradeable system layout is the module inverter, in which adding an additional AC module does not disturb the operation of the initial plant. Furthermore, PV modules of different technologies may be used in the module inverter topology without impacting the power production of the other modules in the plant. Concerning the other topologies, they may generally be upgraded but are strongly dependent of the initial converter specifications, especially: power-rating, maximum operating voltage and current values.

	Centralized Inverter	String Inverter	Multi-String Inverter	Parallel-connected DC-DC converter	Series-connected DC-DC converter	Module Inverter
Topology pattern	2	3	2	2	2	3
Internal pattern	1	2	2	2	2	3

Table V.7 : Upgradeability ratings for the studied PV system topologies

A method for evaluating the upgradeability of a PV system topology has been developed by introducing the concept of topology and internal patterns. The results show that the module inverter performs best to these requirements, whereas the centralized inverter is the least upgradeable.

V.5. Topology Grading Method

An evaluation method has been developed to determine the PV system layout that best responds to the needs of a PV plant designer. The evaluation consists in using the Topology Grading Method (TGM) where priorities are attributed to the PV topology evaluation criteria: power production, degraded mode operation, investment costs, and upgradeability. The TGM quantifies the performances by the means of topology scores (TS) to determine the most adapted PV system topology with respect to the priority levels given for each criterion [PIC'09].

V.5.1. Topology score calculation

The topology score (TS) is a grade attributed to a topology depending on its ability to satisfy the evaluation criterion. Thus, one score is assigned to each topology for each of the four before mentioned criteria. The topology scores are dimensionless values, ranging from 0 to 1, that have been normalized and represent the efficiency of the system topology with respect to the studied criterion.

▪ Power production

The first criterion considers the ability of a system topology to produce power in various environmental conditions. The power production topology score is calculated using a weighted formula using the power produced in both non-shaded and partially shaded conditions. For each topology, identified by index j in equation V.6, simulations have been carried out using representative shade scenarios for the studied PV array. The shade scenarios may vary depending on the location of the array and are expected to represent those that are the most likely to be encountered by the solar plant. The power produced by topology j is then compared to the most producing topology in order to normalize results. Then, the power production ratios are weighted to take into account the time distribution in which the arrays operate in normal and partially shaded operation.

$$TS_{1,j} = NO \cdot \frac{P_{GRIDNO}^j}{\max(P_{GRIDNO})} + PSO \cdot \frac{P_{GRIDPSO}^j}{\max(P_{GRIDPSO})} \quad V.6$$

Where $TS_{1,j}$ represents the power production topology score for topology j , P_{GRIDNO} and $P_{GRIDPSO}$ are the power produced in normal operation and partially shaded operation respectively, NO represents the portion of time the array is subject to normal operation, and PSO represents the portion of time the array is subject to partially shaded operation. Both parameters are expressed in percent.

In this work, the time distribution values consider the array to operate in normal operating conditions 80% of the total production time and 20% in partially shaded conditions. These values have been chosen based on the assumption that PV systems are mostly non-shaded but may be subject to periodic partial shading in a smaller proportion. Results from shade scenario s4, one module shaded by 20% for each string, cf. §V.1, have been considered. The proposed power production score may be enhanced by using several shade scenarios with their associated time distribution. They may be incorporated in equation V.6 by using the same principle: power production performance associated with its time distribution.

▪ Degraded mode operation

The topology score for degraded mode operation uses the converter dependency indicator presented in section V.2. In order to normalize the results, the converter dependency value must be modified to be coherent with the adopted methodology. Indeed,

the converter dependency index is maximal when power flow knots are detected. Using equation V.7, the topology score is now maximal when the converter dependency is minimal and is constrained in the $]0,1]$ range.

$$TS_{2,j} = 1 - \frac{CD_j}{2} \quad V.7$$

Where $TS_{2,j}$ is the topology score for degraded mode operation and CD_j is the converter dependency index for topology j .

Degraded mode operation topology scores are presented on Figure V.12. These scores show that the module and string inverter topologies have the best performances when considering continuity of service of the installation. On the contrary, the centralized inverter has no ability to feed energy to the grid when the power converters are down. The remaining topologies obtain medium scores, which corresponds to their hybrid configurations described previously.

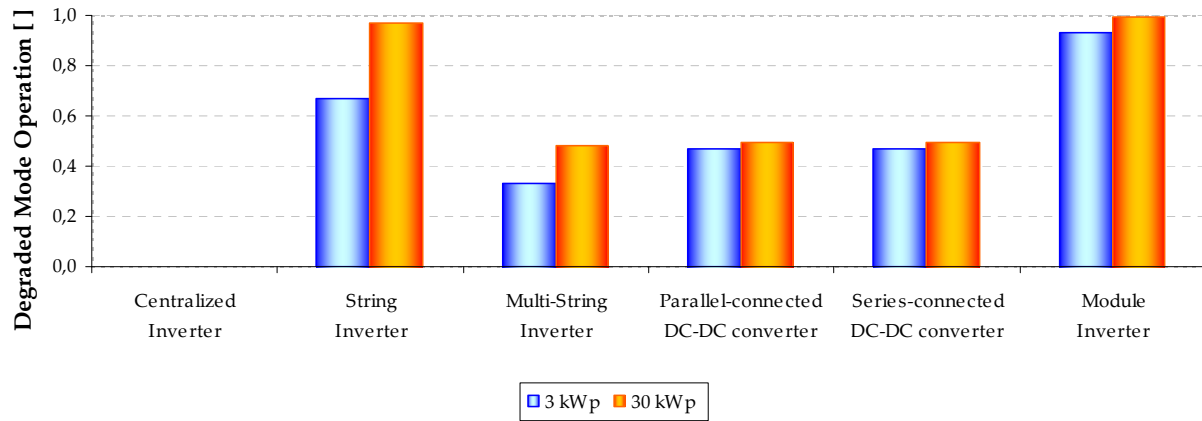


Figure V.12 : Degraded mode operation evaluation using topology scores

▪ Investment costs

The procedure adopted for comparing investment costs of PV system topologies consists in calculating the cost overrun and then normalizing the results. Since topology scores tend to represent the effectiveness of system topologies to fulfill a criterion, the determination of the cost overrun with respect to the least expensive system topology has been considered. The investment cost overrun must later be normalized, as shown on equation V.8, to respect the topology score format.

$$TS_{3,j} = 1 - \frac{IC_j - \min(IC)}{\min(IC)} \quad V.8$$

In the case the investment costs of the most expensive topologies has an overrun exceeding 100%, the formula must be modified in order to respect the topology score value range.

▪ Upgradeability

The upgradeability grading scale, described in V.4., is used to determine the topology score for the upgradeability criterion. The topology score uses the combined topology and internal pattern grades which are then normalized into the [0,1] range, as shown on equation V.9.

$$TS_{4,j} = \frac{TP_j + IP_j - 2}{4} \quad V.9$$

Thus, the topology that is the most upgradeable is attributed a score of one, whereas the least upgradeable topology attains a score of zero. The topology scores for the upgradeability criterion are presented on Figure V.13. Here, the evolutions of both internal and external patterns are of equivalent importance. This may be changed in the case only one type of pattern upgrade is preferred. Likewise, the score calculation chosen for this work may be improved by introducing weights in order to give priorities to the type of pattern upgradeability that is favored.

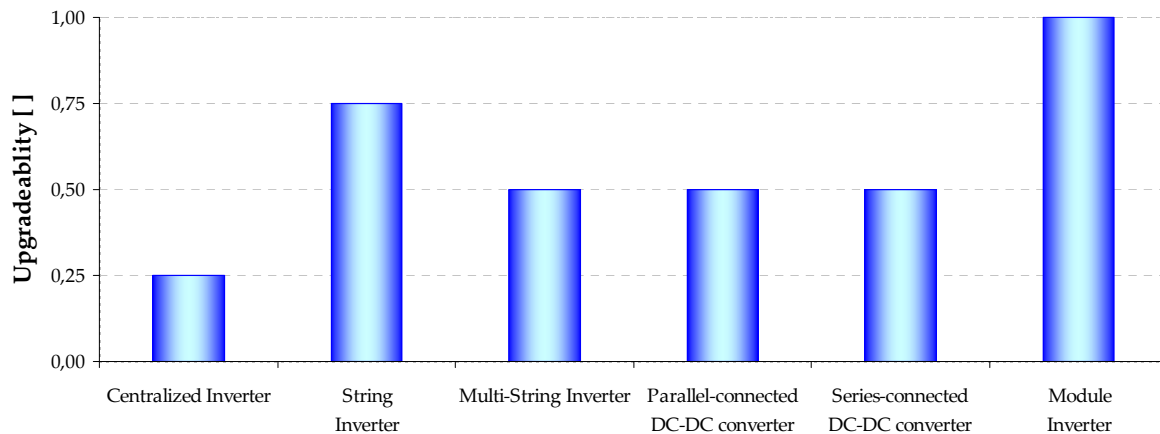


Figure V.13 : Upgradeability evaluation of the studied PV system topologies using topology scores

V.5.2. Topology Grading Method

Once the topology scores have been determined, the priorities for each criterion must be set in order to calculate the overall topology grade using equation V.10.

$$TG_j = \sum_{i=1}^4 w_i \cdot TS_{i,j} \quad V.10$$

Where TG_j is the topology grade for system topology j , w_i is the priority weight for criterion i , and $TS_{i,j}$ is the topology score for criterion i in system topology j .

The priority level for the evaluation criteria is acknowledged by adjusting weights to the chosen priorities. The sum of the priority weights must be equal to the unity. In this work, two scenarios have been considered: balanced scenario and cost-effective scenario. In the balanced scenario each criterion has the same importance, as can be seen on Table V.8. However, in the cost-effective scenario, investment costs have been extensively favored

(80%) with respect to power production (10%), degraded mode operation (5%) and upgradeability (5%) of the PV system.

	Power Production	Degraded Mode Operation	Investement Costs	Upgradeability
Balanced scenario	0,25	0,25	0,25	0,25
Cost-effective scenario	0,1	0,05	0,8	0,05

Table V.8 : Priority weights attributed to the evaluation criteria in both scenarios

Results for a residential and commercial-sized installation in both balanced and cost-effective scenarios are presented on Figure V.14 and Table V.9.

Balanced scenario results show that for residential-sized PV systems that are shaded 20% of the time, as in scenario s4, the module inverter topology is the system topology that most satisfies the evaluation criteria. Even though investment costs are higher and power production levels are slightly lower than the other system topologies, the module inverter's capacity to ensure continuity of service during converter faults and its adaptability for the future makes this solution preminent.

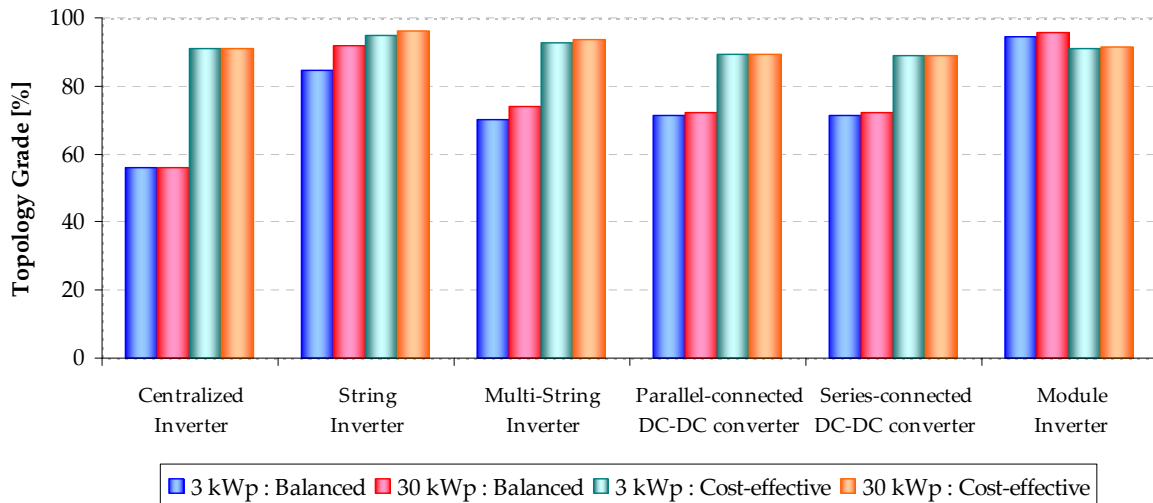


Figure V.14 : Topology grade results for the studied PV system topologies

		Centralized Inverter	String Inverter	Multi-String Inverter	Parallel-connected DC-DC converter	Series-connected DC-DC converter	Module Inverter
Balanced Scenario	3 kWp	56	84	70	71	71	94
	30 kWp	56	92	74	72	72	96
Cost-effective Scenario	3 kWp	91	95	93	89	89	91
	30 kWp	91	96	94	89	89	91

Table V.9 : Topology grading method results

For larger arrays, even though the module inverter has the highest grade, the string inverter grade rises significantly when compared to residential-sized arrays. Likewise, the grades of module-oriented topologies tend to increase whereas the centralized inverter score remains constant.

Considering the cost-effective scenario, the string inverter topology is the best compromise between cost and performance for residential applications that are mildly submitted to shade. Moreover, a considerable evolution of the centralized inverter score can be observed in between the balanced and cost-effective scenarios, yet still remain lower than

the string inverter. Today, the centralized inverter remains the overall most employed topology in PV installations, most probably due to its cost-effectiveness and simplicity. These results show that alternative system topologies may perform better in the long run when other aspects such as continuity of service and upgradeability are considered.

A method for evaluating the performances of PV system topologies considering power production, degraded mode operation, investment costs, and upgradeability has been developed. More evaluation criteria may be added to improve the topology grading method such as: installation complexity, monitoring capacity, energy efficiency, or lifecycle assessments. Furthermore, results have shown that there does not exist an overall best performing system topology, the most suitable one depends on the evaluation criteria and priority levels that have been required. The estimation of cost investments has proven to be an essential but delicate task when considering the system topologies at various power ratings. Further studies on the economies of scale should be carried out in order to give more accurate results.

Conclusion

In this chapter, the performances of six principal PV system topologies have been compared in representative shade scenarios. The study has shown that while module-oriented topologies are capable of extracting more power from the PV modules, through module mismatch reduction, they currently suffer from lower energy conversion efficiencies. Consequently, in normal operating conditions they produce less power to the utility-grid when compared to centralized and string-oriented system layouts. However, in partially shaded conditions their utilization can be beneficial.

The design of PV systems not only takes into account the energy produced by the solar array, but also considers investment costs, reliability and possible evolutions of the installation. A method for determining the best suited system layout to the needs of the designer has been proposed considering power production, degraded mode operation, investment costs and upgradeability. String and module inverters offer more reliable power generation and flexibility for integrating future components than the remaining topologies. Concerning investment costs, the configurations containing the most power converters are the most expensive. The cost savings obtained by economies of scale have not been addressed, but should be considered in further studies to carry out a more accurate comparison. The topology grading method, which aims to determine the most adapted system topology, applied to residential and commercial-sized installations, has shown that installations that are rarely subject to partial shading should continue to adopt centralized and string-oriented layouts. Nevertheless, module-oriented topologies prove to be more reliable, future-proof, and productive for regularly shaded arrays, this should be considered in a long term view for return on investments.

General Conclusion

The promotion of terrestrial photovoltaic (PV) applications in the beginning of the 21st century resulted in an exponential development of grid-connected systems. Accompanying the expansion of this promising energy source, field experience has revealed the presence of losses due to mismatch of PV modules. The purpose of this work was to assess, study, and evaluate solutions to reduce these mismatch losses in grid-connected systems.

Early on in this study, a classification and presentation of the main elements that compose grid-connected PV systems were exposed. The introductory chapter presented a bibliographical review that described and compared the eight principal PV system topologies. The second chapter reviewed the modelling of PV arrays. Specifically, the novel manner of forecasting PV array production was described. This methodology uses an original computing technique that takes into account array shading patterns and interconnection schemes in diverse environmental conditions. This procedure has led to the development of a power production forecasting tool for PV plants, called Toposolver. Toposolver has been validated through experimental results conducted on a 2.2 kW_p array. The third chapter presented the causes and effects of mismatch losses on the power production of solar arrays. Moreover, a first solution for reducing them through the modification of the array interconnections was examined. The study has shown that mismatch losses become considerable in severe partially shaded conditions and may reduce the output power by up to 30%. However losses related to intrinsic module mismatch remain minor (< 2%). Although the modification array interconnection layout may slightly improve the power output in many cases, it is not able to completely eliminate them.

The second solution consists in introducing power electronic devices within the array. The power converter average models and control strategies presented in the fourth chapter were then applied in the final chapter. The second solution performs much better than the first in extracting power from PV modules, thus reducing mismatch losses. However, the gain in solar power extraction is in part negated by higher power conversion losses in module-oriented system topologies. In contrast, centralized systems have higher efficiencies but are more sensitive to environmental conditions. In order to compare the overall advantages of each system topology, a performance evaluation method has been developed and applied to residential and commercial-sized arrays. The outcome of the evaluation demonstrated that the best suited topology depends on the array power rating and requirements demanded by the designer in terms of power production, continuity of service, investment costs and upgradeability. Cost-effective needs would resort to centralized or string-oriented systems, whereas balanced requirements are most fulfilled by choosing a module-oriented system topology.

In a few words, this work has exposed the principal solutions for reducing mismatch losses in photovoltaic systems. The presence of these losses is closely linked to the interdependence of modules in the power generation process. Future solutions should aim to

limit this dependency through power flow control while managing the power losses in electronic devices. The series-connected DC-DC converter topology appears to be a first-step in this approach. Further development of this latter arrangement would be beneficial by optimizing the control strategy and power conversion losses. Additional outlooks for this work include pursuing the comprehension of the mismatch loss phenomenon by understanding the evolution of mismatch lines when bypass diodes are activated; developing the array forecasting tool by introducing PV module models with reverse-biased behavior to increase the prediction performances; and improving the topology evaluation method by introducing new criteria, such as monitoring and lifecycle assessments. The technical and economical viability of the proposed solutions should be thoroughly addressed in order to plan their deployment on the PV market

More generally, solar electricity offers a bright future in satisfying our appetite for energy by providing an almost infinite resource, in colossal proportions, that is available to all. The main challenge for achieving a sustainable energy balance resides in the improvement of its accessibility, global efficiency and environmental footprint while continuing the effort to consume energy soberly. This work was motivated by these issues and hopes to have contributed to their progression.

Bibliography

[ABE'90] A. Abete et al, Analysis of photovoltaic modules with protection diodes in presence of mismatching, Conference record of the 21st IEEE Photovoltaic Specialists Conference, vol.2 (1990) pp.1005-1010

[ABU'92] M.T. Abuelma'Atti, Improved approximate analytical solution for generalized diode equation, Electronic Letters 12th March 1992 Vol.28 No.6, pp.594-595

[ADE'06] Agence de l'Environnement et de la Maitrise de l'Energie (ADEME) report, Guide de redaction du cahier des charges techniques des générateurs photovoltaïques connectées au réseau, ADEME/PVC/V1 available at www.ademe.fr/

[AND'96] A.J. Anderson, Photovoltaic Translation Equations: A New Approach, American Institute of Physics (1996) pp.604-612

[ANT'06] F. Antony et al. "Le photovoltaïque pour tous : conception et réalisation d'installations", Observ'ER (2006) pg. 39

[ASIF'09] Asociacion de la Industria Fotovoltaica, Informe Anual 2009 : Hacia la cnsolidacion de la energia solar fotovoltaica en Espana, Annual Report from the Spanish Photovoltaic Industry Association (2009) available at <http://www.asif.org/>

[AST'08] S. Astier, Conversion photovoltaïque : du rayonnement solaire à la cellule, Techniques de l'Ingénieur D 3935-1 to D 3935-20

[BAB'06] D.K.R. Babajee et al, An analysis of the properties of the variants of Newton's method with third order convergence, Applied Mathematics and Computation 183 (2006) pp.659-684

[BAC'06] S. Bacha et al, Systèmes photovoltaïques couplés au réseau
Nouvelles Technologies de l'Energie 1 - Chapter 10 (2006)

[BACH'06] S. Bacha et al, L'exploitation des réseaux d'énergie électrique avec l'électronique de puissance, Editions Hermès ISBN 2-7462-1118-X (2006) Chapter 6 : Elements de modélisation pp.121-139

[BAN'00] T.C. Banwell et al, Exact analytical solution for current flow through diode with series resistance, Electronic Letters 17th February 2000 Vol.36 No.4, pp.291-292

[BAS'01] P. Bastiani, Stratégies de commande minimisant les pertes d'un ensemble convertisseur-machine alternative : application à la traction électrique, thesis from INSA-Lyon exposed February 23, 2001

[BEC'06] G. Becker et al, An approach to the impact of snow on the yield of grid-connected PV systems, Bavarian Association for the promotion of Solar Energy, available at www.sev-bayern.de/content/snow.pdf/

- [BIS'88]** J.W. Bishop, Computer simulation of the effects of electrical mismatches in photovoltaic cell interconnection circuits, *Solar Cells* 25 (1988) pp.73-89
- [BLA'88]** G. Blaesser et al, Extrapolation of Outdoor Measurements of PV array I-V Characteristics to Standard Test Conditions, *Solar Cells*, 25 (1988) pp.91-96
- [BRA'09]** A.Bratcu et al, Power Optimization Strategy for Cascaded DC-DC Converter Architectures of Photovoltaic Modules, *ICIT'09 Conference Proceedings* (2009) pp.1-8
- [BRA'10]** A. Bratcu et al, Cascaded DC-DC Converter Photovoltaic Systems: Power Optimization Issues, *IEEE Transactions on Industrial Electronics*, Issue 99 (2010) to be published
- [BUC'79]** L.L. Bucciarelli, Power loss in photovoltaic arrays due to mismatch cell characteristics, *Solar Energy* Vol.23 (1979) pp.277-288
- [BUR'09]** B. Burger et al., Extreme High Efficiency PV-Power Converters, *European Conference EPE'09* (2009) pp. 1-13
- [CAR'06]** J.M. Carrasco et al, Power-Electronic Systems for the Grid Integration of Renewable Energy Sources : A Survey, *IEEE Transactions on Industrial Electronics*, Vol. 53, No. 4 (2006) pp.1002-1016
- [CEC'01]** California Energy Commission (CEC) report, A guide to photovoltaic (PV) system design and installation, report 500-01-020 available at www.energy.ca.gov
- [CHA'87]** Chan et al, Analytical methods for the extraction of solar-cell single-and double-diode model parameters from I-V characteristics, *IEEE Transactions on Electron Devices*, Vol. ED-34 No.2 February (1987) pp.286-292
- [CHA'95]** C.E. Chamberlin et al, Effect of mismatch losses in photovoltaic arrays, *Solar Energy* Vol.54 No.3 (1995) pp.165-171
- [CHO'06]** S. Chokmaviroj et al, Performance of a 500 kWp grid connected photovoltaic system at Mae Hong Son Province, Thailand, *Renewable Energy* 31 (2006) pp.19–28.
- [CHO'09]** A.Chouder et al, Analysis model of mismatch power losses in PV arrays, *Journal of Solar Energy Engineering* Vol.131 Issue 2 May (2009) 024504-(5 pages)
- [COR'96]** R.M. Corless et al, On the Lambert W Function, *Advanced Computational Maths* (1996) pp.329-359
- [DAN'97]** M. Danner, Reverse characteristics of commercial silicon solar cells – impact on hot spot temperatures and module integrity, 26th IEEE Photovoltaic Specialists Conference, Anaheim California (1997) pp.1137 – 1140
- [DAN'06]** V. Dang, Conception d'une interface d'électronique de puissance pour Pile à Combustible, thesis from Université Joseph Fourier Grenoble, exposed December 8, 2006

- [DES'04] W. De Soto, Improvement and validation of a model for photovoltaic array performance, Master of Science in Mechanical Engineering, Solar Energy Laboratory – University of Wisconsin-Madison (2004) pp.20-66
- [DIN'08] J. Ding et al, A new method to determine optimum load of a real solar cell using the Lambert W-function, *Solar Energy Materials & Solar Cells* 92 (2008) pp.1566-1569
- [DRI'07] M. Drif et al, Univer Project. A grid connected photovoltaic system of 200 kW_p at Jaén University. Overview and performance analysis, *Solar Energy Materials & Solar Cells* 91 (2007) pp.670-683
- [EDF'03] Electricité de France (EDF) report, Accès au réseau basse-tension pour les installations photovoltaïques : Conditions techniques et contractuelles du raccordement
- [EER'10] Energy Efficiency and Renewable Energy (EERE) U.S. Department of Energy, 2008 Solar technologies market report, available at www.eere.energy.gov/
- [EPIA'09] European Photovoltaic Industry Association (EPIA), Global market outlook for photovoltaics until 2013, April 2009, available at www.epia.org/
- [FEL'81] J. Feldman et al, Solar cell interconnections and the shadow problem, *Solar Energy* Vol.26 (1981) pp.419-428.
- [FEM'05] N. Femia et al, Optimization of Perturb and Observe Maximum Power Point Tracking Method, *IEEE Transactions on Power Electronics* Vol.20 No.4 (2005) pp.963-973
- [FER'06] J.P. Ferrieux, Alimentations à découpage, convertisseurs à resonance : Principes, composants, modélisation, Editions Dunod, 3e édition , pp.32-38
- [FJE'91] T.A. Fjeldy, Approximate analytical solution of the generalized diode equation, *IEEE Transactions on Electron Devices*, Vol. 38 No. 8 August 1991, pp.1976-1977
- [GAU'01] N.K. Gautam et al, Network analysis of fault-tolerant solar photovoltaic arrays, *Solar Energy Materials & Solar Cells* 69 (2001) pp.25-42
- [GAUE'02] N.K. Gautam et al, An efficient algorithm to simulate the electrical performance of solar photovoltaic arrays, *Energy* 27 (2002) pp.347-361
- [GAUSE'02] N.K. Gautam, Reliability Evaluation of Solar Photovoltaic Arrays, *Solar Energy* Vol.72 No.2 (2002) pp.129-141
- [GET'06] program available at <http://www.math.ucla.edu/~getreuer/lambertw.html/>
- [GRA'06] MOSFET Power Losses Calculation Using the Data-Sheet Parameters, Dr. Dusan Graovac, Marco Purschel, Andreas Kiep, Application note v1.1 July 2006, www.infineon.com/
- [GRA'09] IGBT Power Losses Calculation Using the Data-Sheet Parameters, Dr. Dusan Graovac, Marco Purschel, Application note v1.1 January 2009, www.infineon.com/

- [GRE'09] A. Green et al, Solar cell efficiency Tables (Version 33), Progress in photovoltaics : Research & Applications 17 (2009) pp. 85-94
- [HER'97] W. Hermann et al, Hot spot investigations on PV modules – new concepts for a test standard and consequences for module design with respect to bypass diodes, 26th IEEE Photovoltaic Specialists Conference, Anaheim California (1997) pp.1129 – 1132
- [JAI'05] A. Jain et al, A new method to determine the diode ideality factor of real solar cell using Lambert W-function, Solar Energy Materials & Solar Cells 85 (2005) pp.391–396
- [JAI'06] A. Jain et al., Solar cell array parameters using Lambert W-function Solar Energy and Materials & Solar Cells 90 (2006) pp.25-31
- [KAN'07] V. Kanwar et al, Modified families of Newton, Halley, and Chebyshev methods, Applied Mathematics and Computation, Vol.192 (2007) pp.20-26
- [KAR'07] E. Karatepe et al, Development of a suitable model for characterizing photovoltaic arrays with shaded solar cells, Solar Energy 81 (2007) pp.977-922
- [KAU'03] N.D. Kaushika, Energy Yield Simulations of Interconnected Solar PV Arrays, IEEE Transactions on Energy Conversion, Vol.18 No.1, March 2003 pp.127-134
- [KAU'05] N.D. Kaushika et al, An investigation of mismatch losses in photovoltaic cell networks, Energy 32 (2007) pp.755-759
- [KAW'03] H. Kawamura et al, Simulation of I-V characteristics of a PV module with shaded PV cells, Solar Energy Materials & Solar Cells 75 (2003) pp.613-621
- [KAZ'09] S. Kazmi et al, An improved and very efficient MPPT controller for PV systems subjected to rapidly varying atmospheric conditions and partial shading, AUPEC'09 Conference Proceedings (2009) pp.1-6
- [KEN'69] K.L. Kennerud, Analysis of performance degradation in CdS solar cells, IEEE Transactions on Aerospace and Electronic Systems Vol. AES-5 No.6 (1969) pp.912-917
- [KIR'08] R. Kiranmayi, Modeling and a MPPT method for solar cells, Journal of Engineering and Applied Sciences 3 (2008) pp.128-133
- [KJA'05] S. Kjaer et al, A review of single-phase grid-connected inverters for photovoltaic modules, IEEE Transactions on Industry Applications, Vol.41 No.5 (2005) pp.1292-1306.
- [LAV'10] L. Lavado Villa, Maximizing the power output of a partially shaded PV plant by optimizing the interconnections among its modules, Master of Science in Electrical Engineering (2010)
- [LI'09] J.Li et al, A novel stand-alone PV generation system based on variable step size INC MPPT and SVPWM control, IPEMC'09 Conference Proceedings (2009) pp.2155-2160
- [MAR'02] B. Marion, A Method for Modeling the Current-Voltage Curve of a PV module for Outdoor Conditions, Progress in Photovoltaics : Research & Applications vol.10 (2002) pp.205-214

-
- [MAT'07]** Matos et al, A model for semiconductor photovoltaic (PV) solar cells: the physics of the energy conversion, from the solar spectrum to dc electric power, ICCEP'07 (2007) pp.352-359
- [MEG'04]** M. Megdiche, Sureté de fonctionnement des réseaux de distribution en présence de production décentralisée, INPG thesis presented December 13th 2004
- [MEI'00]** M. Meinhardt, Past, present and future of grid-connected photovoltaic and hybrid power systems, PESSM'00 (2000) pp.1283-1288
- [MEY'04]** E.L. Meyer et al, Assessing the reliability and degradation of photovoltaic module performance parameters, IEEE Transactions on Reliability Vol.53. No.1. (2004) pp.83-92
- [MYR'03]** J.M.A. Myrzik et al, String and module integrated inverters for single-phase photovoltaic systems, PowerTech'03 (2003)
- [NASA'07]** G.A. Landis, Reverse bias protected solar array with integrated bypass battery, US Patent assigned to NASA, Pub. No. US 2007/0181175A1 (2007)
- [NGU'08]** D. Nguyen et al, An adaptive solar photovoltaic array using model-based reconfiguration algorithm, IEEE Transactions on Industrial Electronics, Vol.55 No.7 (2008) pp.2644-2654
- [NOR'10]** B. Norton et al, Enhancing the performance of building integrated photovoltaics, Solar Energy (2010)
- [NREL'06]** NREL report, A review of PV inverter technology cost and performance projections, NREL/SR-620-38771, January 2006
- [ORT'92]** A. Ortiz-Conde et al, Approximate analytical expression for equation of ideal diode with series and shunt resistances, Electronic Letters 8th October 1992 Vol.28 No.21, pp.1964-1965
- [PAT'08]** H. Patel et al, MATLAB-based Modeling to Study the Effects of Partial Shading on PV Array Characteristics, IEEE Transactions on Energy Conversion, Vol.23 No.1 March 2008, pp.302-310
- [PAV'07]** A. Pavan et al., Power electronics conditioning systems for industrial photovoltaic fields: Centralized or string inverters?, ICCEP'07 (2007) pp.208-214
- [PET'07]** G. Petrone et al, Analytical model of mismatched photovoltaic fields by means of LambertW-function, Solar Energy & Solar Cells 91 (2007) pp.1652-1657
- [PET'08]** D. Petreus et al, An improvement on empirical modelling of photovoltaic cells, ISSE'08 (2008) pp.598-603
- [PIC'09]** D. Picault et al, Guidelines for evaluating grid-connected PV system topologies, ICIT'09 (2009) pp.1-5
- [PIPS'08]** Planning & Installing Photovoltaic Systems : a guide for installers, architects, and engineers, Second Edition Earthscan ISBN-13: 978-1-84407-442-6, pp.54-56

[PVPS'01] IEA PVPS Report, Innovative Electrical Concepts, PVPS T7-7 :2001, available at www.iea-pvps.org/

[PVPS'02] IEA PVPS Report, Grid-connected photovoltaic power systems : Survey of inverter and related protection equipments, PVPS T5-05:2002, available at www.iea-pvps.org/

[PVPS'09] Trends in photovoltaic applications : Survey report of selected IEA countries between 1992 and 2008, Report IEA-PVPS T1-18:2009, available at www.iea-pvps.org/

[PWC'09] L'état de la filière photovoltaïque en France, PriceWaterhouseCooper, 26 mars 2009, pg.22

[QUA'96] V. Quaschnig, Influence of shading on electrical parameters of solar cells, 25th Photovoltaics Specialists Conference Washington D.C. (1996) pp.1287-1290

[RAU'71] H.S. Rauschenbach, Electrical output of shadowed solar arrays, IEEE Transactions on Electron Devices Vol. ED-18 No.8 (1971) pp.483-490

[SAR'09] B. Sarrazin, Rapport Micro-hacheur, Solution PV report (2009)

[SER'07] D. Sera, PV panel model based on datasheet values, International Symposium on Industrial Electronics 2007, pp.2392-2396

[SER'10] Syndicat des Energies Renouvelables, Etat des lieux du parc photovoltaïque français 2010, Report from the French Renewable Energy Association (June 2010) available at <http://www.enr.fr/>

[SHI'01] T. Shimizu et al, Generation Control Circuit for Photovoltaic Modules, IEEE Transactions on Power Electronics, Vol. 16 No.3 (2001) pp.293-300

[SHI'03] T. Shimizu et al, A Novel High-Performance Utility-Interactive Photovoltaic Inverter System, IEEE Transactions on Power Electronics, Vol.18 No.2 (2003) pp.704-711

[SIL'07] S. Silvestre et al, Effects of shadowing on photovoltaic module performance, Progress in Photovoltaics : Research and Applications 16 (2008) pp.141-149

[SIL'09] S. Silvestre et al, Study of bypass diodes configurations on PV modules, Applied Energy 86 (2009) pp.1632-1640

[SOL'10] Solarbuzz.com, Solar Module Price Highlights: June 2010, Solarbuzz LLC (2010) available at <http://www.solarbuzz.com/Moduleprices.htm/>

[SGV'08] EPIA & Greenpeace, Solar Generation V-2008: Solar electricity for over one billion people and two million jobs by 2020, available at www.epia.org/

[TAL'10] D.L. Talavera et al, The internal rate of return of photovoltaic grid-connected systems: A comprehensive sensitivity analysis, Renewable Energy 35 (2010) pp.101-111

-
- [UJI'02] K. Ujiie et al, Study on dynamic and static characteristics of photovoltaic cell, Power Conversion Conference Osaka, Japan (2002) pp.810-815
- [VIG'10] S. Vighetti, Systèmes photovoltaïques raccordés au réseau : Choix et dimensionnement des étages de conversion, Grenoble-INP Thesis defended in 2010
- [VEL'05] G. Velsaco et al, Energy generation in PV grid-connected systems: Power extraction optimization for plant oriented PV generators, ISIE'05 (2005) pp.1025-1030
- [WAL'04] G.R. Walker et al, Cascaded DC-DC Converter Connection of Photovoltaic Modules, IEEE Transactions on Power Electronics, Vol.19 No.4 (2004) pp.1130-1138
- [WAN'09] Y.J. Wang et al., Analysis of Partially Shaded PV Modules Using Piecewise Linear Parallel Branches Model, World Academy of Science, Engineering and Technology 60 (2009) pp.783-789
- [WEI'10] E.W. Weisstein, "Nonlinear Least Squares Fitting." from *MathWorld*--A Wolfram Web Resource. <http://mathworld.wolfram.com/NonlinearLeastSquaresFitting.html>
- [WIL'97] J.C. Wiles et al., Blocking diodes and fuses in low-voltage PV systems, 26th Photovoltaic Specialists Conference, Anaheim, California (1997) pp.1105-1108
- [WIL'98] J. Wiles, Code writing processes and series diodes, Home Power #63, February/March (1998) pp.71-73
- [WOY'03] A. Woyte et al, Partial shadowing of photovoltaic arrays with different system configurations: literature review and field test results, Solar Energy 74 (2003) pp.217-233
- [WRI'59] E. M. Wright, "Solution of the Equation $ze^z=a$." Bulletin of the American Mathematical Society 65 (1959) pp.89-93
- [WUE'94] M. Wuest et al, Single Cell Converter System, WCPEC'94 (1994) pp.813-815
- [YAO'09] W. Yao et al, Improvement of Performance and Flexibility for Photovoltaic Module using Individual DC/DC Converter, IPEMC'09 (2009), pp.441-444
- [YAM'00] T. Yamamoto, Historical developments in convergence analysis for Newton's and Newton-like methods, Journal of Computational and Applied Mathematics 124 (2000) pp.1-23
- [YOS'96] H. Yoshioka et al, Non hot-spot PV module using solar cells with bypass diode function, 25th IEEE Photovoltaic Specialists Conference, Washington DC (1996) pp.1271- 1274

Publications

This work has led to the publication of the following scientific articles:

International Conferences

Conference	Title	Authors	References
IEEE-ICIT'09 Gippsland, Australia February 10-13, 2009	Power Optimization Strategy for Cascaded DC-DC Converter Architectures of Photovoltaic Modules	A. Bratcu, I. Munteanu, S. Bacha, D. Picault, B. Raison	ICIT'09 Conference Proceedings, pp.1-8
IEEE-ICIT'09 Gippsland, Australia February 10-13, 2009	Guidelines for evaluating grid connected PV system topologies	D. Picault, B. Raison S. Bacha,	ICIT'09 Conference Proceedings, pp.1-5
IEEE-EEEIC'10 Prague, May 16-19, 2010-07-09	Changing photovoltaic array interconnections to reduce mismatch losses: a case study	D. Picault B. Raison S. Bacha J. Aguilera J. De La Casa	EEEIC'10 Conference Proceedings, pp.37-40
EUPVSEC'10 Valencia, Spain September 6-9, 2010	Reducing mismatch losses in grid-connected residential BIPV arrays using active power conversion components	D. Picault B. Raison S. Bacha	EUPVSEC'10 Conf. Proceedings, pp.5141-5144

Journals

Journal	Title	Authors	References
IEEE Transactions on Industrial Electronics	Cascaded DC-DC Converter Photovoltaic Systems: Power Optimization Issues	A. Bratcu, I. Munteanu, S. Bacha, D. Picault, B. Raison	in press
Solar Energy	Forecasting photovoltaic array power production subject to mismatch losses	D. Picault B. Raison S. Bacha J. De La Casa J. Aguilera	Solar Energy Volume 84, Issue 7, July 2010, pp 1301-1309
Electrical Review	Reducing mismatch losses in grid-connected PV systems by the means of alternative array topologies	D. Picault B. Raison S. Bacha J. De La Casa J. Aguilera	Przegląd Elektrotechniczny (Electrical Review), Vol 2010, No 11a, pp 1-6

Annexes

ANNEX 1: Influence of single diode model parameters on the I-V characteristics of PV cells

The aim of this annex is to examine the influence of modifying PV cell parameters in the 5-parameter model, better known as the single diode model. To do so, parameter values inspired from [KAW'03] have been chosen as a reference scenario with values presented in Table A1.1. In the following simulations, the maximum power point of each I-V characteristic is identified by a circle and corresponding maximum power is expressed in the legend. Moreover, the current-voltage curves are plotted in both generator and backfeed current quadrants.

I_{ph}	I_0	V_t	R_s	R_{sh}
4 A	$5 \cdot 10^{-5}$ A	$5 \cdot 10^{-2}$ V	0.008 Ω	10 Ω

Table A1.1. : Parameter values used in the PV cell I-V curve simulation

□ Influence of light induced current, I_{ph}

The light induced current parameter mainly represents the influence of solar irradiance on the solar cell production. As shown on Figure A1.1, the short circuit evolves linearly with the photocurrent parameter, whereas the open-circuit voltage tends to remain approximately constant.

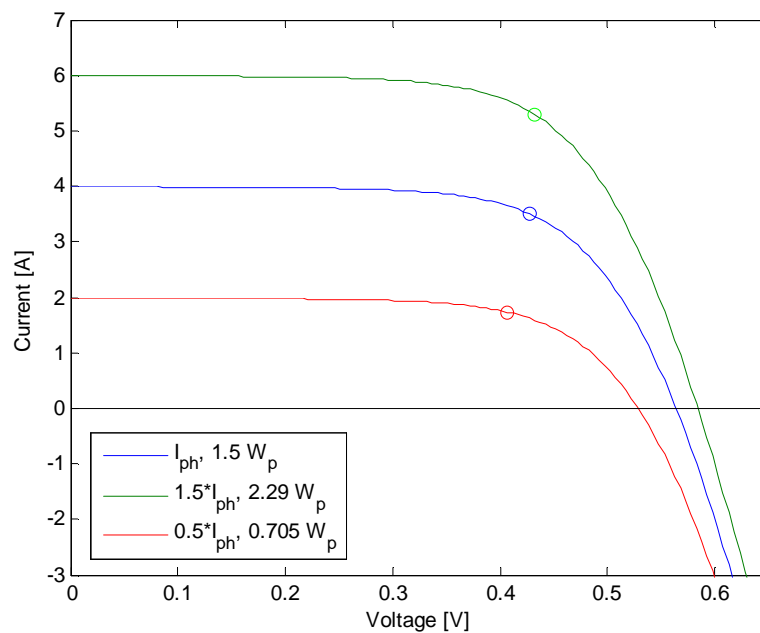


Figure A1.1. : I-V characteristics of solar cell with various light induced current values

□ Influence of reverse saturation current, I_0

The reverse saturation current characterizes the behavior of the photodiode in both forward and reverse bias. The increase of the saturation current value tends to lower open-circuit voltage, thus maximum power of the PV cell, as shown Figure A1.2. It should be noticed that the maximum power current tends to remain the same with various saturation current values. Hence, the parameter mostly affects the maximum power voltage, which tends to shift to the left as the value increases.

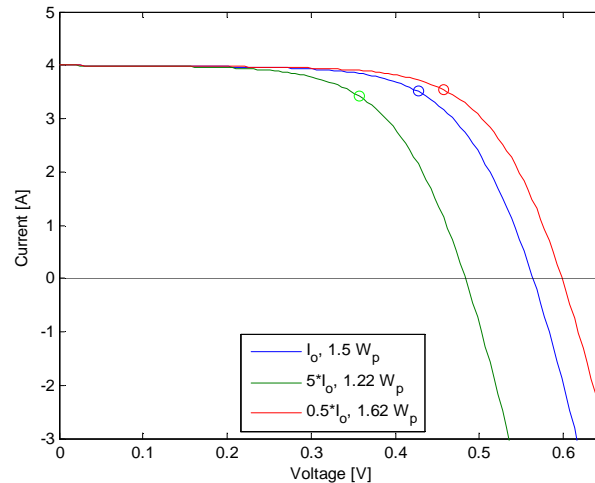


Figure A1.2. : I-V characteristics of solar cell using various reverse saturation current values

□ Influence of thermal voltage, V_t

The thermal voltage parameter is directly linked to the PV cell temperature and the diode ideality factor. When the thermal voltage is increased, the curve shifts to the right therefore increasing maximum power and open-circuit voltage, as shown on Figure A1.3. In the same manner as for the reverse saturation current, the maximum power and short-circuit current are not affected by thermal voltage value modification.

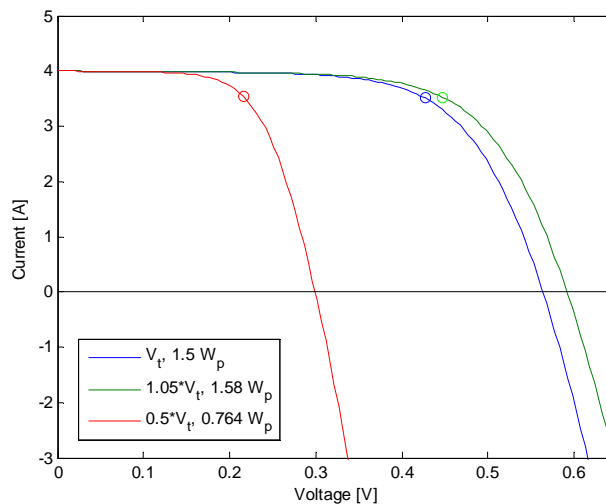


Figure A1.3. : I-V characteristics of solar cell using various thermal voltage values

□ Influence of series resistance, R_s

The series resistance has an important effect on the I-V characteristic, indeed both maximum power point and open-circuit voltage values are shifted as can be seen on Figure A1.4. As shown below, the slope in between the maximum power point and the open-circuit voltage increases when the series resistance decreases.

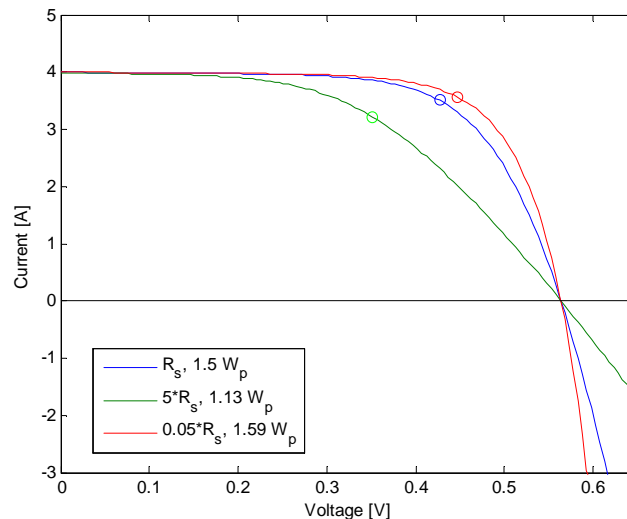


Figure A1.4. : I-V characteristics of solar cell using various series resistance values

The care brought to the PV cell manufacturing process can therefore have a great influence on the final power output.

□ Influence of shunt resistance, R_{sh}

The influence of the shunt resistance is clearly visible at high values of current, that is to say close to the short-circuit current. Surely, as the shunt resistance value decreases we can see that the slope of the curve located between short-circuit and maximum power points tends to increase, as can be seen on Figure A1.5.

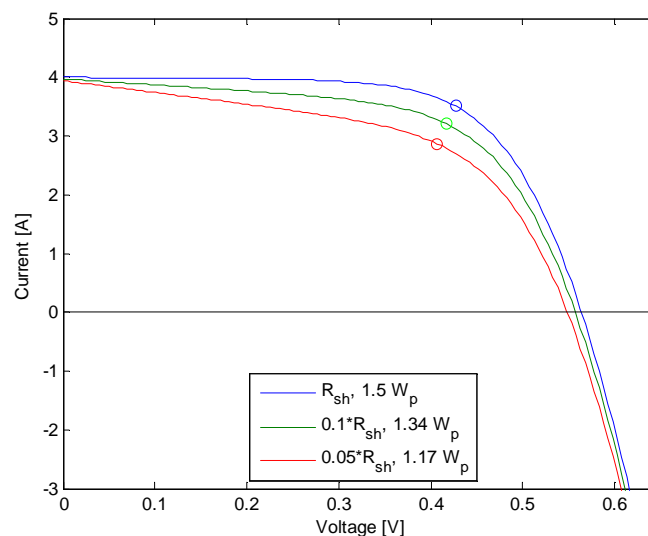


Figure A1.5. : I-V characteristics of solar cell using various shunt resistance values

A possible explanation to this phenomenon consists in taking into account that the shunt

resistance characterizes certain leakage currents in the cell and therefore their impact is far more visible at high current values than at open-circuit conditions, where current leakage is very low. In short, the shunt resistance modifies the slope between short-circuit and maximum power points, lowering the maximum power as the shunt resistance decreases. However, the open-circuit voltage remains almost constant.

ANNEX 2 :

PV module model using LambertW-function

The purpose of this annex is to present results on the PV module model using the LambertW-function. The validation of mathematical hypothesis 2 (cf. section II.2.2.3.) as well as the relevance of the approximation $R_s \ll R_{sh}$ will be investigated. The simulations were carried out using a $200W_p$ module with the following module parameters: $I_{ph}=3.83$ A, $I_o=3.4e-10$ A, $R_s=1.16$ Ω , $R_{sh}=1000$ Ω , and $V_t=2.97$ V. These parameters are considered for Standard Test Conditions (STC) that is to say with an irradiance of 1000 W/m^2 and $25^\circ C$.

□ Validation of mathematical hypothesis 2

In section II.2.2.3., the use of the infinity asymptote was constrained to respect hypothesis 2: $\log(z)>0$. This relation must be verified in order to validate the use of the asymptotic expression when $z = b \cdot e^y$ tends to infinity, that is to say when module voltage V tends to infinity since y is a constant and b is a function of V . Hence, the objective is to verify that $\log(z)$ is positive when V tends to infinity. The plot of $\log(z)$ as function of V , seen on Figure A2.1, shows that $\log(z)$ is positive for high values of V .

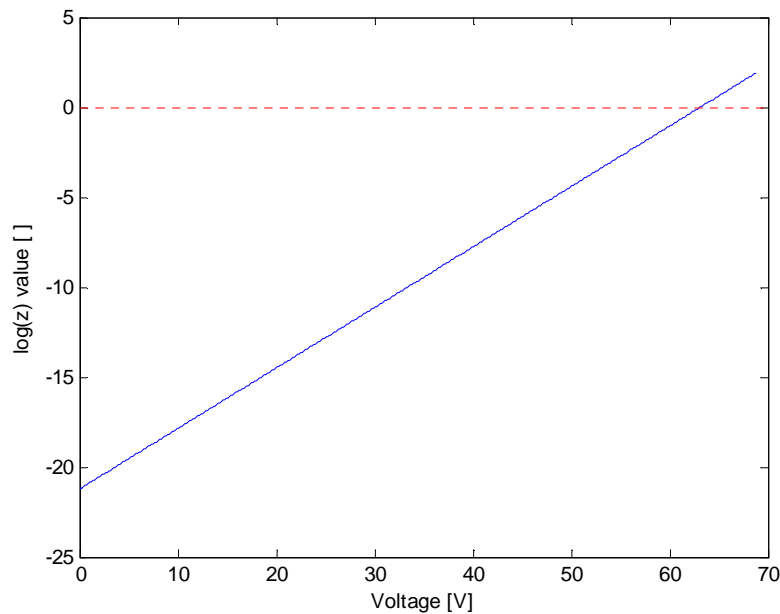


Figure A2.1. : Evolution of $\log(z)$ with module voltage

□ Relevance of the approximation $R_s \ll R_{sh}$

In section II.2.4., simplified expressions using the LambertW-function have been proposed. In order to see the influence of such an approximation, by using real values of module parameters, several simulation results are presented. In Figure A2.2, the values of the parameters b and in Table A2.1 the value of y used in section II.2.2.1 are presented in two scenarios. The *Approximate* scenario simplifies the expression by supposing $R_s \ll R_{sh}$ (equation II.15.), whereas in the *Exact* scenario equation II.11. is used in the algorithm.

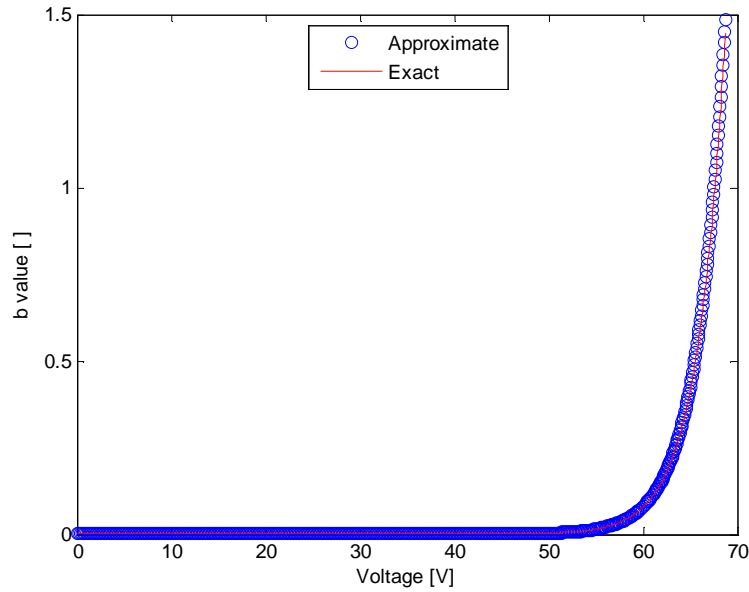


Figure A2.2. : Evolution of b with module voltage in *Approximate* and *Exact* models

y approximate	y exact
1,5039	1,5021

Table A2.1 : Values of parameter y in both *Approximate* and *Exact* models

Results show that both *Exact* and *Approximate* scenarios concur. Indeed, few differences can be seen between both models. However, the determination of parameter y shows a difference of 0.001 between both scenarios, the error being negligible we can understand why results are so similar.

Furthermore, the current-voltage characteristic of the PV module has been plotted using both scenarios, as can be seen on Figure A2.3.

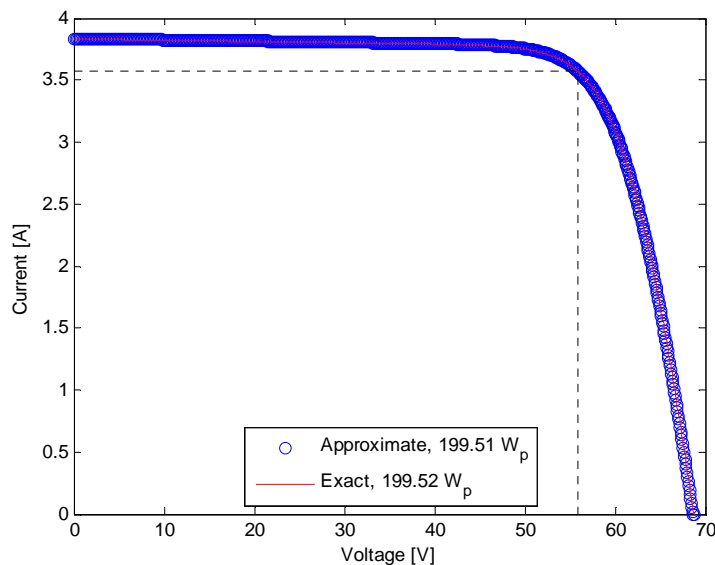


Figure A2.3. : Current-voltage characteristic of PV module using both *Approximate* and *Exact* scenarios

Here again, errors between *Approximate* and *Exact* scenarios are not visible. The maximum powers of both models are exactly the same with a 0.1 W precision, which is more than sufficient when studying PV arrays.

ANNEX 3 :

Parameter Translation Results

The parameter translation method described in Chapter II has been tested in different conditions to validate the procedure. The coefficients for Isofotón I-106 modules have been calculated using the methodology proposed by B. Marion [MAR'02] and are presented on Table A3.2.

α [A·°C ⁻¹]	β [V·°C ⁻¹]	δ []
0,009	-0,0028	-0,0039

Table A3.2 : I-V curve translation coefficients for I-106 modules

The accuracy of the parameter translation method depends on the accuracy of the I-V curve translation method since these are directly linked and the values of translation coefficients. Here, five measurements on module M10 of the Pergola 5 array have been reported on Table A3.3

Experiment	Irradiance [W/m ²]	Temperature [°C]	Pmax [W _p]	Translation Error [W _p]	Translation Error [%]
Reference	598	31,5	49,2	0,15	0,3%
E1	629,7	33,8	53,5	1,4	3%
E2	650,3	35,1	54,3	0,3	1%
E3	859,6	49,2	64,1	-10,4	-16%
E4	847,3	51,6	63,5	-10,7	-17%

Table A3.3 : Environmental conditions, maximum measured power (Pmax), and maximum power error of translation results expressed in absolute and relative values

The procedure consisted in using a reference measurement I-V curve of module M10 and comparing the measurements of this module in other environmental conditions with the predictive characteristics using the parameter translation method. Hence, the single-diode model parameters were first extracted, then translated to the conditions of each experiment using the coefficients calculated above, and finally the translated characteristic was reconstructed.

Parameter translation results show that the accuracy is highly dependent of the initial reference condition. In this case, the reference condition has been set at conditions (598 W/m², 31.5 °C). For environmental conditions that are similar to the reference condition, as experiments E1 and E2, the parameter translation is sufficiently accurate with maximum power point values below the 5% error threshold.

However, when the I-V curve is translated to environmental conditions that vary significantly from the reference conditions, the parameter translation results are poorer. The P-V characteristics of the four experiments are presented on Figure A3.6. Considering experiments E3 and E4, the correct evolution of the maximum point power and decrease in open-circuit power is confirmed, however the proportions are overestimated. These errors may be due to the translation equations, but most probably show a dependence of the

coefficients with the environmental conditions. Hence, a more accurate method would consist in using coefficients that are not constant, but rather dependent of the reference conditions.

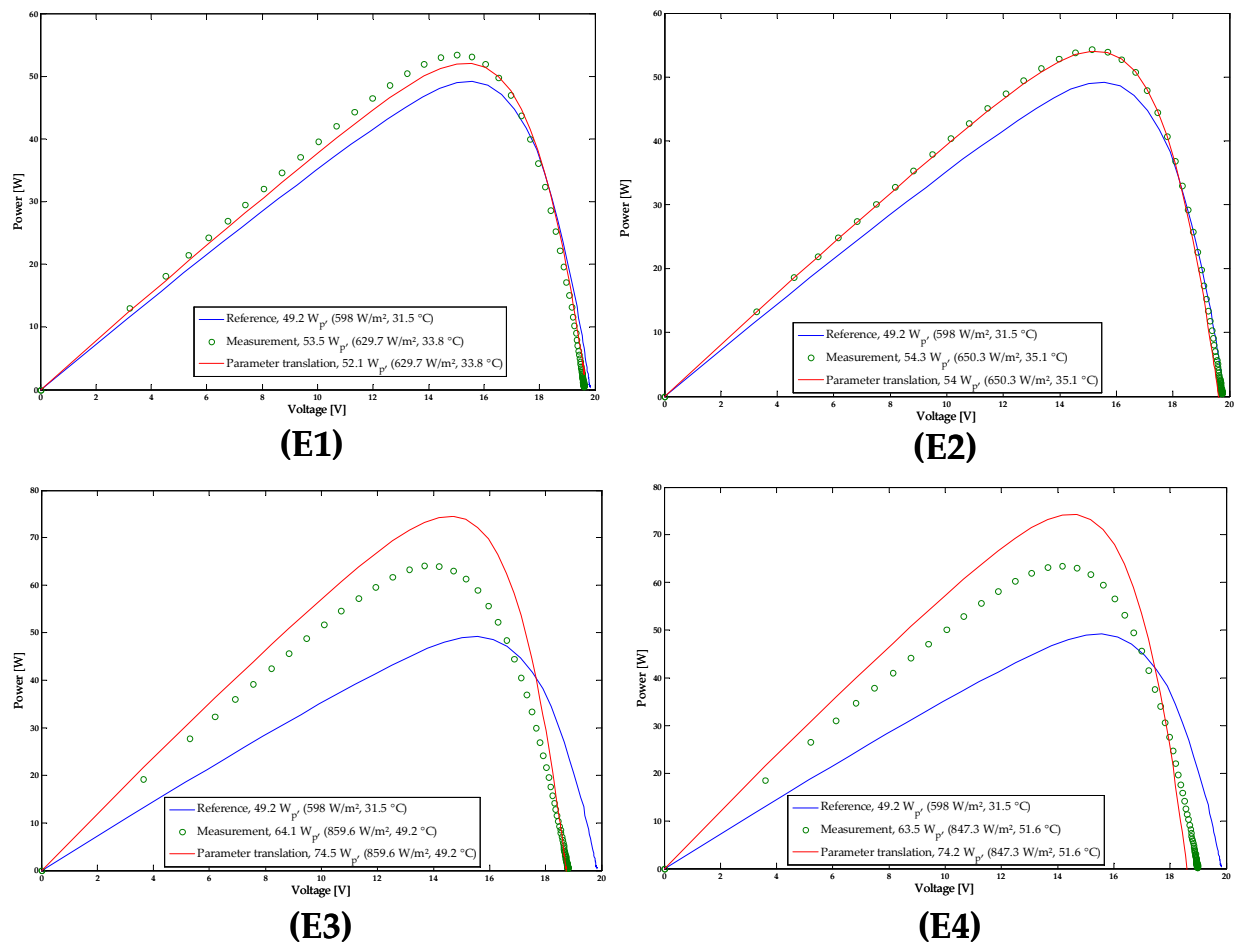


Figure A3.6 : Power-voltage characteristics of reference, measurement and translated curve results

Practical experience has shown that the limit to the validity of the parameter translation method with these coefficients is accurate when considering environmental condition dispersion from the reference condition of $200 W/m^2$ and $10^\circ C$. In this work, the parameter translations are within this limit, which guarantees an error limitation of at most 5% for maximum power point determination.

Comparison of Marion method and Parameter Translation Equations

The Marion method and parameter translation equations have been implemented in MATLAB/Simulink in order to compare the precision of the developed translation equations with respect to the well established Marion method. Two comparisons were carried using a given set of module parameters that have been translated from STC conditions to several irradiance conditions ($100, 200, 400, 600,$ and $800 W/m^2$) without modifying the temperature. The first test was done using an identical voltage values (in order to calculate the corresponding current) for both methods, whereas the second test used different voltage

values for both methods. Results of the comparison are presented on figures A3.7 and A3.8.

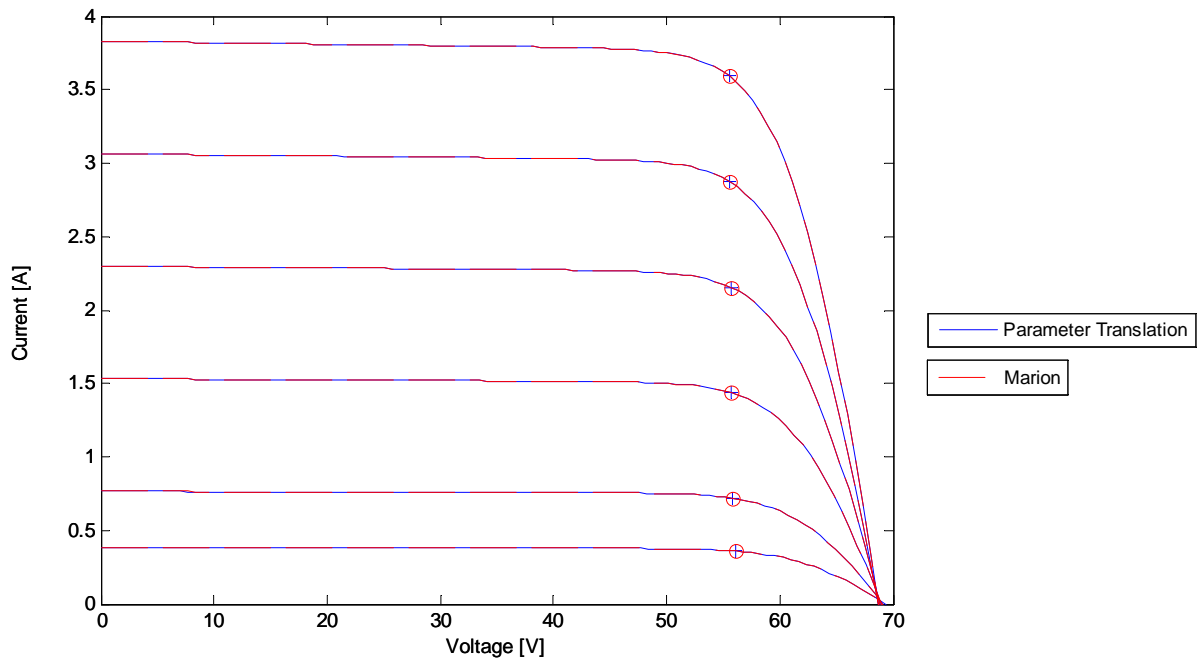


Figure A3.7 : Current-voltage characteristic of translation using both methods with the same voltage vector

In the first case, the I-V curves and maximum power points (red dot and blue cross) are superimposed.

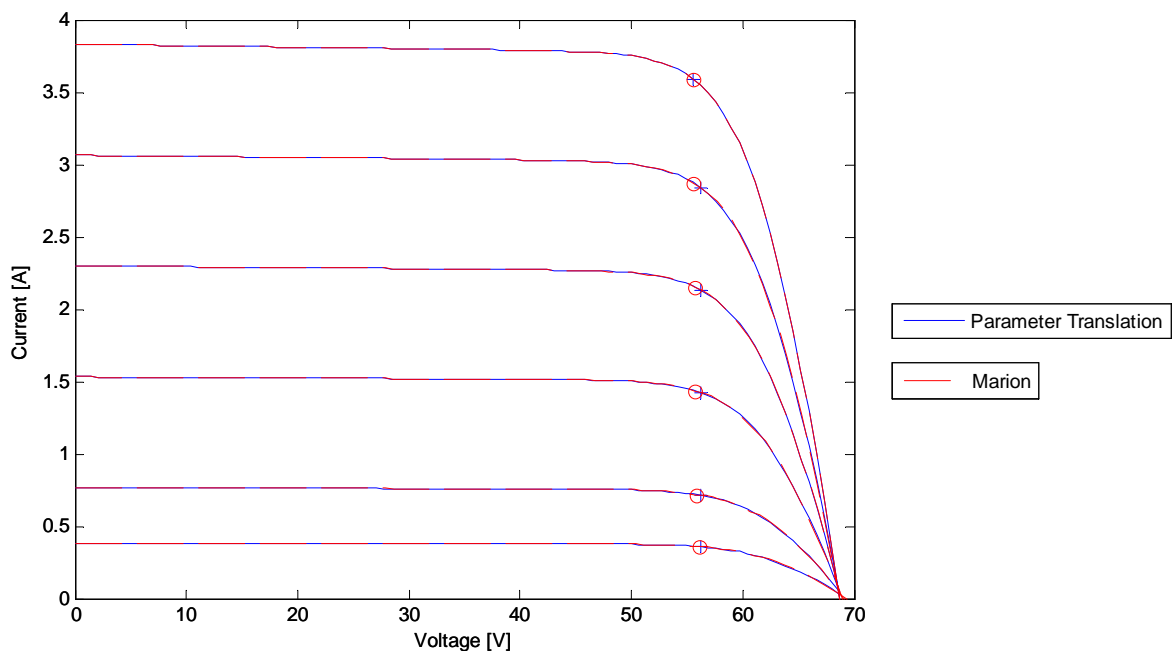


Figure A3.8 : Current-voltage characteristic of translation using both methods with different voltage vectors

In the second case, the I-V curves remain superimposed but the maximum power points are not. This is due to the differences between the voltage vectors used for both methods. Indeed, the maximum power points are located in the same area, but do not coincide, since only the voltage value closest to the MPP can be plotted.

Moreover, the evolution of the MPP with irradiance in these methods is unusual since the MPP voltage is almost constant. This is surely due to an error in the calculation of the open-circuit voltage correction factor for irradiance (δ) which has been underestimated and not the applied methodology..

ANNEX 4 :

Applying the Newton-Raphson method for PV array model solving

The purpose of this annex is to detail the procedure for determining the root of the array operation function F expressed in equation II.51. The solution is numerically determined using the iterative Newton-Raphson method applied to matrix equations, presented in equation II.53, where X_k is the root at iteration k , F the array operation function, and J the jacobian matrix of F .

$$X_{k+1} = X_k + J^{-1}(X_k) \times F(X_k) \quad \text{II.53.}$$

The unknown vector X , is made up of module voltages in the array. In the case of an array containing N strings containing M modules per string, the voltage vector contains the voltage x_k of each module M_k where $k \in [1, M \cdot N]$. The array operation function can be expressed thanks to the law matrixes ($FCmat$, $FVmat$ and $FDCbusVect$, cf. section II.5.3.2.), the PV module function f (cf. section II.2.4), and the unknown voltage vector X , as shown in A4.1.

$$F(X) = A \times X + B + C \times f(X) \quad \text{A4.1}$$

The Newton-Raphson procedure requires the calculation of the jacobian matrix for each step in the iteration. The following section will detail how this matrix is obtained.

□ Determining the jacobian matrix of the array operation function

The jacobian matrix is the equivalent of the derivative function applied to a matrix format. If we consider a vector X and the function F , as described in A4.2, the jacobian matrix of the function F at X can be written as shown on A4.3.

$$X = \begin{bmatrix} x_1 \\ \vdots \\ x_N \end{bmatrix} \quad F(X) = \begin{bmatrix} F_1(X) \\ \vdots \\ F_N(X) \end{bmatrix} = \begin{bmatrix} F_1(x_1, \dots, x_N) \\ \vdots \\ F_N(x_1, \dots, x_N) \end{bmatrix} \quad \text{A4.2}$$

$$J_F(X) = \frac{\partial F(X)}{\partial X} = \begin{bmatrix} \frac{\partial F_1(X)}{\partial x_1} & \frac{\partial F_1(X)}{\partial x_2} & \dots & \frac{\partial F_1(X)}{\partial x_{M \cdot N}} \\ \vdots & \vdots & \vdots & \vdots \\ \frac{\partial F_{M \cdot N}(X)}{\partial x_1} & \frac{\partial F_{M \cdot N}(X)}{\partial x_2} & \dots & \frac{\partial F_{M \cdot N}(X)}{\partial x_{M \cdot N}} \end{bmatrix} \quad \text{A4.3}$$

In our case, the F function can be expressed directly in terms of the input vector. Therefore, the calculation of the jacobian goes as follows:

$$J_F(X) = \frac{\partial}{\partial X} (A \times X + B) + \frac{\partial}{\partial X} (C \times f(X))$$

$$J_F(X) = A \times \frac{\partial}{\partial X}(X) + C \times \frac{\partial}{\partial X}[f(X)]$$

$$J_F(X) = A + C \times \frac{\partial f(X)}{\partial X}$$

Hence, the calculation of the jacobian matrix depends on the value of the derivative matrix. By referring to part II.2.4, we can notice that the f function uses the current-voltage relation (cf. equation II.48) for each module voltage x_k , and is independent of other module voltages. Therefore, the derivative matrix is a diagonal matrix having the derivative values at each line k.

□ Determining the derivative of the current-voltage function

The derivative of the current-voltage function, presented in equation II.31, is necessary for the jacobian matrix calculation as shown previously.

Let:

$$z_k = \frac{I_{o_k}}{V_{t_k}} \cdot R_{s_k} \cdot e^{\frac{x_k + R_{s_k} \cdot (I_{ph_k} + I_{o_k})}{V_{t_k}}} > 0$$

The current-voltage function can be expressed as a function of x_k and z_k as shown in A4.4.

$$f_k(x_k) = \frac{V_{t_k}}{R_{s_k}} \cdot \left[\frac{R_{s_k} \cdot (I_{ph_k} + I_{o_k})}{V_{t_k}} - W(z_k) \right] - \frac{x_k}{R_{sh_k}} \quad A4.4$$

Moreover, the LambertW-function derivative expression is presented in equation A4.5 and is valid for $z_k \neq 0$ [Corless 1996].

$$\frac{\partial W(z_k)}{\partial z_k} = \frac{W(z_k)}{z_k \cdot [1 + W(z_k)]} \quad A4.5$$

The calculation of the derivative of the current-voltage function leads to expression A4.6

$$\frac{\partial f_k(x_k)}{\partial x_k} = -\frac{V_{t_k}}{R_{s_k}} \cdot \frac{\partial W(z_k)}{\partial z_k} \cdot \frac{\partial z_k}{\partial x_k} - \frac{1}{R_{sh_k}} \quad A4.6$$

where:

$$\frac{\partial z_k}{\partial x_k} = \frac{I_{o_k}}{V_{t_k}} \cdot R_{s_k} \cdot \left(\frac{1}{V_{t_k}} \right) \cdot e^{\frac{x_k + R_{s_k} \cdot (I_{ph_k} + I_{o_k})}{V_{t_k}}} = \frac{z_k}{V_{t_k}} \quad A4.7$$

Hence, the resolution of equation A4.6 can be continued as follows:

$$\frac{\partial f_k(x_k)}{\partial x_k} = -\frac{V_{t_k}}{R_{s_k}} \cdot \frac{W(z_k)}{z_k \cdot [1 + W(z_k)]} \cdot \frac{z_k}{V_{t_k}} - \frac{1}{R_{sh_k}}$$

$$\frac{\partial f_k(x_k)}{\partial x_k} = -\left[\frac{1}{R_{s_k}} \cdot \frac{W(z_k)}{1 + W(z_k)} + \frac{1}{R_{sh_k}} \right]$$

In conclusion, the complete expression of the current-voltage function derivative takes form by replacing z_k , as presented in equation A4.8

$$\frac{\partial f_k(x_k)}{\partial x_k} = \left[\frac{1}{R_{s_k}} \cdot \frac{W \left(\frac{I_{o_k}}{V_{t_k}} \cdot R_{s_k} \cdot e^{\frac{x_k + R_{s_k} \cdot (I_{ph_k} + I_{k0})}{V_{t_k}}} \right)}{1 + W \left(\frac{I_{o_k}}{V_{t_k}} \cdot R_{s_k} \cdot e^{\frac{x_k + R_{s_k} \cdot (I_{ph_k} + I_{k0})}{V_{t_k}}} \right)} + \frac{1}{R_{sh_k}} \right] \quad A4.8$$

Furthermore, by using the approximation $R_{s_k} \ll R_{sh_k}$ to each module, the previous expression becomes A4.9

$$\frac{\partial f_k(x_k)}{\partial x_k} = - \frac{1}{R_{s_k}} \cdot \frac{W \left(\frac{I_{o_k}}{V_{t_k}} \cdot R_{s_k} \cdot e^{\frac{x_k + R_{s_k} \cdot (I_{ph_k} + I_{k0})}{V_{t_k}}} \right)}{1 + W \left(\frac{I_{o_k}}{V_{t_k}} \cdot R_{s_k} \cdot e^{\frac{x_k + R_{s_k} \cdot (I_{ph_k} + I_{k0})}{V_{t_k}}} \right)} \quad A4.9$$

All in all, the expression of the jacobian matrix of the array operation function can be expressed as follows:

$$J(X) = \begin{bmatrix} 0 \\ \text{FVmat} \\ \text{FDCbusVect} \end{bmatrix} + \begin{bmatrix} \text{FCmat} \\ 0 \\ 0 \end{bmatrix} \times \frac{\partial f(X)}{\partial X} \quad A4.10$$

where $\frac{\partial f(X)}{\partial X}$ is an $M \cdot N \times M \cdot N$ array of the form presented in A4.11

$$\frac{\partial f(X)}{\partial X} = \begin{bmatrix} \frac{\partial f(x_1)}{\partial x_1} & 0 & \dots & \dots & 0 \\ 0 & \ddots & 0 & 0 & \vdots \\ 0 & 0 & \frac{\partial f(x_k)}{\partial x_k} & 0 & 0 \\ \vdots & 0 & 0 & \ddots & \vdots \\ 0 & \dots & \dots & 0 & \frac{\partial f(x_{M \cdot N})}{\partial x_{M \cdot N}} \end{bmatrix} \quad A4.11$$

In conclusion to this annex, the complete procedure for solving the PV array equation system has been presented. This can be done by using the Newton-Raphson method in order to determine the root of the PV array operation function. The explicit formulas used in the iterative process have been detailed. It should be taken into account that the efficiency of this method depends on the initial guess to ensure proper convergence. The initial guess used in all simulations of this work supposes equal distribution of dc-bus voltage on the modules of the array. The research for an optimal initial guess, in order to reduce simulation time and increase precision, could help to raise the process performance.

ANNEX 5 : Toposolver Overview

The purpose of this annex is to briefly describe the software that has been developed to forecast the power output of photovoltaic arrays, baptized Toposolver. The graphical user interface that has been designed, in the Matlab environment, enables the user to easily simulate the power-voltage characteristic of customized arrays, albeit in: size, photovoltaic module technology, environmental conditions, array interconnection scheme and shade scenarios. Furthermore, measurement data may directly be used to compare with simulation results.

The main window, presented on Figure A5.1, allows the user to enter the size of the considered array and gives access to different menus allowing the user to completely customize their simulations: PV Module Properties, Shading Pattern, Toposolver parameters, Load Measurements, and Change Environmental conditions.

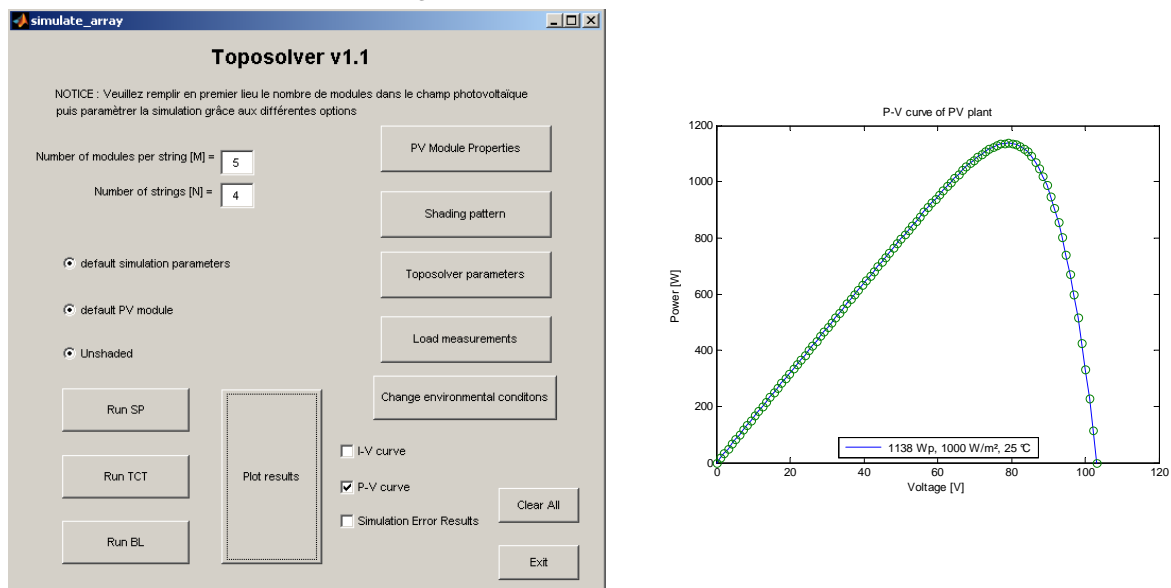


Figure A5.1 : (left) View of Toposolver main window, (right) example of P-V curve plot window using default settings

In the main window, default values have been set and the three principal array interconnection schemes have been predefined: SP, TCT, and BL. Finally, the user may visualize the current-voltage, power-voltage and simulation error results.

The PV module properties window, presented on Figure A5.2, is used to enter the specifications of the modules that make up the array. The user can either enter the specifications from the datasheet or directly enter the 5 parameters from the single-diode model.

The shading pattern window allows the user to simulate the array in four predefined scenarios: one shaded module, a string entirely shaded, each string has one module shaded, and a shade scenario along the diagonal. The shade factor for the shade scenario is entered

manually.

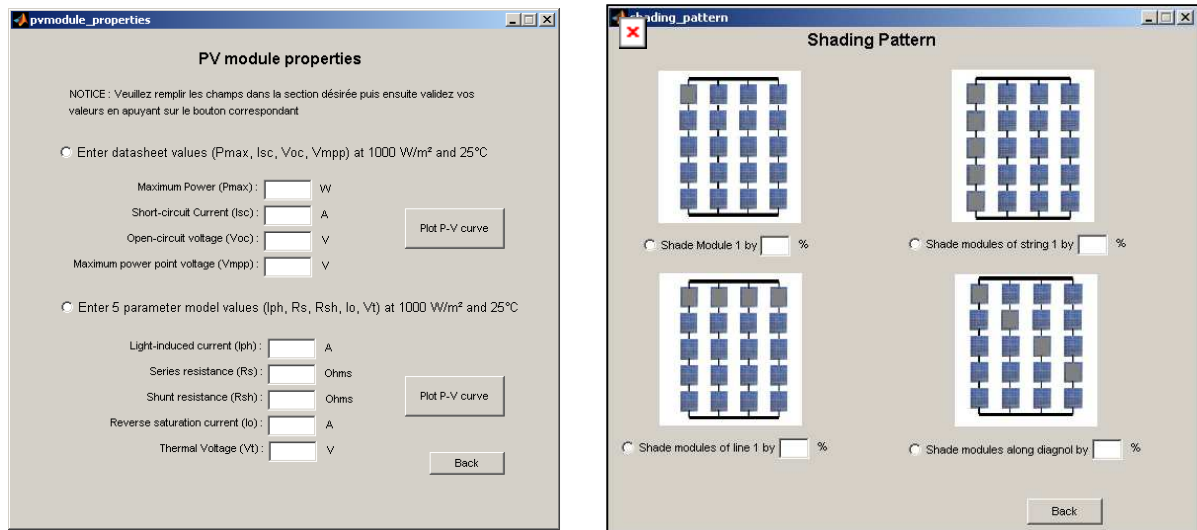


Figure A5.2 : (left) PV module properties window; (right) shading pattern window

The Toposolver simulation parameters window, presented on Figure A5.3, allows the user to change several parameters in the array calculation process such as: the number of points on the I-V and P-V characteristics, voltage and current tolerance values, the maximum number of iterations and function evaluations to be considered, and the possibility to use the Jacobian matrix for faster convergence.

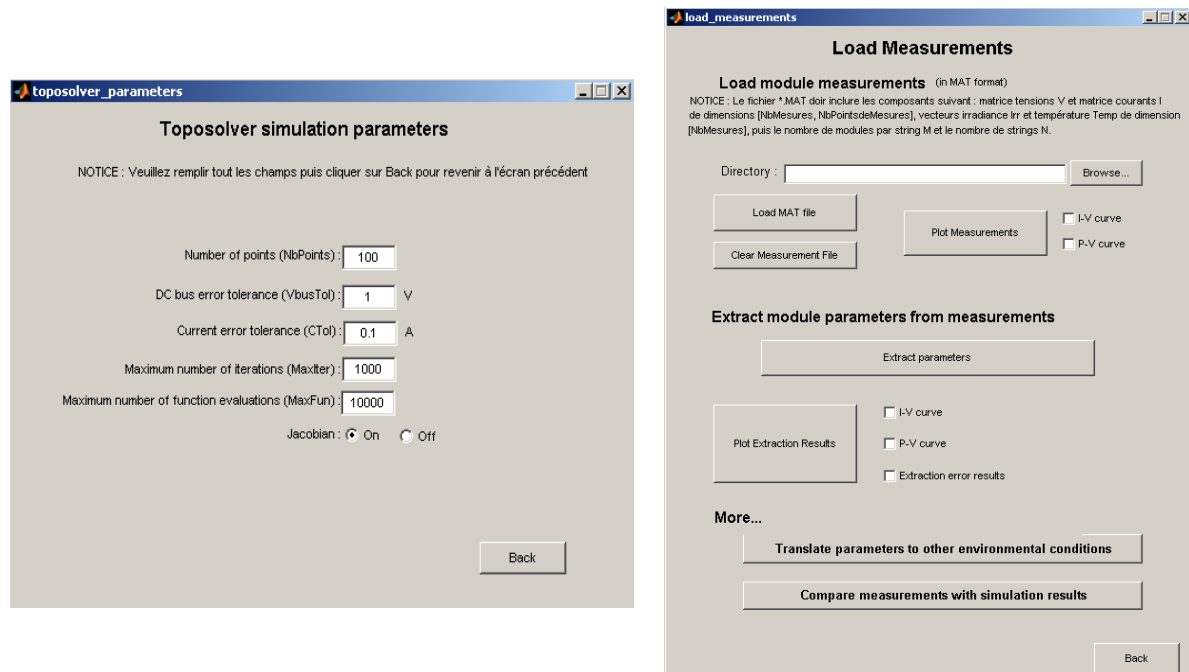


Figure A5.3 : (left) Toposolver simulation parameters window and (right) Load measurements window

The Load measurements window lets the user load experimental PV module measurements, in a Matlab format, extract the parameters from the experimental curves, translate them to desired environmental conditions. This process is very useful when forecasting the production of an array containing heterogeneous modules in which the assumption that each module is exactly the same is not applicable. Finally, the user may compare the simulated array results with the experimental I-V array curve reading to

evaluate the accuracy of the forecast.

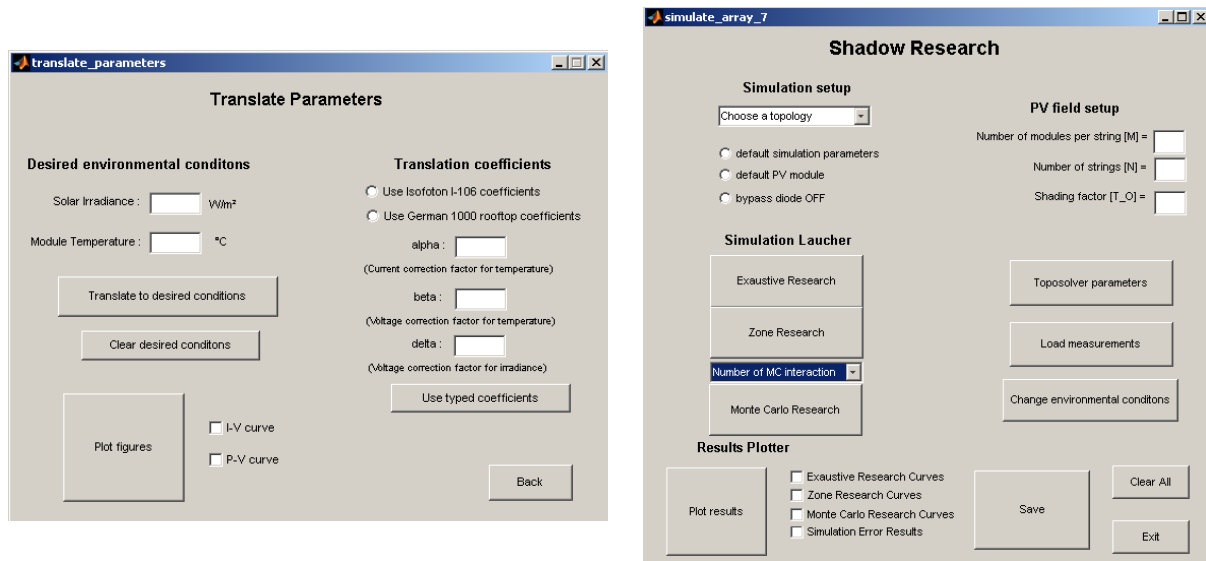


Figure A5.4 : (left) Translate parameters window (right) Shadow research window

Finally, the translate parameters window is used to define the parameter translation coefficients and environmental conditions to which the I-V curve will be translated. The predefined coefficients for the I-106 modules, shown in Annex 3, can be used or be entered manually.

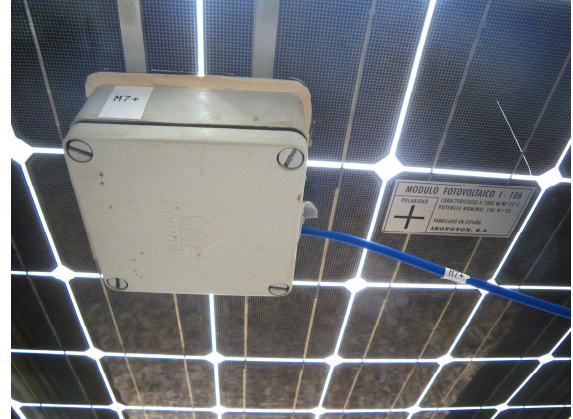
Following the internship of Luiz Lavado-Villa [LAV'10], an additional menu has been created, shown on Figure A5.4(right), for the study of internal and external mismatch. The study of intrinsic PV module mismatch is carried out using the Monte-Carlo research which generates random parameters that are constrained to a given maximum power range with respect to a reference power P_{max} (for example $\pm 5\% P_{max}$). Considering the study of environmental mismatch an exhaustive research can be carried out. In this, all the equivalent shade scenario possibilities (ie. different locations of the shaded modules) are tested for a given shade factor.

Further work on this program would be beneficial such as continuing the customization of the simulations, adding a PV module library in which characteristic parameters of modules are predefined, and eventually the translation of the program code to more universal computing languages (JAVA for example).

ANNEX 6 : Isofotón I-106 modules



Isofotón I-106 module



Junction box of I-106 module M7
with cracked cell

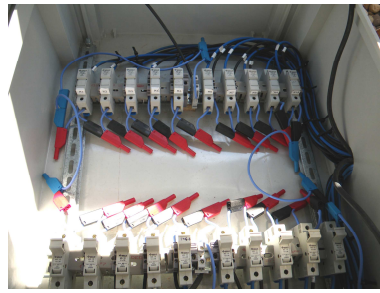
Electrical Characteristics		
<i>Standard Test Conditions : 1000 W/m² , 25°C, AM=1,5</i>		
Nominal Voltage (V _n)	12	V
Maximum Power (P _{max})	106	W
Short Circuit Current (I _{sc})	6,54	A
Open Circuit Voltage (V _{oc})	21,6	V
Maximum Power Point Current (I _{max})	6,1	A
Maximum Power Point Voltage (V _{max})	17,4	V
<i>Normal Operating Conditions : 800 W/m² , 20°C, AM=1,5</i>		
Maximum Power (P _{max})	76	W
Maximum Power Point Current (I _{max})	4,9	A
Maximum Power Point Voltage (V _{max})	15,5	V
Physical Characteristics		
Length (L)	1310	mm
Width (W)	654	mm
Height (H)	39,5	mm
Weight	11,5	kg
Number of cells (series / parallel)	36 / 2	

ANNEX 7 : Connection Box

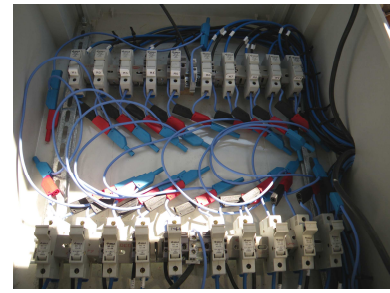
The connection box was designed to rapidly modify module interconnections of the array in order to compare different array arrangements in similar environmental conditions. The solution withheld consisted in bringing each module terminals to a connection box in which reorganization of the array is centralized. The connection box uses FIBOX CAB P705027 polyester cabinet in which four fixation rails have been added to install the electrical devices as can be seen on Figure A7.1.



Closed connection box



Pergola 5 plant in 2x10 array
with SP configuration



Pergola 5 plant in 2x10 array
with TCT configuration

Figure A7.1 : Views of connection box exterior and interior using different interconnection schemes

The connection box and fuses accept a 4 mm² cable size and a maximum current of 6.5 A, which is compatible with the I-106 module short circuit current at STC conditions. The fuses have a maximum allowable current of 6 A; this value for the fuses has been chosen for convenience and real value of the short-circuit current due to the ageing of the modules and the very rarely attained standard test conditions. MultiContact® plugs have been connected to the fuses and connection terminals, using a color code: red for the positive pole, black for the negative pole of the module. The plant topology can then be changed by connecting the MultiContact® plugs together thanks to previously hand-made wires with a blue MultiContact® plug at each end. An electrical scheme of the connection box is presented on Figure A7.2

The standard procedure for changing the topology configuration is as follows:

1. Disconnect the P5 inverter from the grid (AC side) and PV plant (DC side)
2. Open all fuse boxes in the connection box in order to ensure electric isolation from PV modules
3. Rearrange module connections in order to build the desired topology with blue MultiContact® plug wire.
4. Close all fuse boxes (with their fuses inside) in the connection box.
5. Reconnect the P5 inverter to the PV plant and utility grid.

This procedure lets the user change the connections between PV modules of the PV plant safely.

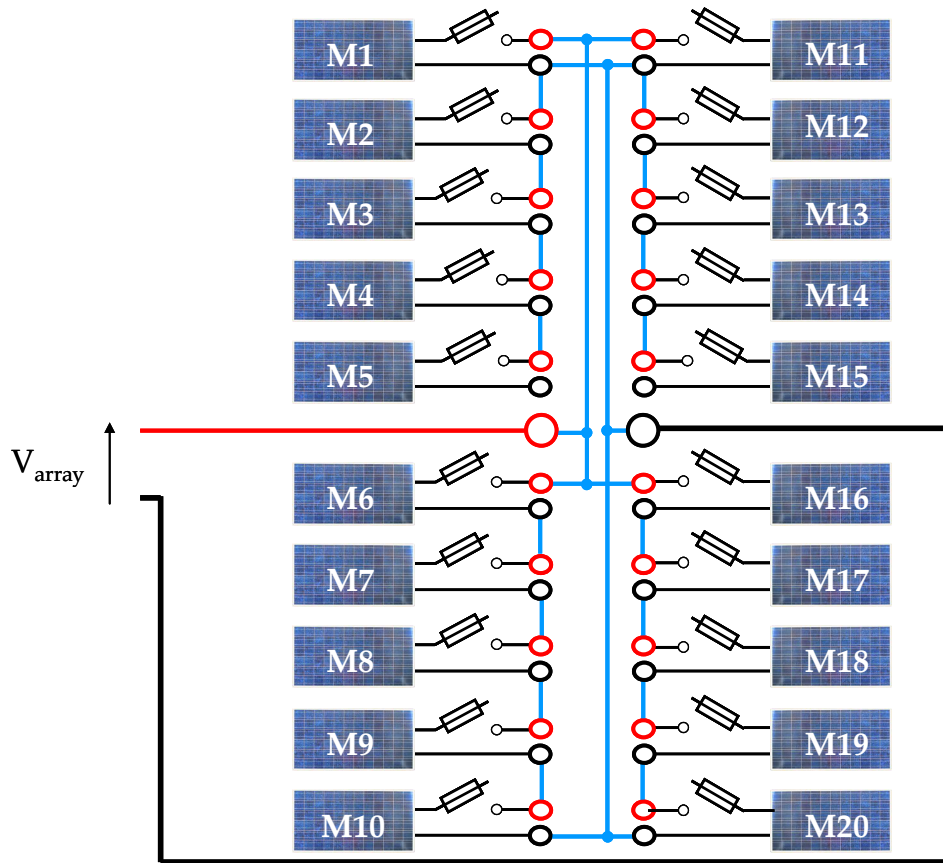


Figure A7.2 : Electrical scheme of connection box connected in a 5x4 array using SP configuration

ANNEX 8 : 200 W_p simulation PV module

The PV module used in the simulations is inspired by a commercial module SANYO HIP-200BA3 which uses a hybrid of monocrystalline silicon with ultra-thin amorphous silicon layers. Commercial module datasheets emphasize that the cell efficiency reaches 19.7%, whereas the module efficiency reaches 17%.

The 200 W_p simulation module has used the datasheet values of HIP-200BA3 module to determine parameters are shown on Figure A8.5. The single diode model parameters used for the simulation module are presented on Figure A8.7.

	Sanyo HIP-200BA3	200 W _p module
P_{max}	200 W	199,5 W
V_{MPP}	55,8 V	55,5 V
I_{MPP}	3,53 A	3,59 A
V_{oc}	68,7 V	68,7 V
I_{sc}	3,83 A	3,83 A

Figure A8.5 : Datasheet values of HIP-200BA3 and 200W_p simulation module

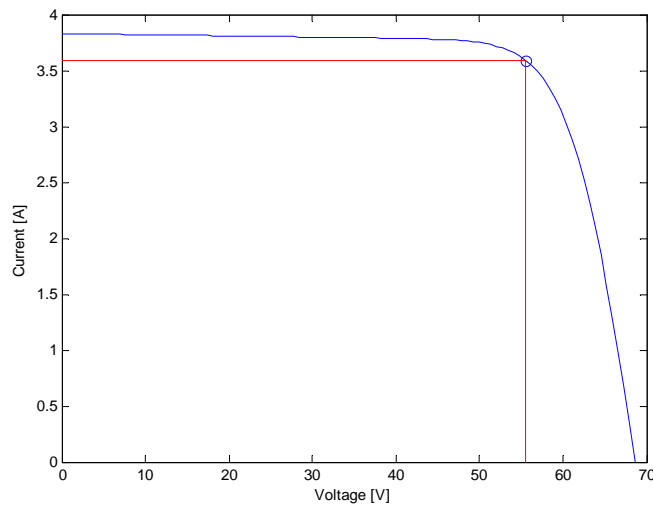


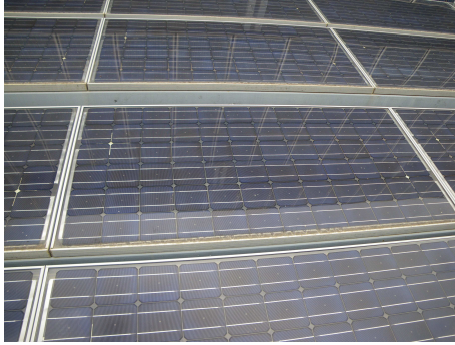
Figure A8.6 : Current-voltage characteristic of simulation module

I_{ph}	I_o	R_s	R_{sh}	V_t
3,83 A	3,3E-10 A	1,16 Ω	999 Ω	2,97 V

Figure A8.7 : Single diode model parameters of 200 W_p simulation module

ANNEX 9 : PV array power forecasting results

- Scenario N1 : non-shaded 5x4 array, SP @ 106.9 W/m², 17.3°C



Accumulated dusts are visible on module frame



Experimental conditions are carried out on a cloudy day

Figure A9.1 : Views of Pergola 5 plant on December 15th 2008

The simulation results, presented on Figure A9.2, show a shift on the P-V characteristic in between the experimental and the simulation curves. On the I-V curve, we can see that low voltage forecast contains a current error of approximately 0.3 A. This can be explained by the lack of precision during the low irradiance measurements of individual module characteristics ranging from 100-300 W/m², shown on Figure A9.3 which have then been translated to the array environmental conditions.

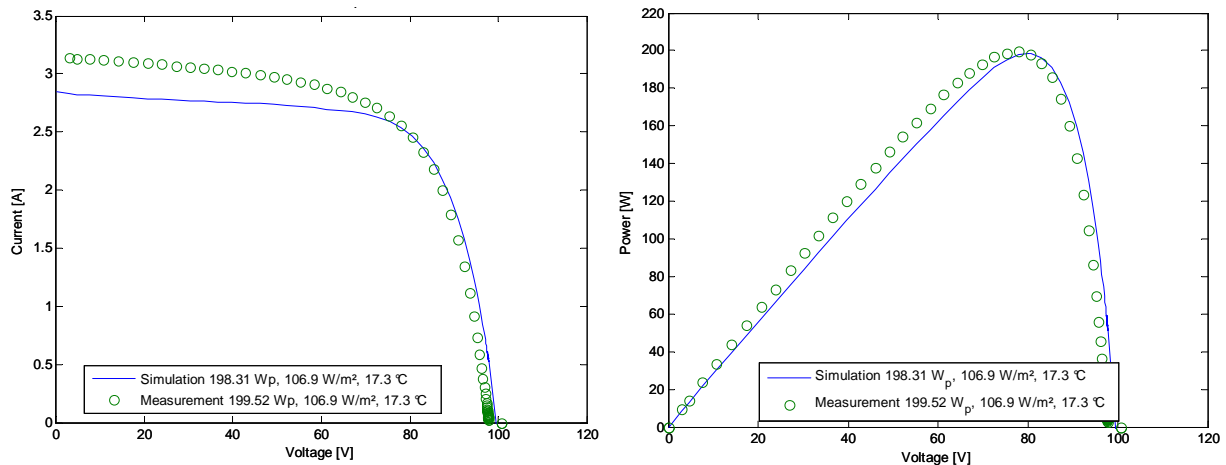


Figure A9.2 : Comparison of experimental and simulation results

However, the maximum power is very precise, with only a 1 W difference with the experimental measurements. Although the maximum power voltage is slightly shifted, we can see that in terms of maximum power forecast the simulation software is accurate.

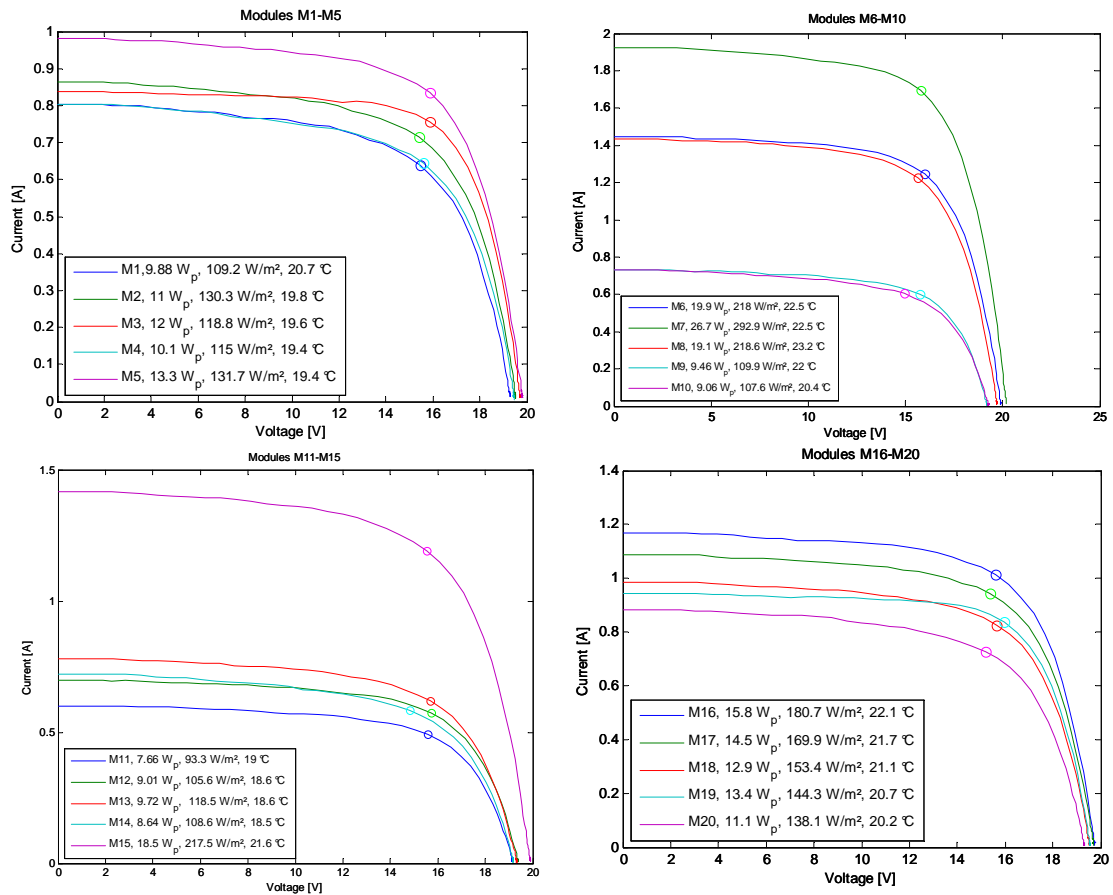


Figure A9.3 : I-V characteristics of modules taken at low irradiance

- **Scenario N2 : non-shaded 5x4 array, SP@(581 W/m^2 , 29.3°C), TCT@(592 W/m^2 , 29°C), and BL@(598 W/m^2 , 31.5°C)**



Pergola 5 array on clear day

Cell discoloration can be observed on module M5

Accumulated dirt on frame covers parts of the cells

Figure A9.4 : Views of Pergola 5 plant on December 18th 2008

In scenario N2, the simulation results coincide even more with experimental results. In scenario N1, Multi-Contact plugs were not yet installed on the connection box which made measurements last for over two hours. In this measurement, the Multi-Contact plugs have been installed and have reduced the entire experimental time to one hour. Thus leading to less dispersion in solar irradiance and temperature values as can be seen on Figure A9.5

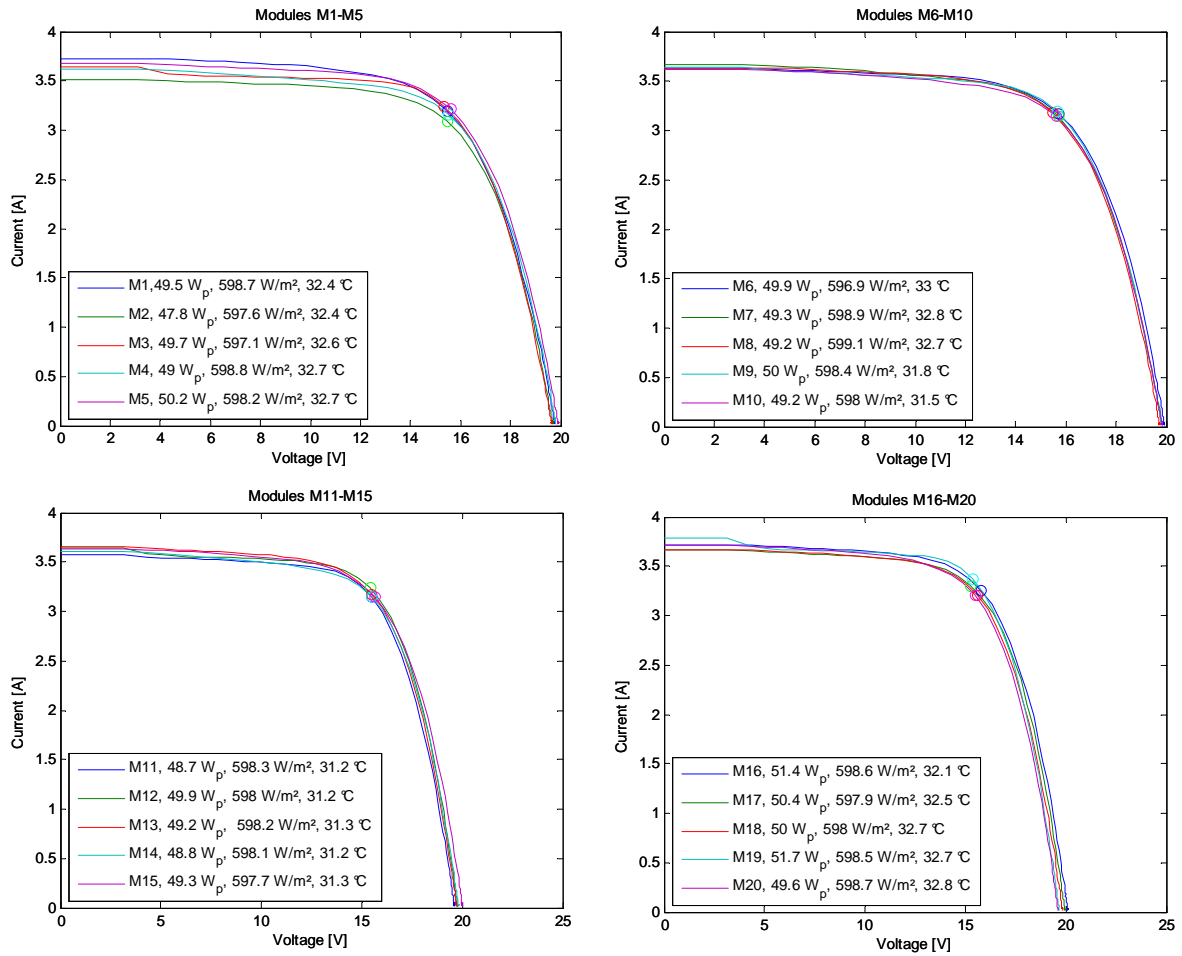


Figure A9.5 : I-V characteristics of modules in scenario N2

As can be seen on the module I-V curves, the batch of 20 modules do not have entirely the same power rating at equivalent environmental conditions. Simulated array results show good concordance with experimental results, both in the P-V curve shape and maximum power value.

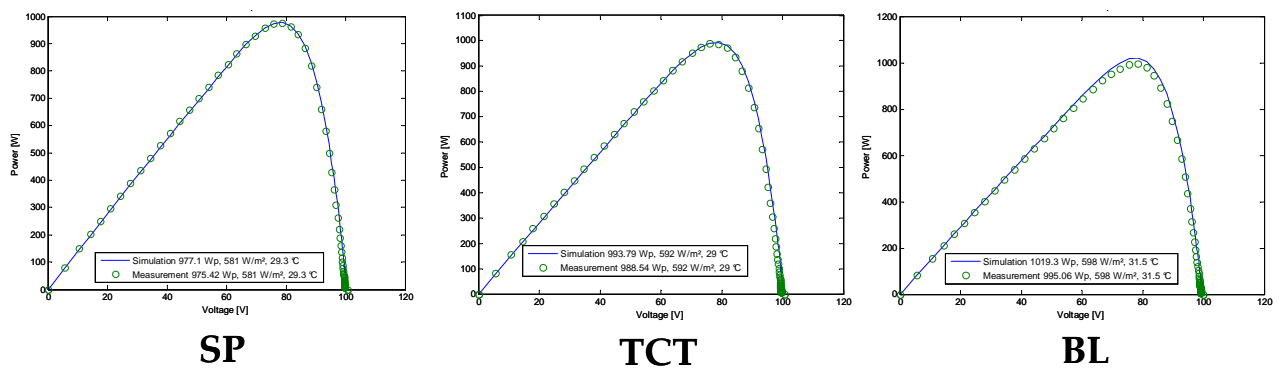
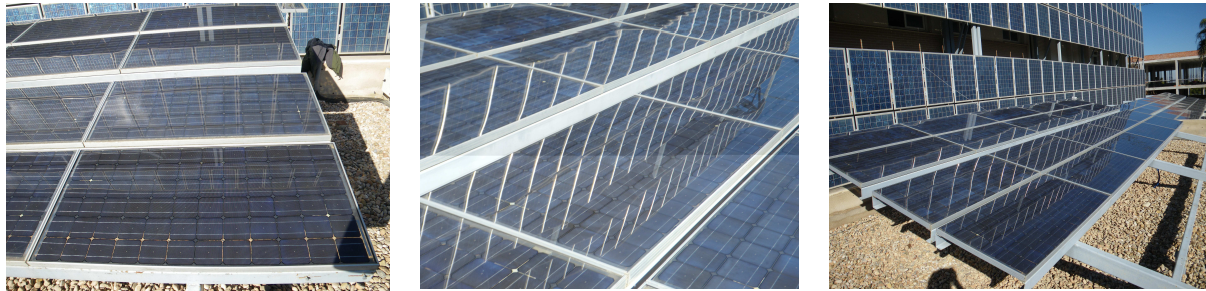


Figure A9.6 : P-V characteristics of Pergola 5 array arranged in a 5x4 array using SP, TCT, and BL topologies

- Scenario N3: non-shaded 5x4 array, SP@(633 W/m², 33.2°C),
 TCT@(633 W/m², 33.3°C), and BL@(631 W/m², 33°C)**



Cleaned module with discoloration of cells less visible

Dust traces have been cleaned off with window cleaning products

Pergola 5 array with cleaned modules

Figure A9.7 : Views of Pergola 5 array on January 12th 2009

The dispersion of module measurement environmental conditions varied more than scenario N2 with irradiances ranging from 620-633 W/m² and values are 32-35°C as shown on Figure A9.8

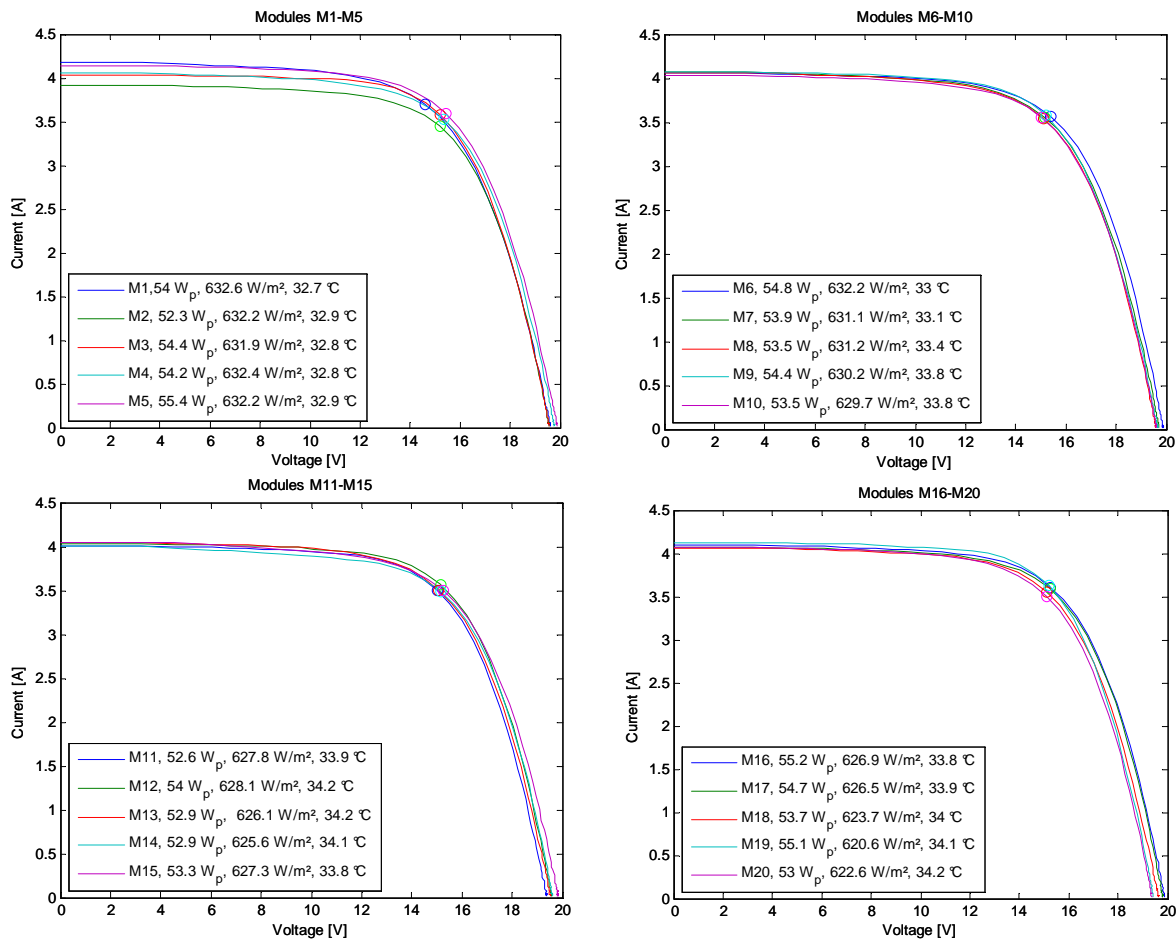


Figure A9.8 : Measured I-V characteristics of modules for scenario N3

As previously, simulation results predict a correct shape of the array characteristic and maximum power attains at most 20W difference (2% error) with the measured values, as can be observed on Figure A9.9.

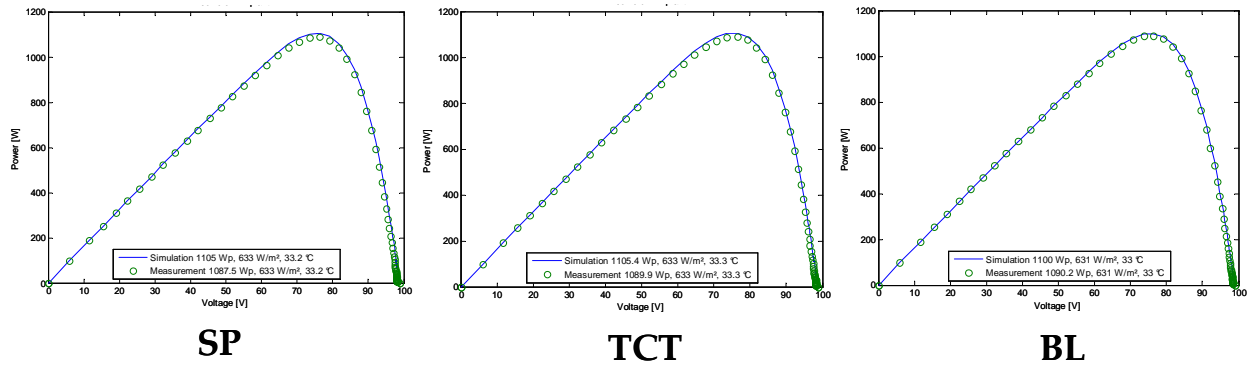


Figure A9.9 : Comparison of experimental and simulation results for scenario N3

- **Scenario S1 : partially shaded 5x4 array, SP@(650 W/m², 35.5°C), TCT@(651 W/m², 35.4°C), and BL@(650 W/m², 36°C)**



Module M1 is entirely covered by plastic film



Module M2 is partially covered by plastic film

Figure A9.10 : Views of Pergola 5 array on the January 14th 2009

In this partially shaded scenario, module M1 is entirely covered by a double layer of commercial bubble-wrap whereas module M2 has approximately 75% of its surface covered. The impact of the shade is clearly visible on Figure A9.12, where the short-circuit current is reduced by 33%.

Considering the simulation results, presented on Figure A9.11, the shape of the current-voltage characteristic is reproduced, but in all three cases the inflexion at low voltage is not sufficiently accurate. This can be explained by the bypass diode model that is quasi-ideal in the simulation model, which therefore leads to more abrupt curves in the 20-40 V range.

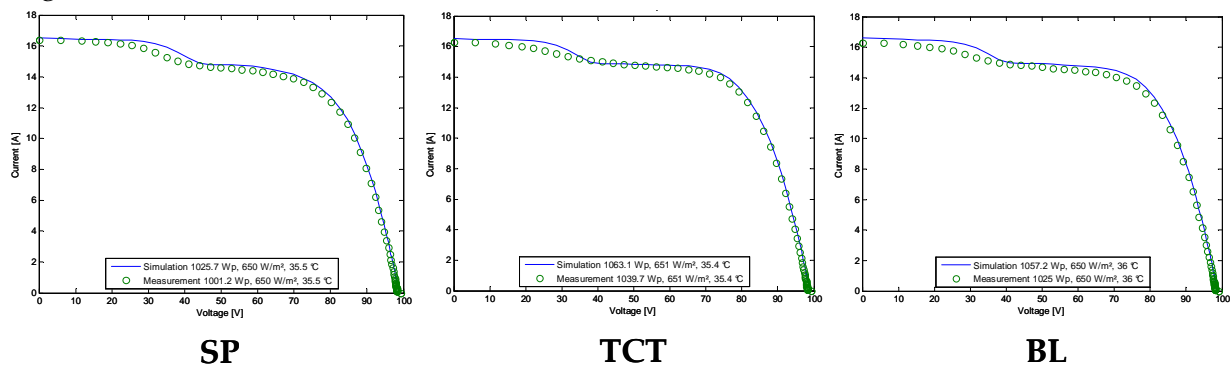


Figure A9.11 : Comparison of experimental and simulation results for scenario S1

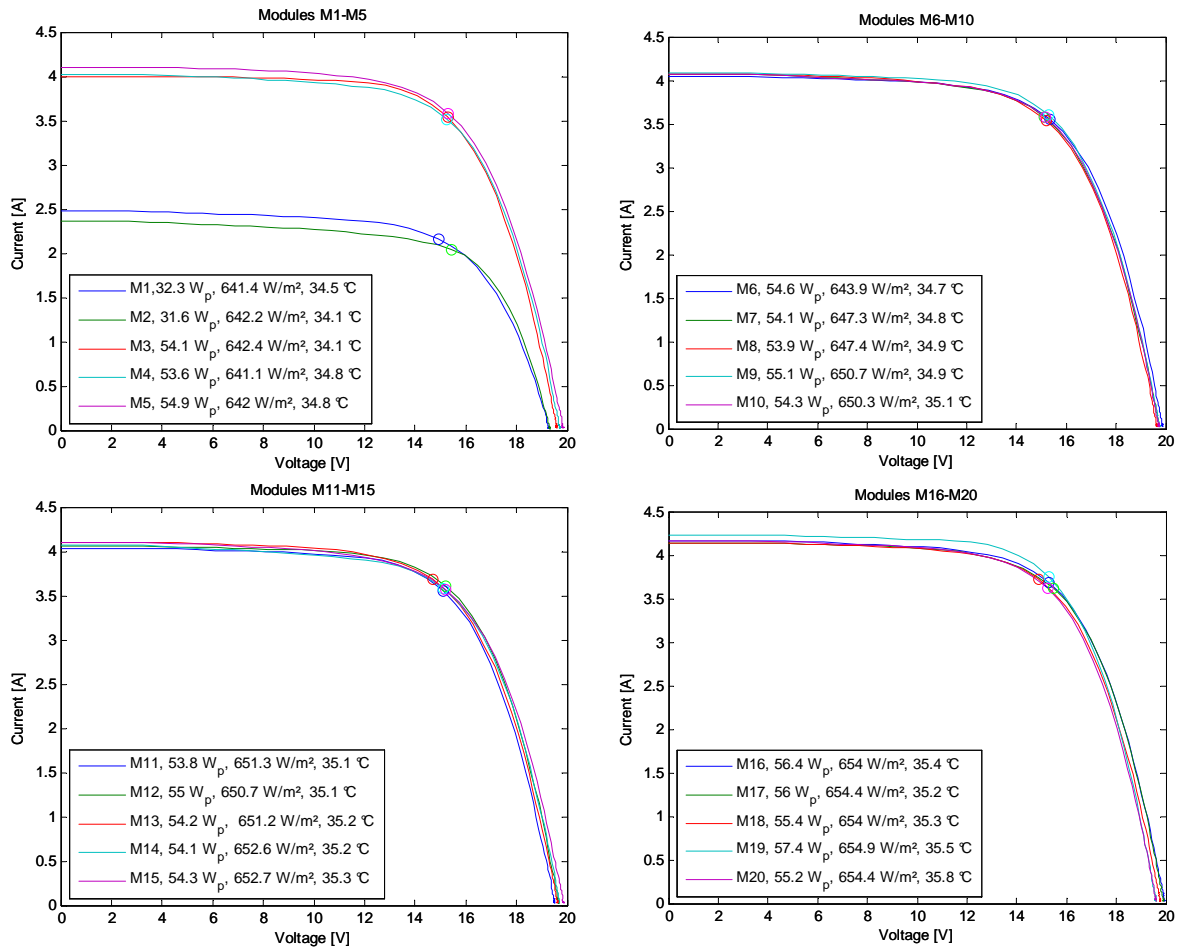


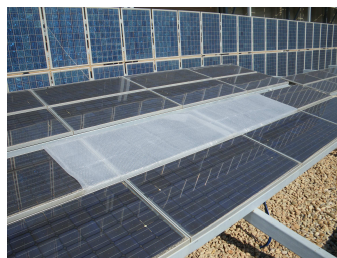
Figure A9.12 : Experimental I-V characteristics of modules in shade scenario S1

- **Scenario S2 : partially shaded 10x2 array, SP@(863 W/m², 50.2°C), TCT@(850 W/m², 50.7°C), and BL@(863 W/m², 51.3°C)**

In shade scenario S2, three modules have been shaded inducing approximately 33% shade factor on modules M7, M8, and M9. The measurements were taken on a clear sunny day, which explains the elevated solar irradiance level and module temperatures. As shown on Figure A9.14, maximum power of non-shaded modules average 65W whereas the shaded modules range from 40-50 W.



Pergola 5 array in shade scenarios S2 and S3



Modules M7 and M8 are entirely covered, and M9 is partially covered



Pergola 5 array solar irradiance and temperature sensor

Figure A9.13: View of Pergola 5 array on March 12th 2009

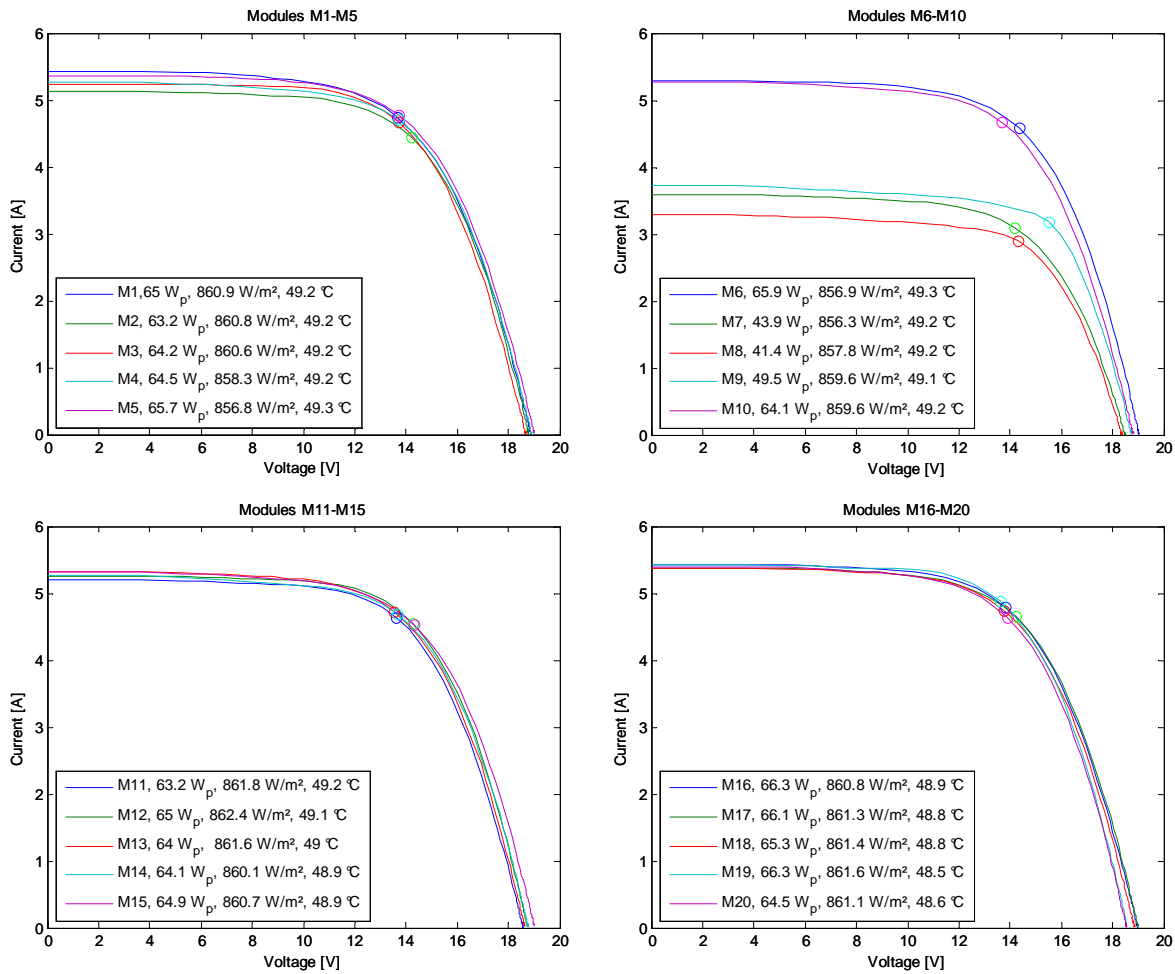


Figure A9.14 : I-V characteristics of modules recorded for scenarios S2 and S3

The simulation results presented on Figure A9.15 show a close prediction of power production for the SP arrangement ($\Delta P_{max}=2$ W, 0.2%) with a small error near the bypass diode deactivation zone in the 60-100V. However, the maximum power precision decreases in the TCT ($\Delta P_{max}=24$ W, 2%) and BL ($\Delta P_{max}=32.4$ W, 2.7%) arrangement, while remaining in an acceptable error margin. The bypass diode modelling and parameter extraction related errors are suspected causes for the differences in between experimental and simulation results.

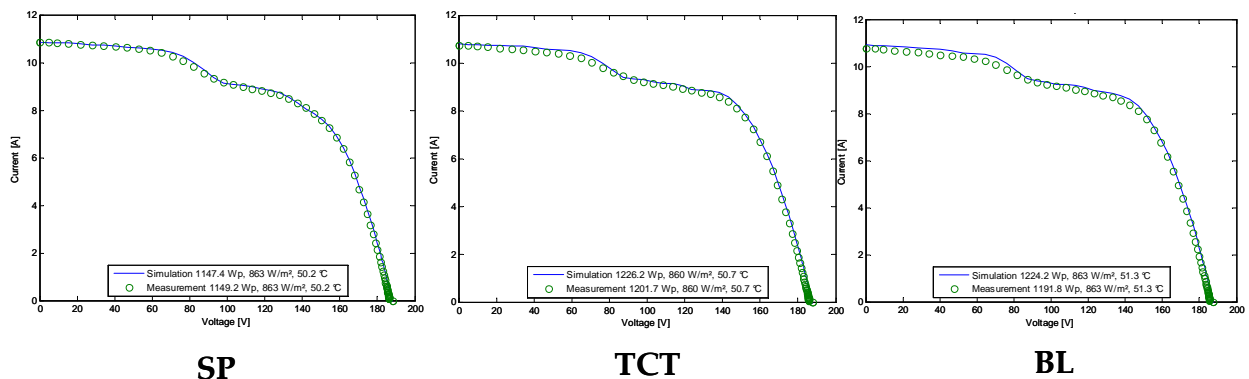


Figure A9.15 : Comparison of experimental and simulation results for scenario S2

- **Scenario S3: partially shaded 5x4 array, SP@(847 W/m², 47.5°C) and TCT@(848 W/m², 47.8°C)**

In scenario S3, the partial shading of modules is identical to scenario S2, but the array design has been modified into a 5x4 array. This is visible when noticing the decrease of open circuit voltage from approximately 190 V in a 10x2 array to 95 V in a 5x4 array. Confrontation of experimental and simulation results are presented on Figure A9.16. Results show that both shape and maximum power point precision are obtained in both SP ($\Delta P_{\max}=9.9$ W, 0.8%) and TCT ($\Delta P_{\max}=2.3$ W, 0.2%).

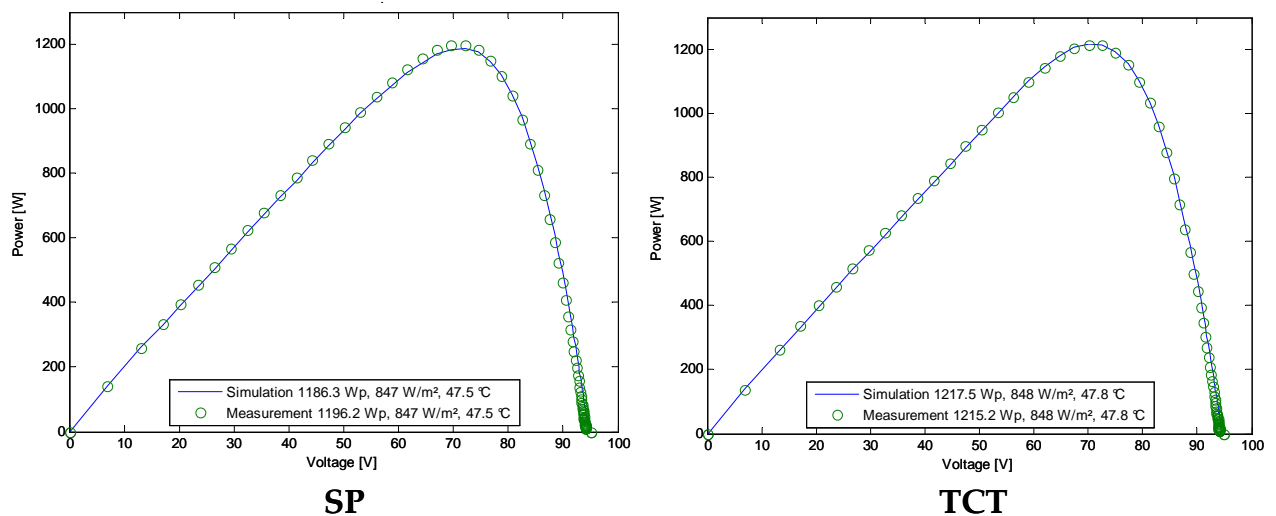


Figure A9.16 : Experimental and simulation results of scenario S3

- **Scenario S4: partially shaded 10x2 array, SP@(831 W/m², 50.2°C), TCT@(834 W/m², 51.2°C), and BL (840 W/m², 51.3°C)**



Modules M11 and M20 are entirely shaded



Shade scenario S4 and S5

Figure A9.17 : Views of Pergola 5 array on March 12th 2009

In shade scenario S4, the Pergola 5 array is arranged in a 10x2 array and has 4 partially shaded modules: M11 & M20 are entirely shaded and M12 & M19 are partially shaded. Experimental records of these modules show that modules M11 & M20 have a shade

factor of 50%, whereas modules M12 & M19 have 33% less incoming irradiance due to the plastic film mask as can be seen on Figure A9.18.

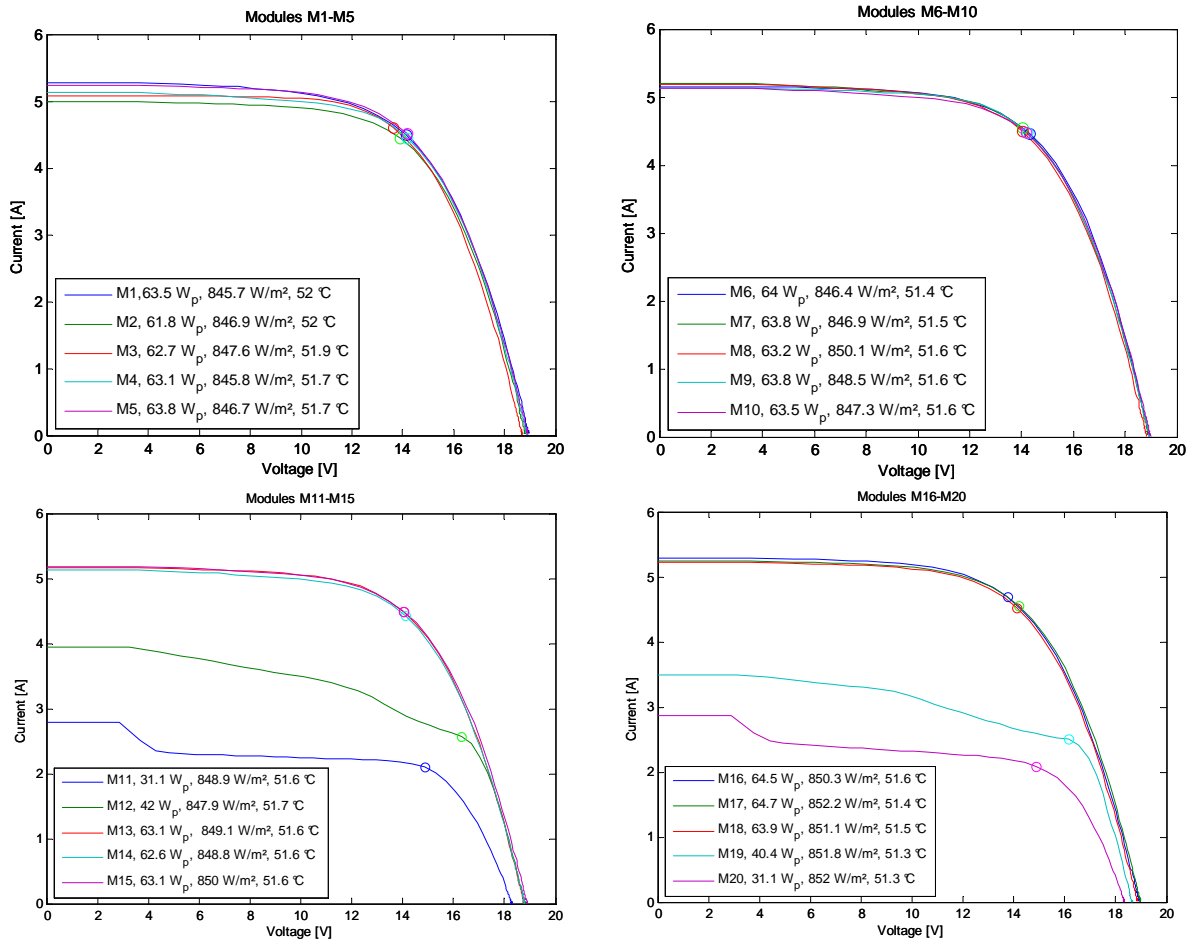


Figure A9.18 : I-V characteristics of modules in shade scenario S4 and S5

The shaded modules have characteristics that are not compatible with the one diode model, this leads to greater errors in the power production forecast as can be seen on Figure A9.19. Indeed, the difference between experimental values and predicted values for SP, TCT, and BL topologies are of 1 W (0.1%), 37.4 W (3.5%), and 28 W (2.6%) respectively.

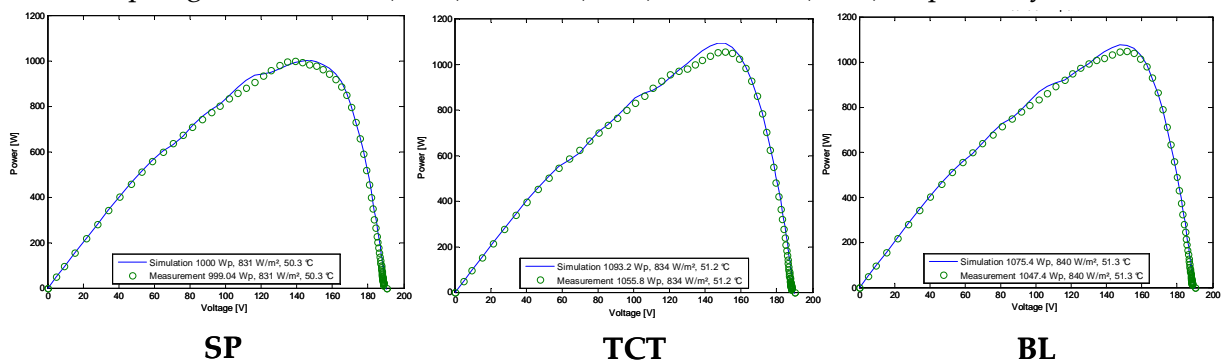


Figure A9.19 : Experimental and simulation results of scenario S4

- Scenario S5: partially shaded 5x4 array, SP@(810 W/m², 45.4°C),
TCT@(816 W/m², 46.3°C)**

In shade scenario S5, the covered modules remain the same. However, as previously, the array design has been changed into a 5x4 array. Power prediction results, presented below, show much more errors than in the previous shade scenario with forecast errors adding up to 13 W (1.3%) and 92.6W (9.2%) for SP and TCT respectively.

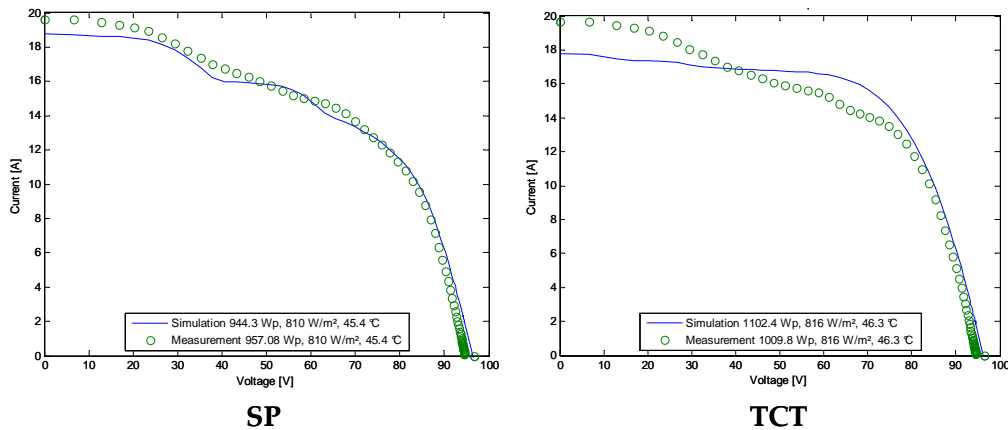


Figure A9.20 : Experimental and simulation results for shade scenario S5

These errors are believed to come from the one-diode model errors. Indeed, in longer strings the modelling error is reduced because of the larger amount of correctly modeled modules. However, when strings become shorter, the prediction is more sensitive to modelling precision due to the higher number of shaded modules in the string.

ANNEX 10 : Power electronics datasheet values

The power losses for each converter were determined using parameter values found on the components datasheet. Only the necessary values have been transcribed in this annex. Furthermore, some IGBT switches have integrated diodes, for this reason the same product number is used for both IGBT switches and diodes.

IGBT switches

Product Identification	Manufacturer	V_{CE0}	R_{CE}	E_{ON}	E_{OFF}	V_{REF}	I_{REF}
SKM 145GB066D	SEMIKRON www.semikron.com	0,85 V (@ $V_{GE}=15V, T_J=125^{\circ}C$)	0,008 Ω (@ $V_{GE}=15V, T_J=125^{\circ}C$)	8500 μJ	5500 μJ	300 V	150 A
IRGB4062DPbF	International Rectifier www.irf.com	1 V (@ $V_{GE}=15V, T_J=175^{\circ}C$)	0,033 Ω (@ $V_{GE}=15V, T_J=175^{\circ}C$)	420 μJ	840 μJ	400 V	24 A
IRGB4060DPbF	International Rectifier www.irf.com	1 V (@ $V_{GE}=15V, T_J=175^{\circ}C$)	0,113 Ω (@ $V_{GE}=15V, T_J=175^{\circ}C$)	165 μJ	240 μJ	400 V	8 A
IRGB4059DPbF	International Rectifier www.irf.com	0,92 V (@ $V_{GE}=15V, T_J=175^{\circ}C$)	0,303 Ω (@ $V_{GE}=15V, T_J=175^{\circ}C$)	40 μJ	120 μJ	400 V	4 A

Table A10.1 : IGBT switches datasheet values

MOSFET switches

Product Identification	Manufacturer	R_{DSON}	t_{ON}	t_{OFF}	C_{OSS}
SIHF640	VISHAY www.vishay.com	0,288 Ω	51 ns	36 ns	430 pF

Table A10.2 : MOSFET switch datasheet values

Diodes

Product Identification	Manufacturer	U_{D0}	R_D	Q_{RR}
MBR10200CT	TAIWAN SEMICONDUCTOR www.tmsc.com	0,976 V	0,004 Ω	0 μJ
15ETH06	VISHAY www.vishay.com	0,731 V	0,023 Ω	0 μJ
150K60	International Rectifier www.irf.com	0,775 V	0,001 Ω	0 μJ
SKM 145GB066D	SEMIKRON www.semikron.com	0,7 V *	0,01 Ω *	3500 μJ
IRGB4062DPbF	International Rectifier www.irf.com	0,7 V *	0,01 Ω *	621 μJ
IRGB4060DPbF	International Rectifier www.irf.com	0,7 V *	0,01 Ω *	165 μJ
IRGB4059DPbF	International Rectifier www.irf.com	0,7 V *	0,01 Ω *	145 μJ

* estimated values

Table A10.3 : Diode datasheet values

ANNEX 11 : PI corrector coefficient calculations

The purpose of this annex is to detail the calculations of the PI corrector coefficients used in the grid-connected inverter and Boost converter. The PI corrector calculations will be presented beginning with the fastest time constants to the slowest ones, in other words from the inverter controller to the PV voltage controller.

▪ Inverter current control C_1

The PI controller C_1 is used to control the grid-fed current by respecting grid frequency and harmonic distortion constraints. Since the inverter control is the fastest control loop, that is to say with the smallest time constant, the DC bus voltage can be considered constant with respect to the grid-fed current control dynamics. By using the equations presented in Figure A11.1, the closed loop transfer function $CLTF_1(p)$ between the inverter duty cycle (β_{INV}) and grid-fed current (I_{GRID}) can be determined.

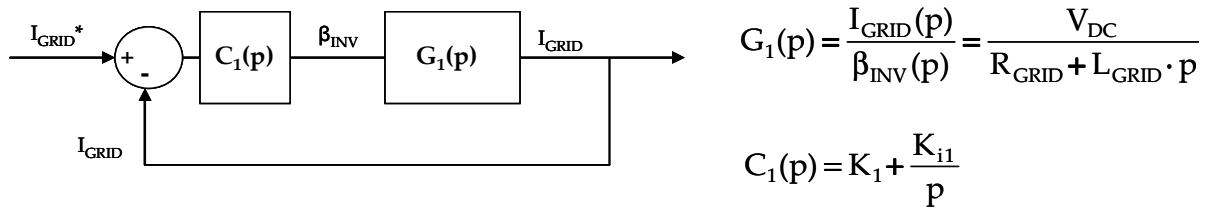


Figure A11.1 : (right) Inverter current control diagram and (left) associated equations

Considering the order of transfer functions $C_1(p)$ and $G_1(p)$, the $CLTF_1$ will be a transfer function of second order. The objective is to put $CLTF_1(p)$ into the characteristic format $H(p)$ using the process time constant τ_1 , the damping factor ζ_1 , and the numerator $NUM(p)$ as shown in equation A11.1.

$$H(p) = \frac{NUM(p)}{1 + 2 \cdot \tau_1 \cdot \xi_1 \cdot p + \tau_1^2 \cdot p^2} \quad A11.1$$

The calculation of the closed loop transfer function is presented below.

$$CLTF_1(p) = \frac{C_1(p) \cdot G_1(p)}{1 + C_1(p) \cdot G_1(p)} = \frac{\left(1 + \frac{K_{i1}}{K_1} \cdot p\right)}{1 + \left(\frac{K_1}{K_{i1}} + \frac{R_{GRID}}{V_{DC} \cdot K_{i1}}\right) \cdot p + \frac{L_{GRID}}{V_{DC} \cdot K_{i1}} \cdot p^2} \quad A11.2$$

Using this last relationship, the PI corrector coefficients K_1 and K_{i1} can be expressed as functions of R_{GRID} , L_{GRID} , and V_{DC} by identification to $H(p)$, as shown in equation A11.3.

$$\begin{cases} 2 \cdot \xi_1 \cdot \tau_1 = \frac{1}{K_{i1}} \cdot \left(K_1 + \frac{R_{GRID}}{V_{DC}}\right) \\ \tau_1^2 = \frac{L_{GRID}}{V_{DC} \cdot K_{i1}} \end{cases} \Rightarrow \begin{cases} K_1 = \frac{2 \cdot \xi_1 \cdot L_{GRID}}{V_{DC} \cdot \tau_1} - \frac{R_{GRID}}{V_{DC}} \\ K_{i1} = \frac{L_{GRID}}{V_{DC} \cdot \tau_1^2} \end{cases} \quad A11.3$$

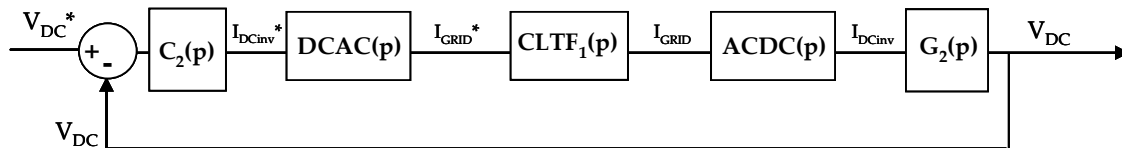
The parameters used in the simulations are presented in Table A11.4. The grid inductance and resistance values represent the order of magnitude from the low voltage grid. The time constant has been chosen considering the control frequency of the power switches to be equal to 1 MHz. Finally, the damping factor has been chosen since the value is an optimal solution for the convergence speed and oscillation compromise for second order systems.

V_{DC}	L_{GRID}	R_{GRID}	τ_1	ζ_1	K_1	K_{i1}
400 V	1 mH	10 m Ω	10 μ s	0.7	0,35	25000

Table A11.4 : Parameters for inverter current control

▪ DC bus voltage control C_2

The DC bus voltage controller C_2 is also a PI controller that takes into account several intermediate blocs DCAC, $CLTF_1$, and ACDC. The DCAC control uses a phase-locked loop and power conservation equation to convert the input DC reference current to the sinusoidal AC reference by taking into account the different voltage levels from the DC side (400 V) and grid side (230 V_{RMS}). The $CLTF_1$ was described in the previous section. Its time constant being the fastest of the PV system, it can be considered as a unitary gain. This can be verified by considering $p \gg 1$, that is to say when it attains its steady state operation, using equation A11.2.



$$G_2(p) = \frac{V_{DC}(p)}{I_{DCinv}(p)} = \frac{-1}{C_{DC} \cdot p} \quad C_2(p) = K_2 + \frac{K_{i2}}{p}$$

Figure A11.2 : DC bus voltage control diagram

Lastly, the ACDC bloc uses grid-fed current to determine the amount of input DC current that has been extracted from the DC bus, by using RMS measurement devices and power conservation equations. The DCAC and ACDC transformation blocs have been considered to have instantaneous time constants in this work. The complete control scheme is presented on Figure A11.2.

As explained in the previous section, the closed-loop transfer function $CLTF_2$ will be determined and parameters will be identified to characteristic second order transfer function H to calculate the coefficients. The expression of $CLTF_2$ is shown on equation A11.4.

$$CLTF_2(p) = \frac{C_2(p) \cdot G_2(p)}{1 + C_2(p) \cdot G_2(p)} = \frac{\left(1 + \frac{K_2}{K_{i2}} \cdot p\right)}{1 + \left(\frac{K_2}{K_{i2}}\right) \cdot p - \frac{C_{DC}}{K_{i2}} \cdot p^2} \quad A11.4$$

The calculation of coefficients can then be carried out as follows:

$$\begin{cases} 2 \cdot \xi_2 \cdot \tau_2 = \frac{K_2}{K_{i2}} \\ \tau_2^2 = \frac{-C_{DC}}{K_{i2}} \end{cases} \Rightarrow \begin{cases} K_2 = \frac{-2 \cdot \xi_2 \cdot C_{DC}}{\tau_2} \\ K_{i2} = \frac{-C_{DC}}{\tau_2^2} \end{cases} \quad \text{A11.5}$$

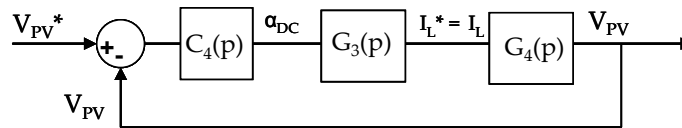
The simulation parameters and resulting corrector coefficients are presented on Table A11.5. Here, the time constant has been chosen to be one hundred times greater than the inner loop time constant τ_1 .

C_{DC}	τ_2	ζ_2	K_2	K_{i2}
500 μF	1 ms	0.7	-0,20	-500

Table A11.5 : Simulation parameters for DC bus voltage control

▪ PV array voltage controller C_4

The last PI controller is used to control the PV array voltage whose reference value is assigned by the maximum power point tracking (MPPT) algorithm. In reality, an additional control must be implemented in the Boost converter (G_3) to control the input current, but the use of the reduced mean model has disregarded the dynamic of the input current control. Therefore, the Boost converter can be reduced to a simple gain as shown on Figure A11.3.



$$G_3(p) = \frac{I_L^*(p)}{\alpha_{DC}(p)} = \frac{V_{DC}}{R_{BOOST}} \quad G_4(p) = \frac{V_{PV}(p)}{I_L(p)} = \frac{-1}{C_{PV} \cdot p} \quad C_4(p) = K_4 + \frac{K_{i4}}{p}$$

Figure A11.3 : PV array voltage control scheme

Hence, the control the PV array voltage using a voltage reference value produced by the MPPT is done using the capacitor C_{PV} . Following the same methodology as described previously, the CLTF₄ obtained is presented in equation A11.6.

$$\text{CLTF}_4(p) = \frac{C_4(p) \cdot G_4(p)}{1 + C_4(p) \cdot G_4(p)} = \frac{1 + \frac{K_4}{K_{i4}} \cdot p}{1 + \frac{K_4}{K_{i4}} \cdot p - \frac{C_{PV}}{K_i} \cdot p^2} \quad \text{A11.6}$$

Likewise, the corrector coefficients are determined using equation A11.7.

$$\begin{cases} 2 \cdot \xi_4 \cdot \tau_4 = \frac{K_4}{K_{i4}} \\ \tau_4^2 = -\frac{C_{PV}}{K_{i4}} \end{cases} \Rightarrow \begin{cases} K_4 = -\frac{2 \cdot \xi_4 \cdot C_{PV}}{\tau_4} \\ K_{i4} = -\frac{C_{PV}}{\tau_4^2} \end{cases} \quad \text{A11.7}$$

The simulation parameters and resulting corrector coefficients are presented on Table A11.6. The time constant τ_4 has been chosen to be ten times greater than that of the inverter

control loop. Here, the time constant of the Boost Converter (τ_3) has not been considered, since the use of the reduced-average model supposes the converter's dynamic is instantaneous.

C_{PV}	τ_4	ζ_4	K_4	Ki_4
500 μ F	10 ms	0.7	-0,07	-5

Table A11.6 : Simulation parameters for DC bus voltage control

In conclusion to this annex, the explicit calculation method for determining the PI controller coefficients have been presented. Furthermore, attention should be brought to the different time constants of the each control (ie. $\tau_1 < \tau_2 < \tau_4$) to ensure correct operation of the global control strategy of the multi-looped system.

Post Scriptum

Thank you for reading up to this point!

Merci à ceux qui en sont arrivés jusque là!

¡Gracias a los que han llegado hasta este punto!